

SOLID-STATE SCIENCES

T. Nakayama
K. Yakubo

Fractal Concepts in Condensed Matter Physics



Springer

Springer-Verlag Berlin Heidelberg GmbH



<http://www.springer.de/phys/>

Springer Series in **SOLID-STATE SCIENCES**

Series Editors:

M. Cardona P. Fulde K. von Klitzing R. Merlin H.-J. Queisser H. Störmer

The Springer Series in Solid-State Sciences consists of fundamental scientific books prepared by leading researchers in the field. They strive to communicate, in a systematic and comprehensive way, the basic principles as well as new developments in theoretical and experimental solid-state physics.

- 126 **Physical Properties of Quasicrystals**
Editor: Z.M. Stadnik
- 127 **Positron Annihilation in Semiconductors**
Defect Studies. By R. Krause-Rehberg and H.S. Leipner
- 128 **Magneto-Optics**
Editors: S. Sugano and N. Kojima
- 129 **Computational Materials Science**
From Ab Initio to Monte Carlo Methods
By K. Ohno, K. Esfarjani, and Y. Kawazoe
- 130 **Contact, Adhesion and Rupture of Elastic Solids**
By D. Maugis
- 131 **Field Theories for Low-Dimensional Condensed Matter Systems**
Spin Systems and Strongly Correlated Electrons
By G. Morandi, P. Sodano, A. Tagliacozzo, and V. Tognetti
- 132 **Vortices in Unconventional Superconductors and Superfluids**
Editors: R.P. Huebener, N. Schopohl, and G.E. Volovik
- 133 **The Quantum Hall Effect**
By D. Yoshioka
- 134 **Magnetism in the Solid State**
By P. Mohn
- 135 **Electrodynamics of Magnetoactive Media**
By I. Vagner, B.I. Lembrikov, and P. Wyder
- 136 **Nanoscale Phase Separation and Colossal Magnetoresistance**
The Physics of Manganites and Related Compounds. By E. Dagotto
- 137 **Quantum Transport in Submicron Devices**
A Theoretical Introduction. By W. Magnus and W. Schoenmaker
- 138 **Phase Separation in Soft Matter Physics**
Micellar Solutions, Microemulsions, Critical Phenomena
By P.K. Khabibullaev and A.A. Saidov
- 139 **Optical Response of Nanostructures**
Microscopic Nonlocal Theory By K. Cho
- 140 **Fractal Concepts in Condensed Matter Physics**
By T. Nakayama and K. Yakubo

Series homepage – <http://www.springer.de/phys/books/sss/>

Volumes 1–125 are listed at the end of the book.

T. Nakayama K. Yakubo

Fractal Concepts in Condensed Matter Physics

With 72 Figures



Springer

Professor Tsuneyoshi Nakayama
Professor Kousuke Yakubo
Department of Applied Physics
Graduate School of Engineering
Hokkaido University
Sapporo 060-8628
Japan

Series Editors:

Professor Dr., Dres. h. c. Manuel Cardona

Professor Dr., Dres. h. c. Peter Fulde*

Professor Dr., Dres. h. c. Klaus von Klitzing

Professor Dr., Dres. h. c. Hans-Joachim Queisser

Max-Planck-Institut für Festkörperforschung, Heisenbergstrasse 1, D-70569 Stuttgart, Germany

* Max-Planck-Institut für Physik komplexer Systeme, Nöthnitzer Strasse 38
D-01187 Dresden, Germany

Professor Dr. Roberto Merlin

Department of Physics, 5000 East University, University of Michigan
Ann Arbor, MI 48109-1120, USA

Professor Dr. Horst Störmer

Dept. Phys. and Dept. Appl. Physics, Columbia University, New York, NY 10027 and
Bell Labs., Lucent Technologies, Murray Hill, NJ 07974, USA

ISSN 0171-1873

ISBN 978-3-642-05711-3 ISBN 978-3-662-05193-1 (eBook)

DOI 10.1007/978-3-662-05193-1

Library of Congress Cataloging-in-Publication Data: Nakayama, T. (Tsuneyoshi), 1945-. Fractal concepts in condensed matter physics/ T. Nakayama, K. Yakubo. p. cm. – (Springer series in solid-state sciences, ISSN 0171-1873 ; 140). Includes bibliographical references and index. (alk.paper) 1. Condensed matter—Mathematics. 2. Fractals. I. Yakubo, K. (Kousuke) II. Title. III. Series. QC173.458.F72N35 2003 530.4'1'01514742-dc21 2003050426

This work is subject to copyright. All rights are reserved, whether the whole or part of the material is concerned, specifically the rights of translation, reprinting, reuse of illustrations, recitation, broadcasting, reproduction on microfilm or in any other way, and storage in data banks. Duplication of this publication or parts thereof is permitted only under the provisions of the German Copyright Law of September 9, 1965, in its current version, and permission for use must always be obtained from Springer-Verlag. Violations are liable for prosecution under the German Copyright Law.

<http://www.springer.de>

© Springer-Verlag Berlin Heidelberg 2003

Originally published by Springer-Verlag Berlin Heidelberg New York in 2003.

Softcover reprint of the hardcover 1st edition 2003

The use of general descriptive names, registered names, trademarks, etc. in this publication does not imply, even in the absence of a specific statement, that such names are exempt from the relevant protective laws and regulations and therefore free for general use.

Data conversion: Le-Tex, Leipzig

Cover concept: eStudio Calamar Steinen

Cover production: *design & production* GmbH, Heidelberg

Printed on acid-free paper SPIN: 10782866 57/3141/ba - 5 4 3 2 1 0

Preface

This book is written with the intention of presenting a systematic description of the underlying concept of fractals in a range of topics in condensed matter physics. The idea of fractals is based on self-similarity, which is a symmetry property of a system characterized by invariance under an isotropic scale transformation. This concept can be used to build simple pictures of the realm of nature. In Chaps. 1 and 2, we have given a brief survey of typical examples of fractal structures. We have also included a concise account of methods for calculating fractal dimensions characterizing their fractalities.

The dynamical properties of fractal structures constitutes the first major part of this book, including spectral densities of states, transport and localization/delocalization of waves. Chapter 3 contains basic results on percolation theory, including the introduction of various exponents characterizing percolating networks. The notion of percolation satisfactorily describes a large number of dynamic phenomena observed in fractal structures, such as gelation processes, transport in amorphous materials, hopping conduction in doped semiconductors, and many other applications. In addition, it forms the basis for studies of the flow of liquids or gases through porous media. For the analysis of these dynamic properties, the problem of diffusion on fractal structures plays a key role. In Chap. 5, we have tried to give a complete description of all standard results on anomalous diffusion, including its relevance to the dynamics of fractal networks. The results in this chapter are applied to the dynamic problems of fractal networks in Chap. 6. We include here many basic results on the dynamics obtained via large-scale numerical simulations. Some classes of diluted Heisenberg magnets take the geometrical structures of percolating networks. Spin waves in diluted Heisenberg magnets should reflect their fractalities. This subject is relatively new. Chapters 7 and 8 contain the dynamic scaling arguments on this subject as well as the important results obtained by large-scale numerical simulations.

Another central issue in this book is the concept of multifractals. Physical quantities often distribute in a complex manner on fractal or non-fractal (Euclidean) supports. Multifractals are currently used to describe such complex distributions. The idea of multifractals, first introduced to analyze energy dissipation in turbulent flow, has widened our view of intricate distributions observed in various fields of science. In particular, multifractal analysis provides a number of significant insights into condensed matter physics, such as current distributions in fractal networks, the

growth dynamics of diffusion-limited aggregations and viscous fingerings, crystallization on bilayer films, and energy spectra of quasicrystals. Among these, we have paid special attention to the relevance of multifractals in quantum critical phenomena, e.g., the multifractal property of electron wavefunctions at the metal–insulator Anderson transition. Multifractal analysis is a standard method for studying quantum critical properties of the Anderson transition. In Chap. 4, we have tried to familiarize the reader with various computational techniques using multifractal exponents, which are currently used in multifractal analysis. An entire spectrum of exponents characterizing multifractality at the transition point can be used to identify the universality class of the system. Chapters 9 and 10 describe the Anderson transition from the multifractal standpoint.

Our primary concern was to make this book as self-contained as possible and we hope that this purpose has been achieved by the above arrangements.

Sapporo
January 2003

*Tsuneyoshi Nakayama
Kousuke Yakubo*

Acknowledgements

We are particularly grateful to Professor Raymond Orbach, who has investigated together on several subjects described in this book. We are also indebted to stimulating discussions with the late Professor Shlomo Alexander. Various parts of the manuscript are benefitted from conversations with Professors Hideo Aoki, Yshai Avishai, Eric Courtens, the late Hironubo Ikeda, Mitsugu Matsushita, Tomi Ohtsuki, Keith Slevin, and Takamichi Terao, and we would like to thank them for their contributions. We wish to appreciate the patient and kind encouragement of Dr. C. E. Ascheron of Springer-Verlag for publication. Dr. T. Haard kindly supplied the computer simulated figure of aerogel. Finally, one of the Autors (T.N.) would like to thank Professor Peter Fulde for his hospitality during the stay at Max-Planck-Institute for the Physics of Complex Systems, where a part of this book was written in the summer of 2002.

The true end is not in the reaching of a limit, but in a completion which is limitless.

R. Tagore (1928)

Notation and Abbreviations

α	Lipschitz–Hölder exponent
μ_i	probability measure at the i th site
$\mu_{b(l)}$	box measure of a box b of size l
v	correlation (or localization) length exponent
$\tau(q)$	mass exponent
ξ	correlation (or localization) length
D_f	fractal dimension
D_q	generalized dimension
$D(\omega)$	density of states
\tilde{d}_{AF}	spectral dimension of antiferromagnetic spin-wave fractons
\tilde{d}_b	spectral dimension for bending fractons
\tilde{d}_s	spectral dimension
\tilde{d}_{st}	spectral dimension for stretching fractons
\tilde{d}_w	diffusion exponent
$\overline{e_\lambda}$	average strain tensor
p_c	percolation threshold
z	dynamic exponent for vibrational fractons
z_{AF}	dynamic exponent for antiferromagnetic spin-wave fractons
$z(q)$	correlation exponent
1D	one dimension (one-dimensional)
2D	two dimensions (two-dimensional)
3D	three dimensions (three-dimensional)
BP	bond percolation
DID	dipole-induced dipole
DLA	diffusion-limited aggregation
DOS	density of states
GOE	Gaussian orthogonal ensemble
GSE	Gaussian symplectic ensemble
GUE	Gaussian unitary ensemble
HRN	hierarchical resistor networks
INS	inelastic neutron scattering
QHS	quantum Hall system
SLSP	single-length scaling postulate
SP	site percolation

Contents

1. Introduction	1
2. Fractals	5
2.1 Fractal Structures	5
2.2 Fractal Dimensions	7
2.3 Methods for Obtaining Fractal Dimensions	10
2.4 Fractal Dimension of Aerogels	13
2.5 Brownian Motion and its Fractal Nature	15
3. Percolating Networks as Random Fractals	19
3.1 Critical Exponents and Scaling Relations	19
3.2 Fractal Dimension	27
3.3 Finite-Size Scaling and Scaling Relations	29
3.4 Nodes–Links–Blobs Model	32
4. Multifractals	35
4.1 Hierarchical Resistor Network Model	35
4.2 Mass Exponent and Generalized Dimension	40
4.3 Multifractal Spectrum	44
4.4 Relation between $\tau(q)$ and $f(\alpha)$	45
4.5 Direct Determination of $f(\alpha)$	47
4.6 Correlations between Box Measures	48
4.7 Profiles of $\tau(q)$, D_q , $f(\alpha)$, and $z(q)$	50
4.8 Parabolic Approximation and Distribution Functions of Measures	54
4.9 Growth Probability of DLA	56
5. Anomalous Diffusion on Fractal Networks	59
5.1 Anomalous Diffusion	59
5.2 Spectral Dimension	62
5.3 Spectral Density of States of Fractal Networks	64
5.4 Scaling Argument for Spectral Density of States	65
5.5 Localization of Excitations on Fractal Networks	66
5.6 Phonons and Fractons in Percolating Networks	68

6. Atomic Vibrations of Percolating Networks	71
6.1 Spectral Density of States and Spectral Dimension	71
6.2 Missing Modes at Low Frequencies	75
6.3 The Hump at High Frequencies	76
6.4 Localized Nature of Fracton Excitations	79
6.5 Networks with Vector Elasticity: Scaling Arguments	81
6.6 Simulation Results for Vector Elasticity	86
7. Scaling Arguments for Dynamic Structure Factors	89
7.1 Dynamic Structure Factors: Inelastic Neutron Scattering	89
7.2 Single-Length Scaling Arguments	91
7.3 Numerical Simulations of $S(q, \omega)$	94
7.4 Inelastic Light Scattering in Percolating Systems	96
8. Spin Waves in Diluted Heisenberg Antiferromagnets	101
8.1 Spin Waves in Percolating Antiferromagnets	101
8.2 Antiferromagnetic Spectral Dimension and the Upper Bound of \tilde{d}_{AF}	104
8.3 Numerical Simulations of Antiferromagnetic Fractons	107
8.4 Scaling Theory of $S(q, \omega)$ for Percolating Antiferromagnets	109
8.5 Large-Scale Simulations for $S(q, \omega)$	110
9. Anderson Transition	115
9.1 Coherent Transport of Electrons	115
9.2 Anderson Localization	117
9.3 Scaling Theory of the Anderson Transition	120
9.4 Universality Classes	125
9.5 Numerical Studies	129
9.6 Dynamical Properties at the Anderson Transition	134
9.6.1 Scaling Form of Dynamic Quantities at Criticality	134
9.6.2 Diffusion of Wave Packets	135
9.6.3 Two-Particle Correlation Function	142
9.6.4 Diffusion Length	144
10. Multifractals in the Anderson Transition	149
10.1 Multifractality of a Critical Wavefunction	149
10.2 Multifractality of Spectral Measures	155
10.3 Relations between Multifractality and Dynamical Properties at the Transition Point	160
10.4 Conformal Invariance	162
10.5 Universality at Higher Landau Levels	168
10.6 Finite-Size Scaling for the q th Moment	172

Appendices	177
A. Multifractality of the HRN Model	177
B. Spectral Dimensions for Deterministic Fractals	182
B.1 Sierpinski Gasket	182
B.2 Mandelbrot–Given Fractal	184
C. Diffusion and Dynamics on Networks	186
C.1 Atomic Vibrations	187
C.2 Spin Waves in Diluted Ferro- and Antiferromagnets	191
C.3 Superconducting Networks	192
D. Wigner Distributions	194
References	197
Subject Index	203

1. Introduction

Fractals provide a simple description of complex structures in nature and are currently used in almost every branch of condensed matter physics. Mandelbrot gave a simple definition of the term fractal: a fractal is a shape made of parts similar to the whole in some way [1.1]. The idea of the fractal is based on the self-similarity of complex structures [1.2, 1.3].

The significance of fractal research in the physical sciences is that the very idea of fractals opposes reductionism. Modern physics has developed by making efforts to elucidate the physical mechanisms of smaller and smaller structures such as molecules, atoms and elementary particles. An example in condensed matter physics is the band theory of electrons in solids. Energy spectra of electrons can be obtained by incorporating group theory based on the translational and rotational symmetry of the systems. The use of this mathematical tool greatly simplifies the treatment of systems composed of 10^{22} atoms. If the energy spectrum of a unit cell molecule is solved, the whole energy spectrum of the solid can be computed by applying group theory. In this context, the problem of an ordered solid is reduced to that of a unit cell. Weakly disordered systems can be handled by regarding impurities as a small perturbation to the corresponding ordered systems.

However, a different approach is required for elucidating the physical properties of strongly disordered/complex systems with correlations, or of medium-scale objects, for which perturbative approaches are not practical. For these systems, the concept of fractals plays an important role. Examples of fractal structures in condensed matter physics are numerous: polymers, colloidal aggregations, porous media, rough surfaces, spin configurations of diluted magnets, and others besides. The critical phenomena of phase transitions are another example where self-similarity plays a crucial role [1.4]. The fractal properties of the critical wavefunctions of electrons themselves at the metal–insulator Anderson transition is a further example in which self-similarity is relevant.

Fractal structures fall into two categories. One is the deterministic fractal: when the system is rescaled by a dilatation transformation, it is identical with a part of the original. The other is the random fractal in which the dilatational symmetry has only a statistical meaning. Unlike the deterministic fractal, the original random fractal structure does not overlap at different magnifications. Fractal structures observed in nature belong mainly to the second category.

The subject of fractal structures themselves has been treated in many books [1.1, 1.5–1.11]. The present book deals mainly with their dynamic properties, such as vibrational excitations, transport, and spin waves in fractal structures. Another topic is the application of multifractals to the quantum phase transition, illustrated by the Anderson metal–insulator transition, where critical wavefunctions at the transition point exhibit multifractality.

Random walks on fractal networks are the central issue for investigating a wide range of dynamic problems. De Gennes opened the way to this subject in his seminal paper [1.12]. He formulated the problem as follows: An ant parachutes down onto a site on the percolation network, and executes a random walk. What is the mean square distance the ant traverses as a function of time? This problem holds the key to later investigations into the dynamic properties of fractal structures. The solution given by Gefen et al. [1.13] and subsequent work by Alexander and Orbach [1.14] greatly influenced the development of the anomalous diffusion concept and its relevance to dynamic problems in the context of fractal structures. Chapter 5 provides detailed descriptions of these subjects. The results obtained in Chap. 5 are applied to the dynamic problems of fractal networks in Chap. 6.

In some classes of diluted Heisenberg magnets, configurations of magnetic atoms adopt the geometrical structures of percolating networks. Spin waves in diluted Heisenberg magnets should reflect their fractality. Diluted Heisenberg ferromagnets possess the same dynamic property as percolating elastic networks. This is because the equations of motion governing ferromagnetic spin waves and elastic vibrations can be mapped onto the master equation for diffusing particles. However, the linearized equation of motion for antiferromagnetic spin waves differs from the equation of motion for vibrational or ferromagnetic systems. This indicates that antiferromagnetic spin waves belong to a different class of dynamics. Spin dynamics in these diluted Heisenberg magnets is currently stimulating considerable research interest. These subjects are treated in Chaps. 7 and 8.

Fractal features can also be observed in quantum phenomena. Electrons on fractal structures such as quasicrystals exhibit fractality in their wavefunctions and energy spectra. This is a direct consequence of the fractal supports. Electron wavefunctions and energy spectra at the Anderson metal–insulator transition point also possess fractal properties, although the electrons lie on non-fractal (Euclidean) supports. In order to describe statistical properties of critical wavefunctions, the concept of multifractals is very useful. For a quantity distributed in a complex manner in space, a portion with large values may have a fractal dimension D_f , while a portion with small values may be described by a different fractal dimension from D_f . When the fractal dimension depends on the strength of the quantity, the distribution is called multifractal. In this sense, the distribution of the squared amplitude of a critical wave function possesses multifractality and an infinite number of exponents are required to characterize the statistical properties of the wavefunction.

The density of states near the Anderson transition point is generally a smooth function of the energy and it seems that multifractality does not appear in the energy spectrum, in contrast to other fractal systems such as quasicrystals. However, if we

describe the spectral property in terms of a local density of states, the multifractal nature of the energy spectrum emerges even for the Anderson transition. Multifractal properties at the Anderson transition point are significant not only for describing the spatial or energy profile of the critical wavefunction, but also for understanding the critical dynamics of electrons. This is because some of the multifractal exponents are related to exponents characterizing dynamical properties at criticality. Electron systems at the transition point are believed to be invariant under the local scale transformation. In 2D systems, this symmetry (conformal invariance) leads to a relation between the scaling amplitude and multifractal exponents. Multifractal analysis at the Anderson transition is crucial for understanding critical properties of the quantum phase transition. We present detailed descriptions of the relevance of multifractals to the Anderson transition in Chaps. 9 and 10.

2. Fractals

2.1 Fractal Structures

Fractal structures are classified into two categories, i.e., deterministic fractals and random fractals. Deterministic fractal structures can be easily understood by presenting some examples. A typical example is the Mandelbrot–Given fractal [2.1], which can be constructed by starting with a structure with 8 line segments as shown in Fig. 2.1a (the first stage of the Mandelbrot–Given fractal). In the second stage, each line segment of the initial structure is replaced by the initial structure itself (Fig. 2.2b). This process is repeated indefinitely. The Mandelbrot–Given fractal possesses an obvious dilatational symmetry, as seen from Fig. 2.1c, i.e., if we magnify a part of the structure, the enlarged portion looks just like the original one.

The Sierpinski gasket is the other well-known example of a deterministic fractal. It is obtained by extracting iteratively central triangles from triangles in the previous step. Figure 2.2 illustrates the Sierpinski gasket up to the third stage of the hierarchy.

Deterministic fractal structures are equivalent to self-similar structures. In other words, fractals are defined to be objects invariant under isotropic scale transformations, i.e., uniform dilatation of the system in every spatial direction. In contrast, there exist systems which are invariant under anisotropic (affine) transformations.

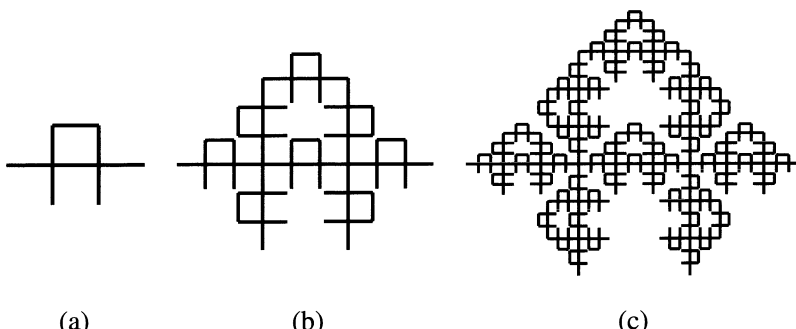


Fig. 2.1. Construction of the Mandelbrot–Given fractal. (a) The initial structure with 8 line segments, (b) the object obtained by replacing each line segment of the initial structure by the initial structure itself (the second stage), and (c) the third stage of the Mandelbrot–Given fractal obtained by replacing each line segment of the second-stage structure by the initial structure

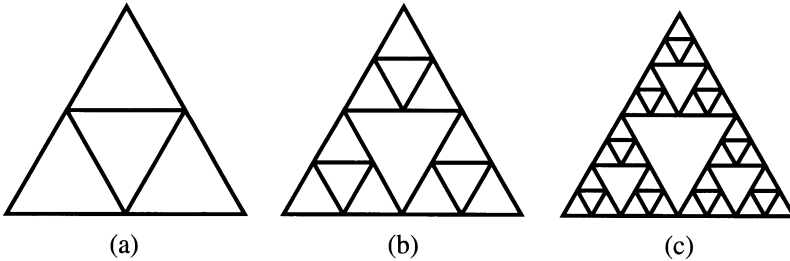


Fig. 2.2. Construction of the Sierpinski gasket. (a) The initial structure with 3 triangles, i.e., the structure obtained by extracting a central inverted triangle from an original triangle. (b) The object obtained by replacing each triangle of the initial structure by the initial structure itself (the second stage). (c) The Sierpinski gasket obtained by performing this procedure iteratively

These are called self-affine fractals [2.2–2.4]. From the above examples of deterministic fractals, we see that there does not exist a characteristic length scale in fractal structures.

The geometric characteristics of random fractals can be understood by considering two extreme cases of random structures. Figure 2.3a represents the case in which particles are randomly but homogeneously distributed in a d -dimensional box of size L . If we divide this box into smaller boxes of size l , the mass density of the i th box is

$$\rho_i(l) = \frac{M_i(l)}{l^d}, \quad (2.1)$$

where $M_i(l)$ represents the total mass inside box i .

This quantity depends on the box i . By plotting the distribution function $P(\rho)$, we may have curves like those in Fig. 2.3b for two box sizes l_1 and l_2 ($l_1 < l_2$). We see that the central peak position of the distribution function $P(\rho)$ is the same for

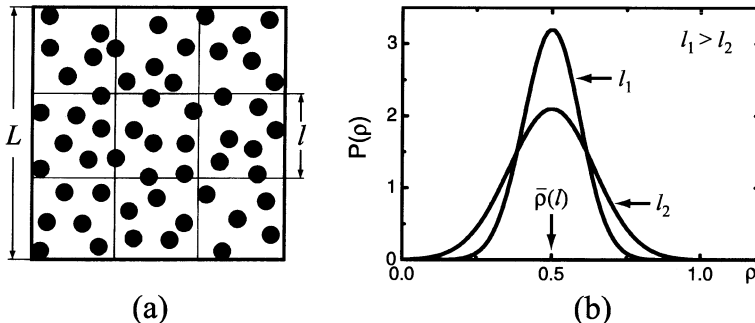


Fig. 2.3. (a) Homogeneous random structure in which particles are randomly but homogeneously distributed, and (b) the distribution functions of local densities ρ , where $\bar{\rho}(l)$ is the average mass density independent of l

each case. This means that the average mass density

$$\bar{\rho}(l) = \frac{\langle M_i(l) \rangle_i}{l^d} \quad (2.2)$$

becomes constant, indicating that $\langle M_i(l) \rangle_i \propto l^d$. In this case, it follows that

$$\bar{\rho} = m/\bar{a}^d, \quad (2.3)$$

where \bar{a} is the average distance between particles and m the mass of a single particle. This indicates that there exists a single length scale \bar{a} characterizing the random system given in Fig. 2.3a.

The other type of random structure is shown in Fig. 2.4a, where particle positions are correlated with each other and $\rho_i(l)$ greatly fluctuates from box to box, as shown in Fig. 2.4b. The relation $\langle M_i(l) \rangle_i \propto l^d$ may not hold at all for this type of structure. Assuming the power law $\langle M_i(l) \rangle_i \propto l^{D_f}$, the average mass density becomes

$$\bar{\rho}(l) = \frac{\langle M_i(l) \rangle_i}{l^d} \propto l^{D_f - d}, \quad (2.4)$$

provided that $\rho_i(l) = 0$ is excluded. In the case $D_f < d$, $\bar{\rho}(l)$ decreases with increasing l . There is thus no characteristic length scale for the type of random structure shown in Fig. 2.4a. If (2.4) holds with $D_f < d$, so that $\langle M_i(l) \rangle_i$ is proportional to l^{D_f} , the structure is said to be fractal in a statistical sense. For both deterministic and random fractals, no characteristic length scale exists, and this is an important feature of fractal structures.

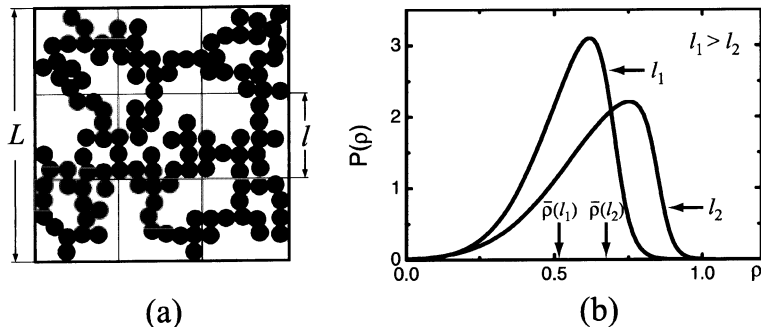


Fig. 2.4. (a) Correlated random fractal structure in which particles are randomly distributed, but correlated with each other, and (b) the distribution functions of local densities ρ with finite values, where the average mass densities depend on l

2.2 Fractal Dimensions

We know from experience that the spatial dimensions of a line and a plane are 1 and 2, respectively, and we understand the meaning of 3D space. These Euclidean

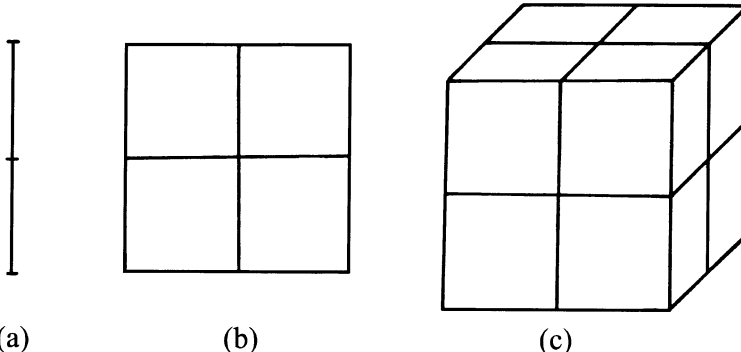


Fig. 2.5. A line divided into two segments (a), a square divided into four parts (b), and a cube divided into eight parts (c)

dimensions d take integer values. One definition for this quantity is as follows: suppose we are to divide a line, a square and a cube into identical forms whose sides are half the length. We thus divide the line into 2 smaller ones, and the square and the cube into 4 and 8 smaller ones, respectively (Fig. 2.5). The numbers 2, 4, and 8 can be related to d by $N(2) = 2^d$. The exponent d ($= 1, 2, 3$) is given by

$$d = \frac{\log N(2)}{\log 2} , \quad (2.5)$$

where the Euclidean dimensions d take integer values.

We generalize this definition of dimension to fractal structures. Deterministic fractal structures can be composed of $N(a)$ identical parts of size $1/a$, as explained in Sect. 2.1. Extending (2.5), the generalized dimension is defined by

$$D_f = \frac{\log N(a)}{\log a} , \quad (2.6)$$

where the quantity D_f is not restricted to integer values. This implies

$$N(a) = a^{D_f} . \quad (2.7)$$

The exponent D_f is called the similarity dimension. For example, let us apply this definition to the Mandelbrot–Given fractal shown in Fig. 2.1. The Mandelbrot–Given fractal is composed of 8 parts of size $1/3$. Hence, from (2.6), the similarity dimension D_f for this structure is

$$D_f = \log_3 8 = 1.89278 \dots , \quad (2.8)$$

which takes a fractional value. The same procedure applied to the Sierpinski structure of Fig. 2.2. Its self-similarity is recognized from the fact that Fig. 2.2a is composed of 3 identical parts of size $1/2$, which gives

$$D_f = \log_2 3 = 1.58496 \dots . \quad (2.9)$$

These similarity dimensions are smaller than the embedding dimension $d_E = 2$. The relation $D_f < d_E$ generally holds for fractal structures observed in nature.

Although the similarity dimension extends the concept of dimensions to non-integer values, the similarity dimension can be defined only for deterministic fractals. In order to allocate a dimension to a random fractal structure, it is necessary to introduce definitions of dimensions other than the similarity dimension. The capacity dimension and the Hausdorff dimension are suitable for this purpose [2.2]. These dimensions are based on the coverage procedure. Here we will not touch on the mathematical details, but rather try to understand the intuitive meaning. This is because a rigorous calculation of the capacity dimension or the Hausdorff dimension is generally difficult, and physics does not generally require such a rigorous treatment.

Let us consider again the dimensions of shapes in Fig. 2.5. We try to cover a line segment, a square, and a cube with spheres of radius l . It is obvious that the least numbers $N(l)$ of spheres required to cover the whole shapes are proportional to (L/l) , $(L/l)^2$, and $(L/l)^3$ for the line segment, the square, and the cube, respectively, where L is the size of the shapes. This gives a new definition of dimension as

$$N(l) \propto l^{-D}, \quad (2.10)$$

where D is the capacity dimension. It is possible to evaluate D for a random fractal structure such as the one shown in Fig. 2.4a. As discussed in Sect. 2.1, the average number of particles in a box of size l is given by $\langle M_i(l) \rangle_i \propto l^{D_f}$. The total number of particles in the system is proportional to $N(l)\langle M_i(l) \rangle_i$, where $N(l)$ is the number of boxes, excluding empty boxes. Since the total particle number does not depend on l , we have $N(l) \propto l^{-D_f}$. This implies that the exponent D_f defined by (2.4) is nothing but the capacity dimension D of the system. The capacity dimension can be defined for deterministic fractals as well.

We can calculate the capacity dimension of the Mandelbrot–Given fractal in Fig. 2.1. The Mandelbrot–Given fractal of unit size satisfies $N(1/3) = 8$, $N((1/3)^2) = 8^2$, and so on. We thus have a relation of the form

$$N(l) \propto l^{-\log_3 8}, \quad (2.11)$$

which gives $D = \log_3 8$. The exponent $\log_3 8 = 1.89278\dots$ is identical to the similarity dimension D_f of the Mandelbrot–Given fractal obtained in (2.8). The capacity dimension of any deterministic fractal is always the same as its similarity dimension. The Hausdorff dimension is defined similarly to the capacity dimension, where the radii of covering spheres are not constant but less than l . The Hausdorff dimension coincides with the capacity dimension for many fractals in nature, although the Hausdorff dimension is mathematically less than or equal to the capacity dimension. There exist non-integer dimensions other than the similarity, the capacity, and the Hausdorff dimensions, such as the information dimension and the correlation dimension, as will be introduced in Chap. 4. Sometimes these take the same value and sometimes not. While the fractal dimension D_f is often defined as a generic term among these non-integer dimensions, this book refers to the capacity dimension as the fractal dimension.

2.3 Methods for Obtaining Fractal Dimensions

There are several methods for obtaining fractal dimensions D_f of fractal objects, especially useful for random fractal structures. In general, we use more than one method to determine the fractal dimension D_f of the object. The following methods for obtaining the fractal dimension D_f are known to be quite efficient [2.5].

Physical Measures. In mathematics, length, area, and volume are special cases of measures. For example, length is the measure of a 1D object, area the measure of a 2D object, and volume the measure of a 3D object. By extending this notion, we can evaluate non-integer dimensions of fractal structures.

Let us consider the example of a cube with unit linear dimension. Magnifying the linear dimension by a factor of two, the surface area S and the volume V become 2^2 and 2^3 times as large as those of the original cube, respectively (Fig. 2.5). Hence, when the linear dimension L is magnified n times, $S^{1/2}$ and $V^{1/3}$ become n times as large. The following relation therefore holds between the length L and the Euclidean measures S and V :

$$L \propto S^{1/2} \propto V^{1/3}. \quad (2.12)$$

This relation leads us to expect the following relation for fractal objects:

$$L \propto M(L)^{1/D_f}, \quad (2.13)$$

where D_f is the fractal dimension and M a suitable measure. In fact, D_f defined by (2.13) is equivalent to the capacity dimension defined by (2.10) if we chose M appropriately.

As an example, we consider a set of particles with unit mass m distributed in a d -dimensional space. We can determine the fractal dimension D_f in the following manner. Draw a sphere of radius r and denote the total mass of particles included in the sphere by $M(r)$. If the particles are uniformly distributed in space, $M(r)$ becomes

$$M(r) \propto r^d, \quad (2.14)$$

where d is the Euclidean dimension taking integer values. When generalizing this relation to a random fractal such as Fig. 2.4a, we should note that $M(r)$ is an average mass over spheres with different centers. The fractal dimension D_f of the mass distribution is determined from the relation

$$\langle M(r) \rangle \propto r^{D_f}, \quad (2.15)$$

where $\langle \dots \rangle$ denotes the average over different spheres of radius r .

This method is efficient if we know a suitable measure for a fractal object. The percolating network illustrated in Fig. 2.6 is a typical example of such a fractal, where the suitable measure is the number of particles. For $2d$ percolating networks, we have a power law of the form

$$\langle M(r) \rangle \propto r^{1.89\dots} \quad (2.16)$$

for the particle distribution, as shown in Fig. 2.6b. This means that the fractal dimension of this system is $D_f = 1.89\dots$

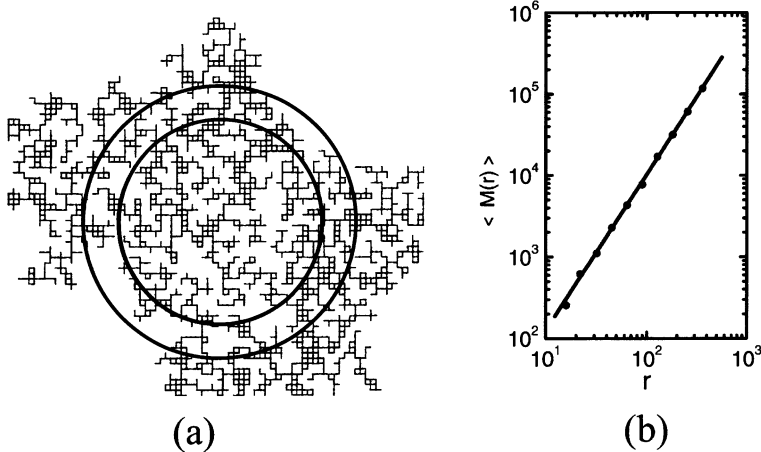


Fig. 2.6. (a) 2D site-percolating (SP) network and circles with different radii. (b) The power law relation between r and the number of particles in the sphere of radius r

Molecular Adsorption Method. The idea of coverage in the definition of the capacity dimension can be applied to obtain the fractal dimension D_f of material surfaces. An example is the fractality of rough surfaces or porous media. The fractal nature is probed by changing the sizes of adsorbed molecules on solid surfaces. Power laws are verified by plotting the total number of adsorbed molecules versus their size r . The area of a surface can be estimated with the aid of molecules weakly adsorbed by van der Waals forces. Gas molecules are adsorbed on empty sites until the surface is uniformly covered with a layer one molecule thick. Provided that we know the radius r of one adsorbed molecule and the number of adsorbed molecules $N(r)$, the surface area S obtained by molecules is given by

$$S = N(r)\pi r^2. \quad (2.17)$$

If the surface of the adsorbate is perfectly smooth, we expect the measured area to be independent of the radius r of the probe molecules, which indicates the power law

$$N(r) \propto r^{-2}. \quad (2.18)$$

However, if the surface of the adsorbate is rough or contains pores that are small compared with r , less of the surface area S is accessible with increasing size r . For a fractal surface with fractal dimension D_f , (2.10) gives the relation

$$N(r) \propto r^{-D_f}, \quad (2.19)$$

and we have from (2.17)

$$S(r) \propto r^{2-D_f}. \quad (2.20)$$

Box-Counting Method. This method is convenient for computer calculations and is essentially the same as the molecular adsorption method mentioned above. Consider as an example a set of particles distributed in a space. First, we divide the space into small boxes of size l and count the number of boxes containing more than one particle, which we denote by $N(l)$. From the definition of the capacity dimension (2.10), the number of boxes is

$$N(l) \propto l^{-D_f} . \quad (2.21)$$

For homogeneous objects distributed in a d -dimensional space, the number of boxes of size l is, of course, given by

$$N(l) \propto l^d . \quad (2.22)$$

Correlation Function. The fractal dimension D_f can be obtained via the correlation function, which is the fundamental statistical quantity observable in X-ray, light, and neutron scattering experiments. Since these techniques are applicable to bulk materials (not surfaces), this method is widely used in condensed matter physics. Let $\rho(\mathbf{r})$ be the number density of atoms at position \mathbf{r} . The density–density correlation function $G(\mathbf{r}, \mathbf{r}')$ is defined by

$$G(\mathbf{r}, \mathbf{r}') = \langle \rho(\mathbf{r})\rho(\mathbf{r}') \rangle , \quad (2.23)$$

where $\langle \dots \rangle$ denotes an ensemble average. This gives the correlation of the number-density fluctuation. Provided that the distribution is isotropic, the correlation function becomes a function of only one variable, the radial distance $r = |\mathbf{r} - \mathbf{r}'|$, which is defined in spherical coordinates. Due to the translational invariance of the system on average, \mathbf{r}' can be fixed at the coordinate origin, i.e., $\mathbf{r}' = 0$. We can write the correlation function as

$$G(r) = \langle \rho(\mathbf{r})\rho(0) \rangle . \quad (2.24)$$

The quantity $\langle \rho(\mathbf{r})\rho(0) \rangle$ is proportional to the probability that a particle exists at a distance r from another particle. This probability is proportional to the particle density $\varrho(r)$ within a sphere of radius r . Since $\varrho(r) \propto r^{D_f-d}$ for a fractal distribution, the correlation function becomes

$$G(r) \propto r^{D_f-d} , \quad (2.25)$$

where D_f and d are the fractal and the embedded Euclidean dimensions, respectively.

The scattering intensity in an actual experiment is proportional to the structure factor $S(q)$, which is the Fourier transform of the correlation function $G(r)$. The structure factor is calculated from (2.25) as

$$S(q) = \frac{1}{V} \int_V G(r) e^{i\mathbf{q} \cdot \mathbf{r}} d\mathbf{r} \propto q^{-D_f} , \quad (2.26)$$

where V is the volume of the system. Here we use the fact that the d -dimensional volume element is given by $d\mathbf{r} \propto r^{d-1} \sin^{d-2} \theta dr d\theta d\varphi_1 d\varphi_2 \dots d\varphi_{d-2}$ in spherical coordinates, where θ is the angle between \mathbf{q} and \mathbf{r} and $\varphi_1, \varphi_2, \dots$ are azimuthal angles. Using this relation, we can determine the fractal dimension D_f from the data obtained by scattering experiments.

When applying these methods to obtain the fractal dimension D_f , we need to take care over the following point. Any fractal structures in nature must have upper and lower limits for their fractality. Fractal properties should be observed only between these limits. These limits play important roles in condensed matter physics. To illustrate this, we show in Fig. 3.4 in Chap. 3 the calculated results of $S(q)$ for 2D bond-percolating (BP) and site-percolating (SP) networks at the critical concentration p_c . We will see the difference between the lower limits for BP and SP networks.

2.4 Fractal Dimension of Aerogels

It is known that aerogels adopt fractal structures. Aerogels are obtained by the method found by Kistler [2.6], which produces extremely light materials with porosities as high as 98%. The initial step in the preparation of silica aerogels is the hydrolysis of an alkoxysilane $\text{Si}(\text{OR})_4$, where R is CH_3 or C_2H_5 . The hydrolysis produces silicon hydroxide $\text{Si}(\text{OH})_4$ groups which polycondense into siloxane bonds $-\text{Si}-\text{O}-\text{Si}-$, and small particles start to grow in the solution. These particles bind to each other by cluster-cluster aggregation, forming more siloxane bonds, until eventually they produce a disordered network filling the reaction volume. At this point the solution gels. The reactions are not normally complete at this gel point and the cluster networks continue to grow in the alcogel phase. After suitable aging, if the solvent is extracted above the critical point, the open porous structure of the network is preserved and decimeter-size monolithic blocks with a range of densities from 50 to 500 kg/m^3 can be obtained.

These blocks have a very low thermal conductivity, solid-like elasticity, and very large internal surfaces. As a consequence, aerogels exhibit unusual physical properties, making them suitable for a number of practical applications, such as Cerenkov radiation detectors, supports for catalysis, or thermal insulators. Silica aerogels possess two different length scales. One is the radius r of primary particles. The other length is the correlation length of the gel. At intermediate length scales, lying between these two length scales, the clusters possess a fractal structure and at larger length scales the gel is a homogeneous porous glass. Figure 2.7 shows a computer-simulated microscopic aerogel structure at a length scale comparable to the correlation length ξ , which is of order 100–200 nm for 2% density. This figure was obtained by applying the diffusion-limited cluster-aggregation model.

In elastic scattering experiments, the scattering differential cross-section measures the Fourier components of spatial fluctuations in the mass density. For aerogels, the differential cross-section is the product of three factors, and is expressed by

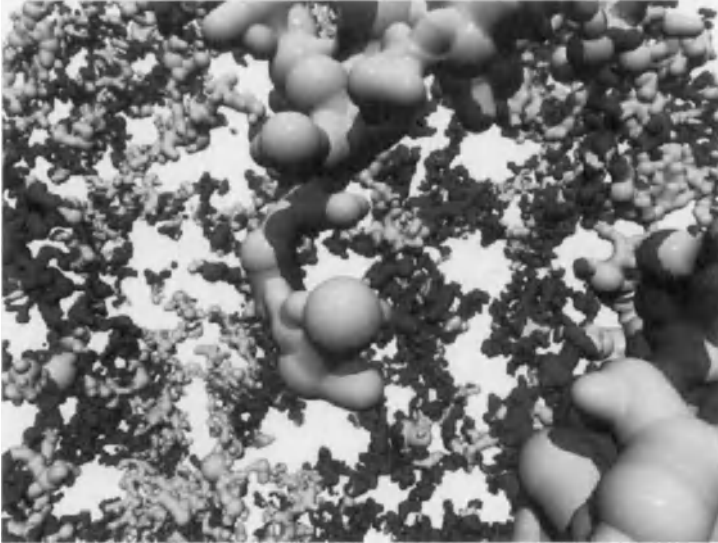


Fig. 2.7. Computer-simulated structure of an aerogel found by applying the diffusion-limited cluster-aggregation model. (Courtesy of T. Haard)

$$\frac{d\sigma}{d\Omega} = A f^2(q) S(q) C(q) + B . \quad (2.27)$$

Here A is a coefficient proportional to the particle concentration and $f(q)$ is the primary-particle form factor. The structure factor $S(q)$ describes the correlation between particles in a cluster and $C(q)$ accounts for cluster-cluster correlations. The incoherent background is expressed by B . The structure factor $S(q)$ is proportional to the spatial Fourier transform of the density-density correlation function defined by (2.24), and is given by (2.26). Since the structure of the aerogel is fractal up to the correlation length ξ of the system and homogeneous at larger scales, the correlation function $G(r)$ is expressed by (2.25) for $r \ll \xi$ and $G(r) = \text{Const.}$ for $r \gg \xi$. Corresponding to this, the structure factor $S(q)$ is given by (2.26) for $q\xi \gg 1$, while $S(q)$ is independent of q for $q\xi \ll 1$. The wavenumber regime for which $S(q)$ becomes a constant is called the Guinier regime. The value of D_f can be deduced from the slope of the observed intensity versus momentum transfer ($q\xi \gg 1$) in a double logarithmic plot. For very large q , there exists a regime called the Porod regime in which the scattering intensity is proportional to q^{-4} .

The beautiful results in Fig. 2.8 are from elastic scattering experiments on silica aerogels [2.7]. The various curves are labelled by the macroscopic density ρ of the corresponding sample in Fig. 2.8. For example, 95 refers to a neutrally reacted sample with $\rho = 95 \text{ kg/m}^3$. Solid lines represent best fits. They are presented even in the particle regime ($q > 0.15 \text{ \AA}^{-1}$) to emphasize that the fits do not apply in that region, particularly for the denser samples. Remarkably, D_f is independent of sample density to within experimental accuracy: $D_f = 2.40 \pm 0.03$ for samples 95

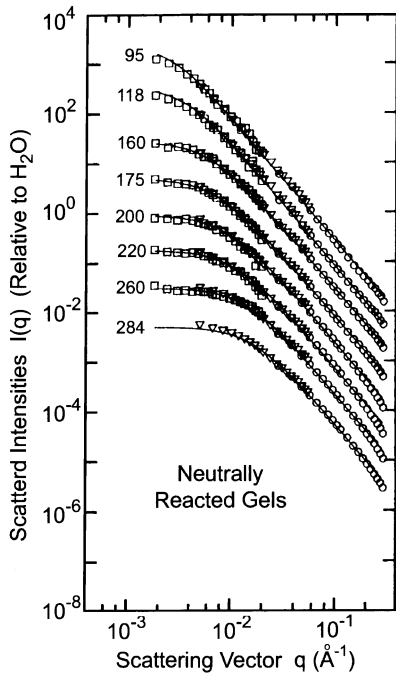


Fig. 2.8. Scattered intensities for 8 neutrally reacted samples. Curves are labelled with ρ in kg/m^3 [2.7]

to 360. The departure of $S(q)$ from the q^{-D_f} dependence at large q indicates the presence of particles with gyration radii of a few Å.

2.5 Brownian Motion and its Fractal Nature

Pioneering work by Einstein [2.8,2.9] opened the way to investigating the movement of small particles suspended in a stationary liquid, i.e., Brownian motion. Figure 2.9 shows a typical example of the Brownian track of a putty grain of radius $0.53 \mu\text{m}$ [2.10], where its positions are measured every 30 s. Einstein [2.8,2.9] demonstrated that Brownian motion can be reduced to a random walk. Since the trail of a random walker provides a good example for understanding the meaning of random fractals, we describe the details here.

The treatment of Brownian motion is simplified by replacing the molecule by an ant on a regular lattice. Suppose that the ant executes a random walk by taking a step every second on a d -dimensional lattice. The ant starts at time $t = 0$ from an arbitrary point of the lattice. The number of possible orientations w for the ant depends on the dimensionality. We have $w = 2$ for a 1D chain, $w = 4$ for a 2D square lattice, and $w = 6$ for a 3D cubic lattice. If the ant walks in each direction with equal probability, the probability of choosing any given walking direction is $p = 1/w$ at each time step.

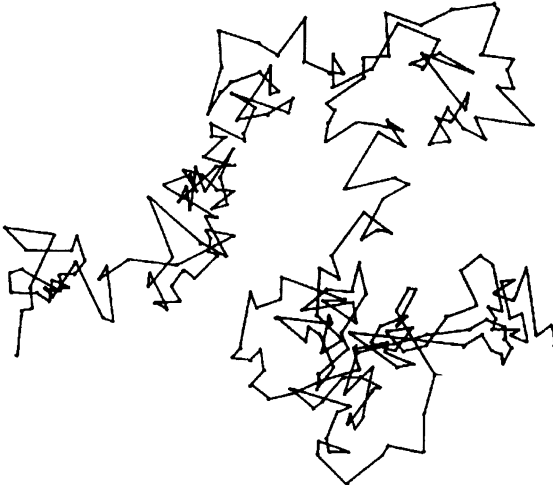


Fig. 2.9. Brownian motion of a putty grain of radius 0.53 μm . Positions are measured every 30 s [2.10]

As a simple example, consider Brownian motion in a 1D chain, for which we have $w = 2$ (right or left orientations) and $p = 1/2$. The displacement of the ant in one step is assumed to be unity. The position of the ant at the N th time step becomes

$$x(N) = \sum_{i=1}^N a(i) , \quad (2.28)$$

where $a(i)$ takes values ± 1 with probability $1/2$. The expectation value of $a(i)$ is given by

$$\langle a(i) \rangle = \sum_{m=1}^2 a_m(i) p = 0 , \quad (2.29)$$

where $a_m(i)$ is the possible value of $a(i)$, i.e., $a_1(i) = 1$ and $a_2(i) = -1$. This leads to

$$\langle x(N) \rangle = 0 . \quad (2.30)$$

Using (2.28), the mean-squared displacement is given by

$$\langle x^2(N) \rangle = \sum_{i,j=1}^N \langle a(i)a(j) \rangle = \sum_{i=1}^N \langle a^2(i) \rangle = N . \quad (2.31)$$

This is the case for independent events.

The relations (2.30) and (2.31) hold for Brownian motion in a lattice of any dimensions. The position of the ant at the N th time step is now expressed as

$$\mathbf{r}(N) = x(N_1)\mathbf{e}_1 + y(N_2)\mathbf{e}_2 + \dots , \quad (2.32)$$

where e_i is the unit vector along the lattice coordinates, $x(N_1), y(N_2), \dots$ are displacements in 1D Brownian motions, given by (2.28), and $N = N_1 + N_2 + \dots$. The expectation value of $\mathbf{r}(N)$ is

$$\langle \mathbf{r}(N) \rangle = 0 , \quad (2.33)$$

because $\langle x(N_1) \rangle = \langle y(N_2) \rangle = \dots = 0$, as shown by (2.30). The vector \mathbf{r} is considered as the end-to-end vector of the displacement after N steps. This is a natural result because the ant chooses a site as a completely independent event. However, the mean-squared displacement of the ant becomes finite and increases monotonically with N as shown below. The displacement vector \mathbf{r} after N steps is the sum of N vectors

$$\mathbf{r} = \mathbf{a}(1) + \mathbf{a}(2) + \dots + \mathbf{a}(N) = \sum_{i=1}^N \mathbf{a}(i) , \quad (2.34)$$

where $\mathbf{a}(i)$ is the displacement vector at the i th step and $|\mathbf{a}(i)| = 1$. The mean-squared displacement is

$$\langle \mathbf{r}^2 \rangle = \sum_{i,j} \langle \mathbf{a}(i) \cdot \mathbf{a}(j) \rangle = \sum_{i=1}^N \langle a^2(i) \rangle = N , \quad (2.35)$$

where all cross-terms vanish after averaging. From (2.35), we see that the spatial extent of the random walk grows as $r = N^{1/2}$.

Suppose that the ant carries a bag filled with grains of rice and leaves behind a single grain at each step. Hence, the analog of the trail of the ant is the distribution of grains of rice. This analog makes it possible to regard the number of steps N as the total mass of distributed grains of rice M . Using (2.35), this leads to the important relation

$$M(r) \propto r^2 , \quad (2.36)$$

where $M(r)$ is the mass of grains of rice within a sphere of radius r . Since the mass $M(r)$ can be considered as a measure of the random walk, the fractal dimension of distributed grains due to the Brownian motion becomes $D_f = 2$, from the definition (2.15).

3. Percolating Networks as Random Fractals

The theory of percolation was initiated in 1957 by Broadbent and Hammersley [3.1] in connection with the diffusion of gases through porous media. At that time Broadbent was a researcher at the British Coal Utilization Research Association working on the design of gas masks made of porous filters. He noticed that if pores are wide and well connected, the gas molecules penetrate deep into the filter. Otherwise the gas cannot pass through. He brought this problem to the mathematician Hammersley [3.2]. They developed the geometrical and probabilistic theory of percolation.

Since their work, it has been widely accepted that percolation theory describes a large number of physical and chemical phenomena such as gelation processes, transport in amorphous materials, hopping conduction in doped semiconductors, the quantum Hall effect, and many other applications. In addition, it forms, of course, the basis for studies of the flow of liquids or gases through porous media [3.3]. It was first noticed by Stanley [3.4] that a percolating network is a fundamental model describing geometrical features of random systems and that it constitutes a fractal structure. Percolating networks thus serve as a model which helps us to understand physical properties of complex fractal structures [3.5].

In the present chapter, we focus our attention on the critical behaviour of percolating networks, particularly with regard to their scaling properties. The scaling ansatz is an important physical postulate, useful for investigating the critical behaviour of percolating networks. This chapter also presents the physical model called the nodes-links-blobs model, which gives a good description of the static and dynamic properties of percolating networks.

3.1 Critical Exponents and Scaling Relations

The percolation theory describes properties of critical phenomena, which include thermodynamic second-order phase transitions. The second-order phase transition is a phenomenon whereby the macroscopic state of a system alters due to the formation of a kind of order in the system. A common feature of second-order phase transitions is that the so-called correlation length $\xi(T)$ diverges at the critical temperature T_c according to the power law

$$\xi = \xi_0 |T - T_c|^{-\nu} , \quad (3.1)$$

where \mathcal{E}_0 is a constant prefactor and ν is the divergence of $\xi(T)$ with temperature T . It is well established that critical behaviour is dominated by one and only one length scale ξ . At temperatures $T > T_c$, ordered clusters of finite sizes appear in the system. When T approaches the critical point T_c , clusters grow and merge together to form an infinite cluster.

In the percolation theory, the occupation probability p of sites or bonds plays the same role as the temperature in thermal critical phenomena. In the analogy with (3.1), the correlation length ξ , defined as the root-mean-square distance between two occupied sites i and j within the same cluster, should diverge at a certain value of p_c according to

$$\xi = \mathcal{E}_0 |p - p_c|^{-\nu}. \quad (3.2)$$

This will be discussed in detail later. Hereafter, we call p_c the percolation threshold or the critical concentration. We emphasize that p_c is defined for infinite systems and the correlation length ξ is defined as an average value. In the scaling theory of percolation, the correlation length ξ is assumed to be a unique characteristic length scale, as in the case of thermal phase transitions. This assumption provides a basis for the scaling ansatz which will be presented later in this section. The difference between second-order thermodynamic phase transitions and percolation transitions is that decreasing temperature T corresponds to increasing p . The exponent ν in (3.1) is called the correlation length exponent. For an infinite cluster obtained at $p = p_c$, the characteristic length scale ξ of the system diverges, indicating that the length scale vanishes in the system. This reminds us of the formation of a fractal structure without a characteristic length scale, i.e., a scale-invariant system.

There are two kinds of percolating networks: site percolating and bond percolating. To construct a site-percolating (SP) network, each lattice point (site) of an initially prepared d -dimensional lattice is occupied at random with probability p . Sites are connected by bonds if they are adjacent along a principal direction. In a bond-percolating (BP) network, adjacent lattice points are randomly connected by bonds on a d -dimensional lattice with probability p . For both types of percolating network, if p is sufficiently small, we have small clusters connected to each other as shown in Fig. 3.1. With increasing p , cluster sizes become large. A critical concentration p_c exists such that, for $p \geq p_c$, a connected cluster will extend continuously across the lattice. The latter is referred to as an infinite cluster. The structural difference between SP and BP networks is on a short scale, i.e., a bond has more nearest neighbors than a site. For example, in a 2D square lattice, a given bond can be connected to six nearest-neighbor bonds, whereas a site has only four nearest-neighbor sites. We have illustrated SP and BP networks in Fig. 3.2. This is why BPs always have a smaller p_c than SPs. Table 3.1 shows the values of p_c for various lattices and dimensions.

Percolating networks are characterized by quantities describing geometrical properties such as the order parameter $P_\infty(p)$, the number of finite clusters $E(p)$, the average cluster size $S(p)$, and the correlation length $\xi(p)$. All these quantities are defined as moments of a distribution function $n_s(p)$ of the number (per site) of finite

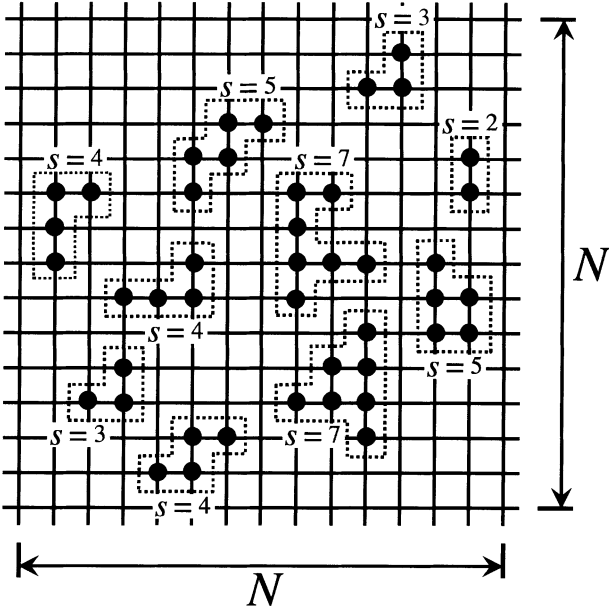


Fig. 3.1. Finite clusters with different sizes are distributed on a 2D square lattice. Cluster sizes s are indicated

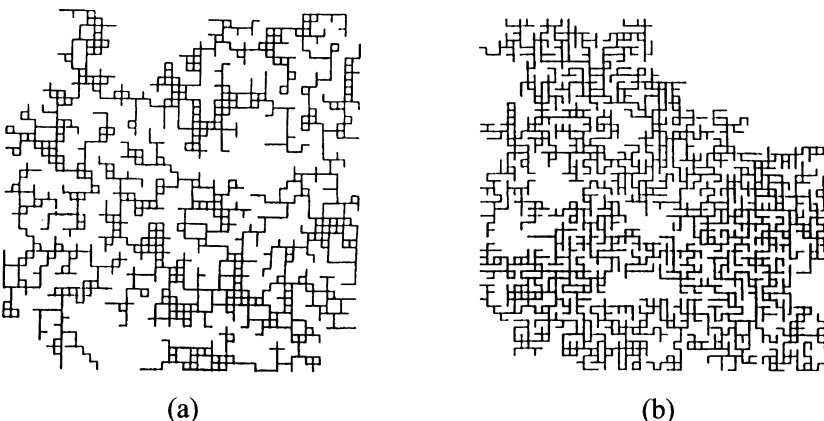


Fig. 3.2. (a) Site-percolating network formed on a 2D square lattice and (b) bond-percolating network at the critical concentration p_c . The difference between these is only crucial at short-range scales

clusters of size s (site number). The critical structure of percolating networks at p_c allows us to apply the scaling ansatz for the distribution function $n_s(p)$. The scaling ansatz is based on the idea that there exists a unique characteristic length scale ξ in a percolating network close to the critical point p_c . This length ξ provides a characteristic cluster size $s_\xi(p)$, namely, the largest cluster size for $p < p_c$ or the largest

Table 3.1. Values of p_c for various lattices and dimensions

d	Lattice	Sites	Bonds
2	Square	0.5927460 ± 0.0000005	$1/2$
	Triangle	$1/2$	$2 \sin(\pi/18)^a$
	Honeycomb	0.6962	$1 - 2 \sin(\pi/18)^b$
	Kagome	0.652704	0.524430
	Penrose	0.5837 ± 0.0003	0.4770 ± 0.0002
3	Simple cubic (1st nn)	0.31161	0.2488 ± 0.0001
	Simple cubic (2nd nn)	0.137	
	Simple cubic (3rd nn)	0.097	
	Body-centered cubic	0.245	0.1795 ± 0.0003
	Face-centered cubic	0.198	0.119
4	Diamond	0.428	0.388
	Simple cubic	0.197 ± 0.001	0.16005 ± 0.00015
	Simple cubic	0.141 ± 0.001	0.11819 ± 0.00004
	Simple cubic	0.108	0.09420 ± 0.0001
	Simple cubic	0.085	0.078685 ± 0.00003
$d \rightarrow \infty$		$1/(2d - 1)$	$1/(2d - 1)$
	Cayley tree	$1/(z - 1)$	$1/(z - 1)$

^a $2 \sin(\pi/18) = 0.34729$.

^b $1 - 2 \sin(\pi/18) = 0.65271$.

void size for $p \geq p_c$ [3.5]. This implies that any statistical quantity as a function of the cluster size s can be scaled by $s_\xi(p)$ alone. The distribution function $n_s(p)$ as a function of s is then expressed as

$$n_s(p) = s^{-\tau} F[s/s_\xi(p)] , \quad (3.3)$$

where $F(x)$ is an unknown function and τ an exponent. The quantity $s_\xi(p)$ is a function of ξ . The functional form should be a power of ξ , otherwise new characteristic length scales are introduced. Therefore, close to p_c , $s_\xi(p)$ takes the form

$$s_\xi(p) \propto |p - p_c|^{-1/\eta} , \quad (3.4)$$

where we introduce a new exponent η . An alternative form of (3.3) for $p \rightarrow p_c$ is found from (3.4) to be

$$n_s(p) = s^{-\tau} \tilde{F}[(p - p_c)s^\eta] , \quad (3.5)$$

where $\tilde{F}(x^\eta) = F(x)$. Scaling forms for various physical quantities characterizing the network are related through (3.5), which we will describe below [3.5].

The Exponent β . The probability $P_\infty(p)$ that a site belongs to the infinite cluster is associated with the exponent β . Note that $P_\infty(p)$ is finite for $p > p_c$, while

$P_\infty(p) = 0$ for $p \leq p_c$. Since an occupied site must either be in a finite cluster or in the infinite cluster, we have the relation

$$P_\infty(p) + \sum_s n_s(p)s = p . \quad (3.6)$$

For $p < p_c$, only finite clusters exist and $\sum_s n_s(p)s = p$. When p approaches p_c ($p > p_c$), the above relation can be written in the form

$$P_\infty(p) = \sum_s [n_s(p_c) - n_s(p)]s + (p - p_c) , \quad (3.7)$$

using the relations $P_\infty(p_c) = 0$ and $\sum_s n_s(p_c)s = p_c$. With the help of (3.5), (3.7) becomes

$$P_\infty(p) = \int s^{1-\tau} [\tilde{F}(0) - \tilde{F}(y)] ds + (p - p_c) , \quad (3.8)$$

where the definition $y = (p - p_c)s^\eta$ is used. Changing the variable s to y , (3.8) yields

$$P_\infty(p) = P_0(p - p_c)^\beta + (p - p_c) , \quad \text{for } p > p_c , \quad (3.9)$$

where P_0 is the constant prefactor given by

$$P_0 = \int_0^\infty y^{(2-\tau-\eta)/\eta} \eta^{-1} [\tilde{F}(0) - \tilde{F}(y)] dy , \quad (3.10)$$

and the critical exponent β is defined as

$$\beta = \frac{\tau - 2}{\eta} . \quad (3.11)$$

The quantity $P_\infty(p)$ was first introduced by Broadbent [3.6] and corresponds to the order parameter for thermal critical phenomena. Since the order-parameter exponent β should always be less than unity but positive, the first term of (3.9) dominates for $p - p_c \ll 1$. Hence,

$$P_\infty(p) = P_0(p - p_c)^\beta , \quad \text{for } p > p_c . \quad (3.12)$$

We should note that $P_\infty(p)$ is proportional to p when approaching unity, as shown in Fig. 3.3.¹

¹ It is obvious from the definition that $P_\infty(1) = 1$. If p is close to unity, voids including plural vacant sites may be very rare since such a void requires vacant sites to gather around one vacant site. The probability of such an event is quite low. This factor is safely neglected and we have the simple relation $P_\infty(p) = p$ as $p \rightarrow 1$ [3.3].

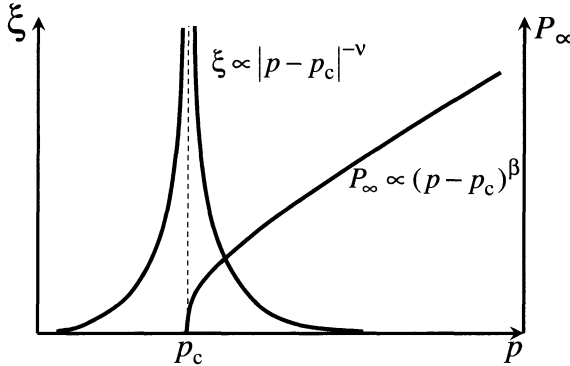


Fig. 3.3. Concentration dependence of the correlation length ξ and of the probability P_∞ of finding a site belonging to an infinite cluster (order parameter)

The Exponent α . This is the exponent for the total number of finite clusters $E(p)$. It is related to the number $n_s(p)$ of clusters of size s by

$$E(p) = \sum_s n_s(p) = \int s^{-\tau} \tilde{F}[(p - p_c)s^\eta] ds . \quad (3.13)$$

We can find the p -dependence of $E(p)$ by the same procedure as in the case of (3.9). To leading order in $|p - p_c|$, $E(p)$ behaves as

$$E(p) \propto |p - p_c|^{2-\alpha} , \quad (3.14)$$

where the critical exponent α is defined as

$$\alpha = \frac{1 - \tau}{\eta} + 2 . \quad (3.15)$$

For thermal phase transitions, α corresponds to the exponent of specific heat, and $E(p)$ to the free energy.

The Exponent γ . The average cluster size $S(p)$ (number of sites or bonds) of finite clusters can also be obtained from the moment of $n_s(p)$. The quantity given by

$$w_s(p) = \frac{s n_s(p)}{\sum_s s n_s(p)} \quad (3.16)$$

is the probability that an occupied site belongs to a cluster of s sites. The average cluster size $S(p)$ is written as

$$S(p) = \sum_s s w_s(p) = \frac{\sum_s s^2 n_s(p)}{\sum_s s n_s(p)} . \quad (3.17)$$

In the limit $p \rightarrow p_c$, $\sum_s s n_s(p) = p_c$ holds and (3.17) becomes

$$S(p) = \frac{\sum_s s^2 n_s(p)}{p_c} . \quad (3.18)$$

Substituting (3.5) into (3.18), we obtain

$$S(p) = S_0 |p - p_c|^{-\gamma} , \quad (3.19)$$

where S_0 is the constant prefactor and the exponent γ is defined as

$$\gamma = \frac{3 - \tau}{\eta} . \quad (3.20)$$

For thermal critical phenomena, the analogous quantity is the susceptibility.

q th Moment. The quantities $E(p)$, $P_\infty(p)$, and $S(p)$ are the zeroth, the first, and the second moments of the distribution function $n_s(p)$. All the statistical quantities of the cluster distribution are characterized by the moments of $n_s(p)$. The q th moment $M_q(p)$ of $n_s(p)$ can be calculated in a similar way to (3.12), (3.14), or (3.19) as

$$M_q(p) \propto (p - p_c)^{\lambda_q} , \quad (3.21)$$

where the exponent λ_q is defined by

$$\lambda_q = \frac{\tau - q - 1}{\eta} . \quad (3.22)$$

It is quite important to note that the exponent of the q th moment depends linearly on q . This fact leads to simple and useful relations between exponents, i.e., the so-called scaling relations. We will see some of these scaling relations in Sect. 3.3. It should be emphasized that the linearity of λ_q with respect to q is a consequence of the scaling ansatz.

The Exponent ν . The lower cutoff scale characterizing the percolating network is the lattice spacing a of the original network. There exists another characteristic length $\xi(p)$, called the correlation length, mentioned at the beginning of this section. We shall see below that the correlation length $\xi(p)$ behaves as (3.2).

The correlation length $\xi(p)$ is defined as the root-mean-square distance between two occupied sites in the same cluster, averaged over all finite clusters. The average distance between two sites in clusters of size s is defined by

$$R_s^2 = \frac{1}{2s^2} \left\langle \sum_{ij} |\mathbf{r}_i - \mathbf{r}_j|^2 \right\rangle_s , \quad (3.23)$$

where \mathbf{r}_i is the position vector of site i , the summation is taken over all pairs of sites in a cluster of size s , and $\langle \dots \rangle_s$ denotes the average over all clusters of size s . Here we consider the probability $z(p)$ that a cluster including a given occupied site has the size s . This probability is given by

$$z(p) = \frac{s^2 n_s}{\sum_s s^2 n_s} , \quad (3.24)$$

because sn_s is the probability that a site belongs to a cluster of size s . The correlation length is an expectation length of R_s with the probability $z(p)$, i.e.,

$$\xi^2(p) = \sum_s z(p) R_s^2 = \frac{\sum_s R_s^2 s^2 n_s}{\sum_s s^2 n_s} . \quad (3.25)$$

It should be noted that there exist other ways to take the average of R_s , such as $\sum_s R_s^2 sn_s / \sum_s sn_s$ and $\sum_s R_s^2 n_s / \sum_s n_s$. Average lengths obtained by such procedures have different meanings from ξ defined by (3.25). The correlation length ξ is the expectation value of the linear dimension of a cluster to which a given occupied site belongs, but not the expectation value of the linear dimension of a given cluster. We postulate the scaling form for R_s as in the case of (3.5),

$$R_s = s^\varpi H [(p - p_c)s^\eta] , \quad (3.26)$$

where ϖ is a new critical exponent. With the help of (3.5) and (3.26), (3.25) leads to the relation

$$\xi(p) = E_0 |p - p_c|^{-\nu} \quad (3.27)$$

for the correlation length, where E_0 is a constant prefactor and the exponent ν is given by

$$\nu = \frac{\varpi}{\eta} . \quad (3.28)$$

The correlation length $\xi(p)$ represents the characteristic scale of clusters when $p < p_c$. Since n_s is the distribution function of finite clusters, $\xi(p)$ for $p > p_c$ gives the characteristic scales of finite clusters (excluding an infinite cluster).

We see from (3.26) that the relation $R_s \propto s^\varpi$ holds at $p = p_c$. This is rewritten in the form

$$s(R_s) \propto R_s^{1/\varpi} . \quad (3.29)$$

Note that $s(R_s)$ can be considered as a measure of the system since $s(R_s)$ corresponds to the total mass $M(R_s)$ within a radius R_s when sites or bonds have unit mass. From (2.17), the exponent $D_f = 1/\varpi$ can be considered as the fractal dimension of the percolating network.

In this section, we introduce several exponents describing the critical behaviour of statistical quantities. It should be emphasized that values of these exponents depend neither on the underlying lattice type nor the percolation type (SP or BP). This is because the correlation length $\xi(p)$ alone characterizes critical behaviour, and any other length scales introduced by microscopic details of the systems are irrelevant. Critical exponents depend only on the dimensionality of percolating networks. This crucial feature of critical exponents is called universality. Values of critical exponents are listed in Table 3.2.

Table 3.2. Percolation exponents for 2D, 3D, 4D and $d \geq 6$. Rational numbers give exact results, whereas those with a decimal fraction are numerical estimates [3.7–3.14]

Exponents	$d = 2$	$d = 3$	$d = 4$	$d = 5$	$d(\geq 6)$
β	5/36	0.405±0.025	0.639±0.020	0.835±0.005	1
γ	43/18	1.805±0.02	1.435±0.015	1.185±0.005	1
ν	4/3	0.872±0.007	0.678±0.050	0.571±0.003	1/2
D_f	91/48	2.48±0.09	3.12±0.02	3.69±0.02	4

3.2 Fractal Dimension

The relation between the fractal dimension D_f and the exponents β and ν can be derived from a simple argument. Consider the number of sites $M(L)$ belonging to an infinite cluster within a box of size L , which is given by

$$M(L) = L^d P_\infty(p), \quad \text{for } p > p_c. \quad (3.30)$$

With the help of (3.12), we can express (3.30) as

$$M(L) = L^d P_\infty(p) \propto L^d [(p - p_c)^{-\nu}]^{-\beta/\nu}. \quad (3.31)$$

Substituting (3.27) into (3.31) leads to

$$M(L) \propto L^d \xi^{-\beta/\nu}. \quad (3.32)$$

If the relation $\xi \gg L$ holds, we can replace ξ by L in (3.32), because L is the unique length scale within the box. This yields the important relation

$$M(L) \propto L^{d-\beta/\nu} = L^{D_f}. \quad (3.33)$$

Thus, the fractal dimension D_f is given by

$$D_f = d - \frac{\beta}{\nu}. \quad (3.34)$$

This relation is called the hyperscaling relation since it depends on the Euclidean dimension d . The exponents β and ν are universal, so that D_f is also universal. Values of D_f are given in Table 3.2.

If $p > p_c$ and $L \gg \xi$, ξ in (3.32) cannot be replaced by L . In this case, $\xi^{-\beta/\nu}$ in (3.32) becomes independent of L (but depends on p). Thus, $M(L)$ is proportional to L^d , which means that the structure can be regarded as homogeneous at length scales larger than $\xi(p)$. Therefore, the networks with $p > p_c$ are homogeneous at length scales $L \gg \xi$ and fractal for $L \ll \xi$, i.e.,

$$M(L) \propto \begin{cases} L^{D_f}, & L \ll \xi, \\ L^d, & L \gg \xi. \end{cases} \quad (3.35)$$

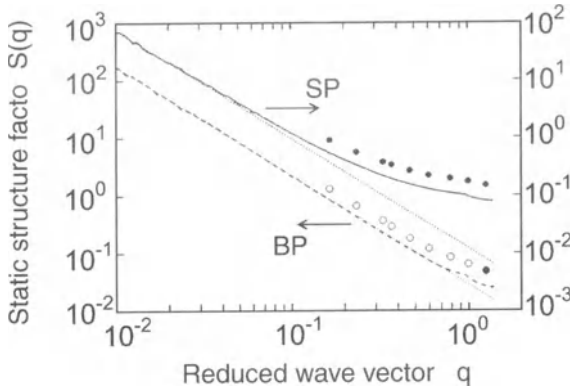


Fig. 3.4. Structure factor $S(q)$ for 2D SP and BP networks. Dots are for $L = 12$ systems (averaged over 20 000 realizations), and full curves for $L = 6\,800$. Dotted lines have slope $D_f = 91/48$ [3.15]

We can interpret $\xi(p)$ as the length scale up to which the cluster can be regarded as fractal. We note that percolating networks at $p = p_c$ take fractal structures over the whole length scale.

The lower limit of a length scale l_a below which the structure is no longer fractal depends on the type of percolation, i.e., SP or BP. This is because random filling produces a relatively small number of neighboring sites around an occupied site in SP networks, whereas BP networks have many occupied sites on neighbors that are not directly connected, as mentioned in Sect. 3.1. This significantly influences the short-range character of these networks. Figure 3.4 presents the results of a calculation by Stoll et al. [3.15], which indicates that the length scale l_a of BP networks is shorter than that of SP networks by one order of magnitude at $p = p_c$.

The Chemical Distance. In the context of the fractal geometry of percolating networks, we should mention that there is an exponent, besides those described so far, that is useful for describing the geometrical properties of percolating networks. This exponent is related to the shortest path from one site in a percolating network to another. We can define the length of the shortest path R_c between sites i and j as the minimum number of steps by which we can reach j from i along the percolating path between connected sites. This length R_c is known as the chemical distance. It is not the same as the slant distance between the two points (referred to as the Euclidean distance). The chemical (or topological) dimension d_c is defined from

$$M(R_c) \propto R_c^{d_c}, \quad (3.36)$$

where $M(R_c)$ is the number of occupied sites within a sphere of radius R_c . From (3.34) and (3.36), we find that the chemical distance between two sites separated by the Euclidean distance L takes the form

$$R_c \propto L^{D_f/d_c}. \quad (3.37)$$

The ratio $D_f/d_c = d_{\min}$ is the fractal dimension of the shortest path. The chemical dimension d_c has been determined numerically and takes the values $d_c = 1.678 \pm 0.005$ and $d_c = 1.885 \pm 0.015$ for 2D and 3D percolating networks, respectively [3.16, 3.17].

3.3 Finite-Size Scaling and Scaling Relations

So far we have introduced several critical exponents such as α , β , γ , τ , η , and D_f . These exponents are defined through quantities which are moments of the distribution function n_s . The scaling form (3.5) of n_s includes two exponents τ and η , so that only two of the critical exponents are independent. In fact, we find the following relations from (3.11), (3.15), (3.20), (3.28), and (3.34):

$$\alpha = 2 - dv , \quad (3.38)$$

$$\eta = \frac{1}{\beta + \gamma} , \quad (3.39)$$

$$\tau = 2 + \frac{\beta}{\beta + \gamma} , \quad (3.40)$$

and

$$dv = 2\beta + \gamma . \quad (3.41)$$

Scaling relations depending on the dimensionality, such as (3.34), (3.38) and (3.41), are called hyperscaling relations, as in the case of (3.34). The upper critical dimension above which the mean-field theory is valid is $d = 6$. Mean-field percolation can be modelled by percolation on a Cayley tree (Bethe lattice). Hyperscaling relations (3.34), (3.38), and (3.41) are valid only for $d \leq 6$, because values of critical exponents for $d > 6$ do not depend on the dimensionality.

Values of these critical exponents have been calculated by various numerical methods: the renormalization group method, cluster expansion methods, and Monte Carlo calculations, as presented in Table 3.2. These numerical calculations have been performed on finite percolating networks, although true critical behaviour is found only in infinite networks. The idea of finite-size scaling gives us an efficient way to extract reliable information about true critical behaviour from numerical results for finite-size networks. To describe finite-size scaling, let us consider a general quantity $x(p, L)$ defined for percolating networks at concentration p on a d -dimensional lattice of linear dimension L . We assume that this quantity for infinite systems is proportional to $(p - p_c)^\chi$, i.e.,

$$x(p) \propto (p - p_c)^\chi . \quad (3.42)$$

The scaling ansatz suggests that the quantity x should be scaled only by the correlation length ξ . Therefore, $x(p, L)$ can be written in the scaling form

$$x(p, L) = \xi^{-\delta} X(L/\xi) , \quad (3.43)$$

where δ is an exponent. For infinite systems ($L \rightarrow \infty$), $x(p, L)$ does not depend on L . This implies $X(z) = \text{Const.}$ for $z \rightarrow \infty$. Since the quantity $x(p, L)$ behaves as (3.42) in this case, we have the relation $\delta = \chi/v$. Thus, the scaling form (3.43) becomes

$$x(p, L) = \xi^{-\chi/v} X(L/\xi) , \quad (3.44)$$

or equivalently

$$x(p, L) = (p - p_c)^\chi \tilde{X}[(p - p_c)L^{1/v}] , \quad (3.45)$$

where $\tilde{X}(z) = X(z^\nu)$. If the correlation length ξ is much larger than the system size L , $x(p, L)$ does not depend on ξ . In this case, from (3.44), the scaling function $X(z)$ should be proportional to $z^{-\chi/v}$, which gives

$$x(p, L) \propto L^{-\chi/v} , \quad \text{for } L \ll \xi . \quad (3.46)$$

At the critical concentration p_c , (3.46) holds for any finite (but large) L because the correlation length ξ diverges, i.e.,

$$x(L) \propto L^{-\chi/v} , \quad \text{at } p = p_c . \quad (3.47)$$

This implies that we can obtain the value of χ from numerical calculations for finite systems if the exponent v and the critical concentration p_c are known.

Values of v and p_c can be calculated from finite-size simulations by the following procedure. Let $\Omega(p, L)$ be the probability of finding a spanning (percolating) cluster over a finite system of size L at concentration p . For infinite systems, $\Omega(p)$ becomes a step function because $\Omega(p) = 0$ for $p < p_c$ and $\Omega(p) = 1$ for $p \geq p_c$. If the system size is finite, there exists a probability of finding a percolating cluster even for $p < p_c$ and also a probability of not finding a percolating cluster for $p \geq p_c$. The p -dependence of $\Omega(p, L)$ for finite L is a smoothly increasing function from 0 to 1 when p is increased from 0 to 1. This function is also scaled by ξ , with the scaling form

$$\Omega(p, L) = K(L/\xi) = \tilde{K}[(p - p_c)L^{1/v}] , \quad (3.48)$$

where $\tilde{K}(z) = K(z^\nu)$. The first derivative of $\Omega(p, L)$ with respect to p is the probability that a percolating cluster in a system of size L appears for the first time at concentration p , because $\int_0^1 (d\Omega/dp) dp = 1$. From (3.48), this probability has the scaling form

$$\frac{d\Omega}{dp} = L^{1/v} \tilde{K}'[(p - p_c)L^{1/v}] . \quad (3.49)$$

Using this probability, we can define the effective percolation threshold $p_{\text{eff}}(L)$ as

$$p_{\text{eff}} = \int_0^1 p \left(\frac{d\Omega}{dp} \right) dp , \quad (3.50)$$

at which clusters in finite systems of size L percolate on average. Substituting (3.49) into (3.50) yields

$$p_{\text{eff}}(L) = p_c + cL^{-1/\nu} , \quad (3.51)$$

where c is the constant given by $c = \int z \tilde{K}'(z) dz$. In numerical calculations, p_{eff} can be obtained by putting particles one by one at randomly chosen sites on a d -dimensional lattice of size L . If we find a percolating cluster for the first time after N particles have been placed, the threshold concentration for this random sequence is N/L^d . Repeating this procedure many times with different random sequences, the average value of the threshold concentrations gives $p_{\text{eff}}(L)$. From (3.51), we plot $p_{\text{eff}} - p_c$ versus L on a log-log scale. This plot gives a straight line for a suitable value of p_c which is the critical concentration for infinite systems. The slope of the straight line provides the value of the exponent ν .

Values of χ , ν , and p_c can also be determined using the scaling form of (3.45) for $x(p, L)$. This method is more straightforward than the method mentioned above, but requires more computational effort. We measure the quantity $x(p, L)$ for many realizations of percolating networks at concentration p , formed on a finite system of size L , and average $x(p, L)$ over the percolation realizations. Performing similar calculations for different values of p and L , $x(p, L)$ is obtained for various p and L . We then plot the quantity $\tilde{X} = (p - p_c)^{-\chi} x(p, L)$ as a function of $(p - p_c)L^{1/\nu}$, where χ , ν , and p_c are fitting parameters. Values of χ , ν , and p_c are determined so that the data of \tilde{X} collapse onto a single curve.

Figure 3.5 shows an example of the finite-size scaling analysis for the order parameter $P_\infty(p)$ defined by (3.7). Values of $P_\infty(p, L)$ for 2D BP networks with

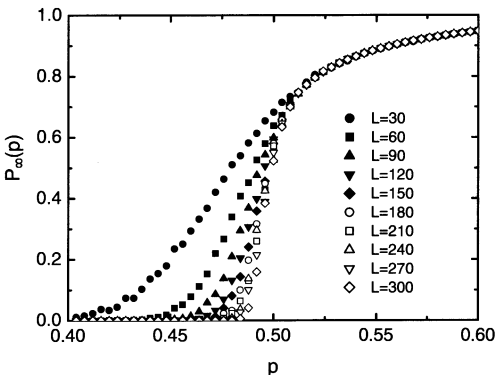


Fig. 3.5. The probability $P_\infty(p, L)$ of finding a site belonging to a spanning cluster. Different symbols represent data for different system sizes. Each data point has been obtained by averaging over many samples (1 000 samples for $L = 30$ and 500 for $L = 150$)

several system sizes L are plotted in the figure as a function of concentration p . Each symbol represents an average value of $P_\infty(p, L)$ over 10^2 – 10^3 samples. $P_\infty(p, L)$ approaches a step-like function with increasing L . Rescaling data by means of $p_c = 0.5$, $\beta = 5/36$, and $\nu = 4/3$, the data in Fig. 3.5 collapse onto a single curve with two branches as shown in Fig. 3.6. The upper and lower branches represent data for $p > p_c$ and $p < p_c$, respectively. If we use $p_c = 0.51$ or $p_c = 0.49$ instead of $p_c = 0.5$ while keeping the values of β and ν , the data significantly scatter around the curve, implying that p_c is very close to 0.5. The idea of the finite-size scaling presented here is quite important in numerical calculations, not only for percolation transitions but also for other critical phenomena. The finite-size scaling technique for the Anderson metal–insulator transition will be presented in Sect. 9.5.

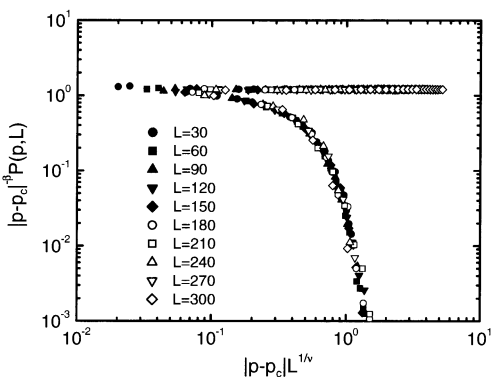


Fig. 3.6. Rescaled plot of data shown in Fig. 3.5. The scaling parameters are chosen as $p_c = 0.5$, $\beta = 5/36$, and $\nu = 4/3$. Corresponding to data for $p > p_c$ and $p < p_c$, there exist two branches of the scaling curve

3.4 Nodes–Links–Blobs Model

A very useful model for an infinite network near p_c was first proposed by Skal and Shklovskii [3.18] and de Gennes [3.19]. This model, called the nodes–links–blobs model, enables us to understand geometrical and dynamical features of percolating networks, such as electron transport or elastic properties, in a transparent manner.

A percolating network is constructed from several parts with different characters. For example, consider an elastic percolating network at $p = p_c$ stretched as shown in Fig. 3.7. For this stretched network, singly-connected bonds bear large deformations, while multiply-connected bonds do not. When cutting a singly-connected bond, the network is decomposed into two networks. We refer to these singly-connected bonds as links and the multiply-connected bonds as blobs. A network for $p > p_c$ cannot be separated into two networks by cutting any bond in the network. As mentioned in Sect. 3.2, a percolating network for $p > p_c$ has a fractal structure on any scale less

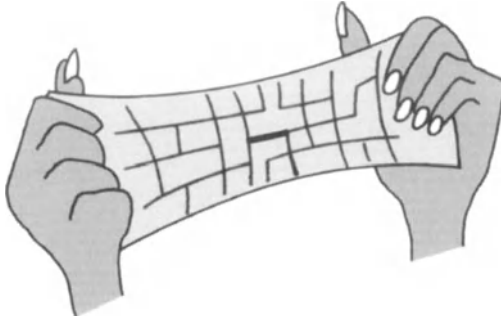


Fig. 3.7. Stretched elastic percolating network. The elastic energy concentrates on a single connected bond (shown by a thick line)

than the correlation length ξ . This means that geometrical features of the network for $p > p_c$ are similar to those of a critical network ($p = p_c$), within the scale of ξ . There thus exist singly-connected bonds in the partial structure of size ξ within the whole percolating network for $p > p_c$. These bonds are also called links. Links and blobs form the backbone of the percolating network. The backbone has translational symmetry on a scale larger than ξ in a statistical sense. Constituents of the percolating network other than the backbone are called dead ends. These are attached to the backbone and do not contribute elasticity in elastic percolating networks.

In the nodes–links–blobs model, the backbone forms a lattice with lattice spacing $\xi(p)$. Lattice points on the backbone lattice are called nodes. The links and blobs

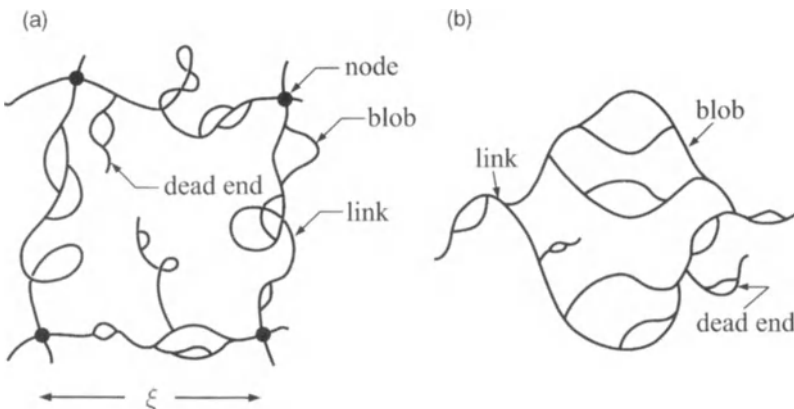


Fig. 3.8. Schematic illustration of the nodes–links–blobs model. (a) A percolating network above p_c . Solid circles indicate nodes forming the homogeneous network at length scales $L > \xi$. (b) Structure between adjacent nodes. The hierarchy of the nested blobs is presented. If the size of this structure becomes infinite, this provides a model for critical percolating networks (the links–blobs model)

connecting adjacent nodes are modelled by 1D line segments and loops, respectively, as shown in Fig. 3.8a. Dead ends modify these links and blobs. In order to reflect the fractality of the percolating network within the nodes-links-blobs model, blobs are iteratively nested as shown in Fig. 3.8b. Since the correlation length ξ diverges at the critical concentration p_c , the critical percolating network corresponds to the model in Fig. 3.8b of infinite size (the links-blobs model). In Sect. 3.2, we pointed out that the Mandelbrot–Given fractal is often used as a deterministic model of 2D percolating networks. It should be noted that the Mandelbrot–Given fractal has links and nested blobs, in addition to similar values of the fractal dimensions.

Stanley [3.4] called the links red bonds and considered the situation where a voltage is applied between two sites at opposite edges of a metallic percolating network. When a singly-connected bond (red bond) is cut, the current flow stops. This bond carries the total current. In his terminology, blue and yellow bonds also exist. Blue bonds belonging to blobs carry current, but cutting a blue bond merely increases the resistance of the system. Yellow bonds belong to dead ends, and can be cut out without changing the resistance.

The critical behavior of the links (red bonds) was derived by Coniglio [3.20,3.21] using renormalization arguments. He verified that the number of red bonds varies with p as

$$L_1 \propto (p - p_c)^{-1} \propto \xi^{1/\nu}. \quad (3.52)$$

This relation also indicates that the fractal dimension of the links is $1/\nu$, because L_1 is the measure in this case.

4. Multifractals

In previous chapters we discussed geometrical properties of fractals characterized by fractal dimensions D_f . However, the fractal dimension D_f is not sufficient to describe all features of complex structures or distributions. For example, a distribution of mineral resources on earth is one such case. Gold is found in high densities only at a few rich places, whereas an extremely small amount of gold exists almost everywhere. Assume that areas with gold density larger than ρ_1 are colored in red on a world atlas, and that areas with gold density larger than $\rho_2 (< \rho_1)$ are colored in blue. Even if the distribution of red portions on the atlas is characterized by a fractal dimension D_f , the fractal dimension of the blue region might differ from D_f . It can be understood intuitively that the fractal dimension of the red region with very large ρ_1 is close to zero, while the dimensionality of the blue region with very small ρ_2 is almost two [4.1].

This type of distribution can be found in many situations: the distribution of dissipation in turbulent flow [4.2], the distribution of growth probabilities of a diffusion-limited aggregation (DLA) [4.3, 4.4], the distribution of energy dissipation in a fractal resistor network [4.5], and inter-arrival time series of Internet traffic data [4.6]. In order to characterize these systems, we need to extend the fractal concept mentioned in Chap. 2. Multifractals described in the present chapter require an entire spectrum comprising infinitely many exponents to characterize their distributions. The concept of multifractals was originally introduced by Mandelbrot to describe the distribution of energy dissipation in turbulent flows [4.2, 4.7], and a vast amount of work has successively developed useful tools or methods for analyzing multifractals [4.8–4.19].

4.1 Hierarchical Resistor Network Model

Before embarking upon a general presentation of multifractals, we illustrate a simple example possessing almost all the relevant features of these objects. This is the distribution of voltage drops in a hierarchical resistor network (HRN). The structure of the HRN is similar to the nodes-links-blobs model mentioned in Sect. 3.4. The multifractality of this deterministic model was first discussed by de Arcangelis et al. [4.5, 4.20] to investigate the voltage-drop distribution of random resistor networks.

We start with a unit cell constructed from four bonds of unit resistance, as depicted in Fig. 4.1a. Next, the four bonds are replaced by unit cells (Fig. 4.1b), and this

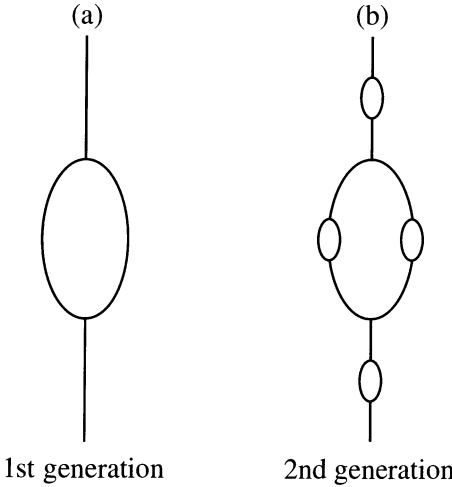


Fig. 4.1. The first and second generations of the hierarchical resistor network (HRN). Each bond has unit resistance. The n th generation is created by replacing every bond in the $(n - 1)$ th generation by the unit cell with four bonds (the same as the first generation)

procedure is repeated indefinitely. The resulting structure possesses a deterministic self-similarity. Constituent bonds belong to either links or blobs. The meanings of links and blobs are the same as those used in the nodes-links-blobs model for a percolating network, described in Sect. 3.4. A link is defined as a bond which, if cut, would render the network disconnected. The remaining bonds constitute blobs. This structure would thus be regarded as a simplified model of the backbone of a percolating network at criticality (see Fig. 3.8b). Note that lengths of individual bonds of the HRN are irrelevant. The system size L is defined in connection with the geometry of the percolating network as follows. In the n th generation HRN model, the number of bonds N_B , the total resistance R , and the number of links L_1 are given by

$$N_B = 4^n , \quad (4.1)$$

$$R = \left(\frac{5}{2}\right)^n , \quad (4.2)$$

and

$$L_1 = 2^n , \quad (4.3)$$

respectively. Using (4.3), quantities N_B and R are expressed as

$$N_B = L_1^{\zeta_B} , \quad (4.4)$$

and

$$R = L_1^{\zeta_R} , \quad (4.5)$$

where $\zeta_B = (\log 4 / \log 2) = 2$ and $\zeta_R = \log(5/2) / \log 2 = 1.32 \dots$. In a percolating network at the critical concentration p_c , the number of links L_1 is proportional to $L^{1/\nu}$, as given by (3.52), where L is the system size and ν is the exponent for the correlation length ξ [4.21]. The system size L of the HRN model can thus be obtained using (4.3) and the relation $L_1 \propto L^{1/\nu}$ as

$$L = 2^{n\nu} . \quad (4.6)$$

From this relation, we have for (4.4) and (4.5)

$$N_B \propto L^{\tilde{\zeta}_B} , \quad (4.7)$$

and

$$R \propto L^{\tilde{\zeta}_R} , \quad (4.8)$$

respectively, where $\tilde{\zeta}_B = \zeta_B/\nu$ and $\tilde{\zeta}_R = \zeta_R/\nu$.

Now let us consider the distribution of voltage drops in the HRN. If a unit voltage is applied across the second generation of the HRN, voltage drops for various bonds become as shown in Fig. 4.2. There exist three values of the voltage drops, i.e., $2^2/5^2$, $2^1/5^2$, and $2^0/5^2$. These are combined into a single expression by

$$V_k = \frac{2^k}{5^2} , \quad (k = 0, 1, 2) .$$

The number of ‘bonds’ with voltage drop V_k is given by

$$N(V_k) = 2^2 \binom{2}{k} .$$

For the n th generation of the HRN, the above argument can be generalized to

$$V_k = \frac{2^k}{5^n} , \quad (4.9)$$

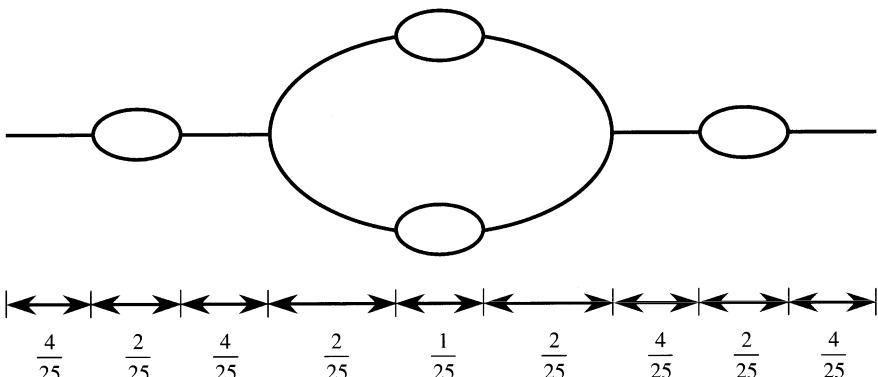


Fig. 4.2. Voltage drops in the second generation of the hierarchical resistor network (HRN) model across which a unit voltage is applied. We define the resistance of a single bond to be unity. Fractional numbers indicate voltage drops between both ends of bonds

and

$$N(V_k) = 2^n \binom{n}{k}, \quad (k = 0, 1, \dots, n). \quad (4.10)$$

Using the distribution function $N(V_k)$ and the binomial theorem, the q th moment $\langle V^q \rangle$ can be calculated as

$$\langle V^q \rangle = \sum_{k=0}^n V_k^q N(V_k) = \left[\frac{2}{5^q} (1 + 2^q) \right]^n. \quad (4.11)$$

We should note that the q th moment of the distributed quantities V is dominated by larger or smaller values of V if $q \gg 1$ or $q \ll -1$, respectively. By introducing an exponent $\tilde{\zeta}_q$ defined by

$$\langle V^q \rangle \propto L^{\tilde{\zeta}_q}, \quad (4.12)$$

we obtain from (4.6)

$$\tilde{\zeta}_q = \frac{\log \left[\frac{2}{5^q} (1 + 2^q) \right]}{\nu \log 2}. \quad (4.13)$$

The exponent $\tilde{\zeta}_0 = 2/\nu$ is the fractal dimension of the 0 th moment. The 0 th moment is just the number of bonds. The value of $\tilde{\zeta}_0$ obtained from (4.13) agrees with that of (4.7). The exponent of the second moment $\tilde{\zeta}_2$ characterizes the distribution of energy dissipations. From (4.13), we have

$$\tilde{\zeta}_2 = -\frac{\log(5/2)}{\nu \log 2} = -\tilde{\zeta}_R. \quad (4.14)$$

Since the second moment given by

$$\langle V^2 \rangle = \sum_k V_k^2 N(V_k)$$

represents the total energy dissipation W , and W is given by V^2/R , where R is the total resistance of the network and $V = 1$ is the total voltage drop, we see that the result of (4.14) is consistent with (4.8).

Equation (4.13) indicates that different orders of moments are characterized by different exponents. In typical fractal systems, such as percolating networks, the exponent of the q th moment also depends on q , but the dependence is always linear as shown in (3.22). This important property gives various scaling relations between exponents, implying that only a finite number of exponents are independent. In contrast, the exponents characterizing $\langle V^q \rangle$ in the HRN are nonlinear with respect to q , as shown in (4.13). This implies that the exponents are not simply related. An infinite set of exponents is required to describe the voltage-drop moments. In general,

a distribution is called multifractal if moments of the distribution are described by an infinite set of independent exponents. In such a case, the usual linear scaling relations between exponents do not hold at all. From the scaling viewpoint, this type of scaling is called anomalous scaling. The concepts of multifractal and the anomalous scaling are almost synonymous, although these terminologies are distinguished in certain contexts.

The distribution function $N(V_k)$ of voltage drops V_k is given by (4.10). If we regard $N(V_k)$ as a function of k , $N(V_k)$ can be expressed by the binomial distribution

$$B_{n,p}(k) = \binom{n}{k} p^k (1-p)^{n-k},$$

with $p = 1/2$ as

$$N(k) = 4^n B_{n,\frac{1}{2}}(k).$$

For large generation number n , the binomial distribution function $B_{n,p}(k)$ asymptotically approaches the normal distribution function

$$B_{n,p}(k) \rightarrow \frac{1}{\sqrt{2n\pi p(1-p)}} \exp \left[-\frac{(k-np)^2}{2np(p-1)} \right]. \quad (4.15)$$

Therefore, for higher generations of the HRN, the distribution $N(k)$ can be written as

$$N(k) = \frac{2 \cdot 4^n}{\sqrt{2n\pi}} \exp \left[-\left(k - \frac{n}{2} \right)^2 / \frac{n}{2} \right]. \quad (4.16)$$

Using (4.9), we find the voltage-drop distribution given by

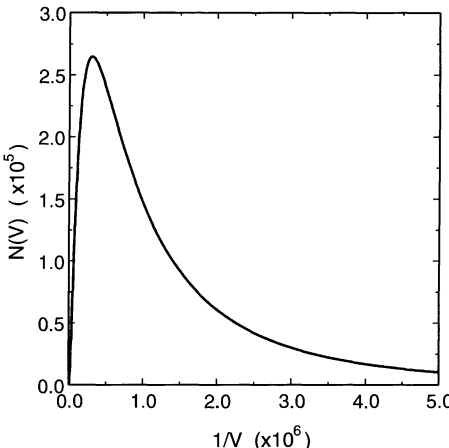


Fig. 4.3. Voltage-drop distribution function for the hierarchical resistor network model with $n = 10$ (the 10th generation). The distribution function is given by (4.17)

$$N(\log V) = \frac{2 \cdot 4^n}{\sqrt{2n\pi}} \exp \left[- \left(\log V - n \log \frac{\sqrt{2}}{5} \right)^2 / \frac{n}{2} (\log 2)^2 \right]. \quad (4.17)$$

This is a log-normal distribution function of V . As can be seen in Fig. 4.3, when plotted as a function of $1/V$, the distribution $N(V)$ is quite broad, a common feature of multifractal distributions.

All characteristics found in the voltage-drop distribution of the HRN model are common to other multifractals. In Sect. 4.2, we present a general definition of multifractals, including those for random fractal structures, and useful tools for quantitative analysis of multifractal distributions. The discussion in this section has aimed to prepare the reader for the generalized concepts and abstract quantities appearing in the next section.

4.2 Mass Exponent and Generalized Dimension

As mentioned in Sect. 4.1, multifractals describe distributions of intensities or densities of quantities on supports. In this section, we treat a distribution of general quantities μ_i , where i stands for spatial position. We assume that μ_i is normalized over the whole system, i.e., $\sum_i \mu_i = 1$. This means that μ_i is not itself a physical quantity, but a probability of finding the quantity at position i . Although we hereafter refer to μ_i as a measure at the position i , borrowing from a mathematical terminology, the reader may regard it merely as a probability of finding a physical quantity [4.22].¹

As in the case of (4.12), we consider a situation in which the system-size dependence of the q th moment $\langle \mu^q \rangle = \sum_i \mu_i^q$ is characterized by q -dependent exponents, i.e.,

$$\langle \mu^q \rangle = \sum_i \mu_i^q \propto L^{-\tau(q)}, \quad (4.18)$$

where the exponent $\tau(q)$ corresponds to $-\tilde{\zeta}_q$ in (4.12). The exponent $\tau(q)$ is called the mass exponent. We assume that the relation (4.18) holds for any unit of length scale. This means that a coarse-grained distribution of μ_i should also satisfy (4.18). Let us

¹ The measure used here is a Lebesgue measure. Measure is a generalized concept of the size of an object, such as length, area, volume, or mass. The size $\mu(A)$ of an object A has the properties: (i) $\mu(A) \geq 0$ and (ii) $\mu(A \cup B) = \mu(A) + \mu(B)$ if $A \cap B = \emptyset$. In general, the quantity $\mu(A)$ satisfying these two conditions is called a Riemann measure. The Lebesgue measure is defined by replacing condition (ii) by (ii)' $\mu(\bigcup_{i=1}^{\infty} A_i) = \sum_{i=1}^{\infty} \mu(A_i)$ if $A_i \cap A_j = \emptyset$ ($i \neq j$). If we regard $\{A_i\}$ as a set of events, we can consider $\mu(A_i)$ as the probability of A_i . In fact, Kolmogoroff defined a probability by $\mu(A)$ satisfying (i)' $0 \leq \mu(A) \leq 1$, (ii)', and (iii) $\mu(S) = 1$ where S is the whole set of events. Therefore, the Lebesgue measure is almost equivalent to a probability.

consider a distribution of measures coarse-grained by a scale l . This coarse-grained measure (box measure) $\mu_{b(l)}$ is given by

$$\mu_{b(l)} = \sum_{i \in b(l)} \mu_i , \quad (4.19)$$

and $b(l)$ is a box of size l in the system. Thus, the moment $\langle \mu_l^q \rangle$ coarse-grained by the scale l is represented by

$$\langle \mu_l^q \rangle = \sum_b \mu_{b(l)}^q , \quad (4.20)$$

where the summation is taken over small boxes of size l (see Fig. 4.4). Since the relation (4.18) should also hold for the box measure $\mu_{b(l)}$, we have

$$\langle \mu_l^q \rangle = \sum_b \left(\sum_{i \in b(l)} \mu_i \right)^q \propto \left(\frac{l}{L} \right)^{\tau(q)} . \quad (4.21)$$

Note that L/l represents the coarse-graining. From this relation, $\tau(q)$ is expressed as

$$\tau(q) = \lim_{l \rightarrow 0} \frac{\log \langle \mu_l^q \rangle}{\log l} . \quad (4.22)$$

If the mass exponent $\tau(q)$ is a nonlinear function of q , we call the distribution of measures multifractal, as in the case of the HRN model, where the exponent $\tilde{\zeta}_q$ is the nonlinear function of q given in the relation (4.13).

Although the quantity $-\tau(q)$ seems to have the meaning of a fractal dimension of $\langle \mu_l^q \rangle$ because of the relation $\langle \mu_l^q \rangle \propto L^{-\tau(q)}$, this is not adequate. Provided that measures are uniformly distributed on a fractal support with dimension D_f , the q th

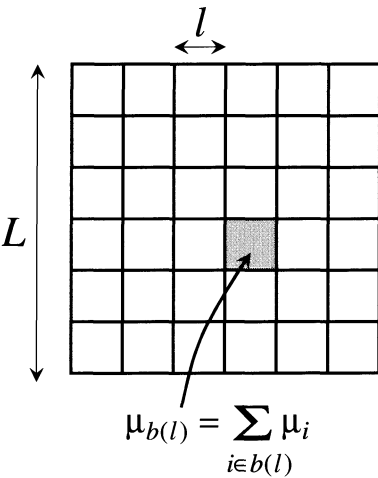


Fig. 4.4. The whole system of size L is divided into small boxes of size l ($< L$). A box measure $\mu_{b(l)}$ of a box b is defined by $\sum_{i \in b(l)} \mu_i$, where μ_i is a measure at a spatial position i

moment of μ should distribute with the same fractal dimension D_f independently of q . In this case, using the normalization condition $\sum_i \mu_i = 1$, we have $\mu_i \propto L^{-D_f}$. From (4.19) and (4.20), the moment $\langle \mu_l^q \rangle$ becomes

$$\langle \mu_l^q \rangle \propto \sum_b (l^{D_f} L^{-D_f})^q ,$$

because the number of sites in the box b is proportional to l^{D_f} . Summation over the boxes in the above relation yields $\sum_b = (L/l)^{D_f}$. As a result, we find

$$\langle \mu_l^q \rangle \propto \left(\frac{l}{L} \right)^{D_f(q-1)} . \quad (4.23)$$

The quantity $\tau(q)$ becomes $D_f(q-1)$ and depends on q . From this argument, the appropriate definition of the fractal dimension of the q th moment should be

$$D_q = \frac{\tau(q)}{q-1} . \quad (4.24)$$

For the case of a uniform distribution, we see that D_q is equal to D_f independently of q because $\tau(q) = D_f(q-1)$ from (4.23). The exponent D_q is called the generalized fractal dimension or simply the generalized dimension. From (4.22) and (4.24), D_q is defined by

$$D_q = \frac{1}{q-1} \lim_{l \rightarrow 0} \frac{\log \langle \mu_l^q \rangle}{\log l} . \quad (4.25)$$

Expressing the definition of multifractals in terms of D_q instead of $\tau(q)$, a distribution is said to be multifractal when the generalized dimension D_q depends on q .

The generalized dimensions for several specific values of q are of particular interest in understanding the meaning of distributions. For $q = 0$, D_0 becomes the fractal dimension D_f of the support. In the case of the HRN model, D_0 is equal to $\tilde{\zeta}_B$, describing the number of bonds [(4.7)]. The generalized dimension with $q = 1$, namely, D_1 , is equivalent to the information dimension D_I [4.23, 4.24]. In statistical mechanics, the entropy of the probability distribution of box measure $\mu_{b(l)}$ is defined by

$$S_l = - \sum_b \mu_{b(l)} \log \mu_{b(l)} , \quad (4.26)$$

where the summation is taken over small boxes of size l . For this entropy, the definition of the information dimension D_I is

$$D_I = \lim_{l \rightarrow 0} \frac{S_l}{\log(1/l)} . \quad (4.27)$$

We verify the relation $D_1 = D_I$ below. Exchanging the order of the two limits ($q \rightarrow 1$ and $l \rightarrow 0$), (4.25) implies

$$D_1 = \lim_{l \rightarrow 0} \frac{1}{\log l} \lim_{q \rightarrow 1} \frac{1}{q-1} \log \left[\sum_b \mu_{b(l)}^q \right] . \quad (4.28)$$

The limit with respect to q can be evaluated by de l'Hôpital's theorem and $\sum_b \mu_{b(l)} = 1$. We thus obtain

$$D_1 = -\lim_{l \rightarrow 0} \frac{\sum_b \mu_{b(l)} \log \mu_{b(l)}}{\log(1/l)} . \quad (4.29)$$

The generalized dimension (4.29) is equivalent to the information dimension D_I given by (4.27). In actual measurements of fractals, the determination of the fractal dimension D_f of the support requires us to observe even very rare events, and this takes an infinitely long measuring time. On the contrary, the information dimension D_I is more easily determined by experiment and characterizes the distribution of information content.

We can show that the generalized dimension D_q with $q = 2$ is equivalent to the correlation dimension D_{co} [4.25]. Consider the case when particles are distributed in a multifractal manner, i.e., the particle density plays the role of a multifractal measure. The total number of particles and the position of the i th particle are denoted by N and x_i , respectively. The probability $C(l)$ that the distance between two particles is less than l is given by

$$C(l) = \lim_{N \rightarrow \infty} \frac{1}{N^2} \sum_i \sum_{j \neq i} \Theta(l - |x_i - x_j|) , \quad (4.30)$$

where $\Theta(x)$ is a step function defined by $\Theta(x) = 1$ for $x > 0$ and $\Theta(x) = 0$ otherwise. The function $C(l)$ is called the correlation integral. The correlation dimension D_{co} is defined by $C(l) \propto l^{D_{co}}$, i.e.,

$$D_{co} = \lim_{l \rightarrow 0} \frac{\log C(l)}{\log l} . \quad (4.31)$$

By dividing the space embedding the particle system into small boxes of size l , we can denote the probability of finding a particle in a box $b(l)$ by $\mu_{b(l)}$. The probability of finding two particles in this box is $\mu_{b(l)}^2$. The average probability of $\mu_{b(l)}^2$ over all boxes, $\sum_b \mu_{b(l)}^2$, is the probability that the distance between two particles is less than l , which is equivalent to the correlation integral $C(l)$. From the definition of the generalized dimension, $\langle \mu_l^2 \rangle = \sum_b \mu_{b(l)}^2 \propto l^{D_2}$. Therefore, we have $D_{co} = D_2$.

We have mentioned that the information dimension D_I can be more readily determined by experimental measurements than the fractal dimension D_f . The correlation dimension D_{co} is even easier to determine than D_I . In measurements of D_f or D_I , the embedding space must be divided into small boxes even if there is no particle (or measure) in the boxes. Procedures for dividing the space and counting measures are arduous tasks when the Euclidean dimension of the embedding space becomes large. Determination of the correlation dimension does not require the division of space. D_{co} can be calculated from the distribution of lengths between all pairs of measured points. Therefore, the correlation dimension is often used to characterize a multifractal distribution.²

² We emphasize once again that the generalized dimension D_q or the mass exponent $\tau(q)$ is required for every value of q within $(-\infty, \infty)$ in order to completely characterize the multifractal distribution, although D_2 is easy to determine.

The limiting values of D_q at $q \rightarrow \pm\infty$ are also meaningful dimensions. The generalized dimensions $D_{\pm\infty}$ represent the distribution of measures with the highest ($q \rightarrow +\infty$) and lowest ($q \rightarrow -\infty$) intensities. From de l'Hôpital's theorem, we have

$$D_{\pm\infty} = \lim_{q \rightarrow \pm\infty} \frac{d\tau}{dq}. \quad (4.32)$$

Evaluation of $D_{\pm\infty}$ will be presented in Sect. 4.7. In the case of the HRN model, D_∞ characterizes the distribution of voltage drops of link bonds, because links give the largest voltage drop among the whole voltage-drop distribution, as seen from Fig. 4.2. Note that the dimension D_∞ is not the fractal dimension of the link distribution itself. On the other hand, $D_{-\infty}$ describes the distribution of the smallest voltage drops, that is, voltage drops of bonds belonging to the most deeply nested blobs, which are depicted in Fig. 4.2 as blobs labelled by 1/25. Values of D_q for $q = 0, 1$ and 2 are presented in Appendix A.

4.3 Multifractal Spectrum

In the n th generation of the HRN model, the voltage drop V_k of a bond is given by (4.9), which is a function of n and k . Since the size L of the HRN depends on n as shown by (4.6), V_k can be regarded as a function of L . From (4.6) and (4.9), the functional form is written as

$$V_k \propto L^{-\alpha_k}, \quad (4.33)$$

where

$$\alpha_k = \frac{1}{n \log 2} \left(\log 5 - \frac{k}{n} \log 2 \right), \quad (4.34)$$

with $k = 0, 1, 2, \dots, n$. It should be noted that the voltage drop characterized by a different index k scales with a different scaling exponent α_k .³ From this deterministic example, we can postulate for a general multifractal distribution that a box measure $\mu_{b(l)}$ is proportional to l^α , from the analogy with (4.21), and that the exponent α depends on the box (see Fig. 4.5). The exponent α is called the Lipschitz–Hölder exponent or the exponent of the singularity:

$$\alpha = \lim_{l \rightarrow 0} \frac{\log \mu_{b(l)}}{\log l}. \quad (4.35)$$

We should remark that (4.34) does not give the correct expression for the Lipschitz–

³ The second term in (4.34) depends on the generation n . Taking $L = 2^{nv}$ into account, this term seems to provide a coefficient of (4.33), but not an exponent. This is, however, due to the peculiarity of the HRN model. The HRN model is not a typical curdling fractal [4.9] where the system size and the generation are independent. The size of the HRN diverges as $n \rightarrow \infty$. Even in this limit ($n \rightarrow \infty$), the ratio k/n in (4.34) is finite and the second term provides an exponent in this limit, as seen in Appendix A [(A.19)].

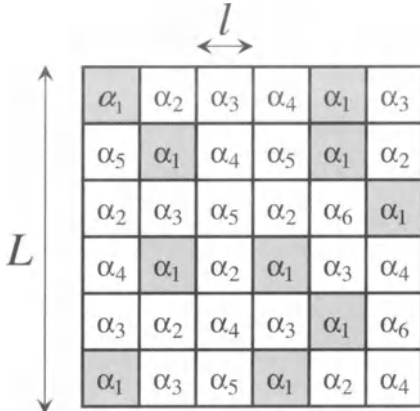


Fig. 4.5. Schematic illustration of the spatial distribution of the Lipschitz–Hölder exponents α characterizing the box-size dependence of box measures. The *dark region* represents boxes with the same Lipschitz–Hölder exponent ($\alpha = \alpha_1$). This region should have a self-similar structure, if measures are distributed in a multifractal manner

Hölder exponent for the HRN model, because the voltage drop V_i of the i th bond in the HRN is not normalized, i.e., $\sum_i V_i \neq 1$, whereas the box measure $\mu_{b(l)}$ in the definition (4.35) should be normalized. The correct expression for the Lipschitz–Hölder exponent of the HRN model is presented in Appendix A.

Let us consider the distribution of small boxes with an exponent α . In the HRN model, bonds with voltage drop V_k distribute in a fractal manner. The fractal dimension of these bonds depends on k . For example, the fractal dimension of the link-bond ($k = n$) distribution is $1/\nu$, because the relation $L_1 \propto L^{1/\nu}$ holds for the HRN model, as mentioned in (4.6) above, where $L_1 = N(V_n)$ is the number of links. On the other hand, the fractal dimension of the distribution of $k = n/2$ bonds is $2/\nu$ as shown below. From (4.10), the number of bonds with $k = n/2$ is given by $N(V_{n/2}) = 2^n \binom{n}{n/2}$. Using Stirling's formula for $n!$, $\binom{n}{n/2} \approx 2^n$ for large n . We thus have $N(V_{n/2}) \approx 2^{2n}$. Taking (4.3) into account, $N(V_{n/2}) \propto L_1^2 \propto L^{2/\nu}$, which implies that the fractal dimension of the distribution of $k = n/2$ bonds is $2/\nu$. Generalizing this, we can suppose that the distribution of boxes specified by an exponent α is fractal with the α -dependent fractal dimension $f(\alpha)$. Hence, denoting the number of boxes with α by $N(\alpha)$, we have the relation $N(\alpha) \propto L^{f(\alpha)}$, or

$$f(\alpha) = \lim_{L \rightarrow \infty} \frac{\log N(\alpha)}{\log L}. \quad (4.36)$$

The fact that the subset specified by α has its own peculiar fractal dimension explains the etymology of the word ‘multifractal’. The exponent $f(\alpha)$ is called the multifractal spectrum. The multifractal spectrum for the HRN model is presented in Appendix A.

4.4 Relation between $\tau(q)$ and $f(\alpha)$

Multifractal distributions are characterized by either of two exponents $\tau(q)$ and $f(\alpha)$ defined by (4.22) and (4.36), respectively. These exponents describe the same aspect

of a multifractal, i.e., $\tau(q)$ and $f(\alpha)$ are related to each other. In order to see this, we consider the q th moment of measures $\langle \mu_l^q \rangle$ given by (4.20). Since the box measure $\mu_{b(l)}$ is proportional to l^α , the q th moment becomes

$$\langle \mu_l^q \rangle \propto \sum_b l^{\alpha q} . \quad (4.37)$$

We replace the summation over boxes in (4.37) by the integral over α . To this end, we consider the subset S_α of boxes with the exponent α . Let $\rho(\alpha)d\alpha$ be the number of subsets S_α in the range $[\alpha, \alpha + d\alpha]$. Since the number of boxes, $N(\alpha)$, in the subset S_α is proportional to $l^{-f(\alpha)}$, the number of boxes included in subsets in the range $[\alpha, \alpha + d\alpha]$ is given by

$$N(\alpha)\rho(\alpha)d\alpha \propto \rho(\alpha)l^{-f(\alpha)}d\alpha . \quad (4.38)$$

Therefore, we can put $\sum_b = \int \rho(\alpha)l^{-f(\alpha)} d\alpha$, which yields

$$\langle \mu_l^q \rangle \propto \int \rho(\alpha)l^{\alpha q - f(\alpha)} d\alpha . \quad (4.39)$$

This integral can be obtained by applying the steepest descent method with respect to α , for which we require

$$\frac{d}{d\alpha} \{\alpha q - f(\alpha)\} = 0 . \quad (4.40)$$

The q th moment $\langle \mu_l^q \rangle$ is found to be

$$\langle \mu_l^q \rangle \propto \rho[\alpha(q)]l^{\alpha(q)q - f[\alpha(q)]} , \quad (4.41)$$

where $\alpha(q)$ is the solution of (4.40). From the definition of the mass exponent, $\langle \mu_l^q \rangle \propto l^{\tau(q)}$, we have the relation

$$\tau(q) = \alpha(q)q - f[\alpha(q)] . \quad (4.42)$$

Equation (4.42) expresses the fact that $\tau(q)$ and $f(\alpha)$ are related to each other by a Legendre transform. Solving (4.42) with respect to $f(\alpha)$ yields

$$f(\alpha) = q(\alpha)\alpha - \tau[q(\alpha)] , \quad (4.43)$$

where $q(\alpha)$ is the inverse function of $\alpha(q)$. The explicit form of $q(\alpha)$ is obtained directly from (4.40) as

$$q = \frac{df(\alpha)}{d\alpha} . \quad (4.44)$$

Substituting (4.43) into (4.44), we obtain

$$q = q + \alpha \frac{dq}{d\alpha} - \frac{d\tau}{dq} \frac{dq}{d\alpha} .$$

The Lipschitz–Hölder exponent is thus given by

$$\alpha = \frac{d\tau(q)}{dq} . \quad (4.45)$$

The multifractal distribution is defined by the fact that the mass exponent is a non-linear function of q , or by the existence of uncountably many different Lipschitz–Hölder exponents. Equation (4.45) demonstrates that the existence of uncountably many different Lipschitz–Hölder exponents also provides a definition of multifractals.

4.5 Direct Determination of $f(\alpha)$

In actual measurements of multifractals, the mass exponent $\tau(q)$ is easily evaluated from its definition (the box-counting method). We first divide a system into boxes of size l , count box measures $\mu_{b(l)}$, and obtain $\tau(q)$ from a log–log plot of l versus $\langle \mu_l^q \rangle = \sum_b \mu_{b(l)}^q$ by using the least-square-fitting method. The generalized dimension D_q is directly calculated from (4.24). The multifractal spectrum $f(\alpha)$ can, in principle, also be calculated from $\tau(q)$ by the Legendre transform, (4.43) and (4.45). It is, however, necessary to perform a numerical differentiation to obtain an exponent α , and this produces large errors in α and therefore in $f(\alpha)$. If we smooth out numerical data for $\tau(q)$ to avoid this, the estimation of errors arising from the smoothing procedure becomes difficult. Methods for calculating $f(\alpha)$ without the numerical Legendre transform greatly improve our multifractal analyses. We describe here a method for computing the multifractal spectrum $f(\alpha)$ directly by a box-counting procedure [4.26].

From the definition of the mass exponent (4.22) of the form

$$\tau(q) = \lim_{l \rightarrow 0} \frac{\log \sum_b \mu_{b(l)}^q}{\log l} , \quad (4.46)$$

the Lipschitz–Hölder exponent α given by (4.45) becomes

$$\begin{aligned} \alpha &= \lim_{l \rightarrow 0} \frac{1}{\log l} \frac{d}{dq} \left(\log \sum_b \mu_{b(l)}^q \right) \\ &= \lim_{l \rightarrow 0} \frac{1}{\log l} \sum_b \frac{\mu_{b(l)}^q}{\sum_{b'} \mu_{b'(l)}^q} \log \mu_{b(l)} . \end{aligned} \quad (4.47)$$

Introducing a new probability measure $m_{b(l)}(q)$ defined in a box of size l by

$$m_{b(l)}(q) = \frac{\mu_{b(l)}^q}{\sum_{b'} \mu_{b'(l)}^q} , \quad (4.48)$$

the exponent α is given by

$$\alpha = \lim_{l \rightarrow 0} \frac{\sum_b m_{b(l)}(q) \log \mu_{b(l)}}{\log l} . \quad (4.49)$$

The quantity $m_{b(l)}(q)$ is often called the q -microscope. Therefore, using (4.43), the multifractal spectrum is expressed by

$$f[\alpha(q)] = \lim_{l \rightarrow 0} \frac{1}{\log l} \left[\sum_b m_{b(l)}(q) \log \mu_{b(l)}^q - \log \sum_b \mu_{b(l)}^q \right] . \quad (4.50)$$

Taking account of $\sum_b m_{b(l)}(q) = 1$, this yields

$$f[\alpha(q)] = \lim_{l \rightarrow 0} \frac{\sum_b m_{b(l)}(q) \log [m_{b(l)}(q)]}{\log l} . \quad (4.51)$$

The exponents α and $f(\alpha)$ given by (4.49) and (4.51) are simply calculated by a box counting of measures. Using these formulae, we can obtain the profile of $f(\alpha)$ through the implicit parameter q without the numerical Legendre transform. It should be noted from (4.51) that the multifractal spectrum $f(\alpha)$ is the information dimension of the q -microscope $m_{b(l)}(q)$.

4.6 Correlations between Box Measures

If a system of size L adopts a conventional fractal structure with fractal dimension D_f , the density-density correlation function $G(r) = \langle \rho(\mathbf{r})\rho(0) \rangle$ is also described by the fractal dimension D_f as shown in (2.25), where $\rho(\mathbf{r})$ is the mass density at position \mathbf{r} . It is worth discussing how the correlation function of box measures in a multifractal system is described by exponents characterizing its multifractality [4.27]. The correlation function is defined by

$$G_{q_1 q_2}(r) = \frac{1}{N_b N_{b_r}} \sum_b \sum_{b_r} \mu_{b(l)}^{q_1} \mu_{b_r(l)}^{q_2} , \quad (4.52)$$

where $\mu_{b_r(l)}$ is the box measure of a box $b_r(l)$ of size l a fixed distance $r-l$ away from the box $b(l)$, N_b (or N_{b_r}) is the number of boxes $b(l)$ [or $b_r(l)$], and the summation \sum_{b_r} is taken over all such boxes $b_r(l)$. The correlation function $G_{q_1 q_2}(r)$ is a function not only of r but also of the box size l and the system size L . Due to the absence of characteristic lengths in the multifractal system, $G_{q_1 q_2}(r)$ should behave as

$$G_{q_1 q_2}(r) \propto l^{x^*(q_1, q_2)} L^{-y^*(q_1, q_2)} r^{-z^*(q_1, q_2)} . \quad (4.53)$$

Our task is to relate the new exponents x^* , y^* , and z^* to previously introduced exponents such as $\tau(q)$.

Let us consider first a situation with $r = l$. In this case, (4.52) with $N_b \propto (L/l)^{D_f}$ and $N_{b_r} = 1$ and (4.21) give

$$G_{q_1 q_2}(l) \propto \left(\frac{l}{L}\right)^{D_f} \sum_b \mu_{b(l)}^{q_1 + q_2} \propto \left(\frac{l}{L}\right)^{D_f + \tau(q_1 + q_2)}, \quad (4.54)$$

where D_f is the fractal dimension of the support. Since we have $G_{q_1 q_2}(l) \propto l^{x^*(q_1, q_2) - z^*(q_1, q_2)} L^{-y^*(q_1, q_2)}$ from (4.53), the exponents are related by

$$y^*(q_1, q_2) = D_f + \tau(q_1 + q_2), \quad (4.55)$$

and

$$x^*(q_1, q_2) - z^*(q_1, q_2) = D_f + \tau(q_1 + q_2). \quad (4.56)$$

In order to determine the exponent $x^*(q_1, q_2)$, we consider $G_{q_1 q_2}(L)$. Since box measures in the system of size L are correlated with each other up to the distance L , we expect no correlations between $\mu_{b(l)}$ and $\mu_{b_L(l)}$. Therefore, in this case, (4.52) becomes

$$G_{q_1 q_2}(L) \propto \left(\frac{l}{L}\right)^{2D_f} \left(\sum_b \mu_{b(l)}^{q_1} \right) \left(\sum_b \mu_{b(l)}^{q_2} \right) \propto \left(\frac{l}{L}\right)^{2D_f + \tau(q_1) + \tau(q_2)}. \quad (4.57)$$

From (4.57) and the relation $G_{q_1 q_2}(L) \propto l^{x^*(q_1, q_2)} L^{-y^*(q_1, q_2) - z^*(q_1, q_2)}$ [from (4.53)], we obtain

$$x^*(q_1, q_2) = 2D_f + \tau(q_1) + \tau(q_2), \quad (4.58)$$

and (4.56) yields

$$z^*(q_1, q_2) = D_f + \tau(q_1) + \tau(q_2) - \tau(q_1 + q_2). \quad (4.59)$$

In particular, for $q_1 = q_2$, the exponents $x(q) = x^*(q, q)$, $y(q) = y^*(q, q)$, and $z(q) = z^*(q, q)$ are given by

$$x(q) = 2D_f + 2\tau(q), \quad (4.60)$$

$$y(q) = D_f + \tau(2q), \quad (4.61)$$

and

$$z(q) = D_f + 2\tau(q) - \tau(2q). \quad (4.62)$$

The exponent $z(q)$ describing the r dependence of the correlation function $G_q(r)$ is quite important, because $G_q(r)$ with $l = 1$ for a system of finite size L characterizes the multifractality of the system without box-counting procedures in actual numerical calculations. We call the exponent $z(q)$ the multifractal correlation exponent or simply the correlation exponent.

4.7 Profiles of $\tau(q)$, D_q , $f(\alpha)$, and $z(q)$

A multifractal distribution is characterized by exponents $\tau(q)$, D_q , $f(\alpha)$, or $z(q)$. The forms of these functions depend on the distribution of measures. However, there do exist several common features in the q -dependences of $\tau(q)$, D_q , and $z(q)$ and the α -dependence of $f(\alpha)$. These features allow us to draw rough profiles of them.

Let us consider first the limiting case $q \rightarrow -\infty$. Since $f(\alpha) > 0$, $d f(\alpha)/d\alpha = -\infty$ from (4.44) in this limit, and $f(\alpha)$ is a single-valued function of α , the Lipschitz–Hölder exponent corresponding to $q \rightarrow -\infty$ provides its maximum value α_{\max} given by

$$\alpha_{\max} = \alpha(q) \Big|_{q \rightarrow -\infty}. \quad (4.63)$$

The derivative of $f(\alpha)$ becomes

$$\frac{df(\alpha)}{d\alpha} \Big|_{\alpha \rightarrow \alpha_{\max}} \rightarrow -\infty. \quad (4.64)$$

For $q \rightarrow -\infty$, the q th moment $\langle \mu_l^q \rangle$ is dominated by boxes with the smallest box measure $\mu_{b(l)}^{\min}$. For $q \rightarrow -\infty$, the q -microscope $m_{b(l)}(q)$ given by (4.48) becomes

$$m_{b(l)}(q) \Big|_{q \rightarrow -\infty} = \begin{cases} \frac{1}{N_b^{\min}} & \text{for boxes with } \mu_{b(l)}^{\min}, \\ 0 & \text{otherwise,} \end{cases} \quad (4.65)$$

where N_b^{\min} is the number of boxes with $\mu_{b(l)}^{\min}$. If boxes with $\mu_{b(l)}^{\min}$ distribute in a fractal manner with fractal dimension $f_{-\infty}$ of the form

$$N_b^{\min} \propto \left(\frac{L}{l}\right)^{f_{-\infty}}, \quad (4.66)$$

substitution of (4.65) and (4.66) into (4.51) yields

$$f[\alpha(q)] \Big|_{\alpha \rightarrow \alpha_{\max}} = f_{-\infty}. \quad (4.67)$$

From (4.42), the asymptotic form of $\tau(q)$ for $q \rightarrow -\infty$ is given by

$$\tau(q) = \alpha_{\max} q - f_{-\infty}. \quad (4.68)$$

The generalized dimension D_q defined by (4.24) and the correlation exponent $z(q)$ given by (4.62) are found to be

$$D_q \Big|_{q \rightarrow -\infty} = \alpha_{\max}, \quad (4.69)$$

and

$$z(q) = D_f - f_{-\infty} . \quad (4.70)$$

In the opposite limit $q \rightarrow \infty$, a similar argument to the one used for $q \rightarrow -\infty$ gives the minimum value of the Lipschitz–Hölder exponent as

$$\alpha_{\min} = \alpha(q) \Big|_{q \rightarrow \infty} . \quad (4.71)$$

At this point, the derivative of $f(\alpha)$ yields

$$\frac{df(\alpha)}{d\alpha} \Big|_{\alpha \rightarrow \alpha_{\min}} \rightarrow \infty . \quad (4.72)$$

For $q \rightarrow \infty$, $\langle \mu_l^q \rangle$ is dominated by boxes with the largest box measure $\mu_{b(l)}^{\max}$. If boxes with $\mu_{b(l)}^{\max}$ distribute in a fractal manner with the fractal dimension f_∞ as given by

$$N_b^{\max} \propto \left(\frac{L}{l} \right)^{f_\infty} , \quad (4.73)$$

where N_b^{\max} is the number of boxes with $\mu_{b(l)}^{\max}$, the multifractal spectrum becomes

$$f[\alpha(q)] \Big|_{\alpha \rightarrow \alpha_{\min}} = f_\infty . \quad (4.74)$$

The asymptotic form of $\tau(q)$ for $q \rightarrow \infty$ is obtained as

$$\tau(q) = \alpha_{\min} q - f_\infty , \quad (4.75)$$

and we have also

$$D_q \Big|_{q \rightarrow \infty} = \alpha_{\min} , \quad (4.76)$$

and

$$z(q) = D_f - f_\infty . \quad (4.77)$$

The following remark should be made. In many cases of statistically distributed measures, the number of boxes possessing the smallest or the largest box measure is unity, which does not depend on L or l . This means that $f_{-\infty}$ and f_∞ vanish.

Next we consider the case of $q = 0$. Since $\mu_{b(l)}^q$ with $q = 0$ is unity for any boxes with $\mu_{b(l)} \neq 0$, the q th moment $\langle \mu_l^q \rangle = \sum_b \mu_{b(l)}^q$ is proportional to l^{-D_f} , where D_f is the fractal dimension of the support. We therefore have

$$\tau(0) = -D_f , \quad (4.78)$$

and

$$D_0 = D_f . \quad (4.79)$$

From (4.62), the exponent $z(q)$ of the correlation function with $q = 0$ is given by

$$z(0) = 0 , \quad (4.80)$$

and

$$\left. \frac{dz(q)}{dq} \right|_{q=0} = 2\alpha(q)|_{q=0} - 2\alpha(2q)|_{q=0} = 0 . \quad (4.81)$$

Since $z(q)$ is always positive, $z(q)$ takes the minimum value $z(0) = 0$ at $q = 0$. From (4.44) and (4.45), the derivative of $f(\alpha)$ for $q = 0$ becomes

$$\left. \frac{df(\alpha)}{d\alpha} \right|_{\alpha=\alpha_0} = 0 , \quad (4.82)$$

where

$$\alpha_0 = \left. \frac{d\tau(q)}{dq} \right|_{q=0} . \quad (4.83)$$

The value of the multifractal spectrum at $\alpha = \alpha_0$ is, from (4.43) and (4.78),

$$f(\alpha_0) = D_f . \quad (4.84)$$

Since the fractal dimension D_f of the support is obviously the largest fractal dimension of subsets of boxes, the condition (4.82) implies that $f(\alpha)$ takes the maximum value at $\alpha = \alpha_0$.

For $q = 1$, the normalization condition for measures μ_i leads to $\langle \mu_i^q \rangle = 1$, and the mass exponent defined by (4.22) with $q = 1$ becomes

$$\tau(1) = 0 . \quad (4.85)$$

Equation (4.62) with (4.85) yields

$$z(1) = D_f - D_2 . \quad (4.86)$$

The generalized dimension for $q = 1$ is equivalent to the information dimension D_I , as mentioned in Sect. 4.2. The value of D_I depends on the measure distribution, as does D_f . If the Lipschitz–Hölder exponent corresponding to $q = 1$ is α_1 , the multifractal spectrum given by (4.43) is expressed as $f(\alpha_1) = \alpha_1 - \tau(1)$. Thus, (4.85) leads to

$$f(\alpha_1) = \alpha_1 . \quad (4.87)$$

The slope of the tangent to $f(\alpha)$ at (α_1, α_1) is unity due to (4.44).

Common features of the exponents presented above are summarized in Table 4.1. From this table, we can draw rough profiles of $\tau(q)$, D_q , $f(\alpha)$ and $z(q)$. As shown in Fig. 4.6a, the function $\tau(q)$ is a monotonically increasing function of q .

Table 4.1. General properties of exponents. The specific values and asymptotic behaviour are common to any multifractal distribution

q	$\tau(q)$	D_q	α	$f(\alpha)$	$z(q)$
$-\infty$	$\alpha_{\max}q - f_{-\infty}$	α_{\max}	α_{\max}	$f_{-\infty}$	$D_f - f_{-\infty}$
0	$-D_f$	D_f	α_0	D_f	0
1	0	D_1	α_1	α_1	$D_f - D_2$
∞	$\alpha_{\min}q - f_{\infty}$	α_{\min}	α_{\min}	f_{∞}	$D_f - f_{\infty}$

Asymptotic profiles of $\tau(q)$ for $q \rightarrow \pm\infty$ are straight lines with slopes α_{\max} and α_{\min} for $q \rightarrow -\infty$ and $\rightarrow \infty$, respectively. The curve of $\tau(q)$ should pass through $(0, -D_f)$ and $(1, 0)$. The generalized dimension D_q is a monotonically decreasing function of q as shown in Fig. 4.6b. The function asymptotically approaches constant values for $q \rightarrow \pm\infty$. The multifractal spectrum is a convex function of α whose maximum value is D_f (see Fig. 4.6c). The curve should come up vertically from $(\alpha_{\min}, f_{\infty})$ and fall down to $(\alpha_{\max}, f_{-\infty})$. Furthermore, the $f(\alpha)$ curve should be tangent to the curve $f(\alpha) = \alpha$ at the point (α_1, α_1) , where α_1 is the Lipschitz–Hölder exponent corresponding to $q = 1$. Figure 4.6d shows a typical profile of the correlation exponent $z(q)$, which is a single-dip function of q .

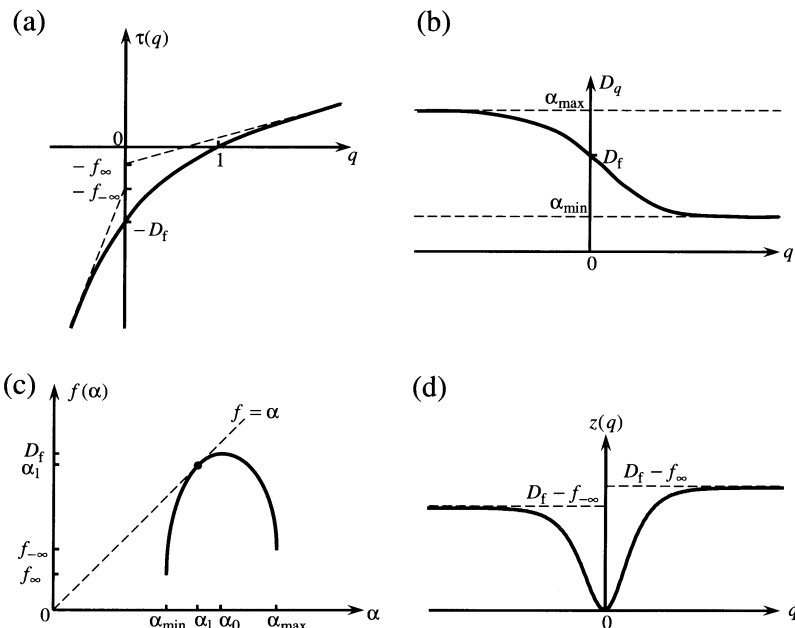


Fig. 4.6. General profiles of (a) the mass exponent $\tau(q)$, (b) the generalized dimension D_q , (c) the multifractal spectrum $f(\alpha)$, and (d) the correlation exponent $z(q)$. Features of these functions are discussed in the text

These exponents (τ , D_q , f , and z) characterizing multifractal distributions can also be defined for conventional fractal systems such as the Koch curve and percolating networks, although these are less interesting. In such cases, $\tau(q)$ becomes a straight line, $\tau(q) = D_f(q - 1)$, and D_q and α degenerate to a single value D_f for any q . The exponent $z(q)$ collapses onto $z(q) = 0$. The function $f(\alpha)$ is defined only at $\alpha = D_f$ and takes the value D_f . Although properties of $\tau(q)$, D_q , $f(\alpha)$, and $z(q)$ described in Table 4.1 are quite general, the functional profiles shown in Fig. 4.6 are merely typical, not general. The profiles of these exponents for the HRN model are presented in Appendix A.

4.8 Parabolic Approximation and Distribution Functions of Measures

As seen in Sect. 4.7, the multifractal spectrum $f(\alpha)$ is a single-hump function with negative curvature. It is convenient in some cases to approximate $f(\alpha)$ by a function characterized by a few parameters. The simplest way is to regard $f(\alpha)$ as a parabolic function of α [4.28,4.29]. Although the function $f(\alpha)$ should satisfy all the conditions presented in Sect. 4.7, three of them uniquely determine the form of the parabolic function. Here, we choose these three conditions as follows: (i) If $\alpha = \alpha_0$, $f(\alpha)$ is equal to D_f , (ii) the derivative $f'(\alpha)$ is zero at $\alpha = \alpha_0$, and (iii) the curve $f = f(\alpha)$ is tangent to the line $f = \alpha$. The general form of parabolic functions satisfying (i) and (ii) can be written as

$$f(\alpha) = D_f - c(\alpha - \alpha_0)^2 , \quad (4.88)$$

where c is a positive constant. When the curve $f = f(\alpha)$ is tangent to $f = \alpha$, the equation $f(\alpha) = \alpha$ has a double root. This gives $c = 1/4(\alpha_0 - D_f)$ and

$$f(\alpha) = D_f - \frac{(\alpha - \alpha_0)^2}{4(\alpha_0 - D_f)} . \quad (4.89)$$

This parabolic approximation characterizes $f(\alpha)$ by the single parameter α_0 , besides the fractal dimension of the support. The parabolic approximation mimics the profile of $f(\alpha)$ well near $\alpha = \alpha_0$, but deviates from the true $f(\alpha)$ away from α_0 . For example, the function given by (4.89) does not satisfy (4.64) and (4.72). Within the parabolic approximation, the mass exponent $\tau(q)$, the generalized dimension D_q , and the correlation exponent $z(q)$ are also calculated from α_0 and D_f as

$$\tau(q) = -(q - 1)[q(\alpha_0 - D_f) - D_f] , \quad (4.90)$$

$$D_q = -q(\alpha_0 - D_f) + D_f , \quad (4.91)$$

and

$$z(q) = 2q^2(\alpha_0 - D_f) , \quad (4.92)$$

respectively. We find from (4.91) that the parabolic approximation is equivalent to a linear approximation of D_q .

We now turn to the distribution function of measures. As mentioned in Sect. 4.1, a broad distribution of measures is one of the common features of multifractals. In fact, in the HRN model, the distribution function of voltage drops is a log-normal distribution. Since the multifractal spectrum (or the mass exponent) completely characterizes the statistical properties of the distribution of measures, the distribution function should be described by $f(\alpha)$ [or $\tau(q)$]. Let us find the relation between the distribution function and the multifractal spectrum. Denoting a distribution function of box measures μ_b coarse-grained by a box size l by $P(\mu_b, \lambda)$, where $\lambda = l/L$ and L is the system size, $P(\mu_b, \lambda)d\mu_b$ is the number of boxes with box measure μ_b lying in $[\mu_b, \mu_b + d\mu_b]$. We express μ_b in terms of the Lipschitz–Hölder exponent α from (4.35), i.e., $\alpha = \log \mu_b / \log \lambda$ for small λ . Thus, the distribution function $P(\mu_b, \lambda)$ can be replaced by $\tilde{P}(\alpha, \lambda)$ according to

$$P(\mu_b, \lambda)d\mu_b = \tilde{P}(\alpha, \lambda)d\alpha . \quad (4.93)$$

Furthermore, we introduce the distribution function $R(\log \mu_b, \lambda)$ defined by

$$R(\log \mu_b, \lambda)d\log \mu_b = \tilde{P}(\alpha, \lambda)d\alpha . \quad (4.94)$$

The function $R(\log \mu_b, \lambda)$ is given by

$$R(\log \mu_b, \lambda) = \frac{\tilde{P}(\alpha, \lambda)}{\log \lambda} . \quad (4.95)$$

According to the argument in Sect. 4.4 [in particular (4.38)], the distribution function $\tilde{P}(\alpha, \lambda)$ is written as $\tilde{P}(\alpha, \lambda) = \rho(\alpha)\lambda^{-f(\alpha)}$, where $\rho(\alpha)$ is the density of the subset S_α composed of boxes with the exponent α . The density $\rho(\alpha)$ can be considered to be a weak function (e.g., a power) of α compared to $\lambda^{-f(\alpha)}$, and we can ignore this factor. The factor $1/\log \lambda$ appearing in the right-hand side of (4.95) is also weaker than $\lambda^{-f(\alpha)}$ and can be treated as a constant. We thus have the relation $R(\log \mu_b, \lambda) \propto \lambda^{-f(\alpha)}$ or

$$R(\log \mu_b, \lambda) = \frac{1}{N(\lambda)} \exp \left[-f \left(\frac{\log \mu_b}{\log \lambda} \right) \log \lambda \right] , \quad (4.96)$$

where $N(\lambda)$ is a normalization factor. This function is quite broad with respect to μ_b , because $f(\alpha)$ is a compact convex function of α . In fact, the parabolic approximation of $f(\alpha)$ yields

$$R(\log \mu_b, \lambda) \propto \exp \left[\frac{(\log \mu_b - \alpha_0 \log \lambda)^2}{4(\alpha_0 - D_f) \log \lambda} \right] . \quad (4.97)$$

This is a log-normal distribution function because $\log \lambda < 0$. The exponent α_0 plays an important role in determining the distribution function of box measures in the parabolic approximation. The average value of $\log \mu_b$ is $\alpha_0 \log \lambda$ for the distribution

function given by (4.97), which means that the geometric mean of μ_b defined by $\mu_{\text{geo}} = \exp[\langle \log \mu_b \rangle]$ is equal to λ^{α_0} . Due to the broadness of the distribution function, a typical value of μ_b such as the geometric mean μ_{geo} provides intrinsic information about the distribution rather than the arithmetic mean $\langle \mu_b \rangle$, as will be discussed in Sect. 10.2. The typical value μ_{typ} defined by the mode of $P(\mu_b, \lambda)$ also behaves as

$$\mu_{\text{typ}} \propto \lambda^{\alpha_0}, \quad (4.98)$$

because the distribution function (4.96) gives the maximum value at

$$\frac{\log \mu_b}{\log \lambda} = \alpha_0.$$

The typical value defined as the mode is more convenient than the geometric mean, because (4.98) does not require the parabolic approximation (4.97).

4.9 Growth Probability of DLA

We showed in Sect. 4.1 that the voltage-drop distribution of the HRN model exhibits multifractality. In this case, the distribution is deterministic and the mass exponent $\tau(q)$ or the multifractal spectrum $f(\alpha)$ can be calculated analytically, as explained in Appendix A. The concept of multifractals is, of course, applicable to stochastic distributions, in which numerical or experimental procedures are required to obtain $\tau(q)$ or $f(\alpha)$. Remembering that the HRN model describes approximately the backbone of a percolating network, it is easy to understand that the voltage-drop distribution of a percolating-resistor network at criticality would be multifractal [4.20, 4.30]. Another striking example of multifractals in stochastic distributions is the growth probability of the diffusion-limited aggregation (DLA) [4.3, 4.4, 4.11, 4.31, 4.32]. Interest in the DLA model is maintained by a wide range of applications in both the physical and biological sciences.

In the simplest version of the DLA model, a particle is located at an initial site r_0 in a discrete lattice as a seed for cluster formation. Another particle starts a random walk from a randomly chosen site in the spherical shell of radius r with width $dr (\ll r)$ and center r_0 . If the random walker moves outside the sphere of radius $R (\geq r + dr)$, the particle is removed and a new random walk restarts from a new site in the spherical shell. The random walk is continued until the particle contacts the seed (the particle reaches a nearest neighbor site of the seed). The cluster composed of two particles is then formed. This procedure is repeated many times, in each of which the radius r of the starting spherical shell should be much larger than the gyration radius of the cluster. If the number of particles contained in the DLA cluster is huge (typically 10^4 – 10^8), the cluster takes a fractal structure in a statistical sense. Figure 4.7 illustrates a simulated result for a 2D DLA cluster obtained by the procedure mentioned above. The number of particles N inside a sphere of radius L (\ll the gyration radius of the cluster) is given by

$$N \propto L^{D_f}.$$



Fig. 4.7. Simulated result of a 2D diffusion-limited aggregation (DLA). The number of particles contained in this DLA cluster is 10^4

The fractal dimensions D_f of 2D and 3D DLA clusters are 1.71 and 2.49, respectively. The number of sites N_p in the perimeter of the cluster, i.e., the number of nearest-neighbor sites of the cluster, is known to be proportional to N , so that N_p is also characterized by D_f .

Let us consider a distribution of growth probabilities of a DLA cluster. The growth probability p_i of a perimeter site i is the probability that a new random walker contacts the site i . Therefore, the support of the growth-probability distribution is the set of perimeter sites of the DLA cluster. In order to obtain the growth-probability distribution of a given DLA cluster by a numerical simulation, we perform the growth

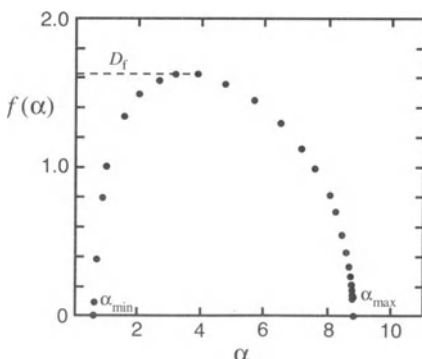


Fig. 4.8. Multifractal spectrum for a 2D diffusion-limited aggregation. The growth probability distribution is calculated by numerically solving the discretized Laplace equation in a 2D square lattice [4.33]

procedure described above by using the DLA cluster as a starting seed. If a random walker contacts the cluster, we record the contact perimeter site and the particle is removed. This procedure is repeated M times ($M \gg 1$). The growth probability p_i is obtained by $p_i = m_i/M$, where m_i is the number of times that the i th perimeter site is contacted.⁴ It is obvious that the growth probability near tips of the cluster is larger than that inside a deep ‘fjord’. Thus, different sites have different growth probabilities, intimating the multifractality of the growth-probability distribution. In fact, the multifractal spectrum calculated numerically for a 2D DLA cluster has a convex profile, as shown in Fig. 4.8. The maximum value of $f(\alpha)$ is close to $D_f = 1.71$ (2D), as we expected.

Another important example illustrating the fact that stochastic distributions in condensed matter physics can exhibit multifractality is the critical wavefunction at the Anderson metal–insulator transition. This will be discussed in Chap. 10.

⁴ This numerical method has a weak point, viz., a huge amount of computing time is required to obtain a precise value of the minimal p_i . A more efficient technique for calculating the growth probability is to solve the Laplace equation $\Delta\phi = 0$ with the boundary conditions $\phi(\mathbf{r}) = \text{Const.}$ on the cluster and $\phi(\mathbf{r}) = 0$ as $\mathbf{r} \rightarrow \infty$ [4.33].

5. Anomalous Diffusion on Fractal Networks

This chapter is concerned with the problem of diffusion on fractal networks, which plays a central role when we investigate dynamical properties of fractals. The relation between vibrational excitations on fractal networks and diffusion is also discussed. We start by describing in detail the diffusion of random walkers on a percolating network. In uniform systems, the mean-squared displacement $\langle r^2(t) \rangle$ of a random walker is proportional to the time t , i.e., $\langle r^2(t) \rangle \propto t$, for any Euclidean dimension d . How does $\langle r^2(t) \rangle$ behave in the case of fractal percolating networks? For this, de Gennes [5.1] posed the following problem called an ant in the labyrinth:

An ant parachutes down onto an occupied site of the infinite cluster of a percolating network. At every time unit, the ant makes one attempt to jump to one of its adjacent sites. If that site is occupied, it moves there. If it is empty, the ant stays at its original site. What is the ensemble-averaged squared distance that the ant travels in time t ?

Gefen et al. [5.2] gave a fundamental description of this problem in terms of a scaling argument. This work triggered further developments in the dynamics of fractal systems. This is because the diffusion equation can be mapped onto equations governing various types of dynamics [5.3]. For example, the basic properties of vibrations of fractal networks, such as the density of states, the dispersion relation and the localization/delocalization property can be derived from the same arguments for diffusion on fractal networks. These dynamical properties are described in a unified way by introducing a new dynamic exponent called the spectral or fracton dimension.

5.1 Anomalous Diffusion

We consider diffusion on an infinite percolating network with $p > p_c$. Choosing the origin as the point where the ant parachutes down, the mean-squared displacement $\langle r^2(t) \rangle$ after a sufficiently long time t satisfying the relation $\langle r^2(t) \rangle^{1/2} \gg \xi$ should be linearly proportional to the time t , where ξ is the correlation length of the percolating network. This is because the structure of the percolating network at scales larger than ξ is uniform, as discussed in Sect. 3.2, and the random walk of the ant exhibits

typical diffusion behaviour (normal diffusion). This gives a relation of the form

$$\langle r^2(t) \rangle = 2D_\infty t , \quad \text{for } \langle r^2(t) \rangle^{1/2} \gg \xi , \quad (5.1)$$

where the diffusion coefficient D_∞ is defined by

$$D_\infty = \frac{1}{2} \frac{d\langle r^2(t) \rangle}{dt} . \quad (5.2)$$

The subscript ∞ on D reflects the fact that D_∞ describes diffusion spread over an infinite network. The diffusion coefficient D_∞ is related to the dc conductivity σ_{dc} through the Einstein relation

$$\sigma_{dc} = \frac{e^2 n D_\infty}{k_B T} . \quad (5.3)$$

Here e denotes the carrier charge, n their density, k_B the Boltzmann constant, and T the temperature, respectively. It is obvious that the dc conductivity vanishes for $p < p_c$ due to the absence of any infinite cluster. The value of σ_{dc} becomes nonzero for $p > p_c$. In the vicinity of p_c , σ_{dc} is assumed to behave as

$$\sigma_{dc}(p) = \Sigma_0(p - p_c)^\mu , \quad \text{for } p > p_c , \quad (5.4)$$

where μ is called the conductivity exponent. Noting that the carrier density n in (5.3) is proportional to the percolation order parameter $P_\infty(p)$ given by (3.12), we have from (5.3)

$$D_\infty \propto (p - p_c)^{\mu - \beta} . \quad (5.5)$$

It should be emphasized that $\mu - \beta$ is always positive because $D_\infty \rightarrow 0$ for $p \rightarrow p_c + 0$. From (5.1) and (5.5), we obtain the relation

$$\langle r^2(t) \rangle \propto (p - p_c)^{\mu - \beta} t . \quad (5.6)$$

Next we consider diffusion on finite clusters in a percolating network with $p < p_c$. In this case, ξ means the average linear dimension of finite clusters and $\langle r^2(t) \rangle$ becomes independent of time t after a sufficiently long time. Hence, for such a long time, the ant reaches the cluster boundary and cannot move out any further. In this case, we have $\langle r^2(t) \rangle \propto \xi^2$ for $p < p_c$, and (3.27) implies

$$\langle r^2(t) \rangle \propto |p - p_c|^{-2\nu} . \quad (5.7)$$

Here we assume that a unique length scale is introduced by diffusion on a percolating network and that this length scale obeys a power law in t . Thus, the relations (5.6) and (5.7) can be unified into a scaling form

$$\langle r^2(t) \rangle^{1/2} = t^x G[(p - p_c)t^y] , \quad (5.8)$$

where $G(z)$ is a scaling function. For percolating networks with $p > p_c$, (5.8) should take the asymptotic form (5.6) for long times t , and the scaling function becomes

$$G(z)_{z \rightarrow \infty} \propto z^{(\mu - \beta)/2}. \quad (5.9)$$

Combining (5.9) and (5.8), we find from (5.6) the relation

$$\frac{y(\mu - \beta)}{2} + x = \frac{1}{2}. \quad (5.10)$$

For $p < p_c$, $\langle r^2(t) \rangle$ becomes independent of time t , as shown by (5.7). The scaling function in (5.8) thus takes the form

$$G(z)_{z \rightarrow -\infty} \propto z^{-x/y}. \quad (5.11)$$

Substituting (5.11) into (5.8), we obtain from (5.7) the relation

$$\frac{x}{y} = \nu. \quad (5.12)$$

From (5.10) and (5.12), we have

$$x = \frac{\nu}{2\nu + \mu - \beta}, \quad (5.13)$$

and

$$y = \frac{1}{2\nu + \mu - \beta}. \quad (5.14)$$

Substituting (5.13) into (5.8) gives the relation for a percolating network at $p = p_c$ as

$$\langle r^2(t) \rangle \propto t^{2/\tilde{d}_w}, \quad (5.15)$$

where \tilde{d}_w is defined by

$$\tilde{d}_w = 2 + \frac{\mu - \beta}{\nu} = 2 + \theta, \quad (5.16)$$

with $\theta = (\mu - \beta)/\nu$. Due to the condition $\mu > \beta$, and hence $\theta > 0$, diffusion described by (5.15) becomes slow compared with the case of normal diffusion (5.1). This slow diffusion given by (5.15) is called anomalous diffusion.

The above results indicate that diffusion in percolating networks becomes anomalous for length scales smaller than ξ and that the mean-squared displacement is described by (5.15). The slowing down of diffusion ($\theta > 0$) is caused by the diffusing particle wandering through hierarchically intricate structures, in which it may encounter dead ends. The exponent \tilde{d}_w in (5.15) is called the anomalous diffusion exponent.

Table 5.1. Various exponents characterizing dynamics in percolating networks. The values of \tilde{d}_s are taken from [5.4]

Exponents	$d = 2$	$d = 3$	$d = 4$	$d = 5$	$d(\geq 6)$
\tilde{d}_w	2.871 ± 0.001	4.00 ± 0.05			6
μ	1.264 ± 0.054	1.876 ± 0.035	2.39	2.72	3
\tilde{d}_s	1.325 ± 0.002	1.317 ± 0.003	1.31 ± 0.03	1.36	4/3

From (5.8), we can estimate the crossover time τ from anomalous to normal diffusion. Anomalous diffusion occurs when $t \ll \tau$, whereas normal diffusion is expected for $t \gg \tau$. The characteristic time τ can be obtained by setting the argument in the function $G(z)$ in (5.8) to be of the order of unity, i.e.,

$$\tau \approx (p - p_c)^{-(2\nu + \mu - \beta)} . \quad (5.17)$$

The value of \tilde{d}_w can be obtained by direct numerical calculation of $\langle r^2(t) \rangle$, or from the fact that the number of distinct sites $V(t)$ visited by the random walker within the time t is, from (2.15) and (5.15), given by $V(t) \propto t^{D_f/\tilde{d}_w}$. When using these quantities, we must note that (5.15) describes diffusion for $t \ll \tau$ on a single infinite cluster. Values of \tilde{d}_w are given in Table 5.1, together with other exponents describing dynamics. From Table 5.1, we see that for any Euclidean dimension d , \tilde{d}_w is larger than 2, which is the value for normal diffusion.

We see from the above discussion that diffusion becomes anomalous for a critical percolating network ($p = p_c$) with fractal structure. Anomalous diffusion defined by (5.15) is not peculiar to percolating networks, but is quite general for fractal systems. We should note that the diffusion distance for a deterministic fractal is actually a complicated function of t . The relation (5.15) should be read as a smoothed expression of the diffusion distance for deterministic fractals.¹

5.2 Spectral Dimension

The spectral (or fracton) dimension \tilde{d}_s is a key dimension for describing the dynamics of fractal networks, in addition to the fractal dimension D_f . The fractal dimension D_f characterizes how the geometrical distribution of a static structure depends on its length scale, whereas the spectral dimension \tilde{d}_s plays a central role in characterizing critical properties of dynamic quantities on fractal networks.

The diffusion distance of a random walker after t time steps is expressed by (5.15). Therefore, the number of visited sites $V(t) \propto \langle r^2(t) \rangle^{D_f/2}$ is found to be

$$V(t) \propto t^{\tilde{d}_s/2} , \quad (5.18)$$

¹ In addition to (5.15), the relation (5.18) in Sect. 5.2 and (5.40) in Sect. 5.3 should be considered as smoothed expressions over suitable time and frequency intervals, respectively.

where the exponent \tilde{d}_s is called the spectral or fracton dimension,² defined by

$$\tilde{d}_s = \frac{2D_f}{\tilde{d}_w} . \quad (5.19)$$

For percolating networks, the spectral dimension is given by

$$\tilde{d}_s = \frac{2D_f}{2 + \theta} = \frac{2\nu D_f}{2\nu + \mu - \beta} , \quad (5.20)$$

using (5.16). Alexander and Orbach [5.5] estimated the values of \tilde{d}_s for percolating networks on d -dimensional Euclidean lattices from the then-known values of the exponents D_f , ν , μ , and β . They pointed out that while these exponents depend dramatically on d , \tilde{d}_s does not. They conjectured from the numerical values of \tilde{d}_s for $2 \leq d \leq 5$ and the fact that $\tilde{d}_s = 4/3$ for $d \geq 6$ that the following relation holds for percolating networks:

$$\tilde{d}_s = 4/3 , \quad \text{for } 2 \leq d . \quad (5.21)$$

This conjecture, the so-called the Alexander–Orbach conjecture, is crucial because, if exact, the dynamic exponent μ can be related to static exponents such as ν , β through the relation

$$\mu = \frac{1}{2} [(3d - 4)\nu - \beta] . \quad (5.22)$$

Confirming the Alexander–Orbach conjecture has been a challenge over the past decade. If the Alexander–Orbach conjecture is valid, the relation (5.19) leads to $\tilde{d}_w = 91/32 = 2.8437\dots$ for 2D percolating networks. The Monte Carlo calculation of $\langle r^2(t) \rangle$ is an efficient way of estimating the exponent \tilde{d}_w , using the relation (5.15). The calculated values of \tilde{d}_w are somewhat larger than $91/32$, which corresponds to $\tilde{d}_s \lesssim 4/3$. Although calculated values of the spectral dimension \tilde{d}_s depend weakly on numerical methods, the Alexander–Orbach conjecture is considered to be incorrect and the true value of \tilde{d}_s is slightly smaller than $4/3$ for $d < 6$. Numerically obtained values of \tilde{d}_s are listed in Table 5.1.

The spectral dimension can be obtained exactly for deterministic fractals [5.6, 5.7]. In the case of the d -dimensional Sierpinski gasket, the spectral dimension is given by

$$\tilde{d}_s = \frac{2 \log(d+1)}{\log(d+3)} . \quad (5.23)$$

We see from this that the upper bound for a Sierpinski gasket is $\tilde{d}_s = 2$. A system with $\tilde{d}_s < 2$ is called compact fractal. The spectral dimension for the Mandelbrot–Given fractal depicted in Fig. 2.1 is also calculated analytically as

$$\tilde{d}_s = \frac{2 \log 8}{\log 22} = 1.345\dots . \quad (5.24)$$

² The term fracton, coined by Alexander and Orbach [5.5], denotes a localized vibrational mode peculiar to fractal structures, as discussed later.

This value is close to $\tilde{d}_s \approx 4/3$ for percolating networks, in addition to the fact that the fractal dimension $D_f = \log 8 / \log 3$ of the Mandelbrot–Given fractal is close to $D_f = 91/48$ for 2D percolating networks and that the Mandelbrot–Given fractal has a structure with nodes, links, and blobs as in the case of percolating networks. Derivations of (5.23) and (5.24) are given in Appendix B.

5.3 Spectral Density of States of Fractal Networks

The probability of finding a diffusing particle at the starting point at time t is, for compact diffusion ($\tilde{d}_s \leq 2$) [5.6], given by

$$P_0(t) \propto \frac{1}{V(t)} \propto \frac{1}{\langle r^2(t) \rangle^{D_f/2}}, \quad (5.25)$$

where $V(t)$ is the number of sites visited within a time t . With the help of (5.18), (5.25) is expressed as

$$P_0(t) \propto t^{-\tilde{d}_s/2}, \quad (5.26)$$

where the spectral dimension \tilde{d}_s is defined by (5.19).

We can evaluate the spectral density of states $D(\omega)$ for atomic vibrations of fractal networks by using the formula

$$D(\omega) = -\frac{2\omega}{\pi} \text{Im } \tilde{P}_0(-\omega^2 + i0^+), \quad (5.27)$$

where $\tilde{P}_0(\omega)$ is the Laplace transform of the return probability $P_0(t)$. The derivation of (5.27) is presented in Appendix C.1 [(C.22)]. From (5.26), the Laplace transform of $P_0(t)$ for fractal networks is expressed as

$$\tilde{P}_0(\omega) \propto \omega^{\tilde{d}_s/2-1} \int_0^\infty e^{-x} x^{-\tilde{d}_s/2} dx. \quad (5.28)$$

It should be noted that \tilde{d}_s must be smaller than 2 for convergence of the integral in (5.27). By letting $\omega \rightarrow -\omega^2 + i0^+$ in (5.28), we obtain

$$\text{Im } \tilde{P}_0(-\omega^2 + i0^+) \propto \omega^{\tilde{d}_s-2}. \quad (5.29)$$

Substituting (5.29) into (5.27), the frequency dependence of the spectral density of states is obtained from

$$D(\omega) \propto \omega^{\tilde{d}_s-1}. \quad (5.30)$$

By analogy with the Debye density of states ω^{d-1} , Alexander and Orbach [5.5] called the related vibrational excitations fractons, and \tilde{d}_s the fracton dimension. Rammal and Toulouse [5.6] called \tilde{d}_s the spectral dimension, because it characterizes the spectral density of states for the vibrational spectrum.

5.4 Scaling Argument for Spectral Density of States

In this section, we derive the spectral density of states and the dispersion relation of elastic fractal networks from a scaling argument. In order to explain the physical implications of the scaling argument, we start by showing a simple (perhaps the simplest) derivation of the Debye density of states of a homogeneous elastic system. The density of states at ω is defined as the number of modes per particle, which is expressed by

$$D(\omega) = \frac{1}{\Delta\omega L^d}, \quad (5.31)$$

where $\Delta\omega$ is the frequency interval between adjacent eigenfrequencies close to ω and L is the linear size of the system. Concentrating on the lowest frequency region, $\Delta\omega$ is the lowest eigenfrequency which depends on the size L . The relation between the frequency $\Delta\omega$ and L is obtained from the linear dispersion relationship $\omega = vk$, where v is the velocity of phonons, i.e.,

$$\Delta\omega = \frac{2\pi v}{\lambda} \propto \frac{1}{L}. \quad (5.32)$$

Substituting (5.32) into (5.31) yields

$$D(\Delta\omega) \propto \Delta\omega^{d-1}. \quad (5.33)$$

Since this relation holds for any length scale L due to the scale-invariance property of homogeneous systems, we can replace the frequency $\Delta\omega$ by an arbitrary ω . Therefore, we obtain the conventional Debye density of states as

$$D(\omega) \propto \omega^{d-1}. \quad (5.34)$$

It should be noted that this derivation is based on the scale invariance of the system.

Next, let us consider the density of vibrational states of a fractal structure of size L with fractal dimension D_f . The density of states per particle at the lowest frequency $\Delta\omega$ for this system is, as in the case of (5.31), written as

$$D(\Delta\omega) \propto \frac{1}{L^{D_f} \Delta\omega}. \quad (5.35)$$

Assuming that the dispersion relation for $\Delta\omega$ corresponding to (5.32) is

$$\Delta\omega \propto L^{-z}, \quad (5.36)$$

we can eliminate L from (5.35) to obtain

$$D(\Delta\omega) \propto \Delta\omega^{D_f/z-1}. \quad (5.37)$$

The exponent z of the dispersion relation (5.36) is evaluated from the exponent of anomalous diffusion (5.15) as follows. Considering the correspondence between

diffusion and atomic vibrations discussed in Appendix C.1 [(C.8) and (C.9)], we can replace $\langle r^2(t) \rangle$ and t in (5.15) by L^2 and $1/\Delta\omega^2$ for elastic fractal networks. Equation (5.15) can then be read as

$$L \propto \Delta\omega^{-2/\tilde{d}_w}. \quad (5.38)$$

Comparing the dispersion relation (5.36) with (5.38) leads to

$$z = \frac{\tilde{d}_w}{2} = \frac{D_f}{\tilde{d}_s}, \quad (5.39)$$

where (5.19) has been used.

Since the system has a scale-invariant fractal (self-similar) structure, $\Delta\omega$ can be replaced by an arbitrary frequency ω , as in the case of (5.34). Hence, from (5.37) and (5.39), the density of states for fractal networks is found to be

$$D(\omega) \propto \omega^{\tilde{d}_s-1}, \quad (5.40)$$

and the dispersion relation (5.38) becomes

$$\omega \propto L(\omega)^{-D_f/\tilde{d}_s}. \quad (5.41)$$

The spectral/fracton dimension \tilde{d}_s can be obtained from the value of the conductivity exponent μ or vice versa. The expression (5.40) for $D(\omega)$ is identical to (5.30), which is obtained by the Laplace transform of the master equation. In the case of percolating networks, the conductivity exponent μ is related to \tilde{d}_s through (5.16), which means that the conductivity σ_{dc} is also characterized by the spectral dimension \tilde{d}_s . In this sense, the spectral dimension \tilde{d}_s is an intrinsic exponent related to the dynamics of fractal systems.

5.5 Localization of Excitations on Fractal Networks

In this section, we show that excitations on fractal networks are spatially localized. In order to prove this statement, let us consider electrons on a d -dimensional percolating network of size L . The conductance $G(L)$ is defined as the current when a unit voltage is applied across the percolating network, as shown in Fig. 5.1. Since the conductance $G(L)$ is proportional to the area L^{d-1} and the reciprocal of the size L , we have the relation

$$G(L) = \sigma_{dc} L^{d-2}, \quad (5.42)$$

where σ_{dc} is the conductivity. Using (5.4) and (3.2), we obtain

$$G(L) \propto \xi^{-\mu/\nu} L^{d-2}. \quad (5.43)$$

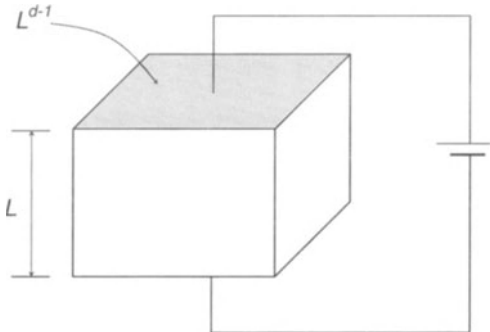


Fig. 5.1. The arrangement for defining the conductance $G(L)$ of a d -dimensional hypercubic system

Provided that the relation $L \ll \xi$ holds, the length scale characterizing this system becomes L alone and we can replace the correlation length by $\xi \rightarrow L$. This implies that

$$G(L) \propto L^\beta , \quad (5.44)$$

where the exponent β is given by

$$\beta = \frac{D_f}{\tilde{d}_s} (\tilde{d}_s - 2) . \quad (5.45)$$

Here we have used (3.34) and (5.20). Equation (5.44) with (5.45) indicates that $G(L)$ goes to zero for $L \rightarrow \infty$, because the exponent β is always negative due to $\tilde{d}_s \approx 4/3$ for percolating networks in any dimension. This means that the current does not flow and electrons are localized in infinite percolating networks. Note that the exponent β is equivalent to the value of the β -function for large conductances. This will be discussed in Sect. 9.3 [5.8]. At length scales greater than ξ ($L \gg \xi$), we can replace \tilde{d}_s and D_f by d , because the system is homogeneous. Thus, for example, for 3D percolating networks, β becomes positive, leading to the localization-delocalization transition (see discussion in Sect. 9.3). This transition, known as the quantum percolation transition, has been extensively studied. The above argument guarantees that the quantum percolation transition point p_q is always larger than the (classical) percolation threshold p_c .

We emphasize that the relation (5.44) with (5.45) holds for general fractal networks, although the derivation has been demonstrated only for percolating networks. This implies that electrons in compact fractals ($\tilde{d}_s < 2$) are localized, while they can be extended for fractals with $\tilde{d}_s > 2$. Furthermore, it should be noted that the above localization argument applies to other excitations on fractal networks, because of the generality of the argument. Vibrational excitations on fractal networks, i.e., fractons, for example, are localized if $\tilde{d}_s < 2$.

5.6 Phonons and Fractons in Percolating Networks

We showed in Sects. 5.4 and 5.5 that vibrational modes called fractons are localized in percolating networks. Their spectral density of states and the dispersion relation are given by (5.40) and (5.41), respectively. As shown in Sect. 5.5, the spectral dimension \tilde{d}_s and the fractal dimension D_f should be replaced by the Euclidean dimension d at length scales larger than the correlation length ξ . In this case, (5.40) and (5.41) give the density of states and the dispersion relation for conventional (extended) phonons, respectively. The relevant length scale for low-frequency vibrational excitations is the wavelength λ . Thus, vibrational modes with λ much larger than ξ are phonons. According to the argument in Sect. 5.5, phonons in percolating networks are extended (3D) or weakly localized. Physically, this is because scattering is determined by the square of the mass-density fluctuation averaged over regions of volume λ^d . Hence, even if the short-range disorder is strong, the effective strength of the disorder for phonons with $\lambda \gg \xi$ is very weak. If the wavelength λ approaches ξ , fractal structures become relevant. When the length scale relevant to vibrational modes becomes shorter than ξ by increasing the frequency, excitations behave as localized fractons. The relevant length scale of fractons is $L(\omega)$ in the dispersion relation (5.41). Vibrational excitations are therefore expected to cross over from phonons to fractons at increasing frequencies. This crossover can be regarded as the dimensionality crossover from d to \tilde{d}_s and D_f .

From (5.41), we can derive the crossover frequency ω_c for vibrational excitations by replacing $L(\omega) \rightarrow \xi$ to yield

$$\omega_c \propto (p - p_c)^{vD_f/\tilde{d}_s}. \quad (5.46)$$

The crossover frequency ω_c is also related to the phonon dispersion relation $\omega = v k$, where v and k are the velocity and wavenumber of phonons. The relation $\omega_c \approx v(p)/\xi$ and (5.46) give the velocity of phonons as

$$v(p) \propto (p - p_c)^{vD_f/\tilde{d}_s - v} \propto (p - p_c)^{(\mu - \beta)/2}. \quad (5.47)$$

Because $\mu - \beta$ is always positive, we have $v(p) \rightarrow 0$ when $p \rightarrow p_c$. The results for the density of states for vibrational excitations are summarized by

$$D(\omega) \propto \begin{cases} \frac{\omega^{d-1}}{v(p)^d}, & \text{for } \omega \ll \omega_c, \\ \omega^{\tilde{d}_s-1}, & \text{for } \omega \gg \omega_c. \end{cases} \quad (5.48)$$

The dispersion relations become

$$\omega \propto \begin{cases} v(p)k, & \text{for } \omega \ll \omega_c, \\ k^{D_f/\tilde{d}_s}, & \text{for } \omega \gg \omega_c, \end{cases} \quad (5.49)$$

where k for $\omega \gg \omega_c$ does not mean the wavenumber due to the lack of translational symmetry of the system, but rather describes the inverse of the localization length $\Lambda(\omega)$. It should be noted that fractons reflect two features of fractal structures, namely, the fractality and the lack of translational symmetry.

6. Atomic Vibrations of Percolating Networks

As discussed in detail in Chap. 5, vibrational excitations in fractal networks behave in a different manner from those in conventional disordered systems. These excitations called fractons are characterized by the spectral dimension \tilde{d}_s . However, all the results on fractons presented in Chap. 5 are deduced from the scaling assumption (5.8). In order to confirm the results derived from the scaling arguments and clarify the nature of fractons, investigation by computer simulations is crucial. This has become possible recently due to a sharp increase in available computer power together with the development of new algorithms suitable for large-scale computations. These have been a great success in quantitatively describing the dynamics of complex systems.

In this chapter, we first present the results of large-scale simulations for the vibrational density of states (DOS) of percolating elastic networks with scalar displacements. These calculations are a rich source of information about properties of fractons including the accurate value of the spectral dimension \tilde{d}_s . The behaviour of the DOS at the crossover region from phonons to localized fractons will be treated in detail. The localized character of fractons is also discussed. In addition, we discuss vibrational excitations of percolating elastic networks taking into account the vector nature of interactions and displacements. A scaling theory predicts the existence of another type of fracton in such systems. The relations between several exponents describing properties of networks with vector displacements are obtained by scaling arguments.

6.1 Spectral Density of States and Spectral Dimension

We showed in Sect. 5.3 that the spectral density of states for vibrational systems can be derived by solving the diffusion problem, or vice versa. These claims are demonstrated in detail in Appendix C, showing that the master equation forms a basis for deriving dynamical properties of fractal networks, such as atomic vibrations, spin waves, or superconducting properties. The correspondence relationship between diffusion and atomic vibrations provides several important predictions concerning fractons, as shown in Chap. 5. In this section, we deal with numerical results for the spectral density of states for elastic percolating networks with scalar displacements.

We consider a bond-percolating (BP) network on a square or (hyper)cubic lattice with periodic boundary conditions, consisting of N particles with unit mass and linear springs connecting nearest-neighbor atoms. The reason why we treat a BP

network is that the fractal nature of BP networks is revealed even at very short-range scales, as demonstrated in Fig. 3.4. The equation of motion for atomic vibrations with scalar displacements is expressed by

$$m\ddot{u}_i(t) = \sum_j K_{ij}u_j(t), \quad (6.1)$$

where u_i is the scalar displacement of the atom with unit mass ($m = 1$). It is assumed that the displacement u_i has only one component. The force constant is chosen as $K_{ij} = 1$ ($i \neq j$) if both nearest-neighbor sites i and j are occupied, and $K_{ij} = 0$ otherwise. The diagonal elements K_{ii} are given by $K_{ii} = -\sum_{i \neq j} K_{ij}$, derived from the condition that forces balance at the site i . Note that the force constants K_{ij} have a different sign from the definition of the dynamical matrix elements Φ_i^j used in the textbook on lattice dynamics [6.1].

The spectral densities of states (DOS) for 2D, 3D, and 4D BP networks at the percolation threshold $p = p_c$ are given in Figs. 6.1a and b, which have been obtained numerically by means of a powerful method called the forced oscillator method [6.3]. The correlation length ξ diverges at $p = p_c$ and the network has a fractal structure at any length scale. Therefore, we can expect DOSs of fractons in the wide frequency range $\omega_L \ll \omega \ll \omega_D$, where ω_D is the Debye cutoff frequency and ω_L is the lower cutoff determined by the system size. The frequency ω_L is quite small ($\omega \approx 10^{-5}$ for the 2D result) for the results in Fig. 6.1 because of the large sizes of the systems treated. The DOS and the integrated DOS per atom are shown by

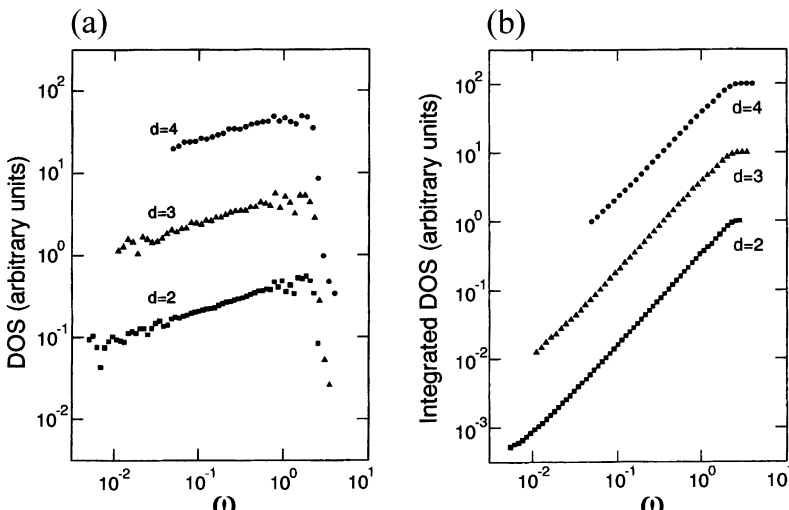


Fig. 6.1. (a) Spectral densities of states per atom for 2D, 3D and 4D BP networks at $p = p_c$. (b) Integrated densities of states for the same. The angular frequency ω is obtained with mass units $m = 1$ and force constant $K = 1$. The networks are formed on 1100×1100 (2D), $100 \times 100 \times 100$ (3D), and $30 \times 30 \times 30$ (4D) lattices with periodic boundary conditions, respectively [6.2]

the filled squares for a 2D BP network at $p_c = 0.5$ formed on a $1\ 100 \times 1\ 100$ square lattice ($N = 657\ 426$) with periodic boundary conditions. The spectral dimension \tilde{d}_s is obtained as $\tilde{d}_s = 1.33 \pm 0.01$ from Fig. 6.1a, whereas data in Fig. 6.1b give the more precise value $\tilde{d}_s = 1.325 \pm 0.002$. It should be emphasized that the approximate $\omega^{1/3}$ law holds even in the low frequency region.

The DOS and the integrated DOS for 3D BP networks are given in Figs. 6.1a and b by the filled triangles (middle). These data show results averaged over three samples at the percolation threshold $p_c (= 0.249)$. The networks, formed on $100 \times 100 \times 100$ cubic lattices, have 155 385, 114 303, and 143 026 atoms. The spectral dimension \tilde{d}_s is obtained as $\tilde{d}_s = 1.31 \pm 0.02$ from Fig. 6.1a and $\tilde{d}_s = 1.317 \pm 0.003$ from Fig. 6.1b.

The DOS and the integrated DOS of 4D BP networks at $p_c = 0.160$, formed on $30 \times 30 \times 30 \times 30$ quartic lattices, are shown in Figs. 6.1a and b by filled circles, obtained by averaging over 15 samples. The network sizes are $N = 8\ 410$ – $64\ 648$. The DOS in the frequency region $0.1 \lesssim \omega \lesssim 1.0$ clearly shows the power-law dependence, as found in the 2D and 3D cases. The spectral dimension \tilde{d}_s is estimated as $\tilde{d}_s = 1.31 \pm 0.03$ from the least-squares fitting using the data of Fig. 6.1a.

The DOS of a 2D site-percolating (SP) cluster with $p = 0.67$ is shown in Fig. 6.2. This percolating network is formed on a 700×700 square lattice with network size $N = 317\ 672$. The percolation correlation length ξ of this system is finite. As shown in Sect. 5.6, we expect a crossover from phonons to fractons in the DOS. The crossover frequency ω_c corresponds to the mode of wavelength λ equal to the correlation length ξ . Hence, the DOS in the frequency regime lower than ω_c should be given by the conventional Debye law $D(\omega) \propto \omega^{d-1}$, while $D(\omega) \propto \omega^{\tilde{d}_s-1}$ for $\omega \gg \omega_c$, where d is the Euclidean dimension. The simulated result is consistent with this view, because the frequency dependence of the DOS for lower frequencies ($\omega \ll 0.05$) clearly obeys the law $D(\omega) \propto \omega$ and the DOS is closely proportional to

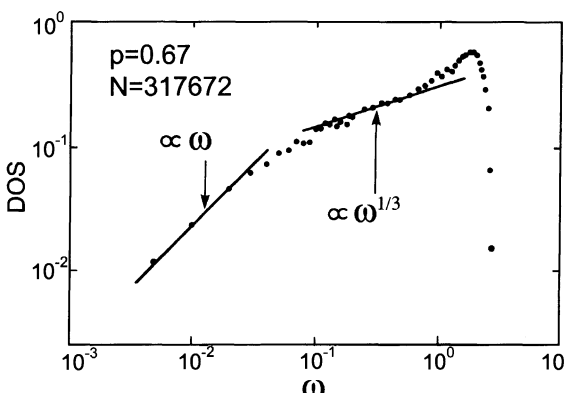


Fig. 6.2. The DOS per atom for a 2D network at $p = 0.67$ formed on a 700×700 square lattice. The network size is 317 672. Solid circles indicate numerical results. The straight line is only meant as a guide to the eye [6.4].

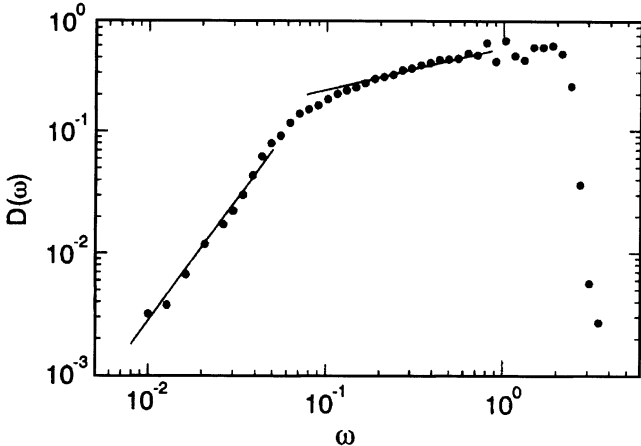


Fig. 6.3. The DOS per atom for a 3D BP network at $p = 0.31$ ($p_c = 0.249$) formed on a $120 \times 120 \times 120$ cubic lattice [6.5]

$\omega^{1/3}$ in the frequency region $0.05 \ll \omega \ll 1$. It is known that excitations in disordered systems with Euclidean dimension $d \leq 2$ should be localized (See Sect. 5.5). In this sense, even phonons excited below $\omega_c \approx 0.05$ are localized, but weakly, whereas fractons are strongly localized. [The term ‘strongly’ means that the value of the exponent β defined by (5.45) for fractons in percolating networks is smaller than that for phonons.]

The region in the vicinity of ω_c in Fig. 6.2 is the crossover region between phonons and fractons. It should be emphasized that the DOS is smoothly connected in this region, without exhibiting any significant steepness or hump. It is remarkable that the DOS does not follow the $\omega^{1/3}$ dependence above $\omega \approx 1$. This will be interpreted in Sect. 6.3 in connection with the discussion on missing modes.

The smooth crossover is also demonstrated in the case of 3D percolating networks. The DOS of a BP network at $p = 0.31$ ($p_c = 0.249$) formed on a $120 \times 120 \times 120$ simple cubic lattice is shown in Fig. 6.3. The network size is $N = 1\,302\,424$ and a periodic boundary condition is used for calculations. The crossover frequency ω_c of this system is estimated from Fig. 6.3 as $\omega_c \approx 0.07$. The DOS in the low frequency regime ($\omega \ll \omega_c$) obeys the Debye law $D(\omega) \propto \omega^2$, while the DOS follows $D(\omega) \propto \omega^{d_s-1}$ ($\tilde{d}_s \approx 4/3$) for $\omega > \omega_c$. A peak at $\omega = 1$ in Fig. 6.3 is attributed to vibrational modes of a single site connected by a single bond to a relatively rigid part of the network (a blob in the sense of the nodes-links-blobs model discussed in Sect. 3.4). It is clear that the DOS exhibits no steepness or hump in the crossover region in the vicinity of ω_c .

6.2 Missing Modes at Low Frequencies

The simulation results presented in Sect. 6.1 confirm the theoretical predictions obtained by scaling arguments in Sects. 5.4–5.6. It is found that the DOS of a percolating network above threshold ($p > p_c$) is characterized by two regimes. The fracton DOS is given by

$$D_{\text{fr}}(\omega, p) = A\omega^{\tilde{d}_s-1}, \quad \text{for } \omega \gg \omega_c, \quad (6.2)$$

and the phonon DOS takes the form

$$D_{\text{ph}}(\omega, p) = B\omega^{d-1}, \quad \text{for } \omega \ll \omega_c, \quad (6.3)$$

where A and B are coefficients. It should be noted that the whole DOS per particle is normalized as

$$\int_0^\infty D(\omega)d\omega = 1. \quad (6.4)$$

Since d is always larger than \tilde{d}_s , $D_{\text{ph}}(\omega)$ is smaller than $D_{\text{fr}}(\omega)$ at low frequencies when the latter is extrapolated to phonon frequencies (see Fig. 6.4). This implies that some modes in the low frequency regime are missing as p increases from the threshold value p_c . Due to the normalization condition (6.4), their spectral weight must be recovered somewhere. If the coefficient A in (6.2) is independent of p , the most probable region to recover these missing modes is near ω_c , which leads to an accumulation of modes in the vicinity of ω_c [6.6, 6.7]. In the early stages of studies on the phonon–fracton crossover, a hump was expected in the DOS at $\omega \approx \omega_c$ for percolating networks above p_c . The point is that such a hump is never observed at the phonon–fracton crossover in simulations of the DOS, as shown in Figs. 6.2 and 6.3.

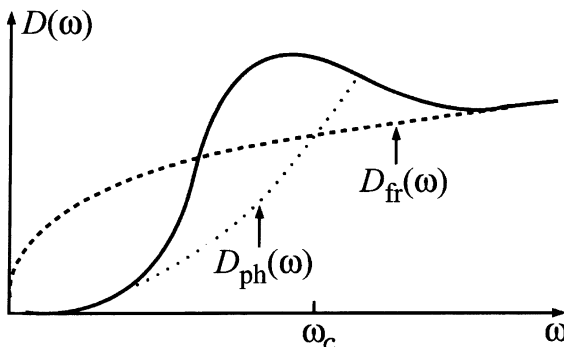


Fig. 6.4. Crossover of the DOS (solid curve). The dotted (dashed) curves represent the continuation of the phonon (fracton) asymptotic behaviour into the crossover regime [6.6]

6.3 The Hump at High Frequencies

In order to explain the absence of a hump in the observed crossover region, we write the scaling form for the DOS of a percolating network for $p > p_c$ as

$$D(\omega, p) = A(p)\omega^{\tilde{d}_s - 1} F(\omega/\omega_c). \quad (6.5)$$

For an infinite percolating network, the phonon–fracton crossover frequency is given by (5.46), i.e.,

$$\omega_c = \Omega(p - p_c)^{vD_f/\tilde{d}_s}. \quad (6.6)$$

The scaling function $F(x)$ should take the form

$$F(x) = 1, \quad \text{for } x \gg 1, \quad (6.7)$$

and

$$F(x) = x^{d - \tilde{d}_s}, \quad \text{for } x \ll 1. \quad (6.8)$$

Equation (6.6) provides a prediction for the p -dependence of $D(\omega, p)$ in the phonon regime of the form

$$D(\omega) \propto A(p)(p - p_c)^{vD_f(\tilde{d}_s - d)/\tilde{d}_s} \omega^{d-1}. \quad (6.9)$$

Figure 6.5 shows the DOS divided by $\omega^{1/3}$ as a function of ω , in which a horizontal line corresponds to the fracton regime. Data for $p_c = 0.593$ are plotted with filled circles, where the network was prepared on a 700×700 lattice with $N = 116\,991$. The rescaled data for the DOS for a network with $p = 0.67$ ($N = 317\,672$) are plotted

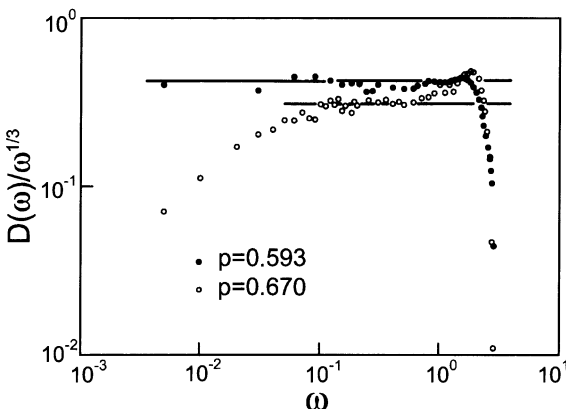


Fig. 6.5. Densities of states divided by $\omega^{1/3}$ as a function of the frequency ω . Solid circles are the result for a percolating network at $p = p_c$, and open circles for $p = 0.67$. Horizontal lines are just guides to the eye [6.8]

with open circles. We can clearly discern two regimes in the data for $p = 0.67$, with a crossover frequency $\omega_c \approx 0.1$. It is found that the magnitude of the DOS in the fracton regime is different in the two simulations. This invalidates the assumption that the coefficient A in (6.2) is independent of p . Furthermore, we should note that the two curves of Fig. 6.5 could not possibly be made to scale towards the upper cutoff of the fracton range. This is the region where modes missing from the low frequency regime have accumulated, exhibiting the violation of the scaling hypothesis in (6.5).

To understand the last observation, it is helpful to consider the simple model illustrated in Fig. 6.6. From the Sierpinski gasket of Fig. 6.6a, we can construct infinite homogeneous systems in different ways. Vibrational modes of the simple gasket in Fig. 6.6a have been investigated in considerable detail in [6.9]. The spectral density peaks at $\omega = \sqrt{5}$, and molecular, or strongly localized modes have the highest density near the upper cutoff at $\omega = \sqrt{6}$. These modes are only slightly modified by the higher coordination of a few sites ($z = 6$) in Fig. 6.6b. The higher z simply produces a few modes at frequencies above the Sierpinski gasket band, in the region $\sqrt{6} < \omega < 3$, where $\omega = 3$ is the upper cutoff of the 2D triangular lattice. An alternative way to construct a large-scale homogeneous system is illustrated in Fig. 6.6c. That model corresponds more closely to the intuitive picture of percolating networks that reach their correlation length by growing into each other. In that case, the whole region $\sqrt{6} < \omega < 3$ becomes rather densely populated with modes, at the expense of the DOS in the fracton regime. The corresponding missing spectral weight is rather uniformly distributed over the low frequency region.

The above considerations can now be extended to percolation with a correlation length ξ [6.8]. The discussion is facilitated by adopting the nodes-links-blobs picture, as illustrated in Fig. 3.7a. The typical separation of the nodes forming the macroscopically homogeneous network equals the correlation length ξ . Using

$$D_{\text{ph}}(\omega) = \frac{A(p)}{\omega_c^{2/3}} \omega, \quad (6.10)$$

and

$$D_{\text{fr}}(\omega) = A(p)\omega^{1/3}, \quad (6.11)$$

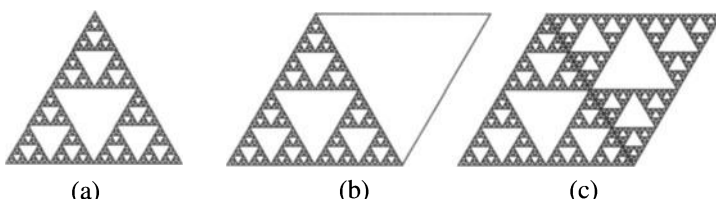


Fig. 6.6. Two different tilings of the Sierpinski gasket. (a) is the original gasket. (b) and (c) represent unit cells of the two types of Sierpinski lattice

we can calculate the number M_{ph} of missing modes associated with the phonon regime as

$$\begin{aligned} M_{\text{ph}} &\approx \int_0^{\omega_c} (D_{\text{fr}} - D_{\text{ph}}) d\omega \\ &= \frac{1}{4} A(p) \omega_c^{\tilde{d}_s} \\ &= \frac{1}{4} A(p) \Omega^{\tilde{d}_s} (p - p_c)^{\nu D_f}. \end{aligned} \quad (6.12)$$

Using $A(p) = A(p_c) \simeq 0.4$ and $\Omega \simeq 13$ from Fig. 6.5, we can estimate $M_{\text{ph}} \simeq 3(p - p_c)^{\nu D_f}$. The number of occupied sites on the infinite network in the correlation box, ξ^d , is $\xi^d P_\infty$, where $P_\infty = P_0(p - p_c)^\beta$. Hence the actual number of missing modes within the correlation box is

$$M \approx \xi^2 P_\infty M_{\text{ph}} \approx 3 \Xi_0^2 P_0, \quad (6.13)$$

where Ξ_0 is defined by $\xi = \Xi_0 |p - p_c|^{-\nu}$, and the hyperscaling relation $-dv + \beta + \nu D_f = 0$ [(3.34)] is used. Using $\Xi_0 = 0.95$ and $P_0 \simeq 1.53$ for 2D percolating networks, the number of missing modes is found to be of the order of unity. There is thus one missing mode per area ξ^2 . This result suggests that missing modes associated with the phonon regime shift to high-frequency vibrations of modes which have higher coordination.

Numerically more important is the number of missing modes M_{fr} produced by the depression of the fracton density from $A(p_c)$ to $A(p)$. Ignoring the hump near the higher cutoff frequency ω_D , this number is

$$M_{\text{fr}} = \int_0^{\omega_D} [D_{\text{fr}}(\omega, p_c) - D_{\text{fr}}(\omega, p)] d\omega = 1 - \frac{A(p)}{A(p_c)}. \quad (6.14)$$

For the second equality, use was made of (6.5) and the fact that the integral of $D_{\text{fr}}(\omega, p_c)$ over the full frequency range is normalized to unity. The simulated values of M_{fr} for several values of p are shown in Fig. 6.7, demonstrating a critical behavior, $M_{\text{fr}} = M_0(p - p_c)^m$. The solid line gives $m = 4/3$ and $M_0 \approx 4.1$.

This behavior can be explained as follows. A number of sites in percolating networks above p_c have higher coordination than in a network at p_c . The number of these sites is much larger than the small number of nodes that form the homogeneous system. Based on the naive picture of Fig. 6.6c, we expect the number N_h of these higher coordination sites to be proportional to the number of perimeter sites of a correlation box. In the case of the percolation network, the perimeter of a correlation box is a fractal of dimension $D_f - 1$. The number N_h is thus proportional to $\xi^{D_f - 1}$. Since the total number of occupied sites within the correlation box is ξ^{D_f} , the relative number of high-frequency modes attributed to higher coordination sites is then

$$M_{\text{fr}} \propto \frac{\xi^{D_f - 1}}{\xi^{D_f}} = \frac{1}{\xi}. \quad (6.15)$$

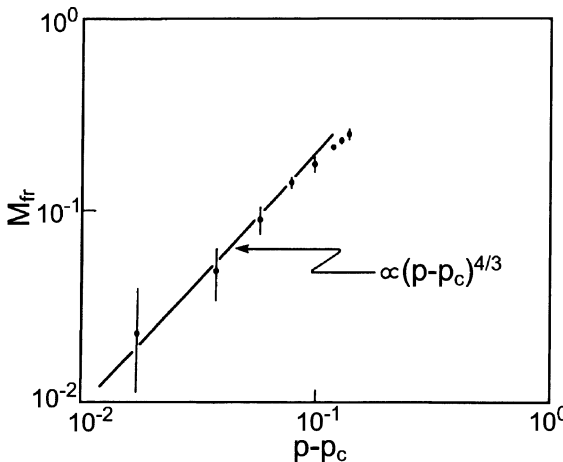


Fig. 6.7. Number of missing modes produced by depression of the fracton DOS as p increases from p_c [6.8]

For 2D percolating networks, taking into account the four sides of the correlation box, this ratio becomes

$$M_{\text{fr}} \approx \frac{4}{\xi} \approx 4.2(p - p_c)^{4/3}, \quad (6.16)$$

Both the exponent and the amplitude agree well with the simulated values (see Fig. 6.7). This supports the validity of this interpretation. Although there is, strictly speaking, no well defined perimeter of a correlation box, the concept of the perimeter appears to remain well defined from an average point of view.

6.4 Localized Nature of Fracton Excitations

We showed in Sect. 5.5 that the scaling theory predicts localization of fracton excitations on a percolating network. The key parameter in the scaling theory is the exponent β given by (5.45), which is always negative because $\tilde{d}_s \approx 4/3$ for percolating networks, in any Euclidean dimension d . This implies that fractons are spatially localized. In this context, the ensemble-averaged envelope function of fracton excitations should in principle be expressed as

$$\langle \phi_{\text{fr}} \rangle \propto \exp \left[- \left(\frac{r}{\Lambda(\omega)} \right)^{d_\phi} \right], \quad (6.17)$$

where $\Lambda(\omega)$ is the frequency-dependent localization length and r a radial distance from the center of the fracton. The exponent d_ϕ denotes the strength of localization.

Bunde and Roman [6.10] have given an analytic explanation for the asymptotic spatial behavior of fractons. For scalar vibrations, the envelope function of the

fracton, $|\phi_{\text{fr}}(r, \omega)|$, is related to the probability density $P(r, t)$ for finding a random walker after time t at a site separated by a distance r from its starting point. From (C.30) in Appendix C, this relation is

$$P(r, t) = \int_0^\infty D(\omega) |\phi_{\text{fr}}(r, \omega)| \exp(-\omega^2 t) d\omega , \quad (6.18)$$

where $D(\omega)$ is the DOS per atom. For a large class of networks, including percolating networks at p_c , $P(r, t)$ decays, upon averaging over typical configurations, according to [6.11]

$$\log P(r, t) \propto -[r/R(t)]^u , \quad u = \frac{\tilde{d}_w}{\tilde{d}_w - 1} , \quad (6.19)$$

where \tilde{d}_w is the diffusion exponent defined in (5.16). Using the asymptotic form of (6.19), we obtain $d_\phi = 1$ by taking the inverse Laplace transform of (6.19) and using the relation $\Lambda(\omega)^{-1} \propto \omega^{2/\tilde{d}_w}$ from (5.19) and (5.41).

We warn the reader that the ensemble average of matrix elements may be very different in general from the matrix element using ensemble averages for the fracton functions. For example, the Raman scattering intensity is proportional to the square

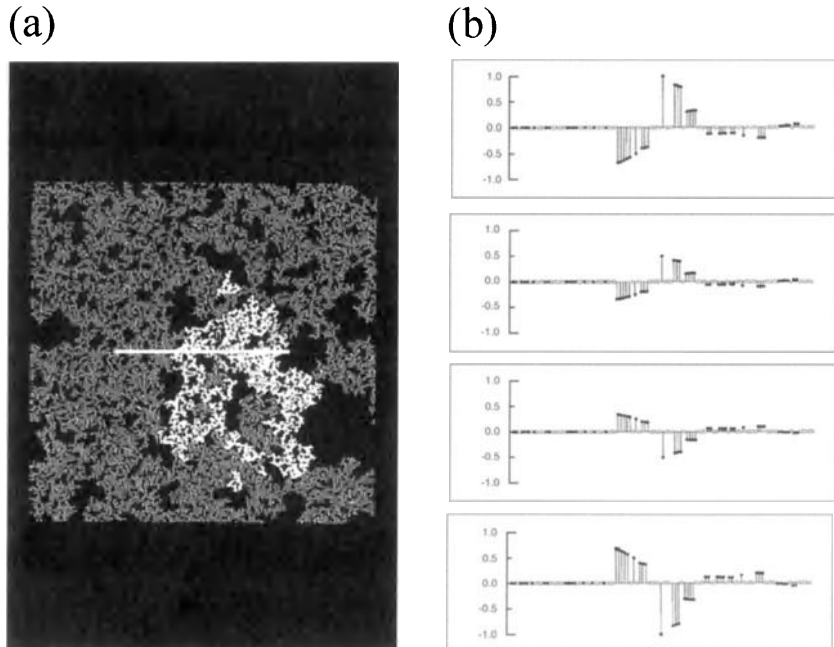


Fig. 6.8. (a) Typical fracton mode ($\omega = 0.04997$) on a 2D BP network, which is obtained by applying the forced oscillator method [6.3]. Bright region represents the large amplitude portion of the mode. (b) Cross-sections of the fracton mode shown in (a) along the *white line*. The four figures are snapshots at four different times [6.12, 6.13]

of the elastic strain induced by fracton excitations. For this case, the ensemble average of the matrix element for individual fractons should be taken into account.

A typical mode pattern of a fracton on a 2D percolating network is shown in Fig. 6.8a, where the eigenmode belongs to the angular frequency $\omega = 0.04997$. The percolating network at $p_c = 0.593$ is formed on a 700×700 square lattice with $N = 169\,576$ occupied sites. To bring out the details more clearly, Fig. 6.8b shows cross-sections of this fracton mode along the line drawn in Fig. 6.8a. Filled and open circles represent occupied and vacant sites in the percolating network, respectively. We see that the fracton core (the largest amplitude) possesses very clear boundaries for the edges of the excitation, with an almost step-like character and a long tail in the direction of the weak segments. This contrasts with the case of homogeneously extended modes (phonons) in which the change in their amplitudes is smoothly correlated over a long distance. It should be noted that displacements of atoms in dead ends (weakly connected portions in the percolating network) move in phase, and fall off sharply at their edges. In addition, the tail extends over a very large distance with many phase changes. This is a natural consequence of the orthogonality condition for the eigenmodes, since vibrational modes belonging to eigenfrequencies $\omega^2 \neq 0$ must be orthogonal to the mode with uniform displacement of $\omega^2 = 0$ (see Fig. 6.9).

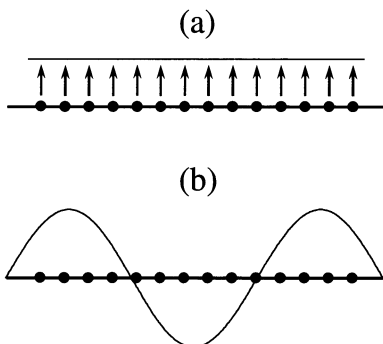


Fig. 6.9. Schematic illustrations of vibrational modes belonging to (a) $\omega = 0$ and (b) $\omega \neq 0$. These modes are mutually orthogonal

6.5 Networks with Vector Elasticity: Scaling Arguments

In actual vibrational systems, the vector nature of atomic displacements is crucial. Percolating networks with vectorial elastic forces have different critical exponents from those with scalar forces. It is more difficult to map the diffusion problem onto the vibrational problem with vector elasticity because the vector nature of the displacements represents a significant additional complication. We describe this aspect in detail in terms of scaling arguments.

The rotationally-invariant Hamiltonian taking account of vector displacements is given by the valence force field (VFF) description. The VFF was originally

introduced to describe molecular vibrations and later adapted to crystals [6.14], providing the most useful phenomenological description of short-range valence forces. The VFF Hamiltonian is described in terms of internal variables as

$$H = \frac{1}{2} \sum_i \dot{\mathbf{u}}_i^2 + \frac{1}{2} \alpha \sum_{ij} K_{ij} [(\mathbf{u}_i - \mathbf{u}_j) \cdot \mathbf{r}_{ij}]^2 + \frac{1}{2} \beta \sum_{ijk} K_{ij} K_{ik} (\Delta\theta_{ijk})^2. \quad (6.20)$$

Here \mathbf{u}_i is the vector displacement of the i th atom with unit mass ($m = 1$), \mathbf{r}_{ij} the unit vector connecting nearest-neighbor sites, and $\Delta\theta_{ijk}$ the small change in angle between bonds (ij) and (ik) due to the displacements of atoms. It should be emphasized that, for square or cubic lattices, both the equilibrium angles $\theta_{ijk} = \pi/2$ and π should be involved in this Hamiltonian. Thus, the rigidity threshold of this system is identical to the percolating threshold p_c . From a model taking into account only $\theta_{ijk} = \pi/2$, the angular force along linear links becomes irrelevant, so that the rigidity threshold becomes larger than the percolation threshold. The parameter K_{ij} takes the value unity if both nearest-neighbor sites i and j are occupied by atoms, and $K_{ij} = 0$ otherwise. The symbols α and β are the bond-stretching and bond-bending force constants, respectively.

There exists an additional characteristic length l_c in percolating networks with vector elasticity, besides the correlation length ξ . This length l_c depends only on the force constants α and β in (6.23), while ξ depends on p . The length l_c determines the crossover from the scale region in which bond-stretching motions are energetically favorable to the region where bond bending becomes dominant. We can connect the characteristic lengths ξ and l_c with two characteristic frequencies, ω_ξ and ω_{l_c} , respectively.

On the basis of the nodes-links-blobs model described in Sect. 3.4, Kantor and Webman [6.15] showed that the effective spring constant K between blobs is expressed by

$$K^{-1} \propto \left(\frac{\alpha}{L_1} \right)^{-1} + \left(\frac{\beta}{L_1 \xi^2} \right)^{-1}, \quad (6.21)$$

where blobs are assumed to be perfectly rigid and L_1 denotes the number of links. From (3.52), the mean number of links varies with p as

$$L_1 \propto (p - p_c)^{-1} \propto \xi^{1/\nu}. \quad (6.22)$$

If $(\alpha/L_1) \ll (\beta/L_1 \xi^2)$, the first term (stretching motions) of the effective spring constant (6.21) dominates. We then have

$$K \propto \frac{\alpha}{L_1}. \quad (6.23)$$

The condition for (6.23) to hold can be written as

$$\xi \ll l_c, \quad (6.24)$$

where

$$l_c = \sqrt{\frac{\beta}{\alpha}}. \quad (6.25)$$

This implies that the elastic energy of the system is primarily associated with the stretching force constant. For the case of $l_c \ll \xi$, the bond-bending spring constant becomes dominant, and the effective force constant is

$$K \propto \frac{\beta}{L_1 \xi^2}. \quad (6.26)$$

Let us derive the formula for the DOS of stretching fractons [6.15–6.17], for a system of size $L \ll \xi$. The DOS at the lowest finite frequency $\Delta\omega$ of this system takes the form

$$D(\Delta\omega) = \frac{1}{L^{D_f} \Delta\omega}, \quad (6.27)$$

where the level spacing $\Delta\omega$ is given by

$$\Delta\omega \propto \left[\frac{K(L)}{M(L)} \right]^{1/2}. \quad (6.28)$$

Quantities $M(L)$ and $K(L)$ are the mass and the effective spring constant of the system of size L . The effective spring constant is obtained for $L \ll l_c$ from (6.22) with $\xi = L$ and (6.23):

$$K(L) \propto \frac{\alpha}{L_1} \propto L^{-1/\nu}. \quad (6.29)$$

Using the relation $M(L) \propto L^{D_f}$, the lowest frequency $\Delta\omega$ is

$$\Delta\omega \propto L^{-(D_f+1/\nu)/2}. \quad (6.30)$$

Using this dispersion relation and replacing $\Delta\omega$ by an arbitrary frequency ω as in Sect. 5.4, the DOS for stretching fractons becomes

$$D(\omega) \propto \omega^{2\nu D_f / (\nu D_f + 1) - 1}. \quad (6.31)$$

Note that the exponent is determined only by the static exponents D_f and ν . This is due to the assumption that blobs are perfectly rigid. Since the conductivity σ_{ij} between sites i and j corresponds to the elastic force constant K_{ij} , as seen from the mapping relation between the resistive and the elastic networks [6.18], rigid blobs behave as superconductors in the conducting nodes-links-blobs model.

The nodes-links-blobs model relates the conductivity exponent μ introduced in (5.4) to static exponents. The conductance $G(L)$ for this model is given by

$$G(L) \propto \frac{1}{L_1}, \quad (6.32)$$

where blobs are assumed to be superconducting. Using (6.22) with $\xi = L$ and the relation (5.42) between the conductivity σ_{dc} and $G(L)$, $G(L) \propto \sigma_{dc} L^{d-2}$, the conductivity can be expressed by

$$\sigma_{dc} \propto L^{2-d-1/\nu}. \quad (6.33)$$

The finite-size scaling discussed in Sect. 3.3 gives the p -dependence of σ_{dc} in infinite systems as

$$\sigma_{dc} \propto (p - p_c)^{\nu(d-2)+1}, \quad (6.34)$$

which implies that the conductivity exponent μ can be expressed by

$$\mu = \nu(d-2) + 1. \quad (6.35)$$

The above exponent μ constitutes a lower bound for the conductivity exponent of actual percolating networks. This is because blobs are assumed to be superconductors in this model, and the actual conductivity σ_{dc} of a percolating network close to p_c is necessarily smaller than that predicted by (6.35).

Using the relation $D_f = d - \beta/\nu$ [(3.34)], the DOS for stretching fractons (6.31) becomes

$$D(\omega) \propto \omega^{\tilde{d}_{st}-1}, \quad (6.36)$$

where

$$\tilde{d}_{st} = \frac{2\nu D_f}{2\nu + \mu - \beta}. \quad (6.37)$$

Note that the exponent \tilde{d}_{st} takes the same form as \tilde{d}_s given in (5.20). Thus, the nodes-links-blobs model for vector elasticity predicts that stretching fractons belong to the same universality class as scalar fractons. We should also note that stretching elasticity is, in general, different from scalar elasticity because the stretching force constant becomes relevant only to motions along the bond connection, whereas scalar displacements respond to any deformation. Nevertheless, under the condition $L \ll l_c$, they both belong to the same universality class.

Consider the opposite case, $l_c \ll L \ll \xi$. The effective spring constant K is given by (6.26), for which bending motions become relevant. The relation corresponding to (6.29) is found to be

$$K(L) \propto L^{-2-1/\nu}. \quad (6.38)$$

Equation (6.28) then implies

$$\Delta\omega \propto L^{-[D_f+(1/\nu)+2]/2}. \quad (6.39)$$

This dispersion relation gives the DOS for bending fractons,

$$D(\omega) \propto \omega^{2vD_f/(vD_f+2v+1)-1}. \quad (6.40)$$

The expression for the DOS contains only static exponents, as in the case of (6.31), because we treat blobs as rigid bodies. Using the relation (6.35) for the nodes-links-blobs model, the above DOS can be written as

$$D(\omega) \propto \omega^{\tilde{d}_b-1}, \quad (6.41)$$

where

$$\tilde{d}_b = \frac{2vD_f}{4v + \mu - \beta}. \quad (6.42)$$

The spectral dimension \tilde{d}_b for bending fractons takes a smaller value than that for stretching fractons given by (6.37), because of $v > 0$. This implies that bending fractons belong to a different universality class than stretching fractons.

The spectral dimension \tilde{d}_b can also be expressed by the elasticity exponent f for the Young's modulus Y . The exponent f is defined by

$$Y \propto (p - p_c)^f. \quad (6.43)$$

The critical exponent f defined above can be related to static exponents within the nodes-links-blobs model as follows. Since the relation $K \propto YL^{d-2}$ holds (this is analogous to the relation between the conductance and the conductivity), and with the help of (6.38), we obtain the relation for the case $l_c \ll L \ll \xi$:

$$Y \propto L^{-d-1/v}. \quad (6.44)$$

Comparing (6.44) with (6.43) leads to

$$f = vd + 1. \quad (6.45)$$

We should note that this relation also gives a lower bound for the elasticity exponent f . From the relations (6.35) and (6.45), we have the relation

$$f = \mu + 2v. \quad (6.46)$$

This relation leads to another expression for \tilde{d}_b given by (6.42) as

$$\tilde{d}_b = \frac{2vD_f}{2v + f - \beta}. \quad (6.47)$$

This is the same as \tilde{d}_{st} in (6.37) if we replace f in (6.47) by μ .

Finally, we should mention the frequency regions of stretching fractons with DOS given by (6.36) and bending fractons with DOS given by (6.41). There exists a characteristic frequency ω_{l_c} corresponding to the mechanical length l_c , as well as ω_ξ corresponding to the correlation length ξ . The frequency ω_ξ is nothing but the crossover frequency ω_c given by (5.46). From the dispersion relation (6.39) with $L = l_c$, the frequency ω_{l_c} is given by

$$\omega_{l_c} \propto \left(\frac{\beta}{\alpha} \right)^{-[D_f + (1/\nu) + 2]/4}, \quad (6.48)$$

where we have used (6.25). The condition $L \ll l_c$, for example, can be read as $\omega \gg \omega_{l_c}$. Therefore, stretching fractons [(6.36)] appear in the frequency regime $\omega \gg \max(\omega_{l_c}, \omega_\xi)$, and bending fractons [(6.41)] for $\omega_\xi \ll \omega \ll \omega_{l_c}$. Vibrational modes in the regime $\omega \ll \omega_\xi$ are phonons with the conventional Debye DOS. Using the known values $f = 3.96$, $\nu = 4/3$, $\beta = 5/36$ and $D_f = 91/48$ for 2D percolating networks, the spectral dimension for 2D bending fractons is estimated to be $\tilde{d}_b \approx 0.78$. This indicates that the DOS weakly diverges at very low frequencies.

6.6 Simulation Results for Vector Elasticity

In this section we present simulation results for the DOS of large-scale percolating networks with vector displacements. In order to clarify the contributions of stretching and bending fractons, elastic percolating networks with $\beta/\alpha = 0.01$ and 1.0 are treated. The ratio $\beta/\alpha = 0.01$ allows exclusive examination of the DOS for the bending fracton regime because the stretching fracton regime is shifted into the high-frequency region. Figures 6.10a and b show the results for the DOS and the integrated DOS for percolating networks at $p = p_c$, respectively, where the percolating network formed on a 500×500 square lattice has 53 673 occupied sites. The sets of force constants $[\alpha, \beta]$ in (6.20) are taken as $[1.0, 0.01]$ (filled circles) and $[0.12, 0.12]$ (open circles), respectively. The cutoff frequency is $\omega_D = 2.0784$, by virtue of the above choice of force constants. The DOS, given by filled circles in Fig. 6.10a, weakly diverges as $\omega \rightarrow 0$ in accord with the theoretical prediction presented in Sect. 6.5. The value of the bending-fracton dimension \tilde{d}_b obtained by a least-squares fitting from Fig. 6.10 is $\tilde{d}_b = 0.79$. This value agrees well with the predicted value ($\tilde{d}_b \approx 0.78$).

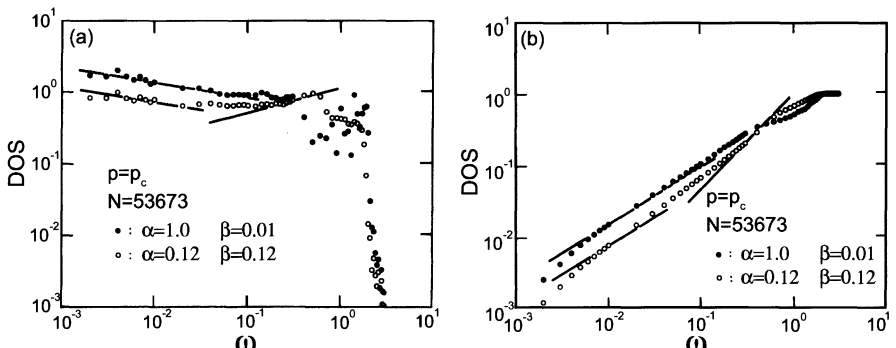


Fig. 6.10. (a) Density of states and (b) integrated density of states of percolating networks with vector displacements. *Solid circles* indicate results for the network with stretching force constant $\alpha = 1.0$ and bending force constant $\beta = 0.01$. *Open circles* are for $\alpha = \beta = 0.12$ [6.19].

In the case of $\beta/\alpha = 0.01$ (filled circles in Fig. 6.10), the mechanical length scale l_c becomes smaller than the lattice constant, resulting in an over-large crossover frequency ω_{l_c} to distinguish the crossover frequency region. For the case of $\beta/\alpha = 1.0$ (open circles in Fig. 6.10), the crossover frequency can be estimated to be close to $\omega \approx 0.1$. Note that the simulation does not exhibit any noticeable hump in the frequency dependence of the DOS around the crossover frequency as shown by the open circles in the vicinity of $\omega \approx 0.1$. The DOS for $\beta/\alpha = 1.0$ does not exhibit a distinct crossover to stretching fractons at ω_{l_c} . This is due to a broad crossover from stretching to bending fractons. Furthermore, it should be emphasized that the magnitudes of the DOS in the bending fracton regimes depend on the ratio β/α , as seen from the filled and open circles in Fig. 6.10. This implies that there exist missing modes accumulating in a high-frequency region around the cutoff frequency ω_D .

7. Scaling Arguments for Dynamic Structure Factors

Inelastic scattering experiments provide rich information on dynamic properties of fractal structures. A variety of scattering experiments have been performed that are sensitive to vibrational modes in fractals, among which inelastic neutron scattering (INS) and light scattering experiments are especially important for investigating the dynamics of fractal structures. The energy of neutrons of appropriate wavelengths λ for structural and dynamic studies corresponds to thermal energies at temperatures from a few kelvin to well above room temperature. Because of this wavelength–energy relation, neutron scattering becomes a powerful technique for studying static and dynamic structure on atomic scales.

Analyses and interpretations of data obtained by INS experiments for fractal structures are more complex than those for crystals because of the lack of long-range order in atomic positions. Consequently, there is no strongly destructive or constructive interference for scattered waves of neutrons, giving rise to Bragg peaks in the elastic scattering, and to momentum-conserving selection rules in the one-phonon inelastic scattering, as is the case for crystals. In fractal structures, we cannot work around Bragg peaks as in crystals since coherent INS in the appropriate q – ω space is limited by kinematical conditions due to the conservation of energy and wavevector [7.1, 7.2]. Alexander et al. [7.3] have shown that scaling analysis based on the single-length-scale postulate is an efficient way of interpreting experimental data concerning inelastic scattering for random fractal structures. This chapter describes in detail scaling theories of the dynamic structure factor $S(q, \omega)$ obtained by INS experiments and the Raman intensity $I(\omega)$. Numerical evidence for these theories is also presented.

7.1 Dynamic Structure Factors: Inelastic Neutron Scattering

The dynamic structure factor $S(q, \omega)$ is proportional to the space–time Fourier transform of the density–density correlation function defined by

$$G(|\mathbf{r} - \mathbf{r}'|, t) = \langle \rho(\mathbf{r}, t)\rho(\mathbf{r}', 0) \rangle , \quad (7.1)$$

where $\rho(\mathbf{r}, t)$ is the number density at time t and position \mathbf{r} , and the angular brackets denote the equilibrium ensemble average [7.4, 7.5]. The number density with temporal fluctuations induced by atomic vibration with the displacement $\mathbf{u}_i(t)$ is expressed as

$$\rho(\mathbf{r}, t) = \sum_i \delta(\mathbf{R}_i + \mathbf{u}_i(t) - \mathbf{r}) , \quad (7.2)$$

where \mathbf{R}_i denotes the equilibrium position of the i th nucleus. We usually neglect the contribution of elastic scattering ($\omega = 0$) to $\mathcal{S}(\mathbf{q}, \omega)$. The dynamic structure factor $\mathcal{S}(\mathbf{q}, \omega)$ is then expressed in terms of the Fourier transform of the density fluctuation $\Delta\rho(\mathbf{r}, t)$, i.e.,

$$\mathcal{S}(\mathbf{q}, \omega) = \frac{1}{2\pi N} \int e^{-i\omega t} \langle \Delta\rho_{-\mathbf{q}}(0) \Delta\rho_{\mathbf{q}}(t) \rangle dt , \quad (7.3)$$

where $\Delta\rho_{\mathbf{q}}(t)$ is the spatial Fourier transform of the density fluctuation $\Delta\rho(\mathbf{r}, t)$ and N is the number of sites. The quantity $\Delta\rho(\mathbf{r}, t)$ is defined by

$$\Delta\rho(\mathbf{r}, t) = \sum_i [\delta(\mathbf{R}_i + \mathbf{u}_i(t) - \mathbf{r}) - \delta(\mathbf{R}_i - \mathbf{r})] . \quad (7.4)$$

From this definition, the Fourier transform $\Delta\rho_{\mathbf{q}}(t)$ becomes

$$\Delta\rho_{\mathbf{q}}(t) = \sum_i \left[e^{-i\mathbf{q} \cdot (\mathbf{R}_i + \mathbf{u}_i(t))} - e^{-i\mathbf{q} \cdot \mathbf{R}_i} \right] . \quad (7.5)$$

Decomposing $\mathbf{u}_i(t)$ into normal modes $\mathbf{u}_i(t) = \sum_{\lambda} \mathbf{u}_i^{\lambda} e^{-i\omega_{\lambda} t}$, where ω_{λ} and \mathbf{u}_i^{λ} are the eigenfrequency and eigenvector of the mode λ , we obtain

$$\Delta\rho_{\mathbf{q}}(t) = \sum_{\lambda} \Delta\rho_{\lambda}(\mathbf{q}, t) + O(u^2) , \quad (7.6)$$

where

$$\Delta\rho_{\lambda}(\mathbf{q}, t) = e^{-i\omega_{\lambda} t} \Delta\rho_{\lambda}(\mathbf{q}) , \quad (7.7)$$

and

$$\Delta\rho_{\lambda}(\mathbf{q}) = -i \sum_i (\mathbf{q} \cdot \mathbf{u}_i^{\lambda}) e^{-i\mathbf{q} \cdot \mathbf{R}_i} . \quad (7.8)$$

Substituting (7.6) with (7.7) and (7.8) into (7.3), the dynamic structure factor $\mathcal{S}(\mathbf{q}, \omega)$ becomes

$$\mathcal{S}(\mathbf{q}, \omega) = \frac{1}{N} \sum_{\lambda} \delta(\omega - \omega_{\lambda}) \langle \Delta\rho_{\lambda}(\mathbf{q}) \Delta\rho_{\lambda}(-\mathbf{q}) \rangle . \quad (7.9)$$

The equilibrium ensemble average $\langle \dots \rangle$ contains the thermal average and the ensemble average at zero temperature. The thermal average produces the thermal factor $[n(\omega) + 1]/\omega$, where $n(\omega)$ is the Bose–Einstein distribution function. Hereafter, we consider the dynamic structure factor divided by this thermal factor, namely, $S(\mathbf{q}, \omega) \rightarrow \omega \mathcal{S}(\mathbf{q}, \omega)/[n(\omega) + 1]$. The reduced $S(\mathbf{q}, \omega)$ is then given by

$$S(\mathbf{q}, \omega) = \frac{1}{N} \sum_{\lambda} \delta(\omega - \omega_{\lambda}) \langle \Delta\rho_{\lambda}(\mathbf{q}) \Delta\rho_{\lambda}(-\mathbf{q}) \rangle_{\text{en}}, \quad (7.10)$$

where $\langle \cdots \rangle_{\text{en}}$ denotes the ensemble average at zero temperature. Introducing the density of states (DOS), we can replace the summation over λ in (7.10) by a frequency integral as

$$S(q, \omega) = D(\omega) \langle \Delta\rho_{\lambda}(\mathbf{q}) \Delta\rho_{\lambda}(-\mathbf{q}) \rangle_{\omega}, \quad (7.11)$$

where $D(\omega)$ is the DOS of vibrational modes per atom and $\langle \cdots \rangle_{\omega}$ denotes the average over all modes with frequencies close to ω . It should be noted that the variable $q (= |\mathbf{q}|)$ of $S(q, \omega)$ in (7.11) is a scalar quantity. This is because we assume the isotropy of random fractal systems in our analysis.

In principle, $S(q, \omega)$ can be calculated analytically using (7.11) with (7.8), if we know the eigenvectors \mathbf{u}_i^{λ} for a specific realization. However, this is not easy using analytical arguments because of the extremely complicated character of vibrational modes in fractal structures. In addition, we should emphasize that the dynamic structure factor $S(q, \omega)$ represents plane-wave components of the eigenvectors since it is defined through the spatial Fourier transformation. If the eigenmode is a plane wave, $S(q, \omega)$ of a function of ω becomes a δ -function with a peak at a specific frequency. The dynamic structure factor $S(q, \omega)$, however, has a large frequency (or energy) width for fractons above the phonon-fracton crossover frequency ω_c . We should clarify the meaning of this frequency width. Obviously, exact eigenstates possess definite eigenfrequencies and have no frequency width. A localized fracton can be expanded in plane waves. The width of $S(q, \omega)$ should be understood as the frequency range over which frequencies of the constitutive plane waves vary.

7.2 Single-Length Scaling Arguments

The asymptotic behavior of the dynamic structure factor $S(q, \omega)$ can be analyzed in terms of the single-length-scale postulate (SLSP), by introducing the frequency-dependent length scale $\Lambda(\omega)$ [7.3]. The physical meaning of $\Lambda(\omega)$ is the length scale representing the wavelength and/or localization length of fracton excitations. From the dispersion relation of fractons (5.41), this length scale is given by

$$\Lambda(\omega) \propto \omega^{-\tilde{d}_s/D_f}. \quad (7.12)$$

The SLSP claims that the length scale $\Lambda(\omega)$ is a unique characteristic length of fractons. If the SLSP is valid, $S(q, \omega)$ should be scaled only by $\Lambda(\omega)$, so that

$$S(q, \omega) = q^y H(q\Lambda), \quad (7.13)$$

where y is an exponent. The scaling function $H(x)$ is assumed to behave asymptotically as

$$H(x) \propto \begin{cases} x^a, & \text{for } x \ll 1, \\ x^{-a'}, & \text{for } x \gg 1. \end{cases} \quad (7.14)$$

Here a and a' are new scaling exponents. Combining (7.12) with (7.13), we have

$$S(q, \omega) \propto \begin{cases} q^{y+a} \omega^{-a\tilde{d}_s/D_f}, & \text{for } q\Lambda(\omega) \ll 1, \\ q^{y-a'} \omega^{a'\tilde{d}_s/D_f}, & \text{for } q\Lambda(\omega) \gg 1, \end{cases} \quad (7.15)$$

where we have used the relation (7.12).

The exponents y , a , and a' can be related to other exponents such as D_f and \tilde{d}_s . In the case $q\Lambda \ll 1$, (7.8) can be expanded as

$$\Delta\rho_\lambda(\mathbf{q}) \approx -e^{-i\mathbf{q}\cdot\mathbf{R}_\lambda} \sum_i (\mathbf{q}\cdot\mathbf{R}_i^\lambda)(\mathbf{q}\cdot\mathbf{u}_i^\lambda), \quad (7.16)$$

where $\mathbf{R}_i^\lambda = \mathbf{R}_i - \mathbf{R}_\lambda$ with \mathbf{R}_λ defined as the center of the λ -mode fracton excitations. The summand in (7.16) can be written in terms of the dyadic product as $\mathbf{q}\cdot(\mathbf{R}_i^\lambda \otimes \mathbf{u}_i^\lambda)\cdot\mathbf{q}$. Choosing the center of the fracton excitation as the origin, i.e., $\mathbf{R}_\lambda = 0$, and using the condition $\sum_i \mathbf{u}_i^\lambda = 0$, we have the relation

$$\Delta\rho_\lambda(\mathbf{q}) \approx - \sum_i^{\mathcal{V}_\lambda} \mathbf{q}\cdot[\mathbf{R}_i^\lambda \otimes (\mathbf{u}_i^\lambda - \mathbf{u}_\lambda)]\cdot\mathbf{q}, \quad (7.17)$$

where \mathbf{u}_λ is the amplitude at the center of the λ -mode fracton and the summation is restricted to a vibrating region \mathcal{V}_λ chosen as the smallest region for which the boundary condition plays no significant role for the vibration λ . We introduce an average strain tensor $\overline{\mathbf{e}_\lambda}$ defined by

$$\mathbf{u}_i^\lambda - \mathbf{u}_\lambda = \overline{\mathbf{e}_\lambda} \mathbf{R}_i^\lambda. \quad (7.18)$$

Using this strain tensor, (7.17) can be written

$$\Delta\rho_\lambda(\mathbf{q}) \approx -\mathbf{q}\cdot \left[\sum_i^{\mathcal{V}_\lambda} (\mathbf{R}_i^\lambda \otimes \mathbf{R}_i^\lambda) \overline{\mathbf{e}_\lambda} \right] \cdot \mathbf{q}. \quad (7.19)$$

The \mathbf{R}_i^λ in \mathcal{V}_λ are at most of order $\Lambda(\omega)$, so that the magnitude of $\Delta\rho_\lambda(\mathbf{q})$ can be estimated as

$$\Delta\rho_\lambda(q) \propto q^2 \Lambda(\omega)^{D_f+2} \overline{\mathbf{e}_\lambda}. \quad (7.20)$$

Substituting (7.20) into (7.11), we have

$$S(q, \omega) \propto D(\omega) q^4 [\Lambda(\omega)]^{2D_f+4} \langle \overline{\mathbf{e}_\lambda}^2 \rangle_\omega. \quad (7.21)$$

Alexander et al. [7.3] assumed that $\langle \overline{e_\lambda^2} \rangle_\omega$ has a scaling form. To leading order,

$$[\langle \overline{e_\lambda^2} \rangle_\omega]^{1/2} \propto \frac{u(\omega)}{[\Lambda(\omega)]^\sigma}, \quad (7.22)$$

where the root-mean-squared amplitude $u(\omega)$ of the fracton modes is defined by

$$u(\omega) = \left[\left\langle \frac{1}{N_\lambda} \sum_i^{V_\lambda} |\mathbf{u}_i^\lambda|^2 \right\rangle_\omega \right]^{1/2}. \quad (7.23)$$

Here N_λ is the number of sites contained in the region of vibrations, V_λ [i.e., $\langle N_\lambda \rangle_\omega \propto \Lambda(\omega)^{D_f}$]. The new exponent σ thus characterizes an effective length relevant to the average strain, analogous to the relationship between the chemical and Euclidean lengths. The magnitude of $u(\omega)$ is proportional to $[\Lambda(\omega)]^{-D_f/2}$ because of the normalization condition $\sum_i |\mathbf{u}_i^\lambda|^2 = 1$. From (7.21), (7.22), and (7.12), we have

$$S(q, \omega) \propto q^4 \omega^{(2\sigma-4)(\tilde{d}_s/D_f)-1}, \quad \text{for } q\Lambda(\omega) \ll 1. \quad (7.24)$$

Thus, the exponents y and a in (7.15) are determined as

$$y = 2\sigma - \frac{D_f}{\tilde{d}_s}, \quad (7.25)$$

and

$$a = 4 + \frac{D_f}{\tilde{d}_s} - 2\sigma. \quad (7.26)$$

In the case $q\Lambda(\omega) \gg 1$, the phase factor $e^{-i\mathbf{q}\cdot\mathbf{R}_i}$ in (7.8) is uniform (coherent) only over small regions of size $l_q \propto q^{-1}$ [$\ll \Lambda(\omega)$]. Provided that the vibrating region V_λ is divided into blobs of size $l_q \ll \Lambda(\omega)$, the number of blobs in the region V_λ is proportional to $[q\Lambda(\omega)]^{D_f}$ and each blob has $\approx (qa)^{-D_f}$ particles. Then, as for the derivation of (7.16), we can expand (7.8) for small \mathbf{q} to obtain

$$\Delta\rho_\lambda(\mathbf{q}) \approx \sum_\beta e^{-i\mathbf{q}\cdot\mathbf{R}_\beta} \left[-i(qa)^{-D_f} (\mathbf{q}\cdot\mathbf{U}_\lambda^\beta) - \sum_i^{V_\lambda^\beta} (\mathbf{q}\cdot\mathbf{r}_i)(\mathbf{q}\cdot\mathbf{u}_i^\lambda) \right], \quad (7.27)$$

where \mathbf{R}_β is the center of mass of the blob β and $\mathbf{r}_i = \mathbf{R}_i - \mathbf{R}_\beta$. The factor $\mathbf{U}_\lambda^\beta \approx (qa)^{D_f} \sum_i^{V_\lambda^\beta} \mathbf{u}_i^\lambda$ is the averaged motion of the blob β in the eigenmode λ . The second summation in (7.27) is taken over the region of the blob β . Inserting (7.27) into (7.11), we have the phase factor $\exp[-i\mathbf{q}\cdot(\mathbf{R}_\beta - \mathbf{R}_{\beta'})]$. Because there is no coherent contribution of the scattering from different blobs in this limit [$q\Lambda(\omega) \gg 1$], only terms with $\beta = \beta'$ remain. Alexander et al. [7.3] suggest that the first term dominates the second term in (7.27) for $q\Lambda(\omega) \gg 1$.

We thus have the result

$$S(q, \omega) \propto D(\omega)[\Lambda(\omega)]^{D_f} q^{2-D_f} \langle (U_\lambda^\beta)^2 \rangle_\omega . \quad (7.28)$$

When the number of particles in each blob becomes large, i.e., $(qa)^{-D_f} \gg 1$, the magnitude of $\langle (U_\lambda^\beta)^2 \rangle_\omega$ is assumed to be

$$\langle (U_\lambda^\beta)^2 \rangle_\omega \approx (qa)^x \langle u_\lambda^2 \rangle_\omega , \quad (7.29)$$

where x is a new exponent. The dynamic structure factor $S(q, \omega)$ is expressed using the relation $u(\omega) \propto [\Lambda(\omega)]^{-D_f/2}$, which yields

$$S(q, \omega) \propto \omega^{\tilde{d}_s - 1} q^{2-D_f+x} . \quad (7.30)$$

Comparing this expression with (7.15), we have

$$2 - D_f + x = y - a' , \quad (7.31)$$

and

$$a' = \frac{D_f}{\tilde{d}_s} (\tilde{d}_s - 1) . \quad (7.32)$$

The exponent x can be related to σ using (7.25) and (7.31), which yields

$$x = 2(\sigma - 1) . \quad (7.33)$$

To summarize, the scaling argument based on the SLSP predicts that $S(q, \omega)$ behaves as

$$S(q, \omega) \propto \begin{cases} q^{4\omega^{(2\sigma-4)(\tilde{d}_s/D_f)-1}} , & \text{for } q\Lambda(\omega) \ll 1 , \\ q^{2\sigma-D_f} \omega^{\tilde{d}_s-1} , & \text{for } q\Lambda(\omega) \gg 1 . \end{cases} \quad (7.34)$$

7.3 Numerical Simulations of $S(q, \omega)$

This section presents numerical results for $S(q, \omega)$ in percolating networks by applying the powerful numerical technique called the forced oscillator method [7.6]. The method enables us to calculate various types of linear response functions in large-scale systems and has been successfully applied to various physical problems including quantum systems [7.6].

Figure 7.1 shows the results for 3D BP networks formed on $120 \times 120 \times 120$ simple-cubic lattices with (a) $p = 0.249 (= p_c)$ and (b) $p = 0.31$ [7.7]. The ω -dependencies of $S(q, \omega)$ are given for five different q along the [100] direction. Periodic boundary conditions are adopted for calculations and the Bose factor $[n(\omega)+1]$ is factored out. The dynamic structure factors $S(q, \omega)$ at and above p_c have completely different profiles at low wavenumbers. There should be a crossover from

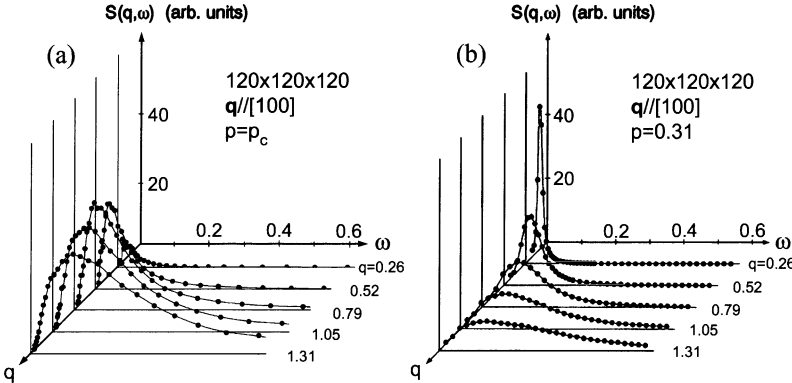


Fig. 7.1. Calculated dynamic structure factors $S(q, \omega)$ for 3D BP networks formed on $120 \times 120 \times 120$ cubic lattices with (a) $p = 0.249 (= p_c)$ and (b) $p = 0.31$

phonons to fractons in Fig. 7.1b, because the correlation length of the percolating network above p_c is finite. The crossover frequency ω_c of the system for Fig. 7.1b is estimated from Fig. 6.3 as $\omega_c \approx 0.07$. For small wave vectors $q (\ll \xi^{-1})$, sharp peaks appear in the low-frequency regime. With increasing $q = |q|$, peak positions shift to the higher-frequency region. When the peak position shifts above $\omega_c \approx 0.07$, the widths (τ^{-1}) of peaks increase very rapidly. This indicates that linewidths of fractons are very broad, originating from the Ioffe–Regel strong scattering limit ($\tau^{-1} \approx \omega$).

Figure 7.2 is a rescaled plot of Fig. 7.1a. The abscissa in Fig. 7.2 represents the reduced frequency $\omega/\omega_0(q)$, where $\omega_0(q)$ is the frequency at which $S(q, \omega)$ takes the maximum value $S_{\max}(q)$ for each fixed wavenumber. Values of $S(q, \omega)$ are also

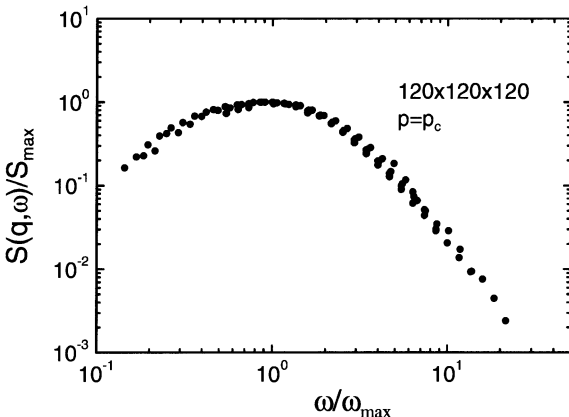


Fig. 7.2. Rescaled plot of Fig. 7.1a. The abscissa represents the reduced frequency $\omega/\omega_0(q)$, where $\omega_0(q)$ is the frequency at which $S(q, \omega)$ takes the maximum value S_{\max} for each fixed wavenumber. Values of $S(q, \omega)$ are also reduced by $S_{\max}(q)$

rescaled by $S_{\max}(q)$. All data collapse onto a single curve. This fact demonstrates a universal behavior of $S(q, \omega)$ that can be scaled by the single frequency ω_0 .

We have demonstrated the validity of the single-length-scale postulate (SLSP) by analyzing the simulated result for $S(q, \omega)$. The SLSP is based on the idea that, for strongly disordered fractals, fractons always lie in the Ioffe–Regel strong scattering limit [7.9]. This means that the three distinct length scales (the wavelength λ , the scattering length l_s , and the localization length Λ) collapse into one. For percolating networks, this length scale should have the frequency dependence $\Lambda(\omega) \propto \omega^{-\tilde{d}_s/D_f}$. Hence, all waves with the wavelength $\lambda < \xi$ satisfy the Ioffe–Regel condition $\lambda \approx l_s$, indicating that fractons are strongly localized with localization length $\Lambda(\omega)$. The numerical simulations presented in this section confirm this postulate and show that the asymptotic behavior of $S(q, \omega)$ can be characterized by the exponent σ introduced to describe the average strain [7.3]. For weakly localized phonons, the characteristic lengths have different frequency dependencies [7.10].

7.4 Inelastic Light Scattering in Percolating Systems

The single-length-scale postulate (SLSP) can also be applied to analyze the frequency dependence of inelastic light scattering intensities from random fractal materials. The validity of the SLSP can be demonstrated by inelastic light scattering experiments, in addition to neutron scattering experiments and numerical simulations. Tsujimi et al. [7.11] have performed Raman scattering experiments for silica aerogels and found the power-law dependence of the Raman scattering intensity on frequency. The Raman scattering intensity $I_{\alpha\beta}(\omega)$ ($\alpha, \beta = x, y, z$) is given by

$$I_{\alpha\beta}(\omega) = \frac{1}{2\pi N} \int dt e^{i\omega t} \sum_{i,j} \langle \mu_{\alpha\beta}^i(t) \mu_{\alpha\beta}^j(0) \rangle , \quad (7.35)$$

where $\langle \dots \rangle$ is the thermal average, N the number of sites, and $\mu_{\alpha\beta}^i(t)$ the polarizability at the site i . The polarizability $\mu_{\alpha\beta}^i(t)$ can be expanded in terms of small displacements around the equilibrium positions of the atoms as

$$\mu_{\alpha\beta}^i(t) = \mu_{\alpha\beta}^i + \sum_{j,\gamma} \frac{\partial \mu_{\alpha\beta}^i}{\partial u_\gamma^j} u_\gamma^j(t) , \quad (7.36)$$

where $\mu_{\alpha\beta}^i$ and $\partial \mu_{\alpha\beta}^i / \partial u_\gamma^j$ are defined at the equilibrium positions. The displacement $u_\alpha^i(t)$ is further decomposed into eigenmodes of the system as

$$u_\alpha^i(t) = \sqrt{\frac{\hbar}{2N}} \sum_\lambda \frac{A_\lambda(t)}{\sqrt{\omega_\lambda}} e_\alpha^i(\lambda) , \quad (7.37)$$

where $e_\alpha^i(\lambda)$ and ω_λ are the α -component of the eigenvector $e^i(\lambda)$ of the mode λ at the site i and the corresponding eigenfrequency, respectively. The quantity $A_\lambda(t)$ is the

time-dependent expansion coefficient. Here we assume that the atom has unit mass ($M = 1$). Substituting (7.36) and (7.37) into (7.35) and neglecting the contribution from elastic scattering, we obtain

$$I_{\alpha\beta}(\omega) = \frac{\hbar}{4N^2\pi} \sum_{\lambda,\lambda'} \frac{1}{\sqrt{\omega_\lambda\omega_{\lambda'}}} \sum_{j,j'} \sum_{\gamma,\gamma'} e_\gamma^j(\lambda) e_{\gamma'}^{j'}(\lambda') f_{\alpha\beta\gamma}^j f_{\alpha\beta\gamma'}^{j'} \times \int e^{i\omega t} \langle A_\lambda(t) A_{\lambda'}(0) \rangle dt , \quad (7.38)$$

where

$$f_{\alpha\beta\gamma}^j = \sum_i \frac{\partial \mu_{\alpha\beta}^i}{\partial u_\gamma^j} . \quad (7.39)$$

We note that the coefficient $A_\lambda(t)$ satisfies

$$\frac{1}{2\pi} \int e^{i\omega t} \langle A_\lambda(t) A_{\lambda'}(0) \rangle dt = \delta_{\lambda\lambda'} \{ [n(\omega_\lambda) + 1] \delta(\omega - \omega_\lambda) + n(\omega_\lambda) \delta(\omega + \omega_\lambda) \} , \quad (7.40)$$

where $n(\omega)$ is the Bose–Einstein distribution function expressed by $n(\omega) = 1/(e^{\beta\omega} - 1)$. Using (7.40) without the second term on the right-hand side due to $\omega > 0$, the relation (7.38) becomes

$$I_{\alpha\beta}(\omega) = \frac{\hbar}{2N^2} \frac{n(\omega) + 1}{\omega} \sum_\lambda \delta(\omega - \omega_\lambda) \left[\sum_{j,\gamma} f_{\alpha\beta\gamma}^j e_\gamma^j(\lambda) \right]^2 . \quad (7.41)$$

Let us introduce a new quantity $C_{\alpha\beta}(\omega)$ called the Raman coupling coefficient, which is defined by

$$C_{\alpha\beta}(\omega) = \frac{\hbar \sum_\lambda \delta(\omega - \omega_\lambda) \left[\sum_{j,\gamma} f_{\alpha\beta\gamma}^j e_\gamma^j(\lambda) \right]^2}{2N^2 \sum_\lambda \delta(\omega - \omega_\lambda)} . \quad (7.42)$$

Using the Raman coupling coefficient, (7.41) becomes

$$I_{\alpha\beta}(\omega) = \frac{n(\omega) + 1}{\omega} D(\omega) C_{\alpha\beta}(\omega) , \quad (7.43)$$

where $D(\omega)$ is the DOS.

There exist several mechanisms to produce the Raman scattering intensity. Inelastic light scattering is a consequence of oscillating dipoles which are proportional to the local electric field $\mathbf{E}(\mathbf{r}_i, t)$ at scatterers. If the local field $\mathbf{E}(\mathbf{r}, t)$ is proportional to the applied field $\mathbf{E}_{\text{ex}}(\mathbf{r}, t)$, the frequency dependence of the scattering intensity becomes the same as that of the dynamic structure factor $S(q, \omega)$ for $q\Lambda(\omega) \ll 1$,

because the polarizability is proportional to the mass fluctuation [see (7.24) in Sect. 7.2]. This scattering mechanism is called the direct mechanism. In many disordered materials, however, the local field $\mathbf{E}(\mathbf{r}, t)$ is the sum of the applied external field $\mathbf{E}_{\text{ex}}(\mathbf{r}, t)$ and the additional field $\delta\mathbf{E}(\mathbf{r}, t)$ induced by all other surrounding dipoles. This mechanism, called the dipole-induced dipole (DID) mechanism, leads to a different expression for $I_{\alpha\beta}(\omega)$ than the one due to the direct mechanism. Hereafter, we discuss the Raman scattering intensity due to the DID mechanism.

Within the DID mechanism, $f_{\alpha\beta\gamma}^j$ is found to be [7.12]

$$f_{\alpha\beta\gamma}^j = \sum_i \tilde{\mu}^i \tilde{\mu}^j \left[-3 \frac{\delta_{\alpha\beta} r_\gamma^{ij} + \delta_{\beta\gamma} r_\alpha^{ij} + \delta_{\gamma\alpha} r_\beta^{ij}}{|\mathbf{r}^{ij}|^5} + 15 \frac{r_\alpha^{ij} r_\beta^{ij} r_\gamma^{ij}}{|\mathbf{r}^{ij}|^7} \right], \quad (7.44)$$

where r_α^{ij} is defined as the α -component of $\mathbf{r}^{ij} \equiv \mathbf{R}^i - \mathbf{R}^j$, and $\tilde{\mu}^j$ is the bare polarizability of the site j . Here the bare polarizability at each site is taken to be isotropic. In the case of percolating networks, the value of $\tilde{\mu}^j$ is given by

$$\tilde{\mu}^j = \begin{cases} 1, & \text{for occupied sites,} \\ 0, & \text{for unoccupied sites.} \end{cases} \quad (7.45)$$

Alexander et al. [7.3] have discussed the frequency dependence of the Raman coupling coefficient $C(\omega)$ by means of the scaling theory based on the single-length-scale postulate (SLSP). Since the average field δE is proportional to the density of dipoles within the vibrating volume V_λ of size $\Lambda(\omega)$, we have

$$\delta E \propto [\Lambda(\omega)]^{D_f-d} \bar{e}_\lambda^- E_{\text{ex}}, \quad (7.46)$$

where \bar{e}_λ^- is the average strain introduced by (7.18) and E_{ex} is the applied external field. This induced field acts equally upon all $[\Lambda(\omega)]^{D_f}$ dipoles in V_λ . The total dipole moment is thus proportional to $[\Lambda(\omega)]^{2D_f-d} \bar{e}_\lambda^-$. Using (7.12) and (7.22), we obtain [7.3]

$$C(\omega) \propto \omega^{2\tilde{d}_s(\sigma+d)/D_f - 3\tilde{d}_s}, \quad (7.47)$$

where σ is the exponent describing the average strain defined by (7.22). Alexander et al. [7.3] have suggested that the value of $\sigma (\geq 1)$ should not be much larger than unity.

Figure 7.3 shows the numerical results for the Raman scattering intensities caused by the DID mechanism for 3D BP networks calculated using the forced oscillator method [7.6]. Figure 7.3a shows the reduced Raman scattering intensity $I_{\alpha\beta}(\omega)/(n+1)$ as a function of frequency ω for a BP network at the percolation threshold ($p_c = 0.249$). The system size is $N = 264\,311$. Solid circles and solid squares in Fig. 7.3a represent the calculated results for polarized scattering $[(\alpha, \beta) = (x, x)]$ and for depolarized scattering $[(\alpha, \beta) = (x, y)]$, respectively. We clearly see the power-law dependence

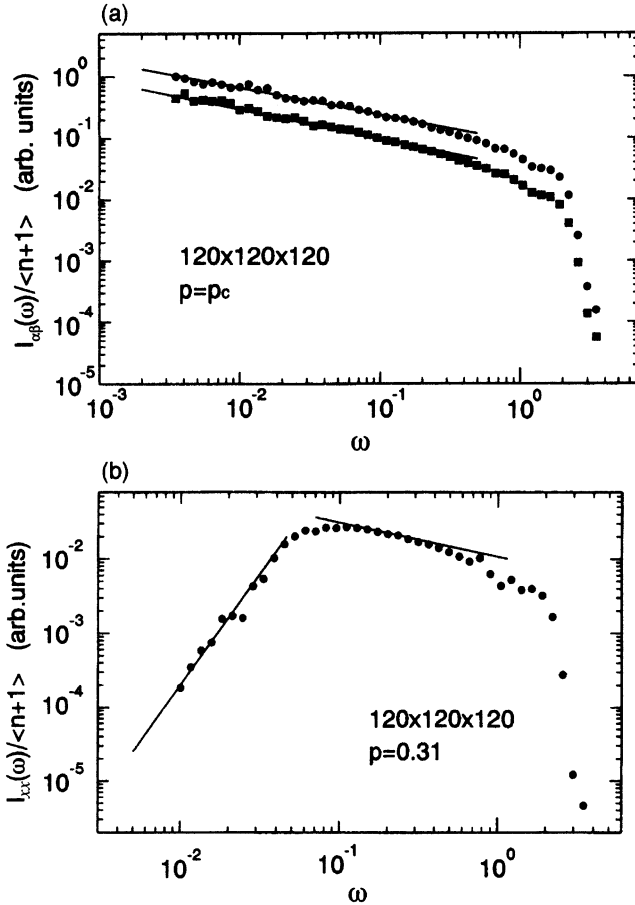


Fig. 7.3. (a) Angular frequency dependence of the reduced Raman intensity $I_{\alpha\beta}(\omega)/(n + 1)$ of a 3D BP network at $p_c (= 0.249)$ formed on a $120 \times 120 \times 120$ cubic lattice. Solid circles and squares represent the calculated results for polarized scattering [$(\alpha\beta) = (x, x)$] and depolarized scattering [$(\alpha\beta) = (x, y)$], respectively. (b) The ω dependence of the reduced Raman intensity $I_{xx}(\omega)/(n + 1)$ of a 3D BP network at $p = 0.31$ formed on a $120 \times 120 \times 120$ cubic lattice [7.7]

$$\frac{I_{xx}(\omega)}{n(\omega) + 1} \propto \omega^{-0.44 \pm 0.05}, \quad (7.48)$$

and

$$\frac{I_{xy}(\omega)}{n(\omega) + 1} \propto \omega^{-0.46 \pm 0.05}. \quad (7.49)$$

Equation (7.43) and the fracton DOS $D(\omega) \propto \omega^{1/3}$ lead to the power-law dependence of the Raman coupling coefficients

$$C_{xx}(\omega) \propto \omega^{0.23 \pm 0.05}, \quad (7.50)$$

and

$$C_{xy}(\omega) \propto \omega^{0.21 \pm 0.05}, \quad (7.51)$$

in the fracton regime. From these results, the value obtained for the exponent σ in (7.47) is close to unity, viz., $\sigma = 0.97 \pm 0.05$.

Figure 7.3b gives the reduced Raman intensity $I_{xx}(\omega)/(n + 1)$ for the 3D BP network at $p = 0.31 (> p_c)$. A drastic change in the ω -dependence of the reduced Raman intensity is observed at $\omega \approx 0.07$. For $\omega \gg \omega_c$, the calculated results show that $I_{xx}(\omega)/(n + 1)$ is proportional to $\omega^{-0.44}$, which is the same power-law dependence as the solid circles in Fig. 7.3a, indicating the contribution from fractons. The intensity from fracton excitations in Fig. 7.3b is smaller than that in Fig. 7.3a. This is because the number of fractons (per atom) in a system above p_c is smaller than that for $p = p_c$ as shown in Fig. 6.5. The calculated ω -dependence of the reduced Raman intensity $I_{xx}(\omega)/(n + 1)$ is proportional to ω^3 for $\omega \ll \omega_c$, indicating the phonon contribution. Substituting the phonon density of states $D(\omega) \propto \omega^2$ and $I_{xx}(\omega)/(n + 1) \propto \omega^3$ into (7.43), it is found that the Raman coupling coefficient behaves as $C_{xx}(\omega) \propto \omega^2$, which is consistent with the expected behavior of $C_{xx}(\omega)$ for phonons obtained using (7.42) with $\tilde{d}_s = D_f = d = 3$ and $\sigma = 1$. Figure 7.3b presents clear evidence for the power-law dependence of the Raman intensity above and below the phonon–fracton crossover frequency ω_c .

To summarize this section, the ω -dependencies of the Raman scattering intensities have been considered for percolating networks, especially for scattering by the dipole-induced dipole mechanism. For 3D percolating networks at p_c , the validity of the SLSP has been confirmed. For the ω -dependence of the Raman scattering intensity for percolating networks above p_c , calculated results indicate clear phonon contributions in the lower-frequency regime ($\omega \ll \omega_c$). In the higher-frequency regime ($\omega \gg \omega_c$), the reduced Raman intensity has the same ω -dependence as that for networks at the percolation threshold p_c , which indicates scattering from fracton modes. This supports the applicability of the scaling theory for the Raman scattering intensity to real systems such as silica aerogels [7.11].

8. Spin Waves in Diluted Heisenberg Antiferromagnets

Randomly diluted magnets provide ideal systems for investigating the dynamic properties of percolating networks. Spin waves excited in diluted magnets possess an anomalous dispersion relation like vibrational fractons when:

- magnetic ions form a percolating structure,
- coupling between spins is described by the Heisenberg interaction,
- anisotropy is negligible,
- spin–spin interactions are short range,
- randomness does not introduce spin frustration.

We show in Appendix C that spin waves in ferromagnetic percolating systems belong to the same universality class as vibrational ones. This is because the equations of motion for vibrational excitations and those for ferromagnetic spin waves can both be mapped onto the master equation for diffusing particles. However, the linearized equation of motion for antiferromagnetic spin waves is described by a different type of equation to the above cases. The spectral dimension \tilde{d}_{AF} of percolating antiferromagnets should therefore take a different value from $\tilde{d}_s \approx 4/3$. What value does \tilde{d}_{AF} take for percolating antiferromagnets? This is not only an intriguing problem, but it is also vital for our understanding of the dynamics in diluted antiferromagnets.

For these reasons, the present chapter is mainly concerned with spin-wave dynamics in diluted Heisenberg antiferromagnets. We present the theoretical upper bound of the spectral dimension \tilde{d}_{AF} from dynamic scaling arguments. We also show the frequency and wavenumber dependencies of the dynamic structure factor $S(q, \omega)$ of percolating Heisenberg antiferromagnets at p_c , based on the single-length-scale postulate (SLSP). These results will be confirmed by means of direct numerical simulations for $S(q, \omega)$.

8.1 Spin Waves in Percolating Antiferromagnets

There are several diluted Heisenberg antiferromagnet systems satisfying the five conditions listed above. Among these, $\text{RbMn}_x\text{Mg}_{1-x}\text{F}_3$ is an ideal isotropic Heisenberg antiferromagnet since the magnitude of anisotropy is very small and the exchange interaction is dominant only for nearest neighbours. A pure system of RbMnF_3 has a cubic perovskite structure in which magnetic ions lie on a simple cubic lattice

with the exchange interaction energy $J = 0.29$ meV [8.1, 8.2]. In a diluted system, the magnetic Mn^{2+} and nonmagnetic Mg^{2+} atoms are randomly arranged on the cubic lattice. $\text{Mn}_x\text{Zn}_{1-x}\text{F}_2$ (x is the concentration of magnetic ions) is a 3D diluted antiferromagnet with spins $S = 5/2$ that satisfies most of the above conditions, but has weak anisotropy [8.3]. A pure system of MnF_2 ($x = 1$) is a representative 3D Heisenberg antiferromagnet with the rutile structure. Below the Néel temperature, $T_N = 67.4$ K, Mn spins align along the c axis because of weak anisotropic Ising interaction between Mn moments. Hereafter we use the concentration of magnetic ions p instead of x . The Néel temperature T_N of a percolating antiferromagnet is proportional to $(p - p_c)^{\mu-\nu}$, where the exponents μ and ν are the conductivity and the correlation length exponents of a percolating system, respectively [8.4, 8.5]. The Néel temperature T_N vanishes at the critical concentration p_c . We assume that the length scale ξ_N of the Néel order is much longer than the wavelengths of spin waves. Note that ξ_N is different from the correlation length defined by (3.2).

The Hamiltonian for a diluted Heisenberg antiferromagnet on a percolating network is given by

$$H = \frac{1}{2} \sum_{i,j} J_{ij} \mathbf{S}_i \cdot \mathbf{S}_j , \quad (8.1)$$

where \mathbf{S}_i denotes the spin vector with magnitude S at site i , and J_{ij} is the exchange coupling between nearest-neighbor spins at sites i and j . We choose J_{ij} as $J_{ij} = 1$ if both sites i and j are occupied, and $J_{ij} = 0$ otherwise. For $p < p_c$, there is no long-range magnetic order of spin configurations, even at $T = 0$, because no infinitely connected cluster exists below p_c .

Introducing new quantities $S_i^\pm \equiv S_i^x \pm iS_i^y$, the Hamiltonian is rewritten in the form (see Appendix C)

$$H = \frac{1}{2} \sum_{i,j} J_{ij} \left[\frac{1}{2} (S_i^+ S_j^- + S_i^- S_j^+) + S_i^z S_j^z \right] . \quad (8.2)$$

The Heisenberg equation of motion for S_i^+ is found to be

$$i\hbar \frac{\partial S_i^+}{\partial t} = [S_i^+, H] \quad (8.3)$$

$$= \frac{1}{2} \sum_{j \neq i} J_{ij} \left\{ [S_i^+, S_i^+ S_j^- + S_i^- S_j^+] + [S_i^+, S_i^z S_j^z] \right\} . \quad (8.4)$$

If the spin deviations are enough small, S_i^z can be approximated by $S_i^z \approx \sigma_i S$, where σ_i is $+1$ for a site i belonging to the spin-up sublattice and -1 for a site i belonging to the spin-down sublattice. Using this approximation and the relations $[S_i^+, S_j^-] = \delta_{ij} S_i^z$ and $[S_i^z, S_j^\pm] = \pm \delta_{ij} S_i^\pm$, we have

$$i\hbar \frac{\partial S_i^+}{\partial t} = \sigma_i \sum_{j \neq i} J_{ij} S(S_j^+ + S_i^+) . \quad (8.5)$$

The linearized equation of motion for the spin deviation S_i^+ from the perfect Néel order, in units of $S/\hbar = 1$, is expressed by

$$i \frac{\partial S_i^+}{\partial t} = \sigma_i \sum_{j \neq i} J_{ij} (S_j^+ + S_i^+) . \quad (8.6)$$

The same equation holds for $S_i^- (\equiv S_i^x - iS_i^y)$.

This equation has a different structure to the equation for ferromagnetic spin waves. The latter are governed by

$$i \frac{\partial S_i^+}{\partial t} = \sum_{j \neq i} J_{ij} (S_j^+ - S_i^+) , \quad (8.7)$$

which has the same structure as the master equation for diffusing particles shown in (C.1) or the equation of motion for atomic vibrations with scalar displacements given by (C.6). In order to clarify the difference between (8.6) and (8.7), let us consider the secular equation corresponding to (8.6), which has the form

$$\sum_j D_{ij} u_j(\lambda) = \omega_\lambda u_i(\lambda) , \quad (8.8)$$

where $u_i(\lambda)$ is the normal mode belonging to the eigenfrequency ω_λ , i.e.,

$$S_i^+(t) = \sum_\lambda A_\lambda u_i(\lambda) e^{-i\omega_\lambda t} , \quad (8.9)$$

and A_λ is a constant. The matrix element D_{ij} is given by

$$D_{ij} = \sigma_i \left(J_{ij} + \delta_{ij} \sum_k J_{ik} \right) . \quad (8.10)$$

From this definition, we see that the matrix $\{D_{ij}\}$ is asymmetric (that is, $D_{ij} = -D_{ji}$ for $i \neq j$) due to the prefactor σ_i and the sign of the second term in the parentheses on the right-hand side of (8.10), which differs from the symmetric matrix for ferromagnetic spin waves (8.7). In addition, we have the relation

$$\sum_j D_{ij} \neq 0 ,$$

while the corresponding matrix for (8.7) satisfies the condition

$$\sum_j D_{ij} = 0 .$$

Figure 8.1 shows the differences between the two matrices. These differences are crucial in our problem. We must describe the problem from a different point of view from vibrational or ferromagnetic cases.

$$\begin{array}{cc}
 \text{(a)} & \text{(b)} \\
 \left[\begin{array}{ccccccc} \ddots & \ddots & \ddots & & & & 0 \\ \ddots & \ddots & \ddots & \ddots & & & \\ -1 & z & -1 & -1 & & & \\ \ddots & -1 & z & -1 & \ddots & & \\ -1 & -1 & z & -1 & -1 & & \\ \ddots & \ddots & \ddots & \ddots & \ddots & & \\ 0 & \ddots & \ddots & \ddots & \ddots & & \end{array} \right] & \left[\begin{array}{ccccccc} \ddots & \ddots & \ddots & & & & 0 \\ \ddots & \ddots & \ddots & \ddots & & & \\ 1 & z & 1 & 1 & & & \\ \ddots & -1 & -z & -1 & \ddots & & \\ 1 & 1 & z & 1 & -1 & & \\ \ddots & \ddots & \ddots & \ddots & \ddots & & \\ 0 & \ddots & \ddots & \ddots & \ddots & & \end{array} \right]
 \end{array}$$

Fig. 8.1. Characteristics of the matrices $\{D_{ij}\}$ describing (a) ferromagnets and (b) antiferromagnets. The symbol z represents the coordination number

An asymmetric (as well as non-Hermitian) matrix has two different sets of eigenvectors called the right eigenvector $\mathbf{u}(\lambda)$ defined by

$$\omega_\lambda u_i(\lambda) = \sum_j D_{ij} u_j(\lambda) , \quad (8.11)$$

and the left eigenvector $\mathbf{v}(\lambda)$ given by

$$\omega_\lambda v_i(\lambda) = \sum_j v_j(\lambda) D_{ji}^* . \quad (8.12)$$

These eigenvectors belong to the same eigenvalue ω_λ of the matrix (8.10). Although the left (or right) eigenvectors do not form an orthogonal set themselves due to the asymmetry of the matrix $\{D_{ij}\}$, they do satisfy biorthogonality conditions [8.6]. These are written as

$$\sum_\lambda u_i(\lambda) v_j^*(\lambda) = \delta_{ij} , \quad (8.13)$$

and

$$\sum_i u_i(\lambda) v_i^*(\lambda') = \delta_{\lambda\lambda'} . \quad (8.14)$$

Note that $\mathbf{u}(\lambda)$ and $\mathbf{v}(\lambda)$ are linearly independent and form a complete set of vectors, although they do not form an orthogonal set.

8.2 Antiferromagnetic Spectral Dimension and the Upper Bound of \tilde{d}_{AF}

We consider spin-wave excitations on a diluted Heisenberg antiferromagnet with concentration p above p_c , where the correlation length $\xi(p) \propto |p - p_c|^\nu$ becomes

finite. The system can be regarded as homogeneous at length scales longer than ξ and we can expect conventional spin-wave excitations with wavelengths much larger than ξ (the hydrodynamic limit), which are characterized by a linear dispersion relation

$$\omega = c(p)k , \quad (8.15)$$

where k is the wavenumber and $c(p)$ is a concentration-dependent stiffness constant. Using the phenomenological expression for the hydrodynamic long-wavelength spin waves, it has been shown [8.7] that the stiffness constant $c(p)$ in the above is given by

$$c(p) = \gamma \left(\frac{2A}{\chi_{\perp}} \right)^{1/2} . \quad (8.16)$$

Here γ is the gyromagnetic ratio, χ_{\perp} is the transverse susceptibility, and A is defined as a measure of the energy needed to create a spatial variation in the staggered magnetization. The quantity A is proportional to the conductivity of the corresponding resistor network [8.8, 8.9]. The p dependence of χ_{\perp} takes the form

$$\chi_{\perp} \propto (p - p_c)^{-\tau} . \quad (8.17)$$

The exponent τ describes the critical behavior of the transverse susceptibility χ_{\perp} . The stiffness constant $c(p)$ in (8.16) therefore varies with the concentration p as

$$c(p) \propto (p - p_c)^{(\mu + \tau)/2} , \quad (8.18)$$

where μ is the conductivity exponent introduced in (5.4).

The dynamical scaling argument for spin waves in percolating antiferromagnets can be constructed with the aid of the above hydrodynamic descriptions. Since ξ is a unique length scale characterizing the system, the scaling form of the dispersion relation may be written

$$\omega = k^{z_{\text{AF}}} F(k\xi) , \quad (8.19)$$

where we call z_{AF} the dynamical exponent and $F(x)$ is a scaling function. In the hydrodynamic regime ($k\xi \ll 1$), the linear dispersion relation (8.15) should hold, and the scaling function $F(x)$ becomes proportional to $x^{1-z_{\text{AF}}}$ for $x \ll 1$. The dispersion relation (8.15) leads to

$$\omega \propto \xi^{1-z_{\text{AF}}} k . \quad (8.20)$$

With the help of (8.18) and the relation $\xi(p) \propto |p - p_c|^{-\nu}$, we obtain the relation

$$z_{\text{AF}} = 1 + \frac{\mu + \tau}{2\nu} . \quad (8.21)$$

At the opposite extreme, $k\xi \gg 1$, the dispersion relation should not depend on the correlation length ξ , and this leads to the form

$$\omega \propto k^{z_{\text{AF}}} . \quad (8.22)$$

Excitations obeying this dispersion relation are regarded as antiferromagnetic spin-wave fractons.

We can apply the same discussion as in Sect. 5.4 to (8.22). We find that the DOS of antiferromagnetic spin-wave fractons becomes

$$D(\omega) \propto \omega^{\tilde{d}_{\text{AF}}-1}, \quad (8.23)$$

where the exponent \tilde{d}_{AF} is given by [see (5.39)]

$$\tilde{d}_{\text{AF}} = \frac{D_f}{z_{\text{AF}}} = \frac{2\nu D_f}{2\nu + \mu + \tau}. \quad (8.24)$$

The exponent \tilde{d}_{AF} is the spectral dimension of antiferromagnetic fractons. Provided that τ is replaced by $-\beta$ in the above, the expression (8.24) for \tilde{d}_{AF} becomes the same as that for the spectral dimension of ferromagnetic fractons, i.e., \tilde{d}_s , as defined in (5.20). Since τ and β are positive, the following inequality holds for any Euclidean dimension d :

$$\tilde{d}_{\text{AF}} < \tilde{d}_s. \quad (8.25)$$

In the hydrodynamic regime, the linear dispersion relation (8.20) leads to the conventional spin-wave DOS described by

$$D(\omega) \propto (p - p_c)^{-d(\mu+\tau)/2} \omega^{d-1}. \quad (8.26)$$

The crossover frequency ω_c from extended or weakly localized spin waves to fractons is the frequency at which the wavenumber k is equal to $2\pi\xi^{-1}$, i.e., $\omega_c \approx c(p)\xi^{-1}$, so the concentration dependence of the crossover frequency ω_c is given by

$$\omega_c \propto (p - p_c)^{\nu+(\mu+\tau)/2} \propto (p - p_c)^{\nu D_f/\tilde{d}_{\text{AF}}}. \quad (8.27)$$

The lower bound of the susceptibility exponent τ for d -dimensional percolating antiferromagnets is given by [8.7]

$$\tau \geq \mu - \beta + (2 - d)\nu. \quad (8.28)$$

This inequality becomes an equality for $d \geq d_c$, where $d_c = 6$ is the upper critical dimension of percolating systems. Using (8.21), (8.24), and the inequality (8.28), the lower bound of the dynamical exponent z_{AF} and the upper bound of the spectral dimension \tilde{d}_{AF} are given by

$$z_{\text{AF}} \geq \frac{2\mu - \beta + (4 - d)\nu}{2\nu}, \quad (8.29)$$

and

$$\tilde{d}_{\text{AF}} \leq \frac{2(\nu d - \beta)}{2\mu - \beta + (4 - d)\nu}, \quad (8.30)$$

respectively. Here we have used (3.34). Taking into account the Alexander–Orbach conjecture $\tilde{d}_s \approx 4/3$, i.e., $\mu \approx [\nu(3d - 4) - \beta]/2$ [see (5.22)], the exponents τ , z_{AF} , and \tilde{d}_{AF} are bounded by

$$\tau \geq \frac{1}{2}(\nu d - 3\beta), \quad (8.31)$$

$$z_{\text{AF}} \geq D_f, \quad (8.32)$$

and

$$\tilde{d}_{\text{AF}} \leq 1. \quad (8.33)$$

The last inequality (8.33) is particularly interesting, since the upper bound does not depend on the Euclidean dimension d [8.10].

8.3 Numerical Simulations of Antiferromagnetic Fractons

In this section, we try to confirm the above theoretical predictions by numerical simulations. A powerful numerical method called the forced oscillator method [8.11] is applied to calculate the DOS of spin-wave fractons excited on percolating antiferromagnets. Bond-percolating (BP) spin systems are treated here, because the fractality of BP networks is relevant for length scales even shorter than those for site-percolating (SP) networks, as mentioned in Sect. 3.2.

Results for the DOS per spin of antiferromagnetic fractons in BP networks at p_c are shown in Fig. 8.2a. Filled squares represent the result for a 2D spin system which is formed on a 1100×1100 square lattice at $p_c = 0.5$ with periodic boundary conditions. The network contains 657 426 spins. The frequency resolutions of these data are high enough to be able to obtain a definite conclusion. The least-squares fitting for the lower frequency data gives $D(\omega) \propto \omega^{\tilde{d}_{\text{AF}}-1}$ with $\tilde{d}_{\text{AF}} = 0.99 \pm 0.04$. This power law holds even in the very low frequency regime because the correlation length reaches the system size $L (= 1100)$ at $p = p_c$. Above $\omega \approx 1$, the DOS does not follow this power-law dependence. This is due to the fact that the system is not fractal for length scales shorter than the wavelength of these modes with eigenfrequencies $\omega \approx 1$.

The DOS for 3D BP spin networks at $p_c = 0.249$ is also shown in Fig. 8.2a (filled triangles). For display purposes, these are shifted upward by an order of magnitude. The result shows the DOS averaged over three percolation realizations. These three networks are formed on $100 \times 100 \times 100$ simple cubic lattices with periodic boundary conditions. The calculated DOS at low frequencies exhibits constant behavior as a function of frequency, as in the case of the 2D BP network. The least-squares fitting gives $\tilde{d}_{\text{AF}} = 0.98 \pm 0.04$. The DOS for 4D BP networks at $p_c = 0.160$ is represented by filled circles in Fig. 8.2a. These are also shifted upward for display purposes, this time by two orders of magnitude. The BP networks of six realizations are formed on $28 \times 28 \times 28 \times 28$ hypercubic lattices. The result is obtained by averaging

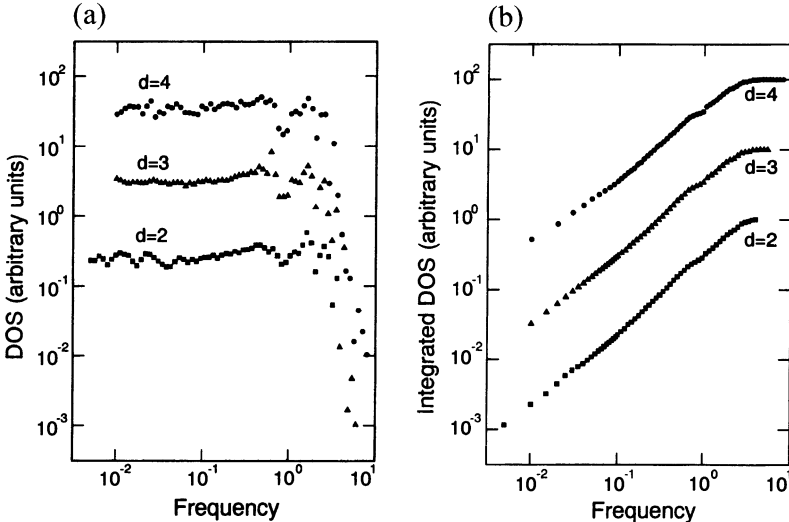


Fig. 8.2. (a) DOS per spin for 2D (squares), 3D (triangles), and 4D (circles) BP antiferromagnets at $p = p_c$. For graphical reasons, the triangles (3D) and the circles (4D) have been shifted upward. (b) Integrated DOSs corresponding to the DOSs shown in (a). Data for the 3D and 4D cases have again been shifted upward [8.10]

over the DOSs of these systems. From the DOS data, we see that the value of the antiferromagnetic spectral dimension is $\tilde{d}_{\text{AF}} = 0.98 \pm 0.04$ for 4D spin systems. The corresponding integrated DOSs are presented in Fig. 8.2b. These data bring out the power-law dependence of the antiferromagnetic fracton DOS more clearly.

These numerical results for the spectral dimensions \tilde{d}_{AF} suggest that, for any Euclidean dimensions, the values of \tilde{d}_{AF} are close to unity, the upper bound of the spectral dimension predicted by the scaling argument. We therefore expect the following relation for any Euclidean dimension d [8.10]:

$$\tilde{d}_{\text{AF}} = 1 . \quad (8.34)$$

This relation becomes rigorous above the upper critical dimension $d_c = 6$. The relation (8.34) for antiferromagnetic fractons corresponds to the Alexander–Orbach conjecture (5.21) for vibrational or ferromagnetic fractons.

Using (8.24) and numerically obtained values for \tilde{d}_{AF} , we can determine the values of the dynamical exponent z_{AF} as 1.91, 2.53, and 3.18 for 2D, 3D, and 4D percolating networks, respectively, where the known values of fractal dimensions $D_f = 91/48$ (2D), 2.48 (3D), and 3.12 (4D) are used. By using the known values of exponents ν and μ ($\nu = 4/3$, 0.88, and 0.68, and $\mu = 1.26$, 2.02, and 2.39 for $d = 2$, 3, and 4, respectively), the values of the susceptibility exponent τ are also obtained from (8.21) as $\tau = 1.18$ (2D), 0.67 (3D), and 0.58 (4D). We list the values of these exponents in Table 8.1.

Table 8.1. Various exponents describing antiferromagnetic fractons [8.10]

Exponents	$d = 2$	$d = 3$	$d = 4$
\tilde{d}_{AF}	0.99	0.98	0.98
z_{AF}	1.91	2.53	3.18
μ	1.26	2.02	2.39
τ	1.18	0.67	0.58

8.4 Scaling Theory of $S(q, \omega)$ for Percolating Antiferromagnets

We claim to begin with that spin-wave fractons can be characterized by a single frequency-dependent length scale $\Lambda(\omega)$, which scales as

$$\Lambda(\omega) \propto \omega^{-1/z_{\text{AF}}} , \quad (8.35)$$

where z_{AF} is the dynamical exponent defined by (8.21). The relation (8.35) corresponds to (7.12) for vibrational fractons. The above assumption implies that the single-length-scale postulate (SLSP) is relevant to antiferromagnetic fractons, as well as vibrational fractons (see Sect. 7.2). This is quite natural, because the SLSP is a general feature of all kinds of fracton excitation. The SLSP leads to a dynamic structure factor $S(q, \omega)$ for percolating antiferromagnets of the form

$$S(q, \omega) = q^{-y} F(q\Lambda) , \quad (8.36)$$

where $F(x)$ is a scaling function and y is a new exponent characterizing $S(q, \omega)$. It should be noted that the dynamic structure factor averaged over all possible realizations of percolating networks is described as a function of q ($= |\mathbf{q}|$) due to the spherical symmetry of the systems, similarly to the vibrational fracton case. The analytic expression for $S(q, \omega)$ in the hydrodynamic regime ($q\xi \ll 1$) is obtained for percolating antiferromagnets above p_c using a Green's function technique [8.12, 8.13]. This analysis suggests that $S(q, \omega)$ takes a Lorentzian form with respect to frequencies. It is reasonable to assume that the frequency dependence of $S(q, \omega)$ keeps the Lorentzian form even in the fracton regime ($q\xi \gg 1$). In this case, $S(q, \omega)$ is written as

$$S(q, \omega) = I(q) \frac{\Gamma(q)}{[\omega - \omega_p(q)]^2 + \Gamma^2(q)} , \quad (8.37)$$

where $\omega_p(q)$ is the frequency at which $S(q, \omega)$ takes its maximum value for fixed q , and $\Gamma(q)$ and $I(q)$ represent a width of the line and a q -dependent intensity, respectively. The SLSP requires both the peak frequency ω_p and the width Γ to have the same wavenumber dependence, i.e., $\omega_p(q) = \omega_0 q^{z_{\text{AF}}}$ and $\Gamma(q) = \Gamma_0 q^{z_{\text{AF}}}$, where z_{AF} is the dynamical exponent defined by (8.21). With the help of (8.35), the right-hand side of (8.37) is thus written in the form $I(q)G(q\Lambda)/q^{z_{\text{AF}}}$, where G is a function of $q\Lambda(\omega)$. The scaling function $F(q\Lambda)$ in (8.35) is then given by

$$F[q\Lambda(\omega)] = I(q) \frac{q^y G(q\Lambda)}{q^{z_{\text{AF}}}} . \quad (8.38)$$

Because the right-hand side of (8.37) should be a function of $q\Lambda(\omega)$, $I(q)$ is proportional to $q^{z_{\text{AF}}-y}$. We therefore obtain $S(q, \omega)$ in the form

$$S(q, \omega) = S_0 \frac{\Gamma_0 q^{2z_{\text{AF}}-y}}{(\omega - \omega_0 q^{z_{\text{AF}}})^2 + \Gamma_0^2 q^{2z_{\text{AF}}}} , \quad (8.39)$$

where S_0 is a numerical constant. Equation (8.39) predicts that $S(q, \omega)$ has asymptotic behavior

$$S(q, \omega) = \begin{cases} \omega^{-2} q^{-y+2z_{\text{AF}}} , & \text{for } q\Lambda(\omega) \ll 1 , \\ q^{-y} , & \text{for } q\Lambda(\omega) \gg 1 . \end{cases} \quad (8.40)$$

We should note that $S(q, \omega)$ does not depend on ω for large wavenumbers [$q\Lambda(\omega) \gg 1$].

8.5 Large-Scale Simulations for $S(q, \omega)$

Numerical calculations help us to confirm the above predictions for the asymptotic profiles of $S(q, \omega)$. To this end, we must treat large-scale percolating antiferromagnets. We first describe in brief an efficient numerical algorithm for calculating the dynamic structure factor [8.14]. The dynamic structure factor $S(q, \omega)$ is related to the generalized susceptibility $\chi(q, \omega)$ by

$$S(q, \omega) = \lim_{\delta \rightarrow +0} \text{Im} [\chi(q, \omega + i\delta)] . \quad (8.41)$$

The generalized susceptibility $\chi(q, \omega)$ is defined as the spatial Fourier transform of the two-point susceptibility $\chi_{ij}(\omega) = S_i^+(\omega)/h_j^+(\omega)$. The symbols $S_i^+(\omega)$ and $h_j^+(\omega)$ represent the temporal Fourier transform of $S_i^+(t)$ and the transverse field $h_j^+(t) = h_j^x(t) + i h_j^y(t)$, respectively. The equation of motion for spin deviations of the antiferromagnet under the staggered transverse field $\sigma_i h_i^+(t)$ is

$$i \frac{\partial S_i^+}{\partial t} = \sigma_i \sum_{j \neq i} J_{ij} (S_i^+ + S_j^+) - \sigma_i h_i^+(t) , \quad (8.42)$$

where σ_i is the quantity introduced below (8.4). The temporal Fourier transform of (8.42) is

$$\sum_j N_{ij}(\omega) S_j^+(\omega) = -h_i^+(\omega) , \quad (8.43)$$

where $N_{ij}(\omega)$ is defined by

$$N_{ij}(\omega) = \sigma_i(\omega\delta_{ij} - D_{ij}) , \quad (8.44)$$

and D_{ij} is given by (8.10). From (8.44) and the definition of the two-point susceptibility, $\chi_{ij}(\omega)$ can be expressed as $\chi_{ij}(\omega) = -[N(\omega)^{-1}]_{ij}$, where $N(\omega)^{-1}$ is the inverse matrix of the matrix $N(\omega)$. The generalized susceptibility $\chi(\mathbf{q}, \omega)$ is then given by

$$\chi(\mathbf{q}, \omega) = -\frac{1}{V} \sum_{ij} e^{i\mathbf{q} \cdot \mathbf{R}_i} [N(\omega)^{-1}]_{ij} e^{-i\mathbf{q} \cdot \mathbf{R}_j} , \quad (8.45)$$

where \mathbf{R}_i denotes the position vector of the spin i . Introducing a vector $\mathbf{v}'(\lambda)$ defined by

$$\sum_{\lambda} v'_i(\lambda) \sigma_j u_j(\lambda) = \delta_{ij} , \quad (8.46)$$

the summand of (8.45) can be expressed as

$$e^{i\mathbf{q} \cdot \mathbf{R}_i} [N(\omega)^{-1}]_{ij} e^{-i\mathbf{q} \cdot \mathbf{R}_j} = \sum_{k,\lambda} e^{i\mathbf{q} \cdot (\mathbf{R}_i - \mathbf{R}_k)} v'_k(\lambda) [N(\omega)^{-1}]_{ij} \sigma_j u_j(\lambda) . \quad (8.47)$$

Substituting this expression into (8.45), we should carry out the summation with respect to the suffix j , i.e., $\sum_j [N(\omega)^{-1}]_{ij} \sigma_j u_j(\lambda)$. This can be calculated as follows. From the definition of $N_{ij}(\omega)$ in (8.44) and (8.11), we have

$$\sum_j N_{ij}(\omega_{\lambda}) u_j(\lambda) = 0 , \quad (8.48)$$

and

$$N_{ij}(\omega) - N_{ij}(\omega_{\lambda}) = \sigma_i(\omega - \omega_{\lambda}) \delta_{ij} . \quad (8.49)$$

We thus obtain the relation

$$\sum_j N_{ij}(\omega) u_j(\lambda) = (\omega - \omega_{\lambda}) \sigma_i u_i(\lambda) . \quad (8.50)$$

This relation leads to

$$\sum_j [N(\omega)^{-1}]_{ij} \sigma_j u_j(\lambda) = \frac{u_i(\lambda)}{\omega - \omega_{\lambda}} . \quad (8.51)$$

With the help of (8.51) and (8.47), the generalized susceptibility $\chi(\mathbf{q}, \omega)$ (8.43) is expressed as

$$\chi(\mathbf{q}, \omega) = -\frac{1}{V} \sum_{\lambda} \frac{1}{\omega - \omega_{\lambda}} \left[\sum_i v'_i(\lambda) e^{-i\mathbf{q} \cdot \mathbf{R}_i} \right] \left[\sum_j u_j(\lambda) e^{i\mathbf{q} \cdot \mathbf{R}_j} \right] . \quad (8.52)$$

Using (8.41), the dynamic structure factor becomes

$$S(\mathbf{q}, \omega) = \frac{\pi}{V} \sum_{\lambda} \delta(\omega - \omega_{\lambda}) \left[\sum_i v'_i(\lambda) e^{-i\mathbf{q} \cdot \mathbf{R}_i} \right] \left[\sum_j u_j(\lambda) e^{i\mathbf{q} \cdot \mathbf{R}_j} \right]. \quad (8.53)$$

Here $u_i(\lambda)$ is the right eigenvector and $v'_j(\lambda)$ is the staggered left eigenvector defined by (8.46). These describe the transverse spin derivations under the linearized spin-wave approximation.

Figure 8.3 shows simulation results for $S(q, \omega)$ obtained by applying the forced oscillator method [8.11] to the above expression (8.53). The ω dependence of $S(q, \omega)$ for 2D BP antiferromagnets at $p = 0.58$ ($p_c = 0.5$) is shown in Fig. 8.3a. The wavevector \mathbf{q} in $S(\mathbf{q}, \omega)$ is chosen along the $[1, 0]$ direction from the magnetic zone center. The ensemble average is taken over six realizations of BP networks formed on 200×200 square lattices. The largest network has 37 449 spins. The correlation length of this system is $\xi \approx 29a$ (a is a lattice constant) and the crossover frequency ω_c is estimated to be $\omega_c \approx 0.12$ from the data corresponding to $q_c = 2\pi/\xi \approx 0.22$ ($a = 1$) in Fig. 8.3a. The calculated results for $S(q, \omega)$ for 3D BP antiferromagnets at $p = 0.32$ ($p_c = 0.249$) are shown in Fig. 8.3b. $S(q, \omega)$ is calculated for four different \mathbf{q} along the $[100]$ direction. The ensemble average is taken over two realizations of BP networks formed on $86 \times 86 \times 86$ cubic lattices under periodic boundary conditions. The largest network has 501 400 spins. The correlation length of this system is $\xi \approx 10a$ and the crossover energy ω_c is estimated to be $\omega_c \approx 0.12$. Figures 8.3a and b indicate that, for small wavenumbers ($q < q_c$), a sharp asymmetric peak exists at small energies with a tail extending towards higher energies. This indicates conventional spin waves (magnons). As q increases, peak widths increase rapidly and peak positions shift to higher energies beyond $\omega \approx \omega_c$.

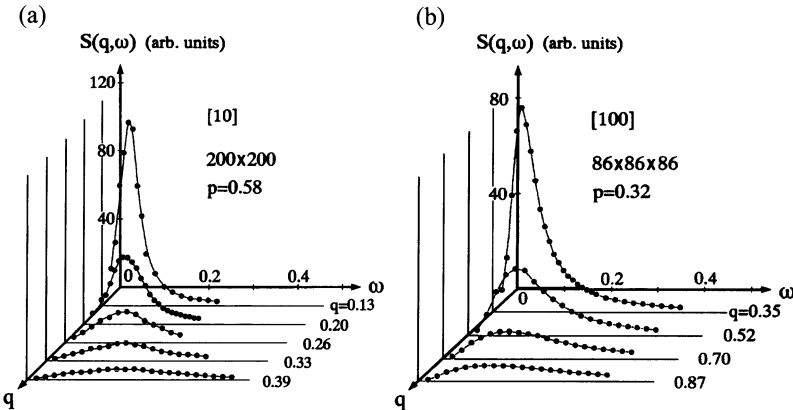


Fig. 8.3. (a) Frequency dependence of $S(q, \omega)$ for 2D percolating antiferromagnets at $p = 0.58$ formed on 200×200 square lattices. The results are obtained by averaging over six realizations of percolating antiferromagnets. (b) Frequency dependence of $S(q, \omega)$ for 3D BP antiferromagnets at $p=0.32$ formed on $86 \times 86 \times 86$ cubic lattices. The results are obtained by averaging over two realizations [8.15]

This corresponds to the crossover from magnons to antiferromagnetic fractons at $\omega \approx \omega_c$.

Figure 8.4 shows the validity of the single-length-scale postulate (SLSP) to $S(q, \omega)$ for percolating antiferromagnets. In this figure, the scaling function $F(q\Lambda) = q^y S(q, \omega)$ given in (8.35) is plotted as a function of $q\Lambda(\omega)$. The value of the exponent y is estimated from the q dependence of $S(q, \omega)$ for $q\Lambda(\omega) \gg 1$ [see (8.40)]. Filled circles represent the averaged value over data within a narrow range of scaling variables $q\Lambda(\omega)$. The vertical error bars indicate the standard deviation of data in this range. The universal curve in Fig. 8.4 shows that antiferromagnetic fractons satisfy the SLSP. The profile of the scaling function $F(q\Lambda)$ shown in Fig. 8.4 indicates that $S(q, \omega)$ behaves asymptotically as

$$S(q, \omega) \propto \omega^{-1.9 \pm 0.1} q^{0.5 \pm 0.1}, \quad \text{for } q\Lambda(\omega) \ll 1, \quad (8.54)$$

and

$$S(q, \omega) \propto q^{-2.8 \pm 0.1}, \quad \text{for } q\Lambda(\omega) \gg 1. \quad (8.55)$$

These results are consistent with (8.40) predicted by the scaling theory, if we choose $y = 2.8$ and $z_{AF} = 1.65$.

The spin-wave dynamics of the 3D diluted Heisenberg antiferromagnet RbMn_xMg_{1-x}F₃ has been studied in terms of inelastic neutron scattering (INS) experiments by Ikeda et al. [8.1, 8.2]. In the case $x = 0.39$, scattering intensities at several wavenumbers from $q = 0$ to $q = 0.375$ rlu (zone boundary) have been observed. This indicates that the peak intensity due to magnons decreases with increasing wavenumber q . The definite magnon peak diminishes beyond q_c , where $q_c (\approx 1/\xi)$ is the crossover wavenumber. Terao and Nakayama [8.16] have performed large-scale

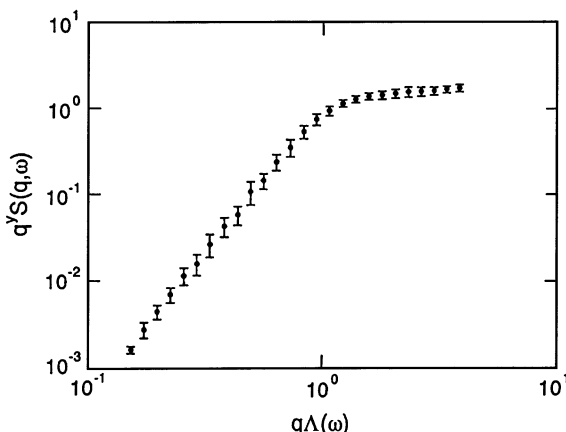


Fig. 8.4. Scaling function $F[q\Lambda(\omega)] = q^y S(q, \omega)$ as a function of $q\Lambda(\omega)$. Filled circles and vertical error bars represent averaged values of $F[q\Lambda(\omega)]$ and their standard deviations, respectively [8.17]

numerical simulations for the dynamic structure factor of spin-wave excitations in 3D diluted antiferromagnets $\text{RbMn}_{0.39}\text{Mg}_{0.61}\text{F}_3$. They have demonstrated that the sharp peak in $S(q, \omega)$ observed at $q < q_c$ (≈ 0.1 rlu) can be attributed to conventional spin waves and broad humps observed in the region $q > q_c$ to antiferromagnetic fracton excitations.

An important problem remains unsolved: why does \tilde{d}_{AF} become unity and what does this mean? This is quite crucial if we are to understand the physical meaning of the antiferromagnetic spectral dimension as a dynamical dimensionality. It seems that one-dimensional dynamics ($\tilde{d}_{\text{AF}} = 1$) is clearer than dynamics in non-integer dynamical dimensions such as those of vibrational fractons.

9. Anderson Transition

The concept of multifractals described in Chap. 4 dramatically improves our understanding of complex distributions of quantities in physical systems. The importance of multifractal analysis is ensured by the fact that an entire spectrum of exponents $\tau(q)$ or $f(\alpha)$ describes not only the profile of the distribution but also dynamical properties of the system. This is well demonstrated by the case of the Anderson transition. The Anderson transition is a disorder-induced metal–insulator transition in a non-interacting electron gas at zero temperature. The insulating phase is a consequence of the localization of electron wavefunctions, which is called Anderson localization. Anderson localization is caused by quantum interference of an electron wave scattered by disordered potentials. At the Anderson transition point, the squared amplitude of the electron wavefunction distributes in a multifractal manner. Critical properties of the Anderson transition are deeply related to the multifractality of critical wavefunctions. It is therefore important to study the multifractal nature of the Anderson transition. In this and the next chapter, we show that distributions of a critical wavefunction at the Anderson transition point and the energy spectrum are multifractal. Some exponents characterizing their multifractality are related to dynamical properties of electrons. This chapter aims to explain what the Anderson transition is, and thus serves as an introduction to the next chapter.

9.1 Coherent Transport of Electrons

Since electronic states are described by quantum mechanical wavefunctions, transport properties of electrons are subject to quantum interference. We know, however, that the conductivity is well approximated by the classical Drude formula, $\sigma = ne^2\tau/m^*$, which ignores quantum interference of the electron. Here n is the electron density, τ is a scattering time, and m^* is the effective mass of electrons. This is due to the fact that the phase memory of the electron is destroyed while traversing a sample. This is the dephasing effect. Dephasing is mainly due to inelastic scattering via electron–phonon and electron–electron interactions. This scattering randomizes electron phases and interference effects are cancelled out. As a consequence, quantum interference effects are negligible when the distance l_ϕ (the phase coherence length) between inelastic scatterings or other phase-randomizing events is much shorter than the system size L . The coherence length l_ϕ generally increases with decreasing temperature T . At several 10 mK, l_ϕ can be as long as or even

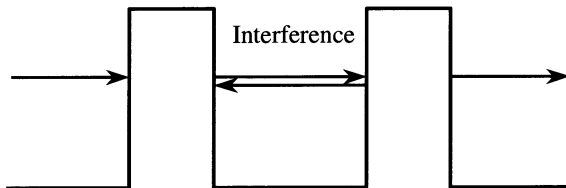


Fig. 9.1. Electron transport through a 1D system with double barriers. Electrons interfere in the well region between the two barriers

longer than several microns in typical metals. If the system size L is smaller than l_ϕ (mesoscopic systems), the effect of quantum interference becomes relevant.

Transport phenomena for coherent electrons are entirely different from classical (Drude) transport. Let us consider a 1D system with a double potential barrier (see Fig. 9.1). When treating the electron as a quantum mechanical wave, the system becomes equivalent to a Fabry-Pérot interferometer. If the electron wavelength is equal to $2d/n$, where d is the inter-barrier distance and n is a positive integer, the transmission probability becomes maximum (resonant tunneling). The conductance is thus maximized under this condition. This behavior is caused by quantum interference between forward and backward waves in the well region sandwiched between two barriers. Such quantum interference effects are also found in a Mach-Zender type electron interferometer. This is known as the Aharonov-Bohm effect [9.1, 9.2]. In a 1D Aharonov-Bohm ring (Fig. 9.2), a coherent electron incident from the left-hand side is separated into two parts at the point A and recombined at the point B. A magnetic flux through the ring tunes the phase of the electron wavefunction. Since the phase difference between two parts of the electron is $2\pi\Phi/\Phi_0$, where $\Phi_0 = hc/e$ is a flux quantum, the current governed by quantum interference is a function of the flux Φ threading the ring with a period Φ_0 .

In the above two examples of coherent transport, the elastic mean free path l_e is assumed to be large compared to the system size and electron propagation becomes ballistic. Although elastic scattering alters the electron phase, the phase shift is deterministic and the phase memory is maintained. As a result, transport phenomena peculiar to coherent electrons should be realized even for mesoscopic systems whose system sizes are much larger than l_e . In such cases, transport is called diffusive. It

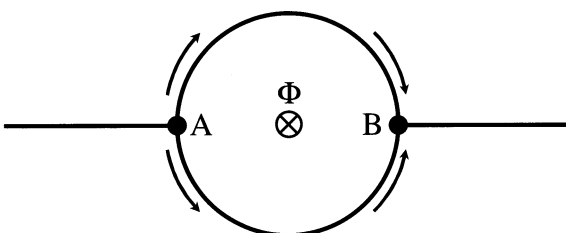


Fig. 9.2. A system exhibiting the Aharonov-Bohm effect. Partial waves of the electron traversing half the ring have different phases at the point B due to a flux Φ threading the ring

is known that coherent electrons in disordered systems could be spatially localized (Anderson localization). Anderson localization is of fundamental importance for understanding diffusive transport of coherent electrons in disordered systems.

9.2 Anderson Localization

Disorder-induced electron localization, i.e., Anderson localization, was first predicted by Anderson in 1958 [9.3]. In his pioneering paper, the continuity or discontinuity of the energy spectrum of electrons in a diagonally disordered system is related to their localization property. The coherent back-scattering effect proposed in [9.4–9.6] gives an intuitive interpretation of localization. Consider the return probability $P_0(t)$ of an electron starting from $\mathbf{r} = 0$ at $t = 0$ and returning to $\mathbf{r} = 0$ at $t = t$. The probability $P_0(t)$ is given by

$$P_0(t) = \left| \sum_{i \in S} A_i(t) \right|^2, \quad (9.1)$$

where $A_i(t)$ is the probability amplitude of the electron that propagates along the i th scattering path starting from $\mathbf{r} = 0$ and returning to this point after a number of scattering events (see Fig. 9.3).

The summation in (9.1) represents the sum over all possible scattering paths. The set of all scattering paths S can be separated into two complementary subsets, say S^+ and S^- . One is the set S^+ in which any two paths are different in shape, while the other subset (S^-) consists of time-reversals of paths in S^+ . The return probability becomes

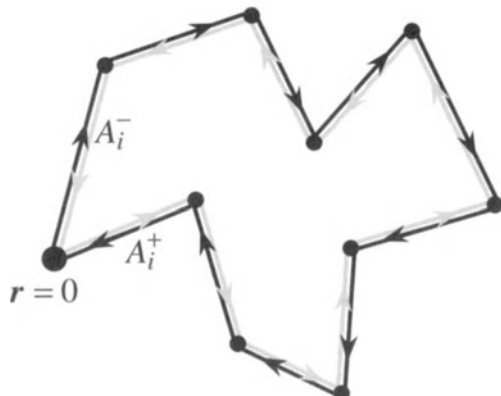


Fig. 9.3. Schematic illustration of coherent back-scattering in a disordered system. An electron starting from $\mathbf{r} = 0$ goes back to the origin with the amplitude A_i^+ after many random scatterings. The amplitude A_i^- of the electron tracing the inverse path (gray path) should also exist

$$\begin{aligned}
P_0(t) &= \left| \sum_{i \in S^+} A_i(t) + \sum_{i \in S^-} A_i(t) \right|^2 \\
&= \left| \sum_{i \in S^+} [A_i^+(t) + A_i^-(t)] \right|^2 \\
&= \sum_{i \in S^+} |A_i^+(t) + A_i^-(t)|^2 \\
&\quad + \sum_{i \neq j \in S^+} [A_i^+(t) + A_i^-(t)] [A_j^+(t) + A_j^-(t)]^* ,
\end{aligned} \tag{9.2}$$

where $A_i^+(t) = A_i(t)$ and $A_i^-(t)$ is the probability amplitude for the time-reversal of path i . In the diffusive transport regime, there exist a large number of different scattering paths whose probability amplitudes have uncorrelated phases. The second term of (9.2) (the interference term) vanishes due to cancellation between constructive and destructive interference. We thus have

$$P_0(t) = \sum_{i \in S^+} |A_i^+(t) + A_i^-(t)|^2 . \tag{9.3}$$

If the system has time-reversal symmetry, the probability amplitudes $A_i^+(t)$ and $A_i^-(t)$ are identical, i.e., $A_i^+(t) = A_i^-(t) = A_i(t)$. In this case, the return probability becomes

$$P_0(t) = 4 \sum_{i \in S^+} |A_i(t)|^2 . \tag{9.4}$$

In contrast, the classical return probability is obtained from (9.1) as $P_0(t) = \sum_{i \in S} |A_i(t)|^2 = 2 \sum_{i \in S^+} |A_i(t)|^2$, by ignoring interference. Therefore, the coherent (quantum mechanical) return probability is twice the classical probability. This result leads to a reduction in the diffusion constant due to constructive interference, which can be thought of as a precursor to localization.

The enhancement of the return probability is a consequence of quantum interference and the time-reversal symmetry of the system. The localization effect therefore strongly depends on symmetries of the system (the Hamiltonian). In the case where there is no time-reversal symmetry, as achieved by applying a magnetic field, constructive interference between A_i^+ and A_i^- is suppressed. Denoting the magnetic flux threading the closed scattering path i by Φ_i , the probability amplitude $A_i^+(t)$ has an additional phase induced by the magnetic flux Φ_i , viz.,

$$A_i^+(t) = A_i(t) \exp(2\pi i \Phi_i / \Phi_0) , \tag{9.5}$$

where Φ_0 is a flux quantum and $A_i(t)$ is the probability amplitude for the system without the magnetic field. Since $A_i^-(t)$ is the probability amplitude of the partial wave propagating along the path i in the opposite direction to that of $A_i^+(t)$, $A_i^-(t)$ is written as

$$A_i^-(t) = A_i(t) \exp(-2\pi i \Phi_i / \Phi_0) . \tag{9.6}$$

Therefore the return probability $P_0(t)$ given by (9.3) becomes

$$P_0(t) = 4 \sum_{i \in S^+} |A_i(t)|^2 \cos^2(2\pi\Phi_i/\Phi_0). \quad (9.7)$$

Comparing the above expression with $P_0(t)$ given by (9.4), it is found that the return probability is suppressed by the magnetic field. Provided that the magnetic field is very strong, the quantity $(\Phi_i/\Phi_0) - [\Phi_i/\Phi_0]$ takes a random variable within the range $[0, 1]$ with respect to i , where $[x]$ is the Gauss notation indicating the largest integer smaller than or equal to x . In this case, $\cos^2(2\pi\Phi_i/\Phi_0)$ can be approximated by its average value $\langle \cos^2(2\pi\Phi_i/\Phi_0) \rangle_i = 1/2$, and the return probability becomes equal to the classical value. The suppression of the return probability by a magnetic field [9.7, 9.8] has been confirmed experimentally through a negative magnetoresistance [9.9, 9.10].

We have not considered the spin degrees of freedom of electrons. All results obtained above hold for any directions of the spin. This means that the system has a spin-rotational symmetry. If the spin-rotational symmetry is broken, quantum interference of electrons provides for other transport properties. Spin-rotational symmetry is violated by spin-orbit interactions. Let us start again from (9.3), where $A_i^\pm(t)$ is described by a two-component spinor taking into account spin degrees of freedom. In the presence of a spin-orbit interaction, the final electron ($t = t$) after a number of scattering events along the path i may possess spin-up and spin-down components, even if the initial electron ($t = 0$) has no spin blend. The probability amplitude $A_i^+(t)$ is then written as

$$A_i^+(t) = \frac{1}{\sqrt{2}} \begin{pmatrix} A_{i\uparrow}(t) \\ A_{i\downarrow}(t) \end{pmatrix}, \quad (9.8)$$

where $A_{i\uparrow}$ and $A_{i\downarrow}$ represent amplitudes of spin-up and spin-down components, respectively.

The quantity $A_i^-(t)$ is the time-reversed probability amplitude of $A_i^+(t)$. The time-reversal operator T should reverse the sign of a spin and a momentum. The orbital momentum can be reversed by complex conjugation (denoted by K) of the orbital wavefunction. Reversing the spin direction is equivalent to rotating the spin state by π with respect to the polar angle. This operation is effected by $e^{-i\pi S_y/\hbar}$, where S_y is the spin operator in the y direction. The time reversal operator is thus represented by [9.11]

$$T = e^{-i\pi S_y/\hbar} K. \quad (9.9)$$

Using $e^{-i\pi S_y/\hbar} |\uparrow\rangle = |\downarrow\rangle$ and $e^{-i\pi S_y/\hbar} |\downarrow\rangle = -|\uparrow\rangle$, we find, for a general state $B_\uparrow |\uparrow\rangle + B_\downarrow |\downarrow\rangle$,

$$T(B_\uparrow |\uparrow\rangle + B_\downarrow |\downarrow\rangle) = B_\uparrow^* |\downarrow\rangle - B_\downarrow^* |\uparrow\rangle. \quad (9.10)$$

The probability amplitude $A_i^-(t) = TA_i^+(t)$ thus becomes

$$A_i^-(t) = \frac{1}{\sqrt{2}} \begin{pmatrix} -A_{i\downarrow}^*(t) \\ A_{i\uparrow}^*(t) \end{pmatrix}. \quad (9.11)$$

Substituting (9.8) and (9.11) into (9.3), we obtain

$$P_0(t) = \sum_{i \in S^+} \left(|A_{i\uparrow}(t)|^2 + |A_{i\downarrow}(t)|^2 \right) = \sum_{i \in S^+} |A_i(t)|^2. \quad (9.12)$$

Hence, $P_0(t)$ becomes equal to half of the classical return probability, which implies that destructive interference excludes diffusing electrons from the starting point. This produces a (weak) antilocalization of electrons [9.7, 9.12]. The antilocalization is a consequence of destructive quantum interference between partial waves propagating along a scattering path and its time-reversed path.

Quantum interference of coherent electrons in disordered systems reduces or enhances diffusion, which gives a precursor of (anti-)localization, i.e., weak (anti-)localization. The phenomenon whereby the amplitude of an electron wavefunction is restricted to a finite region of a system is called Anderson localization. Electrons are expected to be exponentially localized in strongly disordered systems (strong localization), although no microscopic theory can supply a satisfactory mechanism of strong localization taking into account the dimensionality and symmetry of the system. In spite of this lack of a microscopic theory, much work has accumulated on Anderson localization so far, through theoretical, computational, and experimental effort. Among these, the one-parameter scaling theory is of particular importance in understanding Anderson localization and the Anderson transition.

9.3 Scaling Theory of the Anderson Transition

Electrons in strongly disordered systems are expected to be spatially localized, as discussed in Sect. 9.2. Does electron localization occur no matter how weak the disorder is? The answer depends on the dimensionality. If electrons at the Fermi energy switch their states from extended to localized with varying strength of disorder, the system changes from a metal to an insulator. The metal-insulator transition induced by disorder is called the Anderson transition. The scaling theory [9.13, 9.14] gives a significant insight into properties of the Anderson transition and the relation between the transition and the dimensionality. It is assumed in the scaling theory that electrons are exponentially localized in sufficiently strongly disordered systems, without providing a localization mechanism. Since the conductance G is a suitable quantity for distinguishing localized states from extended ones, we consider the dimensionless conductance g of a sample to characterize the Anderson transition, i.e., $g = G/(2e^2/h)$. The conductance g is, in general, a function of the system size L and other external parameters such as the degree of disorder, the Fermi energy, the electron density, and the pressure. We denote the set of these external parameters by x .

The basic assumption of the scaling theory is that the conductance $g(bL, x)$ can be expressed by $g(L, x)$ and b alone, where $g(L, x)$ is the conductance of a sample of size L with external parameters x . This is the expression of the scaling hypothesis proposed by Abrahams et al. [9.13]. Before explaining the meaning of this hypothesis, we express it mathematically. A straightforward expression of the above hypothesis is

$$g(bl, x) = f[g(L, x), b] , \quad (9.13)$$

where f is an appropriate function. An alternative expression of (9.13) will help us to extract valuable information on the Anderson transition. Differentiating the logarithm of (9.13) with respect to $\log(bL)$, we have

$$\begin{aligned} \frac{d \log g(bL, x)}{d \log(bL)} &= \frac{d \log f[g(L, x), b]}{d \log(bL)} \\ &= \frac{d \log f[g(L, x), b]}{d \log(b)} \left(\frac{d \log(bL)}{d \log(b)} \right)^{-1} \\ &= \frac{d \log f[g(L, x), b]}{d \log(b)} . \end{aligned} \quad (9.14)$$

If b is unity, the right-hand side of (9.14) becomes a function of $g(L, x)$. The scaling hypothesis thus requires the function defined by

$$\beta(g) = \frac{d \log g(L, x)}{d \log L} \quad (9.15)$$

to be a function of g alone.

The physical meaning of the scaling hypothesis expressed by (9.13) or (9.15) may not be very clear. The following expression is more transparent with respect to its physical meaning: there is a unique characteristic length scale ξ in a system close to the Anderson transition. This length is obviously considered as a localization length in the localized regime. In the extended regime, ξ can be regarded as a correlation length of the wavefunction amplitudes. The length ξ is a function of the external parameters x . The above assumption requires that any quantity characterizing critical properties can be scaled by the single length ξ . The conductance $g(L, x)$ of a sample of size L is then

$$g(L, x) = f\left(\frac{L}{\xi}\right) , \quad (9.16)$$

where f is an appropriate function, not the same as f in (9.13), which is called a scaling function. From (9.16), we have

$$\beta = \frac{d \log g(L, x)}{d \log L} = \frac{d \log f(L/\xi)}{d \log(L/\xi)} = u\left(\frac{L}{\xi}\right) , \quad (9.17)$$

where u is a function of L/ξ . Since $L/\xi = f^{-1}(g)$ from (9.16), the β -function is a function of g alone. Therefore, we obtain (9.15) once again. The expression

(9.16) of the scaling hypothesis is more convenient for extending the idea of the scaling theory to other problems and understanding the (multi-)fractal nature of the Anderson transition [9.15]. In particular, the theory based on the assumption (9.16) including the single-length scale ξ is called the one-parameter scaling theory. Hereafter, ‘the scaling theory’ shall be taken to mean the one-parameter scaling theory, unless otherwise stated.

Let us consider the profile of the function $\beta(g)$ defined by (9.15). First we evaluate $\beta(g)$ in the localized regime, i.e., $g \rightarrow 0$. In this case, the electron wavefunction is exponentially localized as $\phi(r) \propto e^{-r/\xi}$ at $r \rightarrow \infty$, where $\phi(r)$ is the envelope wavefunction and ξ is the localization length. Since the conductance g proportional to $|\phi(L)\phi(0)|^2$ is written as $g = g_0 e^{-2L/\xi}$, the β -function behaves asymptotically as

$$\beta(g) = \log g - \log g_0 . \quad (9.18)$$

In the metallic phase, that is, the extended regime, the L dependence of the conductance depends on the dimensionality. Since the dc conductivity σ_{dc} of a metal is a constant for given system size, the conductance calculated from Ohm’s law is

$$g(L, x) = \frac{h}{2e^2} \sigma_{dc}(x) L^{d-2} , \quad (9.19)$$

where d is the Euclidean dimension of the system. Therefore, the β -function becomes

$$\beta(g) = d - 2 . \quad (9.20)$$

If we assume that $\beta(g)$ is monotonic and analytical, the profile of the function $\beta(g)$ can be presented schematically as shown in Fig. 9.4.

For $d \leq 2$, $\beta(g)$ is always negative. This means that the conductance g approaches zero regardless of the value of x when $L \rightarrow \infty$, because (9.15) leads to decreasing

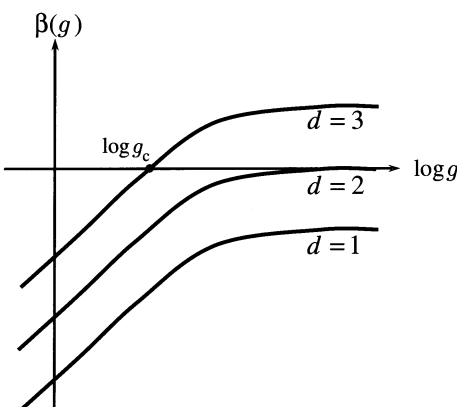


Fig. 9.4. Profiles of the β -functions for 1D, 2D, and 3D disordered systems. The β -function only cuts across the $\beta = 0$ line for 3D systems, implying that there exists a metal–insulator transition in 3D systems

g with increasing L . Therefore, we can conclude that electron wavefunctions are always localized in 1D and 2D systems, unless the system is a perfect conductor. In a 3D system, β can take either negative or positive values, i.e., $\beta < 0$ for $g < g_c$ and $\beta > 0$ for $g > g_c$. If the conductance $g(L, x)$ is smaller than g_c , $g(L, x)$ decreases with increasing L and becomes zero in the thermodynamic limit ($L \rightarrow \infty$). Conversely, if $g(L, x) > g_c$, the conductance diverges in the thermodynamic limit. At $g(L, x) = g_c$, the conductance does not depend on the system size. These facts imply that there exists a metal–insulator transition in 3D systems. Whether $g(L, x)$ is larger or smaller than the critical conductance g_c depends on x , not on L . If we choose x as a degree of disorder W , the system with $W > W_c$ is an insulator, while it is a metal for $W < W_c$, where the critical disorder W_c is given by $g(L, W_c) = g(W_c) = g_c$. Hereafter we choose the external parameters x so that the sample with $x > x_c$ or $x < x_c$ is an insulator or a metal, respectively.

It is obvious that the localization length diverges at the Anderson transition point. Since the localization length ξ is a function of external parameters x , the function $\xi(x)$ should diverge at $x = x_c$. Let us assume that $\xi(x)$ near x_c obeys a power law [9.16]:

$$\xi(x) \propto |x - x_c|^{-\nu}, \quad (9.21)$$

where ν is a positive exponent. The absolute value of $x - x_c$ in (9.21) comes from the assumption that the conductance $g(L, x)$ for finite L is analytic at $x = x_c$.¹

The localization length exponent ν is related to the profile of the β -function near the critical conductance g_c . From the scaling hypothesis (9.16) and the expression (9.21) for the correlation length, the conductance $g(L, x)$ can be written as

$$g(L, x) = f_1[L^{1/\nu}(x - x_c)], \quad (9.22)$$

where $f_1(z)$ is a scaling function. If x is close to x_c , $g(L, x)$ given by (9.22) can be expanded up to first order in $(x - x_c)$ as

$$g(L, x) = g_c + f'_1(0)L^{1/\nu}(x - x_c), \quad (9.23)$$

where $f'_1(z)$ is the first derivative of $f_1(z)$. Inserting (9.23) into the definition of the β -function (9.15), we have

$$\beta = \frac{f'_1(0)L^{1/\nu}(x - x_c)}{\nu[g_c + f'_1(0)L^{1/\nu}(x - x_c)]} \simeq \frac{1}{\nu g_c} f'_1(0)L^{1/\nu}(x - x_c). \quad (9.24)$$

On the other hand, since β is a function of g , expanding $\beta(g)$ around g_c , we obtain

$$\beta(g) = \beta'(g_c)(g - g_c), \quad (9.25)$$

¹ Let us assume $\xi = \xi_1(x - x_c)^{-\nu_1}$ and $\xi = \xi_2(x_c - x)^{-\nu_2}$ for $x > x_c$ and $x < x_c$, respectively. We expand the conductance $g(L, x)$ around $x = x_c$, i.e., $g(L, x) = \sum_{n=0}^{\infty} a_n(L)(x - x_c)^n$. If $g(L, x)$ is metallic, from (9.16), both the expansions of $f_1[L(x - x_c)^{\nu_1}/\xi_1]$ around $x = x_c + 0$ and $f_2[L(x_c - x)^{\nu_2}/\xi_2]$ around $x = x_c - 0$ should be considered. This gives $\nu_1 = \nu_2$.

where $\beta'(g)$ is the first derivative of $\beta(g)$ with respect to g . Here we have used $\beta(g_c) = 0$. Substituting (9.23) into (9.25), the β -function near $g = g_c$ (equivalently $x = x_c$) is given by

$$\beta = \beta'(g_c) f'_1(0) L^{1/\nu} (x - x_c) . \quad (9.26)$$

Comparing (9.24) with (9.26), we find the relation

$$\nu = \frac{1}{g_c \beta'(g_c)} = \frac{1}{\tilde{\beta}'(g_c)} , \quad (9.27)$$

where $\tilde{\beta}'(g)$ is the first derivative of β with respect to $\log g$.

The divergence of the correlation length affects the behavior of several physical quantities other than the conductance. Since the dc conductivity σ_{dc} is directly observed in experiments, it is worth clarifying the behavior of σ_{dc} near $x = x_c$. The conductivity of an infinite system is zero in the localized (insulating) regime and finite in the extended (metallic) regime. We thus examine the x -dependence of the conductivity in the metallic regime. In this regime, using (9.19), σ_{dc} can be expressed as

$$\sigma_{dc} = \frac{2e^2}{h} L^{2-d} g(L, x) .$$

The one-parameter scaling hypothesis (9.16) provides the expression

$$\sigma_{dc} = \frac{2e^2}{h} L^{2-d} f\left(\frac{L}{\xi}\right) . \quad (9.28)$$

Taking into account the fact that the conductivity does not depend on the system size in the metallic regime, the scaling function $f(z)$ should be proportional to z^{d-2} . The conductivity therefore behaves as

$$\sigma_{dc} \propto \xi^{2-d} \propto (x_c - x)^{\nu(d-2)} , \quad (9.29)$$

in the vicinity of x_c . Defining the exponent s by $\sigma_{dc} \propto (x_c - x)^s$, we find the relation

$$s = \nu(d-2) . \quad (9.30)$$

This relation is known as the Wegner scaling law [9.14].

Finally, we should emphasize that the scaling theory assumes that the β -function is monotonic. This assumption is not obvious. In fact, it is believed that the β -function of a system with strong spin-orbit interactions is not monotonic. For systems in which this assumption fails, some of the above results from the scaling theory are suspicious. In order to reveal critical properties of such systems, it is important to determine the precise profile of the β -function. Although the asymptotic behavior of the β -function can be evaluated analytically by perturbative treatment in the weak localization regime, the results lack quantitative reliability. Numerical investigations are the most powerful and reliable way to obtain quantitative information about the Anderson transition and check the validity of the scaling hypothesis.

9.4 Universality Classes

The one-parameter scaling theory of the Anderson transition is based on the hypothesis that properties of an electron system near the transition point are uniquely characterized by the correlation length. This means that specific lengths between scatterers are irrelevant to the behavior of physical quantities very close to the critical point. In other words, critical properties of the Anderson transition do not depend on specific realizations of the impurity distribution or the type of Bravais lattice of the host material. This prominent feature of the Anderson transition is called universality, after the terminology for thermal critical phenomena. We should note that critical exponents such as v and s are universal quantities because they characterize their renormalization properties, while critical external parameters x_c (such as the critical energy E_c and the critical disorder W_c) depend on details of systems. However, it is supposed that universal quantities vary when a global symmetry of the system is changed, because the mechanism of Anderson localization depends on such symmetries (time-reversal or spin-rotational symmetry), as explained in Sect. 9.2.

A set of systems with the same universal quantities is called a universality class. Although the scaling theory cannot distinguish universality classes because it does not take into account global symmetries of systems, it is believed, as described below, that there exist at least three universality classes in the Anderson transition. These universality classes correspond to the three different types of quantum interference noted in Sect. 9.2. Here we demonstrate that the Anderson transition is classified into three classes with qualitatively different properties.

Whether a quantum state is localized or extended is related to the energy spectrum of electrons. This is because mixing of quantum states affects the eigenenergies of electrons. Properties of the energy spectra are characterized by quantities such as the density of states or the rigidity of the spectrum. Here, we pay attention to energy spacings between adjacent levels. First, the level spacing of localized electrons is considered. We assume that the localization is so strong that mixing of wavefunctions localized at adjacent atoms can be ignored. In such a case, the matrix elements of the Hamiltonian in the Wannier basis are represented as $H_{ij} = \epsilon_i \delta_{ij}$, where i and j denote atomic positions corresponding to the Wannier functions and ϵ_i is the energy of the electron localized at the i th atom. We also assume that the ϵ_i s are uniformly distributed in a finite range. Since the eigenenergies of this Hamiltonian are the $\{\epsilon_i\}$ themselves, the distribution function of the level spacing Δ is the Poisson distribution:

$$P(s) = e^{-s}, \quad (9.31)$$

where $s = \Delta/\bar{\Delta}$ is the level spacing normalized by the mean level spacing $\bar{\Delta}$. The derivation of (9.31) is based on two assumptions:

- there is no overlap between electron wavefunctions localized at adjacent atoms,
- the distribution of $\{\epsilon_i\}$ is uniform.

Actually, (9.31) does not require the first assumption for an infinite system. We cannot ignore overlaps between weakly localized wavefunctions close to each other, which cause energy levels to be correlated. However, the probability that two states belonging to adjacent levels overlap is infinitesimal in the infinite system. Therefore, the level spacing distribution function is not affected by the strength of localization, and $P(s)$ should be given by (9.31), even for electron states with very long localization lengths. In the vicinity of the critical point, the second assumption also becomes irrelevant to (9.31). This is because universality guarantees that properties near the Anderson transition are not affected by details of the potential distribution. Therefore, we can conclude that the level-spacing distribution function of localized states is always the Poisson distribution, independently of both the on-site potential distribution and the global symmetries of the system.

If mixing between two states becomes crucial, adjacent energy levels cannot approach each other indefinitely. This is easily understood from the fact that a two-fold degenerate energy level is split by mixing of the two corresponding states. Since such mixing always occurs for extended states, the probability of proximal energy levels is small in the metallic phase. The nature of this level repulsion is deeply related to the symmetry of the Hamiltonian. The Hamiltonian matrix in the Wannier basis has nonzero off-diagonal matrix elements in this case. We can evaluate $P(s)$ in the metallic regime by assuming that the matrix elements H_{ij} ($i \leq j$) are statistically independent. Spectral properties of random (but Hermitian) matrices have been studied in detail by the random matrix theory [9.17–9.19]. This theory predicts that the level-spacing distribution $P(s)$ takes three functional forms according to three types of symmetry of the system. These are the cases in which:²

1. the system has time-reversal symmetry and spin-rotational symmetry,
2. the system does not have time-reversal symmetry,
3. the system has time-reversal symmetry but not spin-rotational symmetry.

Hamiltonian matrices for systems satisfying conditions (1), (2), and (3) are real symmetric, (complex) Hermitian, and self-dual³ Hermitian matrices, respectively. Since sets of random matrices with these three symmetries are invariant under real orthogonal, unitary, and symplectic transformations, respectively, these ensembles of random matrices are called the Gaussian orthogonal ensemble (GOE), the Gaussian unitary ensemble (GUE), and the Gaussian symplectic ensemble (GSE), respectively. The approximate distribution functions $P(s)$ given by the random matrix theory are

$$P(s) = \frac{\pi}{2} s e^{-\pi s^2/4}, \quad \text{for the GOE ,} \quad (9.32)$$

² In addition to these classes of disordered systems, there exist three classes for chiral symmetric systems and four classes for superconducting systems [9.19]. Among these ten classes, only the three classes discussed in this section are relevant to the conventional Anderson transition.

³ A matrix H is self-dual if $H = T^{-1} HT$, where T is the anti-unitary time-reversal operator defined by (9.9).

$$P(s) = \frac{32}{\pi^2} s^2 e^{-4s^2/\pi}, \quad \text{for the GUE ,} \quad (9.33)$$

and

$$P(s) = \left(\frac{8}{3\sqrt{\pi}} \right)^6 s^4 \exp \left(-\frac{64}{9\pi} s^2 \right), \quad \text{for the GSE ,} \quad (9.34)$$

which are derived in Appendix D. These distribution functions are called the Wigner distributions. For $s \ll 1$, these functions are proportional to s , s^2 , and s^4 for the GOE, the GUE, and the GSE, respectively. This implies that systems belonging to the GSE exhibit the strongest level-repulsion amongst the three classes. Profiles of the Wigner distribution functions are shown in Fig. 9.5 together with the Poisson distribution.

The Poisson distribution for the localized phase and the three kinds of Wigner distribution function for the extended phase have been confirmed numerically. Figure 9.6 shows an example of the level-spacing distribution functions calculated numerically for a 3D disordered electron system in a magnetic field.⁴ When the disorder is very strong, electronic states are localized and the level-spacing distribution function $P(s)$ is close to the Poisson distribution (9.31). On the contrary, for a weak disorder, $P(s)$ is well described by the Wigner distribution for the GUE [(9.33)].

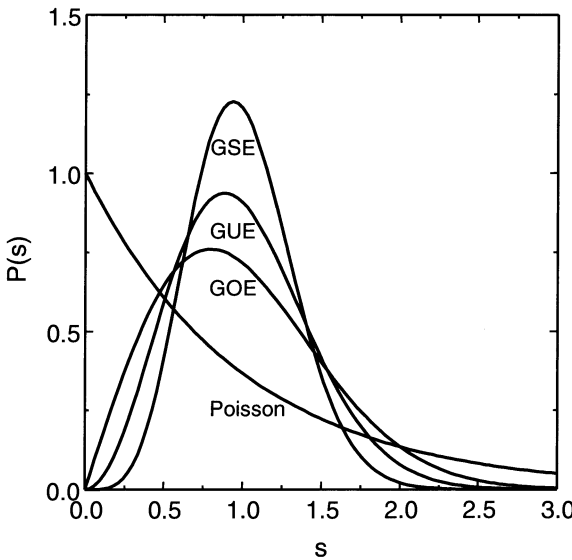


Fig. 9.5. Level-spacing distribution function $P(s)$. The quantity s denotes the rescaled level spacing ($s \equiv \Delta/\bar{\Delta}$). If wavefunctions are localized, $P(s)$ should follow the Poisson distribution. For extended states, $P(s)$ obeys the Wigner distribution function (GOE, GUE, or GSE depending on the symmetry of the Hamiltonian)

⁴ The system is described by a tight-binding Hamiltonian which will be discussed in Sect. 9.5.

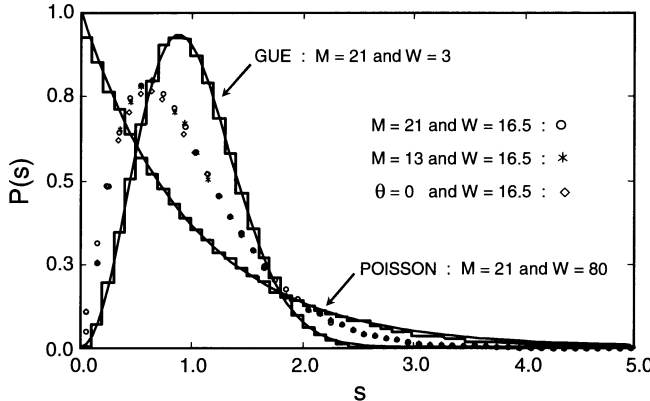


Fig. 9.6. Numerically calculated level-spacing distribution for a 3D electron system in a magnetic field (GUE). The system is described by a tight-binding Hamiltonian with size M^3 and strength of disorder W . The applied magnetic field is chosen so that the magnetic flux threading a plaquette is $0.05\Phi_0$, where Φ_0 is the flux quantum. The critical disorder W_c of this model is 16.5 in units of the hopping energy. The system is in the metallic (insulating) phase for $W = 3$ ($W = 80$). *Histograms* display numerical results, and *continuous lines* reflect the two expected limiting ensembles, viz., the GUE in the metallic regime and the Poisson ensemble in the insulating regime. Data points \circ and $*$ represent $P(s)$ near the critical disorder for $M = 21$ and $M = 13$, respectively. The symbol \diamond denotes the numerical result for the system at criticality in the absence of a magnetic field [9.21]

From the above arguments, there exist at least three types of extended phase whose level statistics are qualitatively different from each other. Localized states are also classified into three distinct families depending on their tendency towards localization, as discussed in Sect. 9.2, although $P(s)$ does not depend on ensembles. From these facts we expect there to be three universality classes in the Anderson transition depending on the symmetries of the system. This is now supported by a large number of numerical studies and field-theoretical arguments [9.20].

The scaling theory predicts that all states of 1D or 2D disordered electron systems are localized and that the Anderson transition (localization-delocalization transition) is manifested in 3D systems. Taking into account the symmetries of systems, it has been shown numerically and analytically that these results of the scaling theory should be modified as follows. In 1D systems, all electronic states are localized independently of the symmetries of systems. All states are also localized in 2D systems described by Hamiltonians belonging to the GOE and the GUE,⁵ while 2D systems with the symmetry of the GSE exhibit the Anderson transition. For 3D systems, the Anderson transition appears for any symmetry. These results are summarized in Table 9.1.

⁵ The fact that quantum states in 2D systems belonging to the GUE are all localized does not mean that all states in a disordered system subject to a uniform magnetic field are localized. This point will be discussed in Sect. 9.5.

Table 9.1. The relation between the Anderson transition and dimensionality. The symbol L means that all states are localized, whilst E signifies the existence of the Anderson transition

	GOE	GUE	GSE
1D	L	L	L
2D	L	L	E
3D	E	E	E

9.5 Numerical Studies

Despite the long history of the Anderson transition, which began as early as 1958, relatively little quantitative information has been obtained analytically. On the contrary, numerical investigations have played a crucial role in clarifying the nature of the Anderson transition. With the advent of modern computers, it has become possible to provide not only quantitative information but also qualitatively new insights into the transition. In this section, we will introduce an efficient numerical technique for obtaining definite information about critical properties.

We have not yet provided concrete examples of Hamiltonians, because many properties near the Anderson transition point do not depend on details of the Hamiltonian, due to universality. In numerical studies, however, a specific form of the Hamiltonian must be adopted. The universality of the Anderson transition suggests that even an analysis of the simplest model can reveal the general properties near the critical point. The most popular and well studied model with such simplicity is the tight-binding Hamiltonian,

$$H = \sum_i \epsilon_i |i\rangle\langle i| - \sum_{i,j} t_{ij} |i\rangle\langle j| , \quad (9.35)$$

where $|i\rangle$ is a basis representing a state localized at the i th site. The site energy ϵ_i corresponds to a random potential energy and t_{ij} represents the hopping energy. If the system has time-reversal symmetry and spin-rotational symmetry, that is, the Hamiltonian belongs to the Gaussian orthogonal ensemble (GOE), parameters ϵ_i and t_{ij} leading to the simplest Hamiltonian are realized by random quantities ϵ_i distributed uniformly in an interval between $-W/2$ and $W/2$, and t_{ij} is given by

$$t_{ij} = \begin{cases} t, & \text{if } i \text{ is the nearest neighbor of } j , \\ 0, & \text{otherwise ,} \end{cases} \quad (9.36)$$

respectively. The parameters W and t express the strengths of disorder and transfer. The Hamiltonian with these parameters is called the Anderson Hamiltonian [9.3]. If the time-reversal symmetry is broken, that is, the Hamiltonian belongs to the Gaussian unitary ensemble (GUE), the hopping matrix elements t_{ij} must be complex. Such a system can be realized by applying a magnetic field. In this case, the diagonal

elements ϵ_i are chosen in the same way as those for the GOE, and the hopping matrix elements are described by the Peierls phase [like (9.5) or (9.6)] as

$$t_{ij} = \begin{cases} t \exp\left(i\frac{2\pi}{\Phi_0}a_{ij}\right), & \text{if } i \text{ is the nearest neighbor of } j, \\ 0, & \text{otherwise,} \end{cases} \quad (9.37)$$

where $\Phi_0 (= hc/e)$ is the unit of flux quanta and a_{ij} is the line integral of a vector potential $\mathbf{A}(\mathbf{r})$ along the link (ij) . If a uniform magnetic field B in the z -direction is applied to a 2D square lattice or a 3D simple-cubic lattice, the quantity a_{ij} is given by

$$a_{ij} = \begin{cases} Ba^2x_i, & \text{if the link } (ij) \text{ is parallel to the } y\text{-direction,} \\ -Ba^2x_i, & \text{if the link } (ij) \text{ is antiparallel to the } y\text{-direction,} \\ 0, & \text{otherwise,} \end{cases} \quad (9.38)$$

where a is the lattice constant and x_i is the x coordinate of the i th site rescaled by a . Here we have chosen the Landau gauge $\mathbf{A} = (0, Bx, 0)$.

Systems belonging to the Gaussian symplectic ensemble (GSE) have time-reversal symmetry but not spin-rotational symmetry. The GSE systems are physically realized by introducing spin-orbit interactions. Several tight-binding models have been proposed for electrons in a system with spin-orbit interactions [9.22–9.24]. Since the spin degrees of freedom must be taken into account in this case, the basis $|i\rangle$ in the tight-binding Hamiltonian (9.35) should be replaced by $|i, \sigma\rangle$, where the index $\sigma = \uparrow$ or \downarrow denotes spin up or spin down. The tight-binding Hamiltonian is then written as

$$H = \sum_{i,\sigma} \epsilon_i |i, \sigma\rangle \langle i, \sigma| - \sum_{i,\sigma; j,\sigma'} t(i, \sigma; j, \sigma') |i, \sigma\rangle \langle j, \sigma'|, \quad (9.39)$$

where $t(i, \sigma; j, \sigma')$ represents hopping from the i th site with spin σ to the j th site with spin σ' . The hopping matrix elements t_{ij} are 2×2 matrices describing spin rotation due to the spin-orbit interaction on every link (ij) . Among several tight-binding models proposed so far (i.e., ways to choose the parameters ϵ_i and t_{ij}), the Ando model [9.22] has been the most extensively studied. In this model, the substrate lattice is assumed to have a square (2D) or a cubic (3D) symmetry. The on-site potentials ϵ_i are uniformly distributed in the range $[-W/2, W/2]$ as in the cases of the GOE and the GUE. The off-diagonal elements t_{ij} are chosen as

$$t_{ij} = \begin{cases} t \exp(-i\theta\sigma_k), & \text{if } i \text{ is the nearest neighbor of } j, \\ 0, & \text{otherwise,} \end{cases} \quad (9.40)$$

where σ_x, σ_y , and σ_z are the Pauli matrices, $k = x, y$, and z denotes the direction of the link (ij) . The quantity θ represents the strength of the spin-orbit interaction. For

$\theta = 0$, the orthogonal symmetry is recovered, as expected. The explicit 2×2 matrix forms of t_{ij} are

$$t_{ii_x} = t \begin{pmatrix} \cos \theta & -i \sin \theta \\ -i \sin \theta & \cos \theta \end{pmatrix}, \quad (9.41a)$$

$$t_{ii_y} = t \begin{pmatrix} \cos \theta & -\sin \theta \\ \sin \theta & \cos \theta \end{pmatrix}, \quad (9.41b)$$

$$t_{ii_z} = t \begin{pmatrix} e^{-i\theta} & 0 \\ 0 & e^{i\theta} \end{pmatrix}, \quad (9.41c)$$

where i_x , i_y , and i_z denote the nearest neighbors of the i th site in the x , y , and z directions, respectively.

Most of the numerical studies reported so far have studied critical properties of the Anderson transition in systems described by the above tight-binding Hamiltonians. The size of a system treated numerically is, of course, finite, while the correlation length ξ diverges at the transition point. This means that numerical results are always influenced by finite-size effects. We have to introduce some devices into numerical calculations to eliminate these effects. The finite-size scaling analysis is one of the most powerful techniques for extracting quantitative information about critical properties of infinite systems from numerical results for finite-size systems [9.25, 9.26].

In the finite-size scaling analysis, we deal with a quasi-1D system of width M and length L ($L \gg M$), which is described by the Hamiltonian (9.35) or (9.39). Since it is rigorously proven that all quantum states are exponentially localized in 1D disordered systems, electronic states can also be considered to be localized in the quasi-1D system when L is long enough. The localization length λ_M of the quasi-1D electron wavefunction can be calculated numerically.⁶ Although the length λ_M is generally a function of the width M and the external parameters x (the eigenenergy E , the strength of disorder W , the hopping energy t , the magnetic field B , and/or the strength of the spin-orbit interaction θ for tight-binding models), the scaling hypothesis explained in Sect. 9.3 requires λ_M to be written as⁷

$$\Lambda_M \equiv \frac{\lambda_M}{M} = f \left(\frac{M}{\xi} \right), \quad (9.42)$$

where ξ is the correlation length of the state in the infinite system with the same parameters x as those of the system giving λ_M . The x dependence of ξ is given by (9.21). Since the argument M/ξ of the scaling function becomes small near the

⁶ The localization length λ_M can be obtained from the Green's function computed recursively or the Lyapunov exponent of the transfer matrix. The value of λ_M calculated by such numerical procedures represents the decay length of the typical wavefunction in the quasi-1D system.

⁷ The general scaling form of λ_M is given by $\lambda_M = M^\alpha f(M/\xi)$, where α is an exponent. At criticality, λ_M should be proportional to M and the scaling function becomes a constant $f(0)$. This gives $\alpha = 1$.

transition point $x = x_c$, the scaling function can be expanded around $x = x_c$. This yields

$$\Lambda_M = \Lambda_c + a_1(x - x_c)M^{1/\nu} + a_2(x - x_c)^2M^{2/\nu} + \dots, \quad (9.43)$$

where the critical scaling amplitude Λ_c is Λ_M at $x = x_c$. Fitting the numerical data of Λ_M for various values of x and M to (9.43), we can obtain Λ_c , x_c , and ν (and also a_1, a_2, \dots). We should note that the coefficients a_1, a_2, \dots for $x > x_c$ are different from those for $x < x_c$ because ξ is a function of the absolute value of $x - x_c$. If the scaling hypothesis is valid, Λ_M as a function of $M|x - x_c|^\nu$ with the obtained x_c and ν falls into a single curve, as expressed by (9.42). The curve has two branches corresponding to $x > x_c$ (localized regime) and $x < x_c$ (extended regime). The branch for $x > x_c$ decreases monotonically with M/ξ , while the branch for $x < x_c$ increases, as illustrated in Fig. 9.7.

The idea of finite-size scaling is also applicable to quantities depending on M and x other than Λ_M . For example, the quantity defined by

$$\Gamma_M = \int_0^1 P_M(s) ds, \quad (9.44)$$

can also be scaled by ξ , where $P_M(s)$ is the level-spacing distribution function for a cubic (or square) system of size M . The integral interval does not need to be chosen as above. Since the distribution $P_M(s)$ is independent of M at the critical point, Γ_M scales

$$\Gamma_M = g\left(\frac{M}{\xi}\right), \quad (9.45)$$

where g is a scaling function. One can obtain x_c and ν by fitting the numerical data Γ_M to the expansion of the scaling function. The curve of the scaling function also has two branches, like Fig. 9.7, but the branches converge to fixed values as $M/\xi \rightarrow \infty$. These convergence values are 0.63212 for the localized branch and 0.54406 (GOE), 0.53305 (GUE), or 0.52373 (GSE) for the extended branch. The

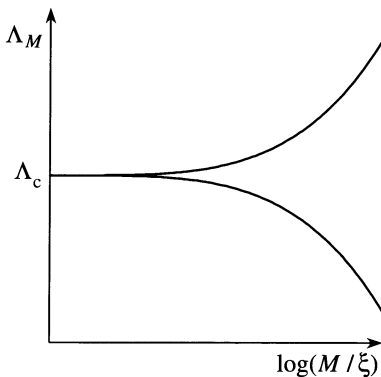


Fig. 9.7. Schematic profile of the scaling amplitude Λ_M as a function of M/ξ . The *upper* and *lower* curves represent the extended and localized branches of the scaling function, respectively. In the limit $M/\xi \rightarrow 0$, Λ_M converges to the critical value Λ_c .

fact that these values are close to each other implies that finite-size scaling analysis for Γ_M defined by (9.44) makes it difficult to obtain precise values for x_c and ν . We should choose an appropriate scaling variable with distinct branches of the scaling function for efficient numerical analysis [9.27].

As shown in Table 9.1, the Anderson transition appears in 2D disordered systems belonging to the GSE and in 3D systems. Extensive numerical studies have clarified the nature of these transitions quantitatively. Results are listed in Table 9.2. In this table, the quantity W_c is defined by the disorder strength above which all states are localized. Values of W_c are not universal and depend on a choice of parameters in the Hamiltonian. Although the localization length exponent ν and the critical scaling amplitude Λ_c should be universal, values of these quantities calculated numerically actually depend to some extent on details of the model. This is because the hypothesis of one-parameter scaling is slightly violated in actual numerical calculations. The scaling hypothesis insists that a system should be characterized only by ξ if the system is very close to the transition point and the system size is large enough. It is difficult in current numerical calculations to satisfy the latter condition adequately. As a consequence, results give apparent non-universal behavior of ν and Λ_c . To avoid this, a technique of scaling correction has been developed, which introduces another length scale into the scaling analysis (two-parameter scaling) [9.28]. Accurate studies of the universality of the Anderson transition based on the scaling correction procedure are now in progress [9.29].

The abbreviation QHS (quantum Hall systems) in Table 9.2 represents 2D disordered electron systems subject to uniform magnetic fields, which exhibit the quantum Hall effect. Since the time-reversal symmetry is violated in such systems, the QHS seems to belong to the GUE and to show no Anderson transition. However, it has been found by a field theoretical argument that the symmetry of the QHS is not the same as the GUE symmetry due to nonzero Hall conductivity. The field

Table 9.2. Numerically obtained values of the localization length exponent ν , the scaling amplitude Λ_c , and the critical disorder W_c (in units of the hopping energy t). Values in this table have been calculated for the following tight-binding systems. For the 2D GSE case, the strength of the spin-orbit interaction is chosen as $\theta = \pi/3$. The strength of the magnetic field for the 3D GUE is chosen so that the magnetic flux threading a lattice cell is $\Phi_0/3$. The value of θ for the 3D GSE is $\pi/6$. For each case, on-site potential energies ϵ_i are uniformly distributed in the range $[-W/2, W/2]$. QHS stands for the quantum Hall system described in the text

	Symmetry	ν	Λ_c	W_c
2D	QHS	2.35	1.19	—
	GSE	2.41	1.98	5.86
3D	GOE	1.57	0.58	16.54
	GUE	1.43	0.57	18.31
	GSE	1.3	0.56	19.0

theory and many numerical calculations have shown that all states are localized except for states at the centers of the Landau subbands, regardless of the disorder strength $W(\neq 0)$. This means that every subband center is at the critical energy and no extended regime exists in the system. The values of v and Λ_c presented in Table 9.2 are results for the lowest Landau band. Values of v for the second lowest Landau band reported so far range from 2.3 to 6.2 depending on the correlation length of disorder, which implies non-universality of the transition in higher Landau bands. However, this non-universality is now believed to be an artefact due to the violation of the one-parameter scaling hypothesis in actual numerical calculations. In fact, the scaling correction recovers the universal behavior of the delocalization transition in higher Landau bands of the QHS. We will discuss the universality of higher Landau bands in more detail in Sect. 10.5.

9.6 Dynamical Properties at the Anderson Transition

In conventional critical phenomena in thermal equilibrium systems, dynamical quantities behave critically with universal exponents at the critical point, just as static quantities do near the critical point. The Anderson transition is regarded as a quantum-critical phenomenon driven by quantum fluctuations rather than thermal ones. In this section, we describe the critical behavior of dynamical quantities in disordered electron systems.

9.6.1 Scaling Form of Dynamic Quantities at Criticality

The scaling hypothesis claims that a single length scale ξ characterizes the system close to the Anderson transition point. However, dynamical phenomena require additional length scales. One is the diffusion length L_{diff} of a wave packet during the time interval $1/\omega$. This length scale is represented by

$$L_{\text{diff}} \propto \sqrt{\frac{D}{\omega}}, \quad (9.46)$$

where D is a diffusion constant. The other length scale is L_Δ defined so that the energy $\hbar\omega$ coincides with the mean level spacing $\bar{\Delta}$ of a system of size L_Δ . Since $\bar{\Delta}$ is proportional to $1/\rho L_\Delta^d$, where ρ is the density of states,⁸ the length L_Δ is given by

$$L_\Delta \propto \frac{1}{(\rho \hbar \omega)^{1/d}}. \quad (9.47)$$

Since the dc conductivity σ_{dc} of a system of size L_{diff} at the transition point is expressed in terms of the dimensionless critical conductance g_c as

$$\sigma_{\text{dc}} = \frac{e^2}{h} g_c L_{\text{diff}}^{2-d}, \quad (9.48)$$

⁸ In this and the next chapter, we use the symbol ρ for the density of states, while the symbol D has been used in previous chapters, to distinguish the DOS from the diffusion constant.

equation (9.46) with $D = \sigma_{\text{dc}}/e^2\rho$ (the Einstein relation) is rewritten as

$$L_{\text{diff}} \propto \left(\frac{g_c}{\rho \hbar \omega} \right)^{1/d}. \quad (9.49)$$

We see from (9.47) and (9.49) that the length L_{diff} is proportional to L_Δ at the transition point. This implies that dynamics with frequency ω introduces a single length scale, say, L_ω . If L_ω is a unique characteristic length introduced by the dynamics even near the transition point, the dynamics can be scaled by two lengths, ξ and L_ω . Thus, an arbitrary dynamical quantity $K(q, \omega)$ characterized by a wavenumber q and a frequency ω should be scaled as

$$K(q, \omega) = \xi^\zeta h(q\xi, qL_\omega), \quad (9.50)$$

where ζ is an exponent and $h(z_1, z_2)$ is a two-variable scaling function.

From the general scaling form (9.50), we can extract crucial information about critical slowing down. We know in general that the internal dynamics of a system should slow down when approaching the critical point. A correlation time τ characterizing the dynamics of the system diverges as the correlation length ξ diverges. This is described by a power law, $\tau \propto \xi^z$, where z is called a dynamical exponent. The value of the dynamical exponent z for the Anderson transition can be drawn from (9.50). Equation (9.50) implies that any dynamical quantity of a disordered electron system not at, but near the critical point is governed by a characteristic frequency ω_c given by $L_{\omega_c} = \xi$. From (9.47) or (9.49), the frequency $\omega_c (= 2\pi/\tau)$ is proportional to ξ^{-d} , which gives $z = d$. The dynamical exponent z (vz to be precise) can be directly determined by experiment. In fact, the value of z for a 2D disordered system in the integer quantum Hall regime was obtained from the frequency dependence of the peak width of the dissipative ac conductivity $\sigma_{xx}(\omega)$ as a function of an applied magnetic field. Experiment suggests $z = 1$, contrary to the above simple prediction $z = d = 2$ [9.30]. The reason for this discrepancy has not yet been completely elucidated, although some explanations have been reported so far.

9.6.2 Diffusion of Wave Packets

One of the most fundamental form of dynamics is diffusion (see Appendix C) of a wave packet described by a probability density $P(r, t) = \langle |\varphi(r, t)|^2 \rangle_D$, where $\varphi(r, t)$ is the wavefunction of the wave packet starting at $r = 0$ and $\langle \dots \rangle_D$ represents the disorder average. If the system is in a metallic phase and $L_\omega (\propto \sqrt{t}) \gg \xi$, the probability density $P(r, t)$ is governed by a conventional diffusion equation,

$$\frac{\partial P(r, t)}{\partial t} - D \nabla^2 P(r, t) = \delta(t)\delta(r), \quad (9.51)$$

where D is a diffusion constant. From this equation, the Fourier transform of $P(r, t)$ is given by

$$P(q, \omega) = \frac{1}{-\text{i}\omega + Dq^2}, \quad (9.52)$$

while its inverse Fourier transform with respect to ω is

$$P(q, t) = \frac{1}{\pi} \int e^{-i\omega t} \frac{Dq^2}{\omega^2 + (Dq^2)^2} d\omega . \quad (9.53)$$

If $L_\omega \ll \xi$ or the system is in an insulating phase, these expressions no longer hold. It is, however, possible to express $P(q, \omega)$ [or $P(q, t)$] in a similar form to (9.52) [or (9.53)] by introducing a diffusion function $D(q, \omega)$ such that

$$P(q, \omega) = \frac{1}{-i\omega + D(q, \omega)q^2} , \quad (9.54)$$

and

$$P(q, t) = \frac{1}{\pi} \int e^{-i\omega t} \frac{D(q, \omega)q^2}{\omega^2 + [D(q, \omega)q^2]^2} d\omega . \quad (9.55)$$

Note that the diffusion function $D(q, \omega)$ should become the diffusion constant D for $L_\omega \gg \xi$ and $q\xi \ll 1$ if the system is metallic. The diffusion function $D(q, \omega)$ governs dynamical properties of the system instead of $P(r, t)$ via (9.54) [or (9.55)]. The quantity $D(q, \omega)$ should be scaled as (9.50), that is,

$$D(q, \omega) = \xi^\zeta h(q\xi, qL_\omega) . \quad (9.56)$$

This equation is valid for an infinite system. For a finite system at criticality, $D(q, \omega)$ can also be expressed by (9.56) with the system size L instead of ξ , i.e.,

$$D(q, \omega) = L^\zeta h(qL, qL_\omega) . \quad (9.57)$$

Since $L_\omega = L$ for $\omega = 0$, this equation gives $D(0, 0) \propto L^\zeta$. At the critical point, the dc conductivity $\sigma_{dc}(\propto D(0, 0))$ is proportional to L^{2-d} because $g = h\sigma_{dc}/(e^2 L^{2-d})$ does not depend on L at criticality. Therefore, $\zeta = 2 - d$ and (9.56) becomes

$$D(q, \omega) = \xi^{2-d} h(q\xi, qL_\omega) . \quad (9.58)$$

In particular, at the critical point, L_ω alone characterizes the dynamics, and this implies that $D(q, \omega)$ scales as

$$D(q, \omega) = q^{d-2} f(qL_\omega) , \quad (9.59)$$

where $f(qL_\omega) = \lim_{\xi \rightarrow \infty} (q\xi)^{2-d} h(q\xi, qL_\omega)$.

We investigate the critical behavior of several dynamical quantities at the Anderson transition point, based on the scaling form (9.59). To this end, the asymptotic behavior of $D(q, \omega)$ should be considered first. In the long-wavelength and/or high-frequency limit, i.e., $qL_\omega \rightarrow 0$, the diffusion function should be independent of q . This implies $f(z) \propto z^{2-d}$. Therefore, $D(q, \omega)$ becomes asymptotically

$$D(q, \omega) \propto \omega^{(d-2)/d} , \quad \text{for } qL_\omega \ll 1 , \quad (9.60)$$

where we have used the relation

$$L_\omega = \frac{1}{(\rho\hbar\omega)^{1/d}}. \quad (9.61)$$

Combined with the Einstein relation $\sigma \propto ne^2D$, (9.60) gives the ac conductivity $\sigma(\omega)$ at high frequencies ($\hbar\omega \gg \bar{\Delta}$) as

$$\sigma(\omega) \propto \omega^{(d-2)/d}, \quad (9.62)$$

as predicted by Wegner [9.14]. The validity of this relation has been demonstrated in terms of large-scale numerical simulations for 3D orthogonal [9.31], unitary, and symplectic systems [9.32], in which the exponent in (9.62) is determined by the finite-time scaling analysis for the forced oscillator method [9.33]. In the opposite limit $qL_\omega \gg 1$, $D(q, \omega)$ also follows a power law behavior. This requires the scaling function to take the form

$$f(z) \propto z^{-\eta}, \quad (9.63)$$

where η is a new exponent. This scaling function yields the diffusion function

$$D(q, \omega) \propto q^{d-2-\eta} \omega^{\eta/d}, \quad \text{for } qL_\omega \gg 1. \quad (9.64)$$

The relations (9.62) and (9.64) have been verified numerically for the quantum Hall transition by computing the dissipative conductivity $\sigma_{xx}(L, \omega)$ [9.34]. The value of η obtained from this is 0.36 ± 0.06 . We will see later that the critical behavior of most dynamical quantities is characterized by the exponent η .

Next we consider the probability density $P(r, t)$. Using (9.64), for $qL_\omega \gg 1$, the Fourier transform of $P(r, t)$ given by (9.55) yields

$$P(q, t) = \frac{1}{\pi} \int e^{-i\omega t} \frac{c\omega^{\eta/d} q^{d-\eta}}{\omega^2 + c^2 \omega^{2\eta/d} q^{2(d-\eta)}} d\omega, \quad (9.65)$$

where c is a constant.⁹ The ratio of the two terms in the denominator of the above integrand, $u \equiv c^2 \omega^{2\eta/d} q^{2(d-\eta)} / \omega^2$, is proportional to $(qL_\omega)^{2(d-\eta)}$, because $L_\omega \propto \omega^{-1/d}$. Since $d - \eta$ is always positive, as we shall see later, the ratio u is much larger than unity for $qL_\omega \gg 1$. This implies that the first term in the denominator of (9.65) can be neglected. This yields

$$P(q, t) \propto \int e^{-i\omega t} \omega^{-\eta/d} q^{\eta-d} d\omega. \quad (9.66)$$

Introducing a new variable s defined by

$$s \equiv (qL_\omega)^d = \frac{q^d}{\rho\hbar\omega}, \quad (9.67)$$

⁹ It should be remarked that (9.65) is valid only if the integral for $qL_\omega \ll 1$ gives a negligible contribution. As shown below, this condition is satisfied for $q^d t / \hbar\rho \gg 1$.

we can rewrite (9.66) as

$$P(q, t) \propto \int \exp\left(-i\frac{q^d t}{\hbar\rho s}\right) s^{\eta/d-2} ds. \quad (9.68)$$

The factor $\exp(-iq^d t/\hbar\rho s)$ is a rapidly oscillating function of s when $s \ll q^d t/\hbar\rho$. Thus, the integral of (9.68) over the range from 0 to $q^d t/\hbar\rho$ vanishes. Since the factor $s^{\eta/d-2}$ in the integrand is justified only for $qL_\omega \gg 1$, i.e., $s \gg 1$, the expression (9.68) is valid for $q^d t/\hbar\rho \gg 1$. In this case, we have

$$P(q, t) \propto q^{\eta-d} t^{\eta/d-1}, \quad \text{for } \frac{q^d t}{\hbar\rho} \gg 1. \quad (9.69)$$

The real-space probability density $P(r, t)$ is calculated from the inverse Fourier transform of $P(q, t)$:

$$P(r, t) = \frac{1}{(2\pi)^d} \int e^{-i\mathbf{q} \cdot \mathbf{r}} P(q, t) d^d q. \quad (9.70)$$

Using the asymptotic form of (9.69) and the isotropy of the system, (9.70) becomes

$$P(r, t) \propto r^{-\eta} t^{(\eta-d)/d} \int e^{-iy\cos\theta} y^{\eta-1} dy d\theta, \quad (9.71)$$

where $y = qr$ and θ is the angle between the vectors \mathbf{q} and \mathbf{r} . Since (9.69) is only valid for $q^d t/\hbar\rho \gg 1$, corresponding to $y \gg (\hbar\rho r^d/t)^{1/d}$, the expression (9.71) is appropriate for $t/\hbar\rho r^d \gg 1$. In such cases, the real-space probability density $P(r, t)$ has the asymptotic form

$$P(r, t) \propto r^{-\eta} t^{(\eta-d)/d}, \quad \text{for } \frac{t}{\hbar\rho r^d} \gg 1. \quad (9.72)$$

From (9.72), we can determine the t -dependence of the temporal autocorrelation function $C(t)$ defined by

$$C(t) = \frac{1}{t} \int_0^t P(r=1, t') dt', \quad (9.73)$$

where $P(r=1, t)$ is the return probability. From (9.72), the long-time behavior of $C(t)$ is given by

$$C(t) \propto t^{(\eta-d)/d}. \quad (9.74)$$

The temporal autocorrelation function is also characterized by the exponent η . The relation (9.74) is convenient for numerical computation of η , because the calculation of $C(t)$ is relatively simple and contains fewer statistical fluctuations. Values of η for several systems calculated in this way are listed in Table 9.3. The behavior of the temporal autocorrelation function for a 3D system is shown in Fig. 9.8.

Table 9.3. Values of the exponent η calculated numerically from the temporal autocorrelation function

	Symmetry	η
2D	QHS	0.38 ± 0.04
	GSE	0.32 ± 0.06
3D	GOE	1.5 ± 0.2
	GUE	1.3 ± 0.2
	GSE	1.4 ± 0.2

Using the asymptotic behavior (9.60) of the diffusion function for $qL_\omega \ll 1$, it seems that we have a similar expression to (9.68) for $P(q, t)$,¹⁰

$$P(q, t) \propto \int \exp\left(-i\frac{q^d t}{\hbar\rho s}\right) s^{(2-d)/d} ds , \quad (9.75)$$

for $q^d t / \hbar\rho \ll 1$. This is incorrect, however, because the factor $s^{(2-d)/d}$ in (9.75) is only valid for $s \ll 1$. We again concentrate on the integral over the range from $s \approx q^d t / \hbar\rho$ to infinity because of the rapidly oscillating factor $\exp(-iq^d t / \hbar\rho s)$. When s becomes larger than unity, the expression for $P(q, t)$ crosses over from

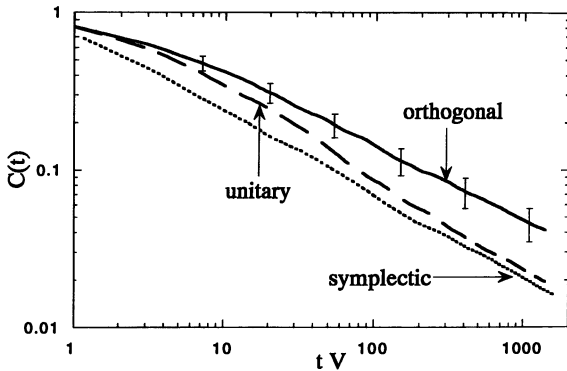


Fig. 9.8. Numerical results for the temporal autocorrelation functions for 3D disordered electron systems at criticality. Error bars around the data for the orthogonal case indicate the standard deviation with respect to 10 realizations of random potential configurations. Errors are almost the same for all universality classes [9.35]

¹⁰ For $qL_\omega \ll 1$, the first term of the integrand of (9.55) dominates the second term, which implies

$$P(q, t) \propto \int e^{-i\omega t} \omega^{-1-2/d} q^d d\omega .$$

(9.75) to (9.68). The lack of information on the crossover behavior of the diffusion function prevents us from calculating in this manner the asymptotic form of $P(q, t)$ for $q^d t / \hbar \rho \ll 1$ and also the short-time long-distance behavior of $P(r, t)$ (the shape of the diffusion front). However, the probability distribution in the tail regions has recently been estimated by approximately solving the generalized master equation describing $P(r, t)$ [9.36]. According to this estimate, the front shape of quantum diffusion at criticality behaves as

$$P(r, t) \propto \exp \left[- \left(\frac{r}{w(t)} \right)^\gamma \right], \quad (9.76)$$

where the width of diffusion $w(t)$ grows as

$$w(t) \propto t^{1/d}, \quad (9.77)$$

and the exponent γ is given by

$$\gamma = \frac{d}{d-1}. \quad (9.78)$$

Let us outline the derivations of (9.76)–(9.78). Since quantum coherence strongly influences the diffusive behavior of electrons, e.g., the enhancement of backward scattering in Anderson localization, the stochastic process of a coherent electron is not Markovian.¹¹ Hence, the probability distribution $P(r, t)$ does not obey the conventional master equation, but rather a generalized master equation of the form

$$\frac{\partial}{\partial t} P(r, t) = \int_0^t \sum_{\Delta r} g(\Delta r, t - t') \Delta P(\Delta r, r, t') dt', \quad (9.79)$$

where $\Delta P(\Delta r, r, t') = P(r + \Delta r, t') - P(r, t')$ and $g(\Delta r, t - t')$ is a memory function. The memory function $g(\Delta r, t - t')$ does not depend on r because of the translational symmetry of the system in a statistical sense. Approximating $\Delta P(\Delta r, r, t')$ up to $(\Delta r)^2$, (9.79) becomes

$$\frac{\partial P(r, t)}{\partial t} = \frac{1}{2} \int_0^t \sum_{\Delta r} g(\Delta r, t - t') \frac{\partial^2 P(r, t')}{\partial r^2} (\Delta r)^2 dt', \quad (9.80)$$

because the linear term of Δr goes to zero due to isotropy of the system. The Laplace transform of (9.80) is

$$s \tilde{P}(r, s) = \mathcal{L} \left[\frac{1}{2} \sum_{\Delta r} g(\Delta r, t) (\Delta r)^2 \right] \frac{\partial^2 \tilde{P}(r, s)}{\partial r^2}, \quad (9.81)$$

where $\tilde{P}(r, s) = \mathcal{L}[P(r, t)]$ denotes the Laplace transform of $P(r, t)$. The integrable solution of (9.81) is

¹¹ If a stochastic process does not depend on its history, the process is said to be Markovian.

$$\tilde{P}(r, s) = B(s)e^{-rf(s)}, \quad (9.82)$$

where

$$f(s) = \left\{ \frac{2s}{\mathcal{L} [\sum_{\Delta r} g(\Delta r, t)(\Delta r)^2]} \right\}^{1/2}, \quad (9.83)$$

and $B(s)$ is a normalization constant. It is natural to assume that the function $f(s)$ is proportional to s^β with a positive exponent β , because of anomalous diffusion at criticality. The probability density $P(r, t)$ is obtained from the inverse Laplace transform of $\tilde{P}(r, s)$,

$$P(r, t) = \frac{1}{2\pi i} \int_{\sigma-i\infty}^{\sigma+i\infty} B(s)e^{J(s)} ds, \quad (9.84)$$

where

$$J(s) = st - f_0 rs^\beta, \quad (9.85)$$

f_0 is a constant defined by $f(s) = f_0 s^\beta$, and σ is a real constant chosen so that all singular points of the integrand lie to the right of the vertical line $s = \sigma$. The integral in (9.84) can be evaluated using the stationary phase approximation. In this evaluation, the integral is approximated by a dominant contribution near $s = s_0$, where

$$s_0 = \left(\frac{t}{f_0 r \beta} \right)^{1/(\beta-1)}, \quad (9.86)$$

and we have

$$P(r, t) \propto e^{J(s_0)}, \quad (9.87)$$

where

$$J(s_0) = - \left[\frac{r}{w(t)} \right]^{1/(1-\beta)}, \quad (9.88)$$

and

$$w(t) = \frac{t^\beta}{f_0 \beta^\beta (1-\beta)^{1-\beta}}. \quad (9.89)$$

Here the quantity $w(t)$ is a diffusion length at time t . Since (9.49) implies that the diffusion length¹² at criticality is proportional to $t^{1/d}$, the exponent β should be $1/d$ for the Anderson transition. Equations (9.87)–(9.89) with $\beta = 1/d$ yield (9.76) with (9.77). The asymptotic form of the quantum diffusion front (9.76) has been confirmed for 3D orthogonal systems. As shown in Fig. 9.9, numerically calculated probability densities are well fitted by curves of (9.76) with $\gamma = 3/2$.

¹² Details of the diffusion length will be discussed later.

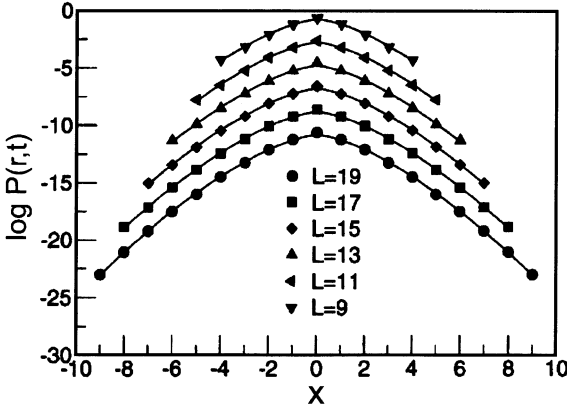


Fig. 9.9. Semi-log plot of the probability density $P(\mathbf{r}, t)$ with $\mathbf{r} = (x, 0, 0)$ and $t = 1$ (in units of \hbar/V , where V is the hopping energy) at the 3D Anderson transition point for different system sizes L^3 . Results for $L = 11, 13, 15, 17$, and 19 have been shifted by -2 for clarity. Curves fit results to (9.76) with $\gamma = 3/2$ [9.36]

9.6.3 Two-Particle Correlation Function

The two-particle correlation function $S(r, \omega)$ is a crucial quantity describing dynamical properties of the Anderson transition. This quantity is a natural extension of the dynamic structure factor $S(\mathbf{q}, \omega)$ for hydrodynamic fluctuations or atomic vibrations (see Chap. 7) to electron systems. The two-particle correlation function is defined as [9.37]

$$S(r, \omega) = \left\langle \sum_{\lambda, \lambda'} \delta(E - E_\lambda) \delta(E + \hbar\omega - E_{\lambda'}) \psi_\lambda(0) \psi_\lambda^*(\mathbf{r}) \psi_{\lambda'}(\mathbf{r}) \psi_{\lambda'}^*(0) \right\rangle_D , \quad (9.90)$$

where $\psi_\lambda(\mathbf{r})$ denotes the eigenfunction belonging to the eigenenergy E_λ , λ labels the eigenstate, and $\langle \dots \rangle_D$ denotes the disorder average. The inverse Fourier transform of $S(r, \omega)$ with respect to ω becomes

$$S(r, t) = \frac{1}{\hbar} \left\langle \sum_{\lambda, \lambda'} \delta(E - E_\lambda) e^{-i(E_{\lambda'} - E)t/\hbar} \psi_\lambda(0) \psi_\lambda^*(\mathbf{r}) \psi_{\lambda'}(\mathbf{r}) \psi_{\lambda'}^*(0) \right\rangle_D . \quad (9.91)$$

In (9.91), the variable E in the exponential function can be replaced by E_λ because of the factor $\delta(E - E_\lambda)$. This delta function is also replaced by the density of states $\rho(E)$. Then we have

$$S(r, t) = \frac{\rho}{\hbar} \left\langle \left| \sum_{\lambda} \psi_\lambda^*(0) \psi_\lambda(\mathbf{r}) e^{-iE_\lambda t/\hbar} \right|^2 \right\rangle_D = \frac{\rho}{\hbar} P(r, t) , \quad (9.92)$$

where $P(r, t)$ is the disorder average of the probability density of the state $\varphi(\mathbf{r}, t) = \sum_{\lambda} \psi_{\lambda}^*(0) \psi_{\lambda}(\mathbf{r}) e^{-iE_{\lambda}t/\hbar}$. Since the initial state

$$\varphi(\mathbf{r}, 0) = \sum_{\lambda} \psi_{\lambda}^*(0) \psi_{\lambda}(\mathbf{r})$$

is $\delta(\mathbf{r})$, $P(r, t)$ represents the diffusion probability. The Fourier transforms of $S(r, t)$, i.e., $S(r, \omega)$ and $S(q, \omega)$, are therefore given by the Fourier transforms of $P(r, t)$. From (9.55), we have

$$S(q, \omega) = \frac{\rho}{\pi \hbar} \frac{D(q, \omega) q^2}{\omega^2 + [D(q, \omega) q^2]^2}. \quad (9.93)$$

This relation and the asymptotic forms of the diffusion function [(9.60) and (9.64)] give the asymptotic profiles of $S(q, \omega)$ at the Anderson transition point. As seen in arguments below (9.65), the first (the second) term of the denominator of (9.93) dominates the second (the first) term for $qL_{\omega} \ll 1$ ($qL_{\omega} \gg 1$). We then have the relations

$$S(q, \omega) \propto q^2 \omega^{-1-2/d}, \quad \text{for } qL_{\omega} \ll 1, \quad (9.94)$$

and

$$S(q, \omega) \propto q^{\eta-d} \omega^{-\eta/d}, \quad \text{for } qL_{\omega} \gg 1. \quad (9.95)$$

The two-particle correlation function $S(r, \omega)$ for $r \ll L_{\omega}$ is calculated from $S(q, \omega)$ for $qL_{\omega} \gg 1$ given by (9.95), in a similar manner to the derivation of (9.72) from (9.65):

$$S(r, \omega) \propto r^{-\eta} \omega^{-\eta/d}, \quad \text{for } r \ll L_{\omega}. \quad (9.96)$$

The value of η can also be estimated from (9.95) or (9.96). Chalker and Daniell [9.37] calculated η for the quantum Hall transition (the lowest Landau level) by computing $S(q, \omega)$, and obtained $\eta = 0.38 \pm 0.04$. This value agrees well with η evaluated from the temporal autocorrelation function $C(t)$. The frequency dependence of $S(r, \omega)$ for $r \ll L_{\omega}$ is equivalent to the $|E - E'|$ dependence of the energy correlation function $Z(E, E') = \int |\psi_E(\mathbf{r})|^2 |\psi_{E'}(\mathbf{r})|^2 d\mathbf{r}$, where $\psi_E(\mathbf{r})$ is the wavefunction belonging to the eigenenergy E [9.38].¹³ The energy correlation function can be calculated much more easily than $S(r, \omega)$ itself, as defined by (9.90). Values of η evaluated in this way are $\eta = 1.5 \pm 0.3$ (3D orthogonal), 0.52 ± 0.1 (quantum Hall transition), and 0.35 ± 0.05 (2D symplectic). Figure 9.10 shows the $|E - E'|$ dependence of $Z(E, E')$ for 2D symplectic systems.

¹³ From the definition (9.90), we have

$$S(r=0, \omega) = \langle \sum_{\lambda \lambda'} \delta(E - E_{\lambda}) \delta(E + \hbar\omega - E_{\lambda'}) \psi_{\lambda}(0) \psi_{\lambda}^*(0) \psi_{\lambda'}(0) \psi_{\lambda'}^*(0) \rangle_D.$$

Assuming that the disorder average is equivalent to a spatial average for a fixed disorder configuration, $S(r=0, \omega)$ is proportional to $Z(E, E + \hbar\omega)$.

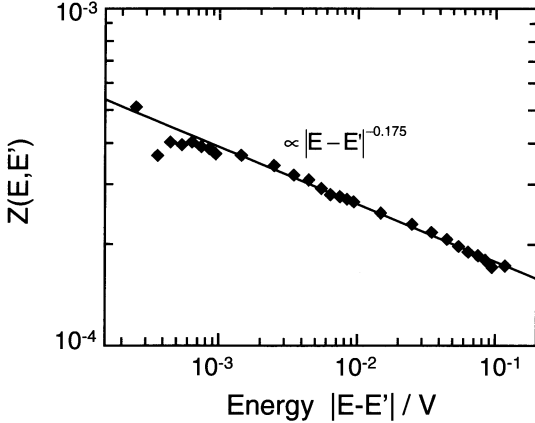


Fig. 9.10. Energy correlation function $Z(E, E')$ of the critical states of a 2D symplectic system described by the tight-binding Hamiltonian (9.39) with (9.41a) and (9.41b) ($t = 1$ and $\theta = \pi/6$). The system size is 150×150 . The power-law behavior $Z(E, E') \propto |E - E'|^{-0.175}$ gives $\eta = 0.35 \pm 0.05$ [9.38]

9.6.4 Diffusion Length

Finally, we address the time dependence of the mean-squared diffusion-length $\langle r^2(t) \rangle$ of quantum diffusion. For generality, we deal with the k th moment of the probability density $P(r, t)$ given by

$$\langle r^k(t) \rangle = \int r^k P(r, t) d^d r . \quad (9.97)$$

Although we know the asymptotic behavior of $P(r, t)$, as shown in Sect. 9.6.2, the above integral requires the whole profile of $P(r, t)$. It is, however, possible to calculate the time dependence of $\langle r^k(t) \rangle$ without knowing an accurate form of $P(r, t)$. Let us consider first the Fourier transform $P(q, t)$ given by (9.55). Using the scaling form of the diffusion function (9.59) and the relation (9.61), we can write

$$\begin{aligned} P(q, t) &= \frac{1}{\pi} \int e^{-i\omega t} \frac{q^d f_1(q^d/\omega)}{\omega^2 + [q^d f_1(q^d/\omega)]^2} d\omega \\ &= \frac{1}{\pi q^d} \int e^{-i\omega t} \frac{(q^d/\omega)^2 f_1(q^d/\omega)}{1 + [(q^d/\omega) f_1(q^d/\omega)]^2} d\omega , \end{aligned} \quad (9.98)$$

where the scaling function f_1 is $f_1(z) = f[(z/\hbar\rho)^{1/d}]$ and f is the scaling function in (9.59). The integrand is a function of q^d/ω , and we write this as $f_2(q^d/\omega)$. This provides

$$P(q, t) = \frac{1}{\pi q^d t} \int e^{-iy} f_2\left(\frac{q^d t}{y}\right) dy , \quad (9.99)$$

where $y = \omega t$. Since the above integral is a function of $q^d t$, $P(q, t)$ can be written as

$$P(q, t) = g(q^d t), \quad (9.100)$$

where $g(z)$ is a new scaling function. The probability density $P(r, t)$, that is, the inverse Fourier transform of $P(q, t)$, is calculated as

$$P(r, t) \propto \int q^{d-1} J(\Omega) e^{-iqr \cos \theta} g(q^d t) dq d\Omega, \quad (9.101)$$

where $d\Omega$ is the solid angle element, $q^{d-1} J(\Omega)$ is the Jacobian of the d -dimensional spherical coordinate, and θ is the angle between \mathbf{q} and \mathbf{r} . Replacing the variable q by $w = qr$, (9.101) becomes

$$P(r, t) \propto r^{-d} \int w^{d-1} J(\Omega) e^{-iw \cos \theta} g\left(\frac{tw^d}{r^d}\right) dw d\Omega. \quad (9.102)$$

The integral in (9.102) becomes a function of t/r^d . Denoting this by $h(t/r^d)$, we obtain

$$P(r, t) \propto r^{-d} h\left(\frac{t}{r^d}\right). \quad (9.103)$$

Substituting this scaling form into (9.97), we find

$$\langle r^k \rangle \propto t^{k/d}. \quad (9.104)$$

It should be noted that this expression for $\langle r^k \rangle$ can be obtained without using the asymptotic forms of $D(q, w)$. This means that the relation (9.104) is valid for any time scale.¹⁴ The relation (9.104) has been confirmed numerically for various systems exhibiting the Anderson transition [9.35]. Figure 9.11 shows the t dependence of $\langle r^k \rangle$ with $k = 2$ for 3D orthogonal, 3D unitary, and 3D symplectic systems. For all symmetries, $\langle r^2(t) \rangle$ is proportional to $t^{2/3}$ over a wide range of t . The moments $\langle r^k \rangle$ with $k = 2, 4, 6$, and 8 for the quantum Hall transition are also shown in Fig. 9.12 [9.39]. These results support the validity of (9.104).

We see that the exponent of the time dependence of the moment $\langle r^k \rangle$ does not depend on the exponent η . This is not surprising, because the length scale L_ω describing the diffusion length during the time interval $1/\omega$ is proportional to $\omega^{-1/d}$ at the critical point, as given by (9.61). In fact, (9.104) can also be derived directly from a scaling argument in terms of L_ω . The Fourier transform $\langle r^k(\omega) \rangle$ should be scaled as

$$\langle r^k(\omega) \rangle = \omega^{-\delta} f\left(\frac{L_\omega}{\xi}\right), \quad (9.105)$$

¹⁴ Of course, the time t should be large enough to ensure that $\langle r^k \rangle^{1/k}$ becomes much larger than the correlation length of disorder.

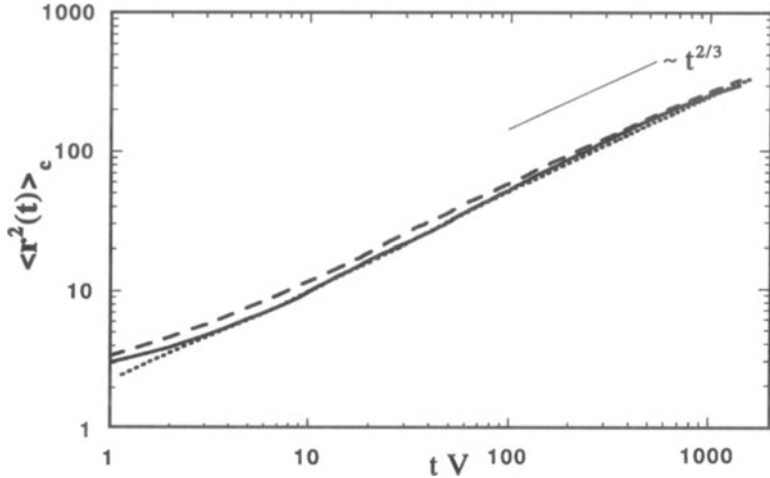


Fig. 9.11. Second moment $\langle r^2(t) \rangle$ of wave-packet diffusion in 3D disordered electron systems at the Anderson transition point. The *solid*, *dashed*, and *dotted curves* represent the results for the orthogonal, unitary, and symplectic cases, respectively. For any symmetry, the $t^{2/d}$ behavior is clearly visible across a wide t regime [9.35]

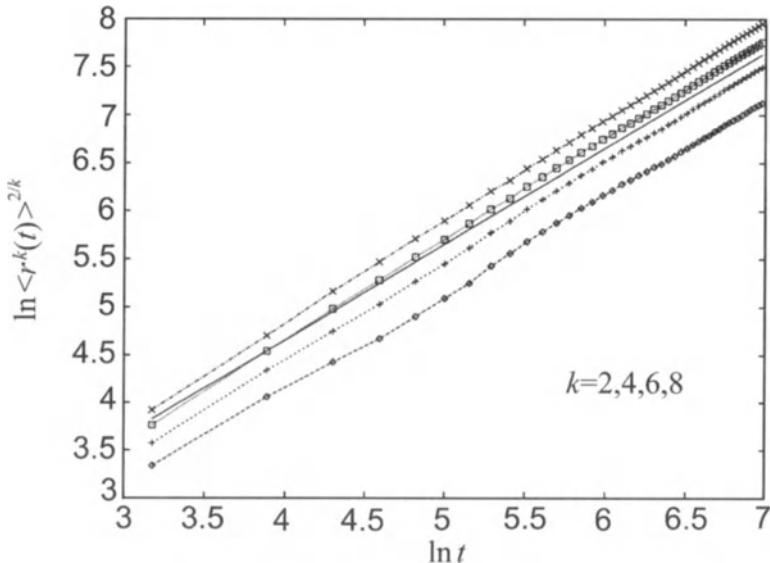


Fig. 9.12. The k th moment $\langle r^k(t) \rangle$ of wave-packet diffusion in a quantum Hall system. The system is described by the Chalker–Coddington network model [9.40] with 300×300 scatterers. The moments $k = 2, 4, 6$, and 8 are shown. The fact that all data are well fitted by straight lines with unit slope implies that the k th moment $\langle r^k(t) \rangle$ is proportional to $t^{k/d}$ [9.39]

where δ is an exponent and f a scaling function. Using the relations $L_\omega \propto \omega^{-1/d}$ and $\xi \propto |x - x_c|^{-\nu}$, the scaling form of the inverse Fourier transform $\langle r^k(t) \rangle$ of $\langle r^k(\omega) \rangle$ becomes

$$\langle r^k(t) \rangle = t^{\delta-1} g(t^{1/\nu d} |x - x_c|) . \quad (9.106)$$

In a metallic phase, $\langle r^k(t) \rangle$ should behave as

$$\langle r^k(t) \rangle \propto (Dt)^{k/2} . \quad (9.107)$$

Since the diffusion constant D is related to the dc conductivity σ_{dc} by the Einstein relation (5.3), D is proportional to $(x_c - x)^s$, where the exponent s is defined by $\sigma_{dc} \propto (x_c - x)^s$. The moment $\langle r^k(t) \rangle$ thus becomes

$$\langle r^k(t) \rangle \propto (x_c - x)^{sk/2} t^{k/2} . \quad (9.108)$$

Comparing this form to (9.106), the scaling function $g(z)$ should behave as $g(z) \propto z^{sk/2}$ for $z \gg 1$. In this case, $\langle r^k(t) \rangle$ expressed by (9.106) takes the form

$$\langle r^k(t) \rangle \propto (x_c - x)^{sk/2} t^{\delta-1+sk/2\nu d} . \quad (9.109)$$

From (9.108) and (9.109), the exponent δ is given by

$$\delta = \frac{k}{2} \left(1 - \frac{s}{\nu d} \right) + 1 . \quad (9.110)$$

The Wegner scaling law (9.30) yields

$$\delta = 1 + \frac{k}{d} . \quad (9.111)$$

Since (9.106) implies that $\langle r^k(t) \rangle$ is proportional to $t^{\delta-1}$ at $x = x_c$, we have again (9.104).

To summarize, most dynamical quantities at the critical point are characterized by the exponent η , besides the spatial dimension d . Of course, this does not mean that η is a special exponent describing critical dynamics. It should also be emphasized that a single exponent such as η is not sufficient to describe all dynamical quantities. For example, in order to characterize a three-particle correlation function, we need another exponent independent of η . In fact, an infinite number of exponents is required to describe all the dynamics at criticality. In the next chapter, we will show that the exponent η is related to the fractal nature of critical wavefunctions, which implies that all critical dynamics is governed by (multi-)fractality of wavefunctions at the critical point.

10. Multifractals in the Anderson Transition

In Chap. 9, we showed the partial similarity between the Anderson transition and the thermal or percolation transition. Critical properties near/at the thermal phase transition or the percolation transition are related to the fractality at the critical point. This is because the local order parameter of such a transition distributes in a fractal manner. It is natural to suppose that the fractality is relevant in the case of the Anderson transition as well. However, it is not easy to find an appropriate order parameter for the Anderson transition itself. What kinds of distribution are fractal at the Anderson transition? The answer is the squared amplitudes of the wavefunction at the transition point and the energy distribution of the spectral measure. These distributions are actually multifractal rather than conventional fractals. Although the multifractilities of the critical wavefunction and the spectral measure should generally be independent, they are closely related in the case of the Anderson transition. This is because the one-parameter scaling hypothesis holds for the Anderson transition.

In this chapter we provide detailed descriptions of the above statements. We also discuss how dynamical properties at the critical point are related to the multifractality of the critical wavefunction or the spectral measure. We showed in Chap. 9 that much of the critical dynamics can be characterized by the exponent η . It will become clear in this chapter that this exponent is related to one of infinitely many exponents describing the multifractality. We also demonstrate that the multifractal analysis is quite efficient in revealing the nature of the Anderson transition.

10.1 Multifractality of a Critical Wavefunction

The Anderson transition corresponds to a fixed point in a real-space renormalization transformation [10.1], which implies that the wavefunction at the Anderson transition (the critical wavefunction) is scale invariant. Motivated by this idea, Aoki [10.2] calculated critical wavefunctions in a quantum Hall system numerically for the first time, considering a 2D disordered electron system in a strong magnetic field. As mentioned in Sect. 9.5, all wavefunctions in this system are localized, except for Landau subband centers. The subband centers provide critical energies in the quantum Hall system. Contour plots of squared wavefunctions $|\psi|^2$ at the lowest subband center [10.2] are shown in Fig. 10.1.

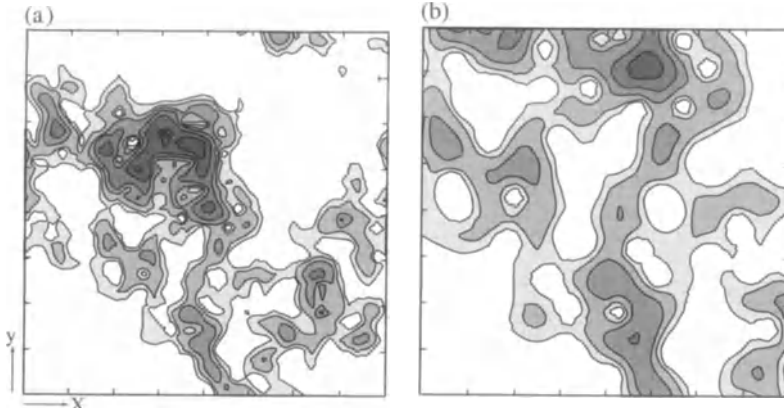


Fig. 10.1. Contour plot of a critical wavefunction in a quantum Hall system. (a) The whole profile of the wavefunction ($40l_B \times 40l_B$, where l_B is the magnetic length). (b) Part of the same wavefunction magnified by a factor of two in linear scale. The two figures are essentially indistinguishable [10.2]

These figures suggest that the distribution of $|\psi|^2$ possesses a fractal nature. In [10.2], the fractal dimension D_f of the critical wavefunction was calculated by counting the number of small boxes of size l covering the entire portion of $|\psi|^2$ with larger values than a certain height value A . The value obtained was $D_f = 1.57 \pm 0.03$. The fact that D_f is smaller than the Euclidean dimension ($d = 2$) proves the fractality of the critical wavefunction.

We should note that the fractal dimension calculated in this way depends on the value of the height A . If we choose A to be infinitesimally small, D_f must be 2 because wavefunctions are in general nowhere exactly zero in a 2D electron system. Moreover, the fractal dimension should become zero, if A is chosen to be the maximum value of $|\psi|^2$. These features allude to the multifractality of the critical wavefunction. The number of small boxes studied in [10.2] gives a rough estimate of the spatial extent of the wavefunction. A more appropriate quantity for evaluating the degree of localization is the inverse participation ratio defined by

$$P^{-1} = \frac{\sum_i |\psi_i|^4}{\left(\sum_i |\psi_i|^2\right)^2},$$

where ψ_i is the wavefunction amplitude at the i th site. The inverse participation ratio gives a measure of the number of sites contributing effectively to a given state. If the wavefunction is strongly localized, P^{-1} does not depend on the system size L , while P^{-1} is proportional to L^{-d} for a metallic state. Since the critical wavefunction has a filamentary self-similar structure, the inverse participation ratio is expected to behave as $P^{-1} \propto L^{-D_f}$, where D_f is less than the Euclidean dimension d [10.3]. The exponent D_f can be regarded as the fractal dimension of the critical wavefunction. In fact, there exists much numerical evidence for such a system-size dependence of P^{-1} [10.4].

Let us compare the definition of the inverse participation ratio to the q th moment $\langle \mu_l^q \rangle$ of measure μ_i given by (4.20). If we choose μ_i as $|\psi_i|^2$ and set l to unity, the second moment $\langle \mu_{l=1}^{q=2} \rangle$ is equivalent to P^{-1} . Therefore, the fractal dimension D_f is nothing but the mass exponent $\tau(2)$ or the correlation dimension D_2 . The fact that D_2 is different from the support dimension d implies that the generalized dimension D_q depends on q and the distribution of $|\psi_i|^2$ is multifractal at the critical point. Figure 10.2 illustrates intuitively the multifractality of a critical wavefunction, in which squared wavefunctions are shown for a 2D disordered system with strong spin-orbit interactions. As discussed in Chap. 9, systems with spin-orbit interactions belong

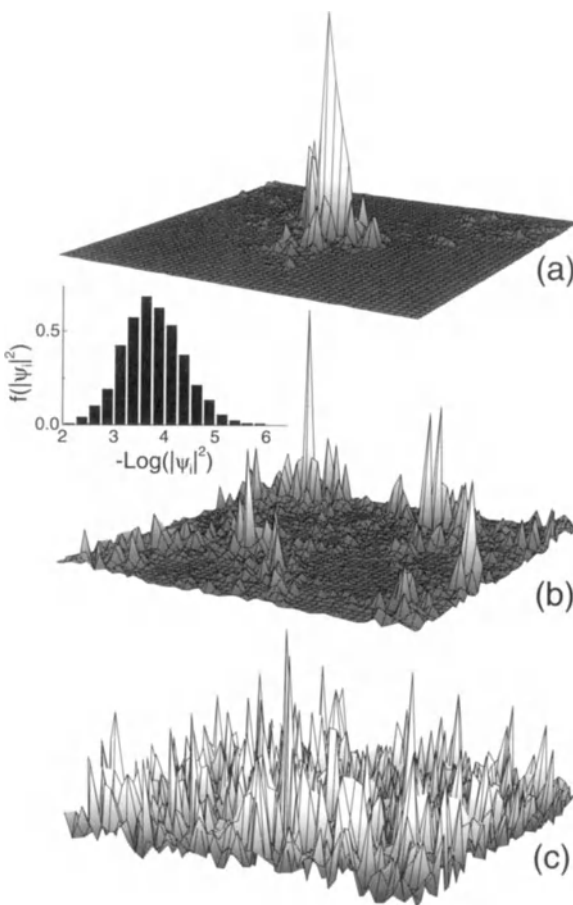


Fig. 10.2. Squared wavefunctions in a 2D disordered system with strong spin-orbit interactions (the symplectic system). The system is described by the tight-binding Hamiltonian (9.39) with (9.40), where θ is chosen to be $\pi/6$. (a), (b), and (c) represent the wavefunctions for $W > W_c$ (localized), $W = W_c$ (critical), and $W < W_c$ (extended), respectively, where $W_c = 5.86$ in units of the hopping energy. The *inset* shows the distribution function $|\psi_i|^2$ for the critical state (b)

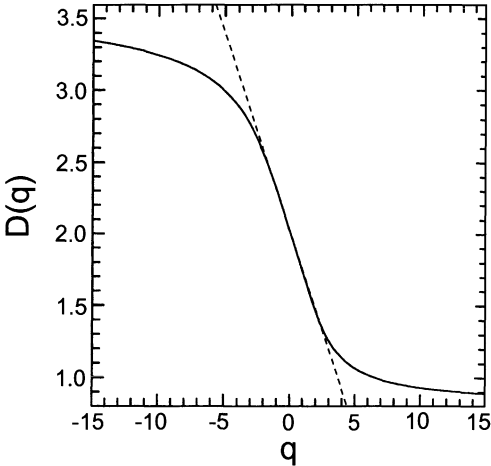


Fig. 10.3. Numerically calculated generalized dimension D_q for a critical wavefunction of a quantum Hall system. The dashed line gives the parabolic approximation (4.91) with $\alpha_0 = 2.28$ and $D_f = d = 2$ [10.5]

to the symplectic class and exhibit the Anderson transition even in 2D systems. The spatial distribution of the critical wavefunction (Fig. 10.2b) has typical multifractal features. As shown in the inset of Fig. 10.2, the distribution function of $|\psi_i|^2$ is quite broad (like a log-normal distribution), a prominent feature of multifractals.

In order to characterize the multifractality of critical wavefunctions quantitatively, the mass exponent $\tau(q)$, the generalized dimension D_q , the multifractal spectrum $f(\alpha)$, and the correlation exponent $z(q)$ have been calculated for Anderson transitions in various dimensions and symmetries. Figure 10.3 shows the generalized dimension D_q for a critical wavefunction at the lowest Landau level of a quantum Hall system [10.5].

The fact that D_q depends on q implies that the spatial distribution of the squared amplitude of the wavefunction has a multifractal character. From this figure, we find $D_2 = 1.43 \pm 0.03$. The precise value of D_2 has been estimated as $D_2 = 1.50 \pm 0.06$ for the lowest Landau band by a recent numerical calculation [10.6] in which considerably bigger systems were treated than those in Fig. 10.3. The multifractal spectrum $f(\alpha)$ can be calculated through the q -microscope, as explained in Sect. 4.5. Figure 10.4 shows the $f(\alpha)$ spectrum of the same eigenstate as in Fig. 10.3 [10.5].

The function $f(\alpha)$ takes its maximum value at $\alpha = \alpha_0 = 2.28$ with $f(\alpha_0) = 2$, because the fractal dimension of the support is the same as the Euclidean dimension of the system.¹ The curve of $f(\alpha)$ is tangent to the line $f(\alpha) = \alpha$ (thin solid line in Fig. 10.4) as expected. The dashed curve in Fig. 10.4 represents the parabolic approximation to $f(\alpha)$ with $\alpha_0 = 2.28$ and $D_f = d = 2$, given by (4.89). The

¹ A recent numerical study dealing with larger systems suggests $\alpha_0 = 2.31 \pm 0.02$ for the lowest Landau level [10.6].

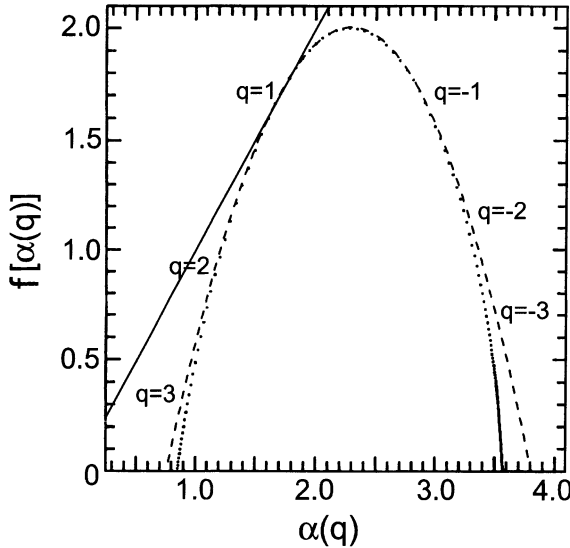


Fig. 10.4. Numerically calculated multifractal spectrum $f(\alpha)$ for the same wavefunction as in Fig. 10.3. The dashed curve gives the parabolic approximation (4.89) with $\alpha_0 = 2.28$ and $D_f = d = 2$ [10.5]

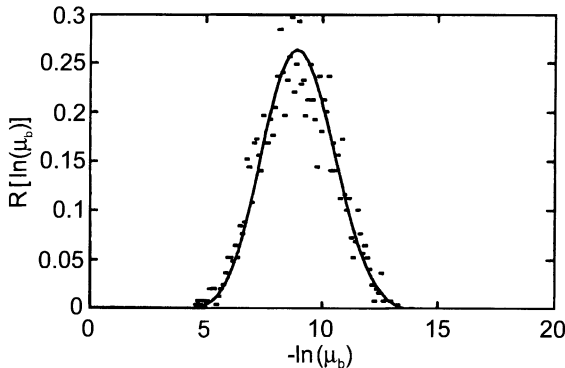


Fig. 10.5. Distribution function of squared amplitudes of a critical wavefunction in a quantum Hall system. μ_b denotes the box measure $\int_{b(2l_B)} |\psi(\mathbf{r})|^2 d\mathbf{r}$, where $b(2l_B)$ represents a box of size $2l_B$ and l_B is the magnetic length. The solid curve is the log-normal distribution obtained from the parabolic approximation (4.97) with $\alpha_0 = 2.28$ and $D_f = d = 2$ [10.7]

generalized dimension D_q calculated from the parabolic approximation [see (4.91)] is also represented by a dashed line in Fig. 10.3. We see from these figures that the parabolic approximation gives a good description of $f(\alpha)$ near $\alpha = \alpha_0$ and D_q near $q = 0$. It is shown in Fig. 10.5 that the distribution function of squared amplitudes of the critical wavefunction in the quantum Hall system is quite broad, as we have already shown for the 2D symplectic system (inset of Fig. 10.2).

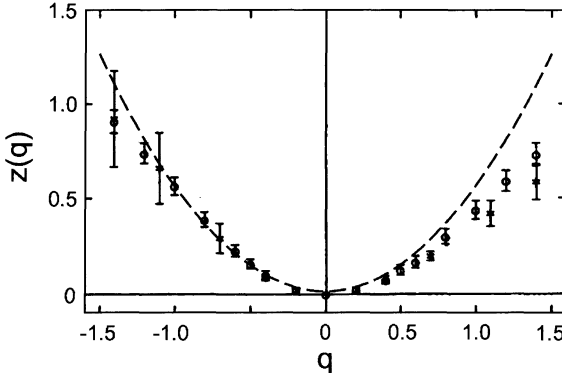


Fig. 10.6. Correlation exponent $z(q)$ for critical wavefunctions (averaged over 100 realizations) of quantum Hall systems. Data calculated from the definition of $z(q)$ [(4.52) and (4.53)] are represented by the symbol $*$, while data estimated by the scaling relation (4.62) are shown by \circ . The *dashed curve* represents the parabolic approximation of $z(q)$ given by (4.92) with $\alpha_0 = 2.28$ and $D_f = d = 2$ [10.7]

The solid curve in Fig. 10.5 represents the log-normal distribution obtained from the parabolic approximation with $\alpha = 2.28$ [see (4.97)]. For critical states in the quantum Hall system, the correlation exponent $z(q)$ has also been calculated. In Fig. 10.6, the average of $z(q)$ data over 100 critical states is shown by asterisks.

The dashed curve represents the parabolic approximation to $z(q)$ expressed by (4.92) with $\alpha = 2.28$. Circles plotted in Fig. 10.6 show the data of $d + 2\tau(q) - \tau(2q)$, which should be equal to $z(q)$ by the scaling relation (4.62). The collapse of asterisks and circles into a single curve provides numerical evidence for the validity of this scaling relation. Table 10.1 lists numerically calculated values of D_2 and α_0 for several types of Anderson transition. Values of D_2 are insensitive both to the dimensionality and the symmetry of systems, while α_0 is sensitive to the dimensionality. We note that multifractal properties of critical wavefunctions have been most extensively studied for quantum Hall systems, because the 2D Anderson transition is numerically tractable, in contrast to systems of higher dimensions, and the critical energies can be precisely determined (at least in a continuum model with a strong magnetic field).

Although we have only shown numerical results concerning the multifractal properties of critical wavefunctions, analytical estimates of $\tau(q)$ or $f(\alpha)$ have been reported so far. These include perturbative renormalization group treatments on replicated [10.3, 10.8] and supersymmetric [10.9, 10.10] nonlinear sigma models. These theories demonstrate sufficient evidence for multifractality at the critical point. However, they do not provide the full spectrum of multifractal exponents. There exists a class of models for which multifractal exponents of critical wavefunctions can be exactly calculated, namely, 2D non-interacting Dirac fermions subject to a random magnetic field. The Dirac fermion model was first introduced in connection with the integer quantum Hall effect [10.11] and has been shown to be deeply

Table 10.1. Numerically obtained values of D_2 and α_0 for critical wavefunctions in several systems exhibiting Anderson transitions

	Symmetry	D_2	α_0
2D	QHS	1.50	2.31
	GSE	1.66	2.19
3D	GOE	1.52	4.1
	GUE	1.49	4.1

related to other intriguing systems [10.12, 10.13]. The multifractality of the critical wavefunction of a Dirac fermion in a random magnetic field can be obtained by reducing the problem to computation of thermodynamic functions in a model with random potentials [10.14]. The Dirac fermion model is, however, a quite exceptional case. Numerical studies are still crucial and represent the most powerful approach to revealing the multifractality of critical wavefunctions of many other systems.

10.2 Multifractality of Spectral Measures

We showed in Sect. 10.1 that the spatial distribution of a wavefunction at the Anderson transition point exhibits multifractal properties. Another class of systems with multifractal wavefunctions involves quasi-periodic systems [10.15] or the Harper model describing Bloch electrons in a magnetic field within the framework of Peierls substitution [10.16]. In these systems, multifractal properties are found not only in the spatial profile of the wavefunction, but also in the spectral density of states [10.17–10.19]. In the case of the Anderson transition, the global density of states is smooth near the transition point and shows no multifractal properties. However, the energy distribution of $\rho(0, E)$ becomes multifractal, where $\rho(0, E)$ is the value of the local density of states defined by

$$\rho(\mathbf{r}, E) = \sum_{\lambda} \delta(E - E_{\lambda}) |\psi_{\lambda}(\mathbf{r})|^2 , \quad (10.1)$$

at $\mathbf{r} = 0$. Here $\psi_{\lambda}(\mathbf{r})$ is the eigenfunction belonging to the eigenenergy E_{λ} . According to the general definition (4.21) of multifractal distributions, the multifractality of the spectral measure $\rho(0, E)$ is represented by

$$\langle \rho_{\epsilon}^q \rangle \equiv \sum_b \left(\sum_{E \in b(\epsilon)} \rho(0, E) \right)^q \propto \epsilon^{\tilde{\tau}(q)} , \quad \text{for } \epsilon \rightarrow 0 , \quad (10.2)$$

where $b(\epsilon)$ is the energy interval of width ϵ near the critical energy E_c . The summations $\sum_{E \in b(\epsilon)}$ and \sum_b represent the sums over energies in the interval $b(\epsilon)$ and over such intervals. The wavefunction $\psi_E(0)$ belonging to the energy E at the spatial position $\mathbf{r} = 0$ is normalized by $\sum_E |\psi_E(0)|^2 = 1$ [10.20]. The definition of the mass

exponent $\tilde{\tau}(q)$ of the spectral measure given by (10.2) is just the spectral version of the general definition of $\tau(q)$ given by (4.21). The multifractality of $\rho(0, E)$ is due to the multifractal correlation of the critical wavefunction.

We show here that the distribution of the spectral measure is multifractal, i.e., the moment of the spectral measure has a power-law dependence of ϵ as shown by (10.2), and the mass exponent $\tilde{\tau}(q)$ (or \tilde{D}_q , the generalized dimension of the spectral measure) is simply related to $\tau(q)$ (or D_q) describing the multifractality of the spatial profile of the critical wavefunction at the transition point. Generalizing the spectral moment $\langle \rho_\epsilon^q \rangle$, we start with the moment defined by

$$\langle \rho^q(l, \epsilon) \rangle = \sum_b^{N_l} \sum_{j=1}^{N_\epsilon} \left(\int_{b(l)} \int_{E_j}^{E_j + \epsilon} \rho(\mathbf{r}, E) dE d\mathbf{r} \right)^q, \quad (10.3)$$

where $\rho(\mathbf{r}, E)$ is defined by (10.1) and $\int_{b(l)} d\mathbf{r}$ represents the integral over spatial positions in a small box $b(l)$ of size l . The energy E_j in (10.3) is given by

$$E_j = \left(E_c - \frac{E_s}{2} \right) + (j-1)\epsilon, \quad (10.4)$$

where E_s is chosen so that the correlation length ξ at $E = E_c - E_s/2$ is larger than the system size L and the energy interval $|E_c - E| \leq E_s/2$ includes a constant number of eigenenergies (N_E) independently of the system size. The number of boxes N_l is $(L/l)^d$ and the number of small energy intervals N_ϵ is E_s/ϵ . The condition for the multifractal spectral measure (10.2) is written as

$$\langle \rho^q(l, \epsilon) \rangle \propto \epsilon^{\tilde{\tau}(q)}, \quad (10.5)$$

where the spectral mass exponent $\tilde{\tau}(q)$ is a nonlinear function of q .

First, we consider the case $\epsilon \ll \Delta$, where Δ is the mean level spacing of the system. There exists at most one eigenvalue in the j th energy interval $[E_j, E_j + \epsilon]$. Therefore, (10.3) yields

$$\langle \rho^q(l, \epsilon) \rangle = \sum_\lambda^{N_E} \sum_b^{N_l} \left(\int_{b(l)} |\psi_\lambda(\mathbf{r})|^2 d\mathbf{r} \right)^q, \quad (10.6)$$

where $\sum_\lambda^{N_E}$ represents the sum over all N_E eigenstates lying in the interval $|E_c - E| \leq E_s/2$. Since this energy interval is included in the critical region, the spatial profile of $|\psi_\lambda(\mathbf{r})|^2$ has the same statistical properties as the critical wavefunction. We thus obtain

$$\langle \rho^q(l, \epsilon) \rangle \propto \left(\frac{l}{L} \right)^{\tau(q)}, \quad (10.7)$$

where $\tau(q)$ is the mass exponent of the multifractal wavefunction. Next, consider the case $\epsilon \gg \Delta$. This condition is equivalent to the limiting case $L \rightarrow \infty$, keeping ϵ

fixed. Even in this case $\langle \rho^q(l, \epsilon) \rangle$ should be finite because the number of eigenvalues N_E is constant, independently of L . Therefore, the moment $\langle \rho^q(l, \epsilon) \rangle$ should not depend on L . The energy scale ϵ , however, introduces new characteristic lengths less than L . For the case of the Anderson transition, the unique length scale L_ϵ is introduced into the system because of one-parameter scaling. The scale L_ϵ is given by (9.61), i.e.,

$$L_\epsilon = \frac{1}{(\rho\epsilon)^{1/d}}, \quad (10.8)$$

where ρ is the global density of states at the critical energy. For $L_\epsilon \ll L$, the whole system can be regarded as a set of uncorrelated subsystems of size L_ϵ . Since the mean level spacing Δ_ϵ of the subsystem is equal to ϵ , the moment $\langle \rho^q(l, \epsilon) \rangle$ for each subsystem can be expressed by (10.7), but with the system size L_ϵ . Thus, for $\epsilon \gg \Delta$, we have

$$\langle \rho^q(l, \epsilon) \rangle \propto \left(\frac{l}{L_\epsilon} \right)^{\tau(q)}. \quad (10.9)$$

Using (10.8), this equation yields

$$\langle \rho^q(l, \epsilon) \rangle \propto \epsilon^{\tau(q)/d}. \quad (10.10)$$

This relation suggests that the spectral measure distributes in a multifractal manner. Comparing (10.10) with (10.5), we obtain

$$\tilde{\tau}(q) = \frac{\tau(q)}{d}, \quad (10.11)$$

or for the generalized dimension $D_q = \tau(q)/(q - 1)$,

$$\tilde{D}_q = \frac{D_q}{d}, \quad (10.12)$$

where \tilde{D}_q is the generalized dimension for the spectral measure. We should note that (10.12) is peculiar to the Anderson transition. For other multifractal wavefunctions such as those of the Harper Hamiltonian or Fibonacci chains, length scales introduced by the energy ϵ are not uniquely determined by (10.8). Therefore, the spectral mass exponent $\tilde{\tau}(q)$ (or the generalized dimension \tilde{D}_q) is generally independent of $\tau(q)$ (or D_q) describing the multifractality of the wavefunction.

The scaling relation (10.12) for the Anderson transition has been confirmed numerically by Huckestein and Klesse [10.21]. They calculated D_q and \tilde{D}_q independently both for the quantum Hall critical states and for the critical states in a 3D disordered system subject to a magnetic field. The results are shown in Figs. 10.7a (2D) and 10.7b (3D). These figures clearly show the validity of (10.12) for 2D and 3D systems.

Let us consider the arguments for using the local density of states as an order parameter of the Anderson transition. In contrast to conventional continuous phase

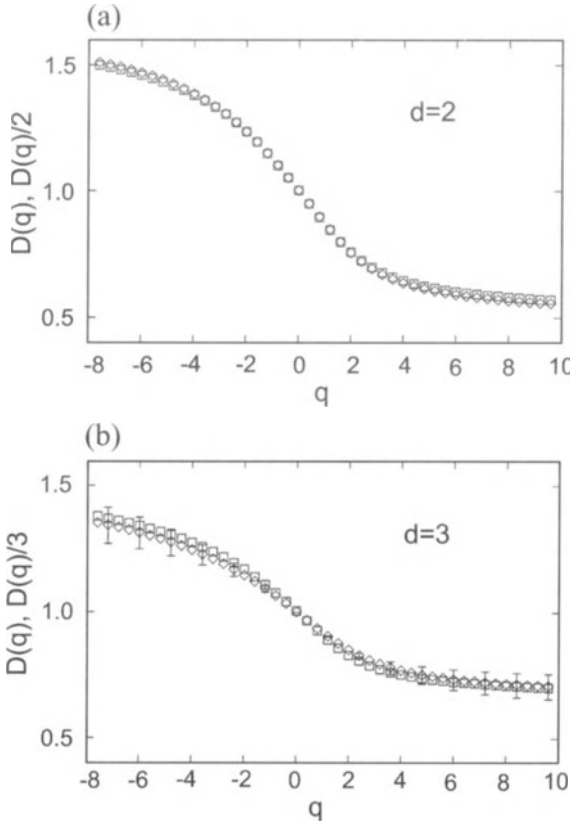


Fig. 10.7. (a) Generalized dimensions of a critical wavefunction (\diamond) and the spectral measure (\square) for a quantum Hall system described by the 2D Chalker–Coddington network model, which includes 150×150 (for \diamond) and 200×200 (for \square) scatterers. (b) Generalized dimensions of a critical wavefunction (\diamond) and the spectral measure (\square) for a 3D GUE system described by the 3D Chalker–Coddington network model, which includes 20^3 (for \diamond) and 35^3 (for \square) scatterers [10.21]

transitions, it is difficult to find a suitable order parameter for the Anderson transition. This seems to be due to the fact that the symmetry breaking accompanying the Anderson transition is not luminous. The order parameter for the Anderson transition should satisfy the following conditions:

- the order parameter vanishes in the localized (or delocalized) phase,
- the order parameter becomes finite and positive in the delocalized (or localized) phase,
- the order parameter exhibits a power-law behavior with a critical exponent near the transition point.

The typical value of the local density of states ρ_{typ} satisfies all these conditions, as will be shown below, and can be regarded as a strong candidate for the order

parameter of the Anderson transition [10.22]. Smearing out the δ -function in (10.1) by a finite width $\Gamma(E) \propto L^{-d}$ for a system of size L , the local density of states is given by

$$\rho(\mathbf{r}, E) = \Gamma^{-1}(E) |\psi_E(\mathbf{r})|^2 . \quad (10.13)$$

The spatial average ρ_{av} of $\rho(\mathbf{r}, E)$ defined by $\rho_{\text{av}} = L^{-d} \int \rho(\mathbf{r}, E) d\mathbf{r}$ becomes

$$\rho_{\text{av}} \propto L^0 . \quad (10.14)$$

From the finite-size scaling argument discussed in Sect. 3.3, (10.14) implies that ρ_{av} does not depend on x for an infinite system near the transition point, where x is one of the external parameters introduced in Sect. 9.3, such as the energy or the strength of disorder. Therefore, the quantity ρ_{av} is not suitable for the order parameter. This is obvious because ρ_{av} is nothing but the global density of states, which is a smooth function of x near the transition point x_c . In contrast, the typical value of $\rho(\mathbf{r}, E)$ has non-trivial L dependence. In general, as mentioned in Sect. 4.8, the typical value of distributed quantities $\{m_i\}$ is defined by the value m_{typ} at which the distribution function $R(\log m)$ becomes maximum, which is equivalent to the geometric mean of $\{m_i\}$ if $R(\log m)$ is a symmetric distribution. Thus, the typical value of the local density of states ρ_{typ} is given by

$$\rho_{\text{typ}} = \Gamma^{-1}(E) \mu_{\text{typ}} , \quad (10.15)$$

where μ_{typ} is the typical value of the box measure μ_b of $|\psi_E(\mathbf{r})|^2$ with box size $l = 1$. The typical value of multifractal measures was discussed in Sect. 4.8, and (4.98) gives

$$\rho_{\text{typ}} \propto \Gamma^{-1}(E) L^{-\alpha_0} \propto L^{d-\alpha_0} , \quad (10.16)$$

where α_0 is the Lipschitz–Hölder exponent giving the maximum value of the multifractal spectrum $f(\alpha)$ of the critical wavefunction. Applying the finite-size scaling argument to (10.16), the typical value ρ_{typ} for an infinite system near the transition point x_c behaves as

$$\rho_{\text{typ}} \propto (x_c - x)^\beta , \quad \text{for } x < x_c , \quad (10.17)$$

where

$$\beta = \nu(\alpha_0 - d) . \quad (10.18)$$

The quantity ρ_{typ} obviously becomes zero in the localized phase, so (10.17) is only valid for $x < x_c$ (extended phase). Since $\alpha_0 > d$, the exponent β is always positive. All these properties of ρ_{typ} satisfy the conditions for the order parameter. The values of the order parameter exponent β can be estimated from the values of ν and α_0 listed in Tables 9.2 and 10.1 ($\beta = 0.46$ for the 2D GSE and 1.73 for the 3D GOE). In contrast to ordinary critical phenomena, the values obtained for β are larger than unity for 3D systems.

10.3 Relations between Multifractality and Dynamical Properties at the Transition Point

Critical wavefunctions and spectral measures at the Anderson transition point possess a multifractal nature and require an infinite set of exponents [$\tau(q)$, D_q , or $f(\alpha)$] to describe their statistical properties. As mentioned in Sect. 10.2, exponents characterizing wavefunctions (τ , D_q , or f) and spectral measures ($\tilde{\tau}$, \tilde{D}_q , or \tilde{f}) are not independent for the Anderson transition due to one-parameter scaling, while these are independent in general. One-parameter scaling also leads to the power-law behavior of dynamical quantities at the transition point, as discussed in Sect. 9.6. An intriguing question arises here: are the exponents describing the critical dynamics (such as η) independent of the multifractal exponents? The answer to this question is quite important if we are to understand the critical dynamics at the Anderson transition from the multifractal viewpoint. We show in this section that the answer is no and that the generalized dimension for $q = 2$ (the correlation dimension) is related to the exponent η by [10.5, 10.23]

$$D_2 = d - \eta . \quad (10.19)$$

This significant relation has been confirmed numerically for several systems exhibiting the Anderson transition.

Let us start with the second moment of the probability measure $\mu(\mathbf{r}) = |\psi(\mathbf{r})|^2$, where $\psi(\mathbf{r})$ is a critical wavefunction. From (4.20), this quantity is defined by

$$\langle \mu_l^2 \rangle = \sum_b \left(\int_{b(l)} |\psi(\mathbf{r})|^2 d\mathbf{r} \right)^2 , \quad (10.20)$$

where the integral $\int_{b(l)} d\mathbf{r}$ is taken over spatial positions in a small box $b(l)$ of size l . Because of the multifractality of the critical wavefunction, the moment should behave as

$$\langle \mu_l^2 \rangle \propto \left(\frac{l}{L} \right)^{\tau(2)} \propto l^{D_2} . \quad (10.21)$$

Introducing the average over boxes $\langle \dots \rangle_b$, (10.20) can be expressed as

$$\langle \mu_l^2 \rangle = \left(\frac{L}{l} \right)^d \left\langle \left(\int_{b(l)} |\psi(\mathbf{r})|^2 d\mathbf{r} \right)^2 \right\rangle_b ,$$

where the factor $(L/l)^d$ denotes the number of boxes in the system. The average $\langle \dots \rangle_b$ is equivalent to a disorder average in a specific box at criticality. We then have

$$\langle \mu_l^2 \rangle = \left(\frac{L}{l} \right)^d \int_{b(l)} \int_{b(l)} \langle |\psi(\mathbf{r}')|^2 |\psi(\mathbf{r}'')|^2 \rangle_D d\mathbf{r}' d\mathbf{r}'' , \quad (10.22)$$

where $\langle \dots \rangle_D$ represents the disorder average. Due to the disorder average, the integrand $\langle |\psi(\mathbf{r}')|^2 |\psi(\mathbf{r}'')|^2 \rangle_D$ is a function of $|\mathbf{r}' - \mathbf{r}''|$. We denote $\mathbf{r}' - \mathbf{r}''$ and

$(\mathbf{r}' + \mathbf{r}'')/2$ by \mathbf{r} and \mathbf{R} , respectively. The Jacobian J of this transformation is unity. The volume of the new integration range after this transformation has the same l -dependence as the original integration range because $J = 1$. Therefore, the second moment becomes

$$\langle \mu_l^2 \rangle \propto L^d \int_{b(l)} \langle |\psi(0)|^2 |\psi(\mathbf{r})|^2 \rangle_D d\mathbf{r} , \quad (10.23)$$

where we have used $\int_{b(l)} d\mathbf{R} \propto l^d$. It should be noted that the integrand in (10.23) is identical to the two-particle correlation function defined by (9.90) with $\omega \rightarrow 0$, except for the density of states at the critical energy, i.e.,

$$\langle |\psi(0)|^2 |\psi(\mathbf{r})|^2 \rangle_D \propto S(r, \omega \rightarrow 0) . \quad (10.24)$$

The asymptotic profile of $S(r, \omega)$ at lower frequencies is given by (9.96). Using this proportionality, (10.23) yields

$$\langle \mu_l^2 \rangle \propto L^d \rho^{-1} \int_0^l r^{d-1} r^{-\eta} dr \propto l^{d-\eta} , \quad (10.25)$$

where $\rho(\propto L^d)$ is the density of states at the critical energy. We then obtain (10.19) by comparing (10.25) with (10.21).

All dynamical quantities discussed in Sect. 9.6 are characterized by the unique exponent η .² The relation (10.19) implies that dynamical properties at the transition point can also be described by a single multifractal exponent. For instance, if we express the long-time behavior of the temporal autocorrelation function defined by (9.73) as $C(t) \propto t^{-\delta}$, the exponent δ is, from (9.74), given by

$$\delta = \frac{D_2}{d} = \tilde{D}_2 . \quad (10.26)$$

Similarly, for the diffusion function $D(q, \omega)$, equation (9.64) implies that the exponents ε and κ describing the asymptotic behavior of $D(q, \omega)$ for $qL_\omega \gg 1$ as $D(q, \omega) \propto q^{-\varepsilon}\omega^\kappa$ can be written as

$$\varepsilon = 2 - D_2 , \quad (10.27)$$

and

$$\kappa = 1 - \frac{D_2}{d} . \quad (10.28)$$

Therefore, (10.19) provides a key relation for understanding the Anderson transition. The validity of the scaling relation (10.19) has been checked numerically [10.20, 10.24]. This can also be seen from Tables 9.3 and 10.1, as shown in Table 10.2.

² This does not mean that the exponent η (or D_2) can describe all the critical dynamics. For example, the asymptotic behavior of the q -particle correlation function which is an extension of the two-particle correlation function defined by (9.90) requires at least the exponent D_q . The following should also be noted: it is not obvious whether the whole spectrum of multifractal exponents is sufficient to describe all dynamical properties, although it is necessary.

Table 10.2. Comparison between $d - \eta$ calculated from Table 9.3 and D_2 listed in Table 10.1. The coincidence of these values implies the validity of the scaling relation (10.19)

	Symmetry	$d - \eta$	D_2
2D	QHS	1.62	1.50
	GSE	1.68	1.66
3D	GOE	1.5	1.52
	GUE	1.7	1.49

In order to clarify numerically whether two given systems belong to the same universality class, it is common to check the equality of the set of critical exponents of these two systems. The scaling relation between η and D_2 allows us to use the multifractal exponent to do this. A comparison between the whole spectra of multifractal exponents makes it possible to distinguish more precisely two universality classes than the comparison of a finite number of exponents (such as ν and η).

10.4 Conformal Invariance

The multifractal nature of critical wavefunctions or spectral measures is deeply related to the critical dynamics, as seen in Sect. 10.3. We will show in this section that the multifractality of the critical state in an infinite 2D system also relates to the scaling amplitude A_c of a quasi-1D system with width M , introduced when discussing the finite-size scaling analysis in Sect. 9.5. This relation is a direct consequence of the conformal invariance of the system.

Before deriving the relation between the multifractality and A_c , we must first explain conformal invariance. For general critical phenomena, it is well known that a physical quantity at a critical point is invariant under a global scale transformation due to the fractal nature of the critical state. Conformal invariance requires the quantity to be invariant even for a local scale transformation with spatially varying scale factors. This represents a very high symmetry of the critical state, and not all critical states possess this symmetry. If a system is, in a statistical sense, invariant under arbitrary uniform translations and rotations, the critical state of this system has translational, rotational, and dilatational (scaling) symmetries. In other words, the fixed-point Hamiltonian³ is invariant under composite transformations g combining these global operations of translation (T), rotation (R), and dilatation (D). We focus on such systems in this section. We can also consider composite transformations $g(\mathbf{r})$ combining a local translation $T(\mathbf{r})$, rotation $R(\mathbf{r})$, and dilatation $D(\mathbf{r})$. The

³ Assuming that a renormalization operation \mathfrak{R} maps the Hamiltonian H onto an effective Hamiltonian H' , i.e., $H' = \mathfrak{R}[H]$, the fixed-point Hamiltonian H^* is defined by $H^* = \mathfrak{R}[H]$. Details of the renormalization group theory for critical phenomena are presented in [10.25].

local-scale transformation is nothing but the transformation $g(\mathbf{r})$. Since the local operators $T(\mathbf{r})$, $R(\mathbf{r})$, and $D(\mathbf{r})$ preserve the angle between two local vectors $\mathbf{a}(\mathbf{r})$ and $\mathbf{b}(\mathbf{r})$, the transformation $g(\mathbf{r})$ also does so.

If the Hamiltonian includes only short-range interactions, it seems plausible that the critical fixed-point Hamiltonian will be invariant under the local transformation $g(\mathbf{r})$. An intuitive explanation of this symmetry is presented as follows. Let us consider, as an example, a spin system on a 2D square lattice (see Fig. 10.8a).

A block-spin transformation performed in a renormalization group treatment replaces all the original spins (thin arrows) inside a cell shown in Fig. 10.8a by a single block spin (thick arrows). The block spin configuration determined by interactions between block spins is similar to the original spin configuration at the critical point because of fractality. We transform this spin system by a local transformation $g(\mathbf{r})$, as shown in Fig. 10.8b. If the spatial modulation of $g(\mathbf{r})$ is sufficiently slow and the spin–spin interactions are short range (e.g., nearest neighbors), the block-spin interaction in the system transformed by $g(\mathbf{r})$ can be approximated by that in the

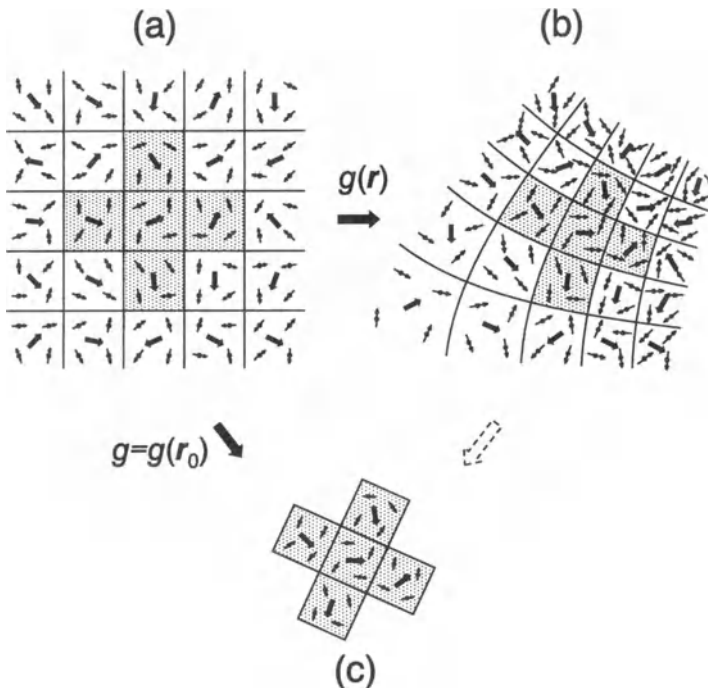


Fig. 10.8. Schematic illustrations of a local-scale transformation for a 2D spin system. Small arrows represent the original spins, while thick arrows express block spins by block-spin transformations. The original spin system (a) is mapped onto (b) by the local transformation $g(\mathbf{r})$. A local spin structure (hatched region) in the mapped system (b) is approximated by the spin structure transformed by a global transformation g from the original system (a), as shown in (c)

system transformed by $g = g(\mathbf{r}_0)$ (Fig. 10.8c), where \mathbf{r}_0 denotes the position of the block spin. Since the Hamiltonian is invariant under the global transformation g , it is also invariant under the transformation $g(\mathbf{r})$. Therefore, the critical system is invariant under the local-scale transformation if the system has translational and rotational symmetries and the spatial modulation of this transformation is slow over the interaction (or hopping) range. In the case of the Anderson transition, uniformly distributed random potentials guarantee translational and rotational symmetries of the system, and the hopping term in the tight-binding Hamiltonian [(9.35)] is usually short range. We thus expect invariance under local-scale transformations for the Anderson transition.

How should a physical quantity $A(\mathbf{r})$ behave spatially if $A(\mathbf{r})$ is locally scale invariant? To see this, we recall the case where $A(\mathbf{r})$ is globally scale invariant. In this case, $A(\mathbf{r})$ should be expressed by

$$A(\mathbf{r}) \propto r^\lambda , \quad (10.29)$$

where λ is a constant exponent [fractal dimension of $A(\mathbf{r})$]. This expression is equivalent to the following statement: the quantity $A(\mathbf{r})$ should satisfy

$$A(a\mathbf{r}) = a^\lambda A(\mathbf{r}) , \quad (10.30)$$

under a global scale transformation

$$\mathbf{r} \mapsto \mathbf{R} = a\mathbf{r} , \quad (10.31)$$

where a is a constant scaling factor. According to this expression of global scale invariance, local scale invariance can be grasped by $A(\mathbf{r})$ satisfying a similar equation to (10.30) under a local scale transformation

$$\mathbf{r} \mapsto \mathbf{R} = g(\mathbf{r}) , \quad (10.32)$$

where $g(\mathbf{r})$ is a transformation composed of a local translation, rotation, and dilatation. Since the global scaling factor a in (10.30) is replaced by a spatially varying scaling factor $|\nabla g(\mathbf{r})|$ for the local scale transformation, the equation corresponding to (10.30) becomes

$$A[g(\mathbf{r})] = |\nabla g(\mathbf{r})|^\lambda A(\mathbf{r}) . \quad (10.33)$$

If the physical quantity A is a function of $\{\mathbf{r}_1, \mathbf{r}_2, \dots, \mathbf{r}_n\}$, like a correlation function, (10.33) can be extended to

$$A[g(\mathbf{r}_1), g(\mathbf{r}_2), \dots, g(\mathbf{r}_n)] = |\nabla_1 g(\mathbf{r}_1)|^{\lambda_1} |\nabla_2 g(\mathbf{r}_2)|^{\lambda_2} \dots |\nabla_n g(\mathbf{r}_n)|^{\lambda_n} A(\mathbf{r}_1, \mathbf{r}_2, \dots, \mathbf{r}_n) . \quad (10.34)$$

This gives a mathematical expression for the local scaling invariance of the quantity A .

The argument above involves no restriction on spatial dimensions of systems, so local scale invariance can be expected for any dimensions [10.26, 10.27]. However,

the mathematical treatment of this invariance simplifies dramatically in 2D systems. If we regard the 2D space as a complex plane, a local scale transformation is described by the conformal mapping

$$z = x + iy \longmapsto w = g(z) = u + iv , \quad (10.35)$$

where $g(z)$ is an analytic function, because the conformal mapping preserves the angle between two local vectors $\mathbf{a}(z)$ and $\mathbf{b}(z)$. Therefore, local scale invariance for 2D systems is, in particular, referred to as conformal invariance. The expression (10.34) is written as

$$A[g(z_1), g(z_2), \dots, g(z_n)] = \left| \frac{\partial g}{\partial z_1} \right|^{\lambda_1} \left| \frac{\partial g}{\partial z_2} \right|^{\lambda_2} \cdots \left| \frac{\partial g}{\partial z_n} \right|^{\lambda_n} A(z_1, z_2, \dots, z_n) . \quad (10.36)$$

In the case of the Anderson transition, conformal invariance yields the transformation law of the two-particle correlation function

$$\langle |\psi[g(z_1)]|^2 |\psi[g(z_2)]|^2 \rangle_{S'} = \left| \frac{\partial g}{\partial z_1} \right|^{-\eta/2} \left| \frac{\partial g}{\partial z_2} \right|^{-\eta/2} \langle |\psi(z_1)|^2 |\psi(z_2)|^2 \rangle_S , \quad (10.37)$$

where $\langle \dots \rangle_S$ and $\langle \dots \rangle_{S'}$ denote disorder averages in a given 2D system S and in the transformed system S' by the conformal mapping (10.35), respectively. The reason for $\lambda_1 = \lambda_2 = -\eta/2$ is that

$$\langle |\psi(\mathbf{r}_1)|^2 |\psi(\mathbf{r}_2)|^2 \rangle_S \propto |\mathbf{r}_1 - \mathbf{r}_2|^{-\eta} , \quad (10.38)$$

which is obtained from (9.96) with infinitesimal ω . It should be emphasized that we expect (10.37) for any kind of conformal mapping $g(z)$.⁴

Let us focus our attention on the special conformal mapping

$$g(z) = \frac{M}{2\pi} \log z , \quad (10.39)$$

where M is a constant. This analytic function maps a point $z = x + iy = r e^{i\theta}$ onto

$$w = \frac{M}{2\pi} \log r + i \frac{M\theta}{2\pi} . \quad (10.40)$$

If the domains of r and θ are $(0, \infty)$ and $[0, 2\pi]$, the ranges of u and v ($w \equiv u + iv$) are $(-\infty, \infty)$ and $[0, M]$, respectively. Therefore, this transformation maps the infinite 2D system onto an infinite quasi-1D system of width M (see Fig. 10.9). Since θ is a variable with period 2π , this quasi-1D system has periodic boundary conditions in the direction of the width. Corresponding to (10.37), this conformal mapping gives

⁴ If $g(z) = az$, the relation (10.37) becomes

$$\langle |\psi[g(z_1)]|^2 |\psi[g(z_2)]|^2 \rangle_{S'} = a^{\lambda_1 + \lambda_2} \langle |\psi(z_1)|^2 |\psi(z_2)|^2 \rangle_S .$$

Thus, we have $\lambda_1 + \lambda_2 = -\eta$. The symmetry between \mathbf{r}_1 and \mathbf{r}_2 in the correlation function gives $\lambda_1 = \lambda_2 = -\eta/2$.

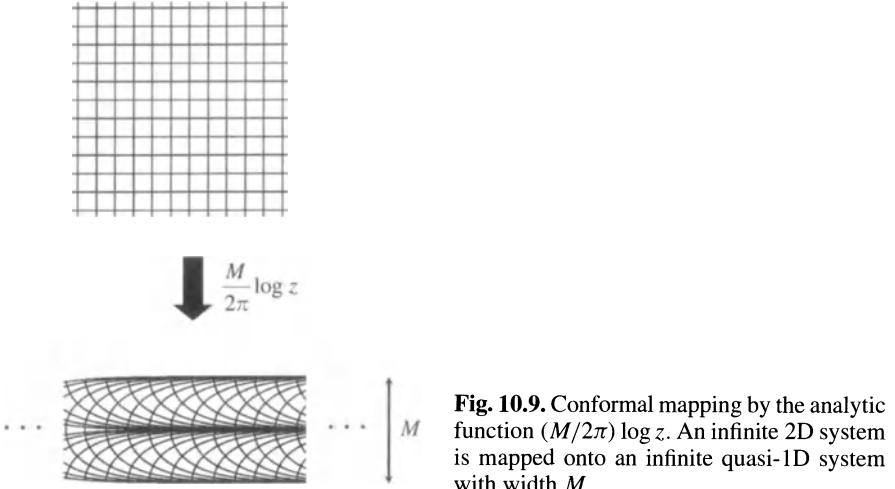


Fig. 10.9. Conformal mapping by the analytic function $(M/2\pi) \log z$. An infinite 2D system is mapped onto an infinite quasi-1D system with width M

$$\langle |\psi(u_1 + iv_1)|^2 |\psi(u_2 + iv_2)|^2 \rangle_{\text{ID}} = \left| \frac{\partial g}{\partial z_1} \right|^{-\eta/2} \left| \frac{\partial g}{\partial z_2} \right|^{-\eta/2} \langle |\psi(z_1)|^2 |\psi(z_2)|^2 \rangle_{\infty}, \quad (10.41)$$

where $\langle \dots \rangle_{\text{ID}}$ and $\langle \dots \rangle_{\infty}$ represent disorder averages in the quasi-1D system and in the infinite 2D system, respectively. This equation implies that the two-particle correlation function of the infinite 2D system is obtained from the exponent η and the correlation function of the quasi-1D system, which is easily calculated from numerical simulations.

Let us express the correlation function of the quasi-1D system in terms of variables u and v . Using the relation

$$\langle |\psi(z_1)|^2 |\psi(z_2)|^2 \rangle_{\infty} \propto |z_1 - z_2|^{-\eta}, \quad (10.42)$$

and

$$\frac{\partial g}{\partial z} = \frac{M}{2\pi z}, \quad (10.43)$$

equation (10.41) becomes

$$\langle |\psi(u_1 + iv_1)|^2 |\psi(u_2 + iv_2)|^2 \rangle_{\text{ID}} \propto \left(\frac{|z_1 - z_2|^2}{|z_1||z_2|} \right)^{-\eta/2}. \quad (10.44)$$

The right-hand side of this relation can be rewritten as

$$\left(\frac{|z_1 - z_2|^2}{|z_1||z_2|} \right)^{-\eta/2} = \quad (10.45)$$

$$\left\{ \exp \left[\frac{2\pi}{M} (u_1 - u_2) \right] + \exp \left[\frac{2\pi}{M} (u_2 - u_1) \right] - 2 \cos \left[\frac{2\pi}{M} (v_1 - v_2) \right] \right\}^{-\eta/2}.$$

Here we used the relation $z = \exp[2\pi(u+iv)/M]$ obtained from (10.39). We evaluate the correlation function of the quasi-1D system for $|u_1 - u_2| \gg M$. The quantity given by (10.45) is dominated by the first term if $u_1 \gg u_2$ and by the second term if $u_1 \ll u_2$. We thus have

$$\langle |\psi(u_1 + iv_1)|^2 |\psi(u_2 + iv_2)|^2 \rangle_{1D} \propto \exp\left(-\frac{\pi\eta}{M}|u_1 - u_2|\right). \quad (10.46)$$

On the other hand, the localization length λ_M^* of the quasi-1D system is given in the complex representation by

$$\int_0^M \int_0^M \langle |\psi(u_1 + iv_1)|^2 |\psi(u_2 + iv_2)|^2 \rangle_{1D} dv_1 dv_2 \propto \exp\left(-\frac{2}{\lambda_M^*}|u_1 - u_2|\right). \quad (10.47)$$

Comparing (10.47) and the integral of (10.46) with respect to v_1 and v_2 , we find

$$\Lambda_c^* \equiv \frac{\lambda_M^*}{M} = \frac{2}{\pi\eta}. \quad (10.48)$$

Using (10.19), we have

$$\Lambda_c^* = \frac{2}{\pi(d - D_2)}. \quad (10.49)$$

This relation implies that the scaling amplitude Λ_c^* of the quasi-1D system is related to the multifractal property (D_2) of the critical wavefunction in the infinite system.

Although (10.49) is a meaningful relation that gives the scaling amplitude of the two-particle correlation function, we should note that the quantity Λ_c^* is not equivalent to the critical scaling amplitude Λ_c introduced in Sect. 9.5. This is because the quasi-1D localization length λ_M in (9.42) gives the decay rate of the typical profile (i.e., the geometric mean) of wavefunctions, as mentioned in the footnote on p. 131, while λ_M^* in (10.47) is defined by the two-particle correlation function, which is the arithmetic mean of $|\psi(r_1)|^2 |\psi(r_2)|^2$ in the quasi-1D system.

In order to obtain the relation between Λ_c calculated by the finite-size scaling technique and exponents defined in an infinite 2D system, we repeat the above discussion but starting with the typical value of $|\psi(r_1)|^2 |\psi(r_2)|^2$ rather than its arithmetic mean in (10.37). The transformation law of the typical value $\langle |\psi(r_1)|^2 |\psi(r_2)|^2 \rangle_{\text{typ}}$ becomes

$$\langle |\psi[g(z_1)]|^2 |\psi[g(z_2)]|^2 \rangle_{\text{typ}}^{1D} = \left| \frac{\partial g}{\partial z_1} \right|^{-\eta/2} \left| \frac{\partial g}{\partial z_2} \right|^{-\eta/2} \langle |\psi(z_1)|^2 |\psi(z_2)|^2 \rangle_{\text{typ}}^\infty, \quad (10.50)$$

where the conformal transformation g is given by (10.39). The symbols $\langle \dots \rangle_{\text{typ}}^{1D}$ and $\langle \dots \rangle_{\text{typ}}^\infty$ represent the typical values in the quasi-1D and infinite 2D systems, respectively. Since the fractal dimension of the typical value of the local density of

Table 10.3. Comparison between $1/\pi(\alpha_0 - d)$ with α_0 listed in Table 10.1 and Λ_c obtained by finite-size scaling analyses (Table 9.2)

Symmetry	α_0	$\frac{1}{\pi(\alpha_0 - d)}$	Λ_c
2D	QHS	2.31	1.03
	GSE	2.19	1.68
3D	GOE	4.1	0.29
	GUE	4.1	0.29

states ρ_{typ} is given by $d - \alpha_0$ [(10.16)], we have $\lambda_1 = \lambda_2 = d - \alpha_0$ and

$$\langle |\psi(z_1)|^2 |\psi(z_2)|^2 \rangle_{\text{typ}}^{\infty} \propto |z_1 - z_2|^{2(d-\alpha_0)}, \quad (10.51)$$

where α_0 is the Lipschitz–Hölder exponent giving the minimum value of the multifractal spectrum $f(\alpha)$ of the critical wavefunction. We can repeat the argument below (10.43) for the quantity $\langle |\psi(u_1 + iv_1)|^2 |\psi(u_2 + iv_2)|^2 \rangle_{\text{typ}}^{\text{1D}}$, replacing η by $2(\alpha_0 - d)$. Finally, we obtain

$$\Lambda_c = \frac{1}{\pi(\alpha_0 - d)}, \quad (10.52)$$

instead of (10.49). The validity of (10.52) can be checked by using the data listed in Tables 9.2 and 10.1. Results are summarized in Table 10.3. For 2D systems, numerically calculated values of Λ_c agree relatively well with $1/\pi(\alpha_0 - d)$, within a precision of about 10%, while the discrepancy between these values for 3D systems exceeds 50%. This suggests that (10.52) [and also (10.49)] holds only for 2D systems, as expected, although local scale invariance may be valid for any dimensions [10.26, 10.27].

10.5 Universality at Higher Landau Levels

The multifractal properties of critical wavefunctions and spectral measures at the Anderson transition are deeply related to its criticality. This implies that multifractality at the transition point is not only conceptually important but also useful for revealing critical properties or universality of the Anderson transition. Here we demonstrate the efficiency of multifractal analysis via a study of the quantum Hall transition.

As mentioned in Sect. 9.5, in a 2D disordered electron system subject to a uniform magnetic field (quantum Hall system), all states are localized except for states at the centers of the Landau subbands. The states at the subband centers have a multifractal property (see Fig. 10.1), which indicates that these states are critical. The transition, say, the quantum Hall transition, from localized to critical states can be considered as an Anderson transition, and has been much more extensively studied so far than

any other Anderson transition. This is because the system is numerically tractable and the transition points are exactly known, in addition to its physical importance. However, the scaling property of the quantum Hall transition is still far from being fully understood. Studies using the finite-size scaling analysis described in Sect. 9.5 indicate that one-parameter scaling holds for the quantum Hall transition for the lowest Landau level ($N = 0$), while values reported so far for the localization length exponent ν , for example, for the second lowest Landau level, range from 2.3 to 6.2, depending on the correlation length of disorder. This seems to show non-universality of the transition at higher Landau levels. In an attempt to reconcile the apparent lack of universality, Huckestein [10.28] has suggested that, if one introduces an irrelevant scaling length ξ_{irr} to describe Λ_M , given by (9.42) as

$$\Lambda_M = f \left(\frac{M}{\xi}, \frac{M}{\xi_{\text{irr}}} \right), \quad (10.53)$$

universality at the higher Landau levels is recovered asymptotically on a length scale much larger than ξ_{irr} . If the irrelevant length scale ξ_{irr} decreases rapidly as the correlation length of disorder σ increases, the asymptotic recovery of one-parameter scaling with increasing σ is expected. What we will do in this section is to confirm this asymptotic recovery by means of the multifractal analysis of critical wavefunctions [10.6].

We can write the Hamiltonian of the quantum Hall system as

$$H = \sum_{NX} |NX\rangle \left(N + \frac{1}{2} \right) \hbar\omega_c \langle NX| + \sum_{NX} \sum_{N'X'} |NX\rangle \langle NX| V |N'X'\rangle \langle N'X'|, \quad (10.54)$$

where ω_c and V are the cyclotron frequency and a random potential, respectively. The quantum state $|NX\rangle$ represents the Landau state for a 2D system without disorder subject to a uniform magnetic field, where the labels N and X denote the Landau index and the x coordinate, respectively. The magnetic field is assumed to be so strong that each Landau subband can be treated separately, i.e., $|\langle NX|V|N'X'\rangle| \ll \hbar\omega_c$ ($N \neq N'$). The random potential is given by an assembly of Gaussian scatterers of the form

$$V(\mathbf{r}) = \sum_i \frac{V_i}{2\pi\sigma^2} e^{|\mathbf{r}-\mathbf{r}_i|^2/2\sigma^2}, \quad (10.55)$$

where the centers of Gaussian scatterers \mathbf{r}_i are randomly distributed and V_i is assumed to be $V_i = \pm V_0$ with an equal probability. In the short-range limit of the potential correlation ($\sigma = 0$), the potential becomes a set of δ functions, i.e., $V(\mathbf{r}) = \sum_i V_i \delta(\mathbf{r} - \mathbf{r}_i)$.

Numerical diagonalizations of the Hamiltonian (10.54) give eigenstates belonging to the higher Landau levels as well as the lowest one. Figure 10.10 depicts spatial profiles of wavefunctions $|\psi(\mathbf{r})|^2$ belonging to eigenenergies closest to the

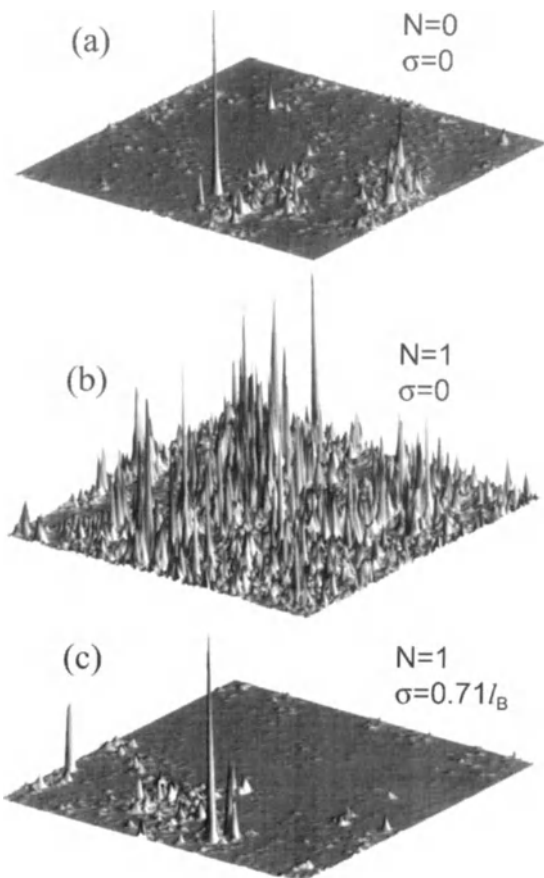


Fig. 10.10. Eigenstates of quantum Hall systems described by the Hamiltonian (10.54). (a) and (b) show the squared critical wavefunctions for the short-range random potential ($\sigma = 0$) belonging to (a) the lowest and (b) the second lowest Landau bands. The critical wavefunction at the second lowest Landau level for $\sigma = 0.71l_B$ is depicted in (c), where l_B is the magnetic length [10.6]

centers of $N = 0$ and $N = 1$ Landau subbands. The wavefunction at the lowest Landau level ($N = 0$) for the short-range random potential (Fig. 10.10a) possesses sparsely distributed spikes, like the critical wavefunction of a 2D disordered system with strong spin-orbit interactions shown in Fig. 10.2b. In contrast, the wavefunction shown in Fig. 10.10b ($N = 1$ and $\sigma = 0$) is more homogeneously distributed. It thus seems that these two wavefunctions have different multifractilities and belong to different universality classes. The spatial profile of the wavefunction shown in Fig. 10.10c ($N = 1$ and $\sigma = 0.71l_B$) is, however, very similar to Fig. 10.10a, where l_B is the magnetic length. This intimates that increasing σ recovers ill-criticality at the higher Landau levels.

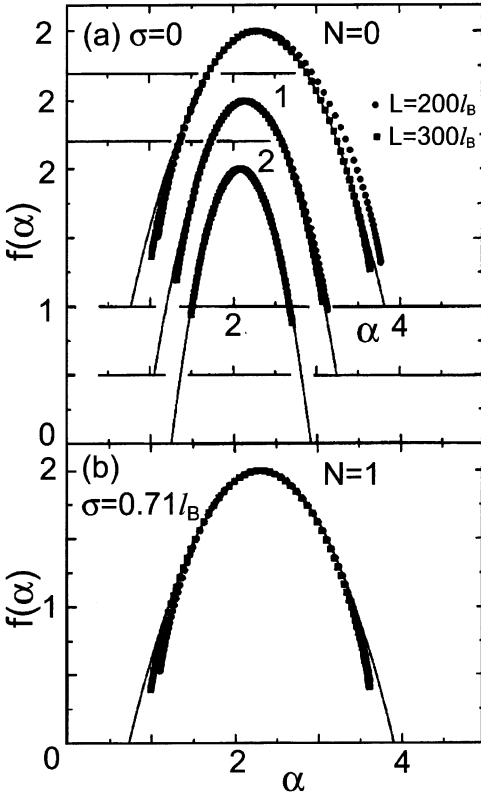


Fig. 10.11. (a) Multifractal spectra $f(\alpha)$ of critical wavefunctions at the lowest ($N = 0$), the second lowest ($N = 1$), and the third lowest ($N = 2$) Landau levels of a quantum Hall system with a short-range random potential ($\sigma = 0$). (b) The same for a finite-range random potential ($\sigma = 0.71l_B$) for the $N = 1$ Landau level [10.6]

We examine the multifractal spectra $f(\alpha)$ of these wavefunctions in order to elucidate this recovery more quantitatively. The multifractal spectrum is readily calculated using the q -microscope of a wavefunction, as explained in Sect. 4.5. Figure 10.11a represents the $f(\alpha)$ spectra of the critical wavefunctions at $N = 0$, 1, and 2 Landau levels with the short-range random potential ($\sigma = 0$). These spectra do vary systematically with N . If we approximate $f(\alpha)$ by a parabolic function (4.89), $f(\alpha)$ is characterized by a single exponent α_0 besides $D_f = d = 2$. From Fig. 10.11a, the value of α_0 decreases from $\alpha_0(N = 0) = 2.31 \pm 0.02$ to $\alpha_0(N = 1) = 2.15 \pm 0.02$, and further down to $\alpha_0(N = 2) = 2.09 \pm 0.01$. In contrast, the correlation dimension D_2 calculated from $D_2 = q\alpha(q) - f[\alpha(q)]$ with $q = 2$ increases from $D_2(N = 0) = 1.50 \pm 0.06$ to $D_2(N = 1) = 1.73 \pm 0.05$ and $D_2(N = 2) = 1.82 \pm 0.05$. These results apparently indicate that critical states belonging to different Landau bands have different criticalities. If we turn to long-range potentials ($\sigma > 0$), however, the values of α_0 and D_2 for $N \geq 1$

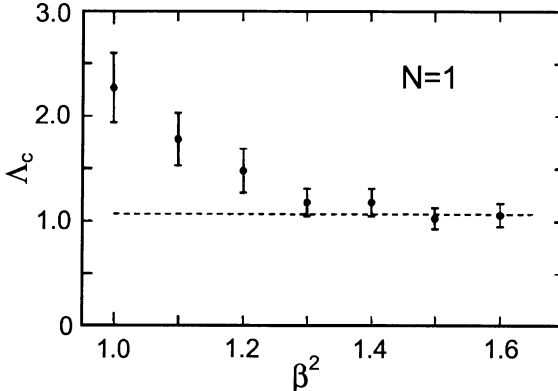


Fig. 10.12. Potential range dependence of the critical scaling amplitude Λ_c for the second lowest Landau level of quantum Hall systems. The abscissa β^2 is the reduced potential range $1 + (\sigma/l_B)^2$, where l_B is the magnetic length. The critical scaling amplitude Λ_c is calculated from (10.52). The horizontal dashed line indicates $\Lambda_c = 1/\log(1 + \sqrt{2})$ [10.6]

almost go back to those for $N = 0$ and $\sigma = 0$ [$\alpha_0(N = 1) = 2.32 \pm 0.03$ and $D_2(N = 1) = 1.51 \pm 0.07$ for $\sigma = 0.71l_B$], as shown in Fig. 10.11b. This fact quantitatively proves the recovery of ill-criticality at the higher Landau levels with increasing σ .

The same conclusion is also obtained by evaluating the critical scaling amplitude Λ_c introduced in Sect. 9.5. As mentioned in Sect. 10.4, conformal invariance of a 2D Anderson transition gives a relation between the multifractality of the critical wavefunction and Λ_c defined on quasi-1D systems.

The σ dependence of Λ_c calculated from (10.52) is shown in Fig. 10.12 for the second lowest Landau level ($N = 1$). As the correlation length σ is increased (increasing β in Fig. 10.12), the value of Λ_c approaches that for $N = 0$ or the value $\Lambda_c = 1/\log(1 + \sqrt{2})$ obtained by Lee et al. [10.29] for the network model of the quantum Hall system. This asymptotic recovery of one-parameter scaling at higher Landau levels with long-range potentials agrees with the finite-size scaling result of Huckestein [10.28].

10.6 Finite-Size Scaling for the q th Moment

We have demonstrated that multifractal analyses are quite useful for studying critical properties of the Anderson transition. If we know the critical point, multifractal analysis gives an infinite set of exponents. Another powerful numerical method for examining the critical properties of the Anderson transition in infinite systems is the finite-size scaling analysis discussed in Sect. 9.5, which provides the critical point x_c , Λ_c , and the localization length exponent v . If we can combine these two methods, it becomes possible to obtain all these quantities by a single procedure.

In this section, we show that such a method is realized by taking account of the scaling for the q th moment $\langle \mu_l^q \rangle$ (or its logarithm). In contrast to the conventional finite-size scaling analysis where only the system size plays a role in the scaling measure, the present scaling analysis uses both the system and the box sizes to alternate the length scale. Due to this feature, it is not necessary to calculate localization lengths λ_M or diagonalize Hamiltonians for many systems with different sizes.

According to (4.20), the q th moment of the probability measures $|\psi_i|^2$ is defined by

$$\langle \mu_l^q \rangle = \sum_b \left(\sum_{i \in b(l)} |\psi_i|^2 \right)^q. \quad (10.56)$$

If the system is at the critical point and $l \ll L$, we have $\langle \mu_l^q \rangle \propto (l/L)^{\tau(q)}$ because of multifractality of the critical wavefunction. However, our interest here is not only precisely at, but also near the critical point. The q th moment $\langle \mu_l^q \rangle$ is a function of the system size L , the box size l , and external parameters x such as the strength of disorder W or the energy E . One-parameter scaling requires $\langle \mu_l^q \rangle$ to be written as

$$\langle \mu_l^q \rangle = \xi^\zeta f_q \left(\frac{L}{\xi}, \frac{l}{\xi} \right), \quad (10.57)$$

where ζ is an exponent, ξ is the correlation (or localization) length of the infinite system, and f_q is a two-variable scaling function which depends on q . Since the length L is always larger than l , the scaling function $f_q(s, t)$ is defined in the range $s \geq t$.

The scaling function $f_q(s, t)$ has two branches corresponding to the localized and extended regimes, as in the case of the conventional finite-size scaling analysis (Fig. 9.7). First we consider the asymptotic form of $f_q(s, t)$ in the localized regime. In the case where both the system size L and the box size l are larger than the localization length ξ , i.e., $s \gg 1$ and $t \gg 1$, the q th moment $\langle \mu_l^q \rangle$ is dominated by the contribution from just one box. Due to the normalization condition on $|\psi_i|^2$, $\langle \mu_l^q \rangle$ becomes unity for this case. This means that the exponent ζ should be zero. If the localization length is smaller than the system size but larger than the box size, i.e., $s \gg 1$ and $t \ll 1$, $\langle \mu_l^q \rangle$ does not depend on L because the wavefunction is localized inside the system. However, the squared amplitudes $|\psi_i|^2$ distribute in a multifractal manner within a scale much less than the localization length. Therefore, $\langle \mu_l^q \rangle \propto (l/\xi)^{\tau(q)}$ and $f_q(s, t) \propto t^{\tau(q)}$. For $s \ll 1$ and $t \ll 1$, the wavefunction has the multifractal character over the whole system. In this limit, $f_q(s, t)$ is proportional to $(t/s)^{\tau(q)}$.

Next we consider the asymptotic profile of $f_q(s, t)$ in the extended branch. If s and t are large enough compared with unity, $|\psi_i|^2$ in (10.56) can be replaced by an averaged value $\bar{\psi}^2$ which is proportional to L^{-d} due to the normalization condition for $|\psi_i|^2$. This replacement leads to

$$\langle \mu_l^q \rangle \propto \left(\frac{L}{l} \right)^d \left(l^d \bar{\psi}^2 \right)^q, \quad (10.58)$$

and

$$f_q(s, t) \propto \left(\frac{t}{s}\right)^{d(q-1)}. \quad (10.59)$$

For $s \gg 1$ and $t \ll 1$, the whole wavefunction can be divided into $(L/\xi)^d$ equivalent boxes (ξ -boxes) of linear size ξ . In order to calculate $\langle \mu_l^q \rangle$, we introduce a rescaled wavefunction $\psi'_i = (L/\xi)^{d/2} \psi_i$ and the moment $\langle \mu_l'^q \rangle_\xi$ defined by

$$\langle \mu_l'^q \rangle_\xi = \sum_{b \in \xi\text{-box}} \left(\sum_{i \in b(l)} |\psi'_i|^2 \right)^q, \quad (10.60)$$

where the summation $\sum_{b \in \xi\text{-box}}$ represents the sum over small boxes of size l contained in the ξ -box. The rescaled wavefunction is normalized within a ξ -box, i.e., $\sum_{i \in \xi\text{-box}} |\psi'_i|^2 = 1$. Since the wavefunction ψ'_i is multifractal on a scale less than ξ , we have $\langle \mu_l'^q \rangle_\xi \propto (l/\xi)^{\tau(q)}$. Expressing $\langle \mu_l'^q \rangle_\xi$ by the original wavefunction ψ_i , we obtain

$$\langle \mu_l'^q \rangle_\xi = \left(\frac{L}{\xi}\right)^{dq} \sum_{b \in \xi\text{-box}} \left(\sum_{i \in b(l)} |\psi_i|^2 \right)^q = \left(\frac{L}{\xi}\right)^{d(q-1)} \langle \mu_l^q \rangle. \quad (10.61)$$

Here we have used (10.56) and the relation $\sum_b = (L/\xi)^d \sum_{b \in \xi\text{-box}}$ resulting from the equivalence of ξ -boxes. From the relation $\langle \mu_l'^q \rangle_\xi \propto (l/\xi)^{\tau(q)}$ due to multifractality of ψ'_i on a scale less than ξ , we have

$$\langle \mu_l^q \rangle \propto \left(\frac{L}{\xi}\right)^{d(1-q)} \left(\frac{l}{\xi}\right)^{\tau(q)}, \quad (10.62)$$

and

$$f_q(s, t) \propto s^{d(1-q)} t^{\tau(q)}. \quad (10.63)$$

Finally, in the case where $s \ll 1$ and $t \ll 1$, the wavefunction distributes in the same way as the localized wavefunction with the localization length much larger than the system size. The scaling function in this limit has the same asymptotic form of $f_q(s, t)$ in the localized branch. Therefore, the asymptotic forms of $f_q(s, t)$ can be summarized as follows. For the localized branch,

$$f_q(s, t) \propto \begin{cases} 1, & \text{if } s \gg 1 \text{ and } t \gg 1, \\ t^{\tau(q)}, & \text{if } s \gg 1 \text{ and } t \ll 1, \\ \left(\frac{t}{s}\right)^{\tau(q)}, & \text{if } s \ll 1 \text{ and } t \ll 1, \end{cases} \quad (10.64)$$

and for the extended branch,

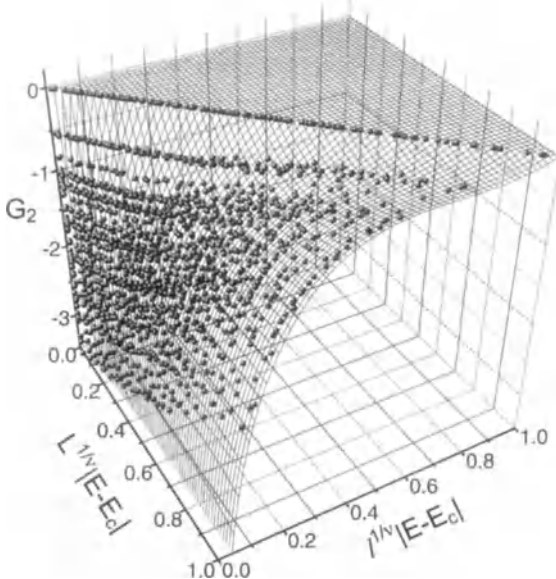


Fig. 10.13. Scaling function (10.66) calculated for a 2D system subject to a random magnetic field with finite mean. The order of the moment is chosen to be $q = 2$, and $\delta B/\bar{B} = 0.5$, where \bar{B} is the average magnetic field and δB is the strength of the fluctuating magnetic field [10.30]

$$f_q(s, t) \propto \begin{cases} \left(\frac{t}{s}\right)^{d(q-1)}, & \text{if } s \gg 1 \text{ and } t \gg 1, \\ s^{d(1-q)} t^{\tau(q)}, & \text{if } s \gg 1 \text{ and } t \ll 1, \\ \left(\frac{t}{s}\right)^{\tau(q)}, & \text{if } s \ll 1 \text{ and } t \ll 1. \end{cases} \quad (10.65)$$

In actual numerical calculations, it is convenient to choose the quantity $G_q = \log\langle\mu_l^q\rangle$ as a scaling variable instead of the moment $\langle\mu_l^q\rangle$ itself. The localization length exponent v and the critical parameter x_c , as well as the mass exponent $\tau(q)$, can be obtained by fitting $\log\langle\mu_l^q\rangle$ to the function

$$G_q = g_q(L^{1/v}|x - x_c|, l^{1/v}|x - x_c|). \quad (10.66)$$

In the fitting procedure, the above function is expanded around $x = x_c$ as in the case of the conventional finite-size scaling analysis [see (9.43)]. The present finite-size scaling analysis includes two scaling lengths L and l . It is therefore possible to perform this analysis for a fixed system size L . This saves a considerable amount of computing time compared to the conventional finite-size scaling analysis. In addition, (10.66) depends on the order q , while v and x_c are independent of q . This implies that v and x_c can be multiply determined by varying the value of q .

The efficiency of this scaling analysis is demonstrated by showing criticality of the Anderson transition in a 2D electron system subject to a random magnetic field with finite mean. Quantum transport and eigenstate properties of non-interacting 2D electrons in a random magnetic field have greatly stimulated theoretical and experimental interest [10.31], because strongly correlated 2D electrons in a magnetic field can be mapped onto this system [10.32]. It has been suggested by a semiclassical theory that the system is equivalent to a quantum Hall system if the average magnetic field \bar{B} is much larger than the strength of the fluctuating magnetic field δB and the correlation length of the random magnetic field is much longer than the cyclotron radius of the average field [10.33]. This prediction has been confirmed in terms of the above scaling analysis. Figure 10.13 shows the calculated scaling function g_q given by (10.66) for $q = 2$ and $\delta B/\bar{B} = 0.5$ [10.30]. Rescaled data of $\log\langle\mu_l^q\rangle$ (filled circles in Fig. 10.13) collapse onto a single scaling surface. This scaling analysis gives $v = 2.308 \pm 0.013$ and $D_2 = 1.614 \pm 0.026$, which agree quite well with those for the quantum Hall transition.

In this chapter, we have shown that the concept of multifractals is highly significant for understanding the Anderson transition. The relevance of multifractals is not, of course, restricted to the Anderson transition. There are vast numbers of physical systems exhibiting multifractality. It is interesting to seek the answer to the fundamental question as to why nature prefers fractals or multifractals. These investigations are now in progress.

Appendices

A. Multifractality of the HRN Model

The hierarchical resistor network (HRN) possesses almost all properties of multifractals which are characterized by exponents $\tau(q)$, D_q , $f(\alpha)$, and $z(q)$. Here we investigate analytical expressions for these exponents in the HRN model.

It seems that the multifractal measure of the HRN model is the voltage drop V_i of the i th bond. In a multifractal analysis, the measure μ_i should be normalized to $\sum_i \mu_i = 1$. The voltage drop V_i is, however, not normalized [$\sum_i V_i = (6/5)^n$ because of (4.11) with $q = 1$]. This is because the total voltage drop is fixed at unity. If the voltage drop V_i is normalized by $\sum_i v_i = 1$, where

$$v_i = \left(\frac{5}{6} \right)^n V_i , \quad (\text{A.1})$$

for the n th generation of the HRN, v_i can be a correct measure in the multifractal analysis. Below we discuss the multifractality of the distribution of normalized voltage drops v_i . For the normalized voltage-drop distribution, (4.9), (4.11), and (4.13) should be rewritten as

$$v_k = \frac{2^k}{6^n} , \quad (\text{A.2})$$

$$\langle v^q \rangle = \left[\frac{2}{6^q} (1 + 2^q) \right]^n , \quad (\text{A.3})$$

and

$$\tilde{\xi}_q = \frac{\log \left[\frac{2}{6^q} (1 + 2^q) \right]}{v \log 2} , \quad (\text{A.4})$$

where the exponent $\tilde{\xi}_q$ is defined by $\langle v^q \rangle \propto L^{\tilde{\xi}_q}$. Comparing this to the definition of the mass exponent $\tau(q)$, $\langle \mu^q \rangle \propto L^{-\tau(q)}$ [(4.18)], we have

$$\tau(q) = -\tilde{\xi}_q = -\frac{\log \left[\frac{2}{6^q} (1 + 2^q) \right]}{v \log 2} . \quad (\text{A.5})$$

The generalized dimension of the HRN model can be obtained from (A.5) and (4.24) as

$$D_q = \frac{\log \left[\frac{2}{6^q} (1 + 2^q) \right]}{\nu(1 - q) \log 2}. \quad (\text{A.6})$$

This equation [or (A.5)] gives the information dimension $D_1 (= D_1)$, the correlation dimension $D_{\text{co}} (= D_2)$, and the values of $D_{\pm\infty}$. The de l'Hôpital's theorem allows us to write D_1 as

$$D_1 = \lim_{q \rightarrow 1} \frac{\tau(q)}{q - 1} = \left. \frac{d\tau}{dq} \right|_{q=1}, \quad (\text{A.7})$$

and (A.5) gives

$$D_1 = \frac{1}{\nu} \left(\frac{1}{3} + \frac{\log 3}{\log 2} \right). \quad (\text{A.8})$$

The value of D_2 is directly calculated from (A.6) as

$$D_2 = \frac{\log \left(\frac{18}{5} \right)}{\nu \log 2}. \quad (\text{A.9})$$

Equations (4.32) and (A.5) lead to

$$D_\infty = \frac{\log 3}{\nu \log 2}, \quad (\text{A.10})$$

and

$$D_{-\infty} = \frac{\log 6}{\nu \log 2}. \quad (\text{A.11})$$

We can easily obtain the analytical expression for the correlation exponent $z(q)$ of the HRN model. From (A.5) and (4.62), $z(q)$ is calculated as

$$z(q) = \frac{2}{\nu} - \frac{1}{\nu \log 2} \log \frac{2(1 + 2^q)^2}{1 + 2^{2q}}, \quad (\text{A.12})$$

where we have used the relation $D_f = D_0 = -\tau(0) = 2/\nu$.

The multifractal spectrum $f(\alpha)$ for the HRN model is obtained as follows. Corresponding to (4.33) and (4.34), we have for the normalized voltage drop,

$$v_k \propto L^{-\alpha_k}, \quad (\text{A.13})$$

where

$$\alpha_k = \frac{1}{v \log 2} \left(\log 6 - \frac{k}{n} \log 2 \right), \quad (k = 0, 1, 2, \dots, n). \quad (\text{A.14})$$

Since α corresponds one-to-one to the index k , the number of bonds with voltage drop v_k can be expressed as $N(\alpha) = N(v_{k(\alpha)})$, where $N(v_{k(\alpha)})$ is equal to $N(V_k)$ given by (4.10), namely,

$$N(v_{k(\alpha)}) = 2^n \binom{n}{k}, \quad (\text{A.15})$$

and k is a function of α . From (4.6) and (A.15), the multifractal spectrum defined by (4.36) is given by

$$\begin{aligned} f(\alpha) &= \lim_{n \rightarrow \infty} \frac{\log \left[2^n \binom{n}{k} \right]}{n v \log 2} \\ &= \frac{1}{v \log 2} \left[\log 2 + \lim_{n \rightarrow \infty} \frac{1}{n} \log \binom{n}{k} \right]. \end{aligned} \quad (\text{A.16})$$

The limit in the second term in (A.16) is calculated as follows. Using the definition of the binomial coefficient and Stirling's formula for $n!$, we have

$$\begin{aligned} \lim_{n \rightarrow \infty} \frac{1}{n} \log \binom{n}{k} &= \lim_{n \rightarrow \infty} \frac{1}{n} \left\{ \log \left[\sqrt{2\pi} e^{-n} n^{n+\frac{1}{2}} \right] \right. \\ &\quad - \log \left[\sqrt{2\pi} e^{-k} k^{k+\frac{1}{2}} \right] \\ &\quad \left. - \log \left[\sqrt{2\pi} e^{-(n-k)} (n-k)^{n-k+\frac{1}{2}} \right] \right\}. \end{aligned} \quad (\text{A.17})$$

Since $k = 0, 1, 2, \dots, n$, the range of k diverges as $n \rightarrow \infty$, so we introduce a parameter $\xi = k/n$. This parameter ξ takes a value in the range $0 \leq \xi \leq 1$. Eliminating k in (A.17) by using ξ , the limit $n \rightarrow \infty$ is easily taken and we have

$$\lim_{n \rightarrow \infty} \frac{1}{n} \log \binom{n}{k} = -\xi \log \xi - (1-\xi) \log(1-\xi). \quad (\text{A.18})$$

Therefore, the exponent $f(\alpha)$ given by (A.16) yields

$$f(\alpha) = \frac{1}{v \log 2} [\log 2 - \xi \log \xi - (1-\xi) \log(1-\xi)]. \quad (\text{A.19})$$

The Lipschitz–Hölder exponent α given by (A.14) can also be expressed in terms of ξ as

$$\alpha = \frac{1}{v \log 2} (\log 6 - \xi \log 2). \quad (\text{A.20})$$

Replacing the parameter ξ in (A.19) by α , we have

$$\begin{aligned} f(\alpha) = \frac{1}{\nu} - \frac{1}{\nu \log 2} & \left[\left(\frac{\log 6}{\log 2} - \alpha \nu \right) \log \left(\frac{\log 6}{\log 2} - \alpha \nu \right) \right. \\ & \left. + \left(\alpha \nu - \frac{\log 3}{\log 2} \right) \log \left(\alpha \nu - \frac{\log 3}{\log 2} \right) \right]. \end{aligned} \quad (\text{A.21})$$

The Legendre transform of the mass exponent $\tau(q)$ of the HRN model surely reproduces the multifractal spectrum (A.21). From (A.5) and (4.45), the Lipschitz–Hölder exponent α is calculated as

$$\alpha = \frac{1}{\nu \log 2} \left(\log 6 - \frac{2^q}{1+2^q} \log 2 \right). \quad (\text{A.22})$$

The Legendre transform of $\tau(q)$ given by (A.5) leads to

$$f[\alpha(q)] = \frac{1}{\nu \log 2} \left[\log(1+2^q) + \log 2 - \frac{2^q}{1+2^q} \log 2^q \right]. \quad (\text{A.23})$$

Since q runs over the range $(-\infty, \infty)$, the parameter $\xi \equiv 2^q/(1+2^q)$ takes a value within $0 < \xi < 1$. Using the parameter ξ instead of q , (A.23) becomes

$$\begin{aligned} f(\alpha) &= \frac{1}{\nu \log 2} \left[\log(1+2^q) + \log 2 - \frac{2^q}{1+2^q} \log \frac{2^q}{1+2^q} - \frac{2^q}{1+2^q} \log(1+2^q) \right] \\ &= \frac{1}{\nu \log 2} [\log 2 - \xi \log \xi - (1-\xi) \log(1-\xi)]. \end{aligned} \quad (\text{A.24})$$

The Lipschitz–Hölder exponent is found to be

$$\alpha = \frac{1}{\nu \log 2} (\log 6 - \xi \log 2). \quad (\text{A.25})$$

Equations (A.24) and (A.25) are the same as (A.19) and (A.20), respectively. We therefore get the same expression for $f(\alpha)$ as (A.21) from the Legendre transform of $\tau(q)$.

We see below that the multifractal spectrum (A.21) satisfies all general properties of $f(\alpha)$, as discussed in Sect. 4.7. In the HRN model, α_{\max} and α_{\min} calculated from $\lim_{q \rightarrow \pm\infty} \alpha(q)$, where $\alpha(q)$ is given by (A.22), are

$$\alpha_{\max} = \frac{\log 6}{\nu \log 2}, \quad (\text{A.26})$$

$$\alpha_{\min} = \frac{\log 3}{\nu \log 2}. \quad (\text{A.27})$$

Substituting these values into (A.21), both $f(\alpha_{\max})$ and $f(\alpha_{\min})$ are equal to $1/\nu$. This means that

$$f_{-\infty} = f_{\infty} = \frac{1}{\nu}, \quad (\text{A.28})$$

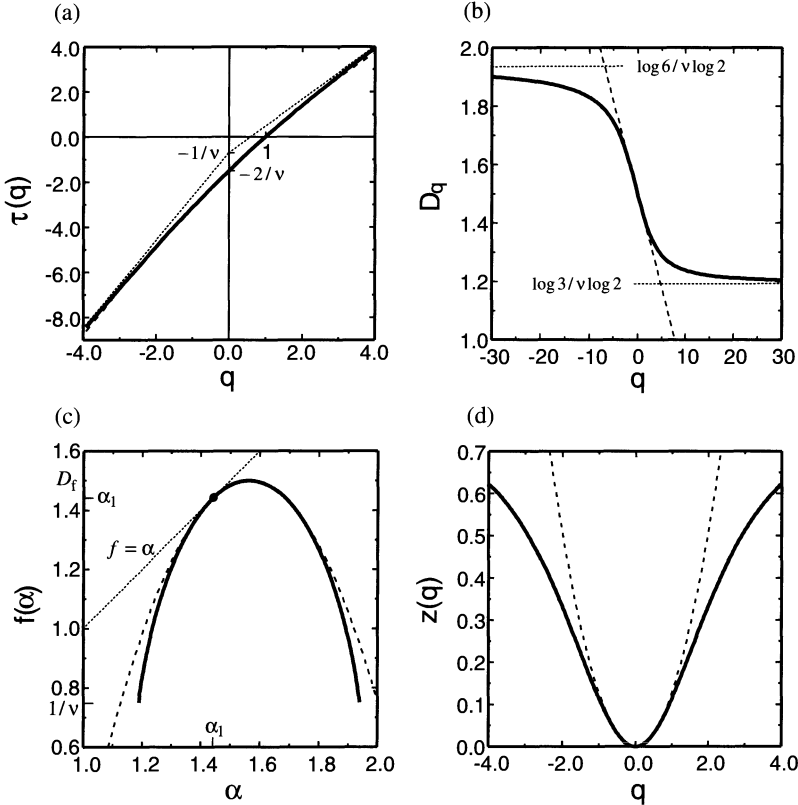


Fig. A.1. (a) Mass exponent $\tau(q)$, (b) generalized dimension D_q , (c) multifractal spectrum $f(\alpha)$, and (d) correlation exponent $z(q)$ for the hierarchical resistor network (HRN) model. Explicit expressions are given by (A.5), (A.6), (A.20), and (A.12), respectively. *Dashed curves* represent profiles within the parabolic approximation. The *dashed curve* for $\tau(q)$ is almost completely covered by the *solid line*

where $f_{\pm\infty}$ are defined by (4.66) and (4.73). The reason for the nonzero $f_{-\infty}$ or f_∞ is that the number of bonds with the smallest or largest voltage drop in this model depends on the system size L . Bonds with the largest or smallest voltage drop are links or bonds belonging to the mostly nested blobs, respectively. As mentioned in Sect. 4.1, the number of links L_1 is proportional to $L^{1/\nu}$, which implies that $1/\nu$ is the fractal dimension of links. Since the number of bonds belonging to the mostly nested blobs is the same as the number of links, $1/\nu$ is also the fractal dimension of bonds with the smallest voltage drop. Since f_∞ and $f_{-\infty}$ are fractal dimensions of the largest and the smallest measures, (A.28) is reasonable. The fractal dimension of the support is calculated from $-\tau(0)$ as

$$D_f = \frac{2}{\nu}. \quad (\text{A.29})$$

This is, of course, identical to $\tilde{\zeta}_B$ defined below (4.8). The value of α_0 giving the maximum value of $f(\alpha)$ can be obtained from (A.22) with $q = 0$ as

$$\alpha_0 = \frac{\log 3\sqrt{2}}{\nu \log 2} . \quad (\text{A.30})$$

Substituting this into (A.21) gives $f(\alpha_0) = 2/\nu = D_f$, and (4.84) is confirmed. From (A.22), the Lipschitz–Hölder exponent α_1 corresponding to $q = 1$ is given by

$$\alpha_1 = \frac{1}{\nu \log 2} \left(\log 3 + \frac{1}{3} \log 2 \right) . \quad (\text{A.31})$$

The relation (4.87) [$f(\alpha_1) = \alpha_1$] can be directly confirmed by (A.21). Profiles of $\tau(q)$, D_q , $f(\alpha)$, and $z(q)$ for the HRN model, whose explicit expressions are given by (A.5), (A.6), (A.21), and (A.12), respectively, are shown in Fig. A.1. Dashed lines in Fig. A.1 indicate the parabolic approximations to $\tau(q)$, D_q , $f(\alpha)$, and $z(q)$ for the HRN model, whose explicit functional forms are obtained by substituting (A.29) and (A.30) into (4.90), (4.91), (4.89), and (4.92), respectively.

B. Spectral Dimensions for Deterministic Fractals

In this appendix, we obtain analytical expressions for the spectral dimension \tilde{d}_s of the Sierpinski gasket and the Mandelbrot–Given fractal. The spectral dimension \tilde{d}_s describes vibrational properties such as the density of states and the dispersion relation, as well as diffusive properties such as the return probability and the mean-squared displacement on a fractal system. Here, we derive the expressions for \tilde{d}_s by means of atomic vibrations with scalar displacements.

B.1 Sierpinski Gasket

The Sierpinski gaskets form a family of deterministic self-similar structures, which can be constructed in any Euclidean dimension (see Figs. 2.2 or B.1 for 2D systems). Their fractal dimension is known to be $D_f = \log(d+1)/\log 2$. The equation of motion for scalar displacement u_1 of particle 1 with mass m in Fig. B.1 is given by

$$m\ddot{u}_1 = K \sum_i (u_i - u_1) , \quad (\text{B.1})$$

where K is the spring constant between nearest-neighbor particles, and the summation is taken over all the nearest neighbors of the site 1. The equation of motion (B.1) can be rewritten as an equation for amplitudes of the eigenmode belonging to the eigenfrequency ω . Denoting such amplitudes in vibrations of u_1, \dots, U_3 by x_1, \dots, X_3 , respectively, we have

$$(\lambda - 4)x_1 + x_2 + x_3 = -X_2 - X_3 , \quad (\text{B.2})$$

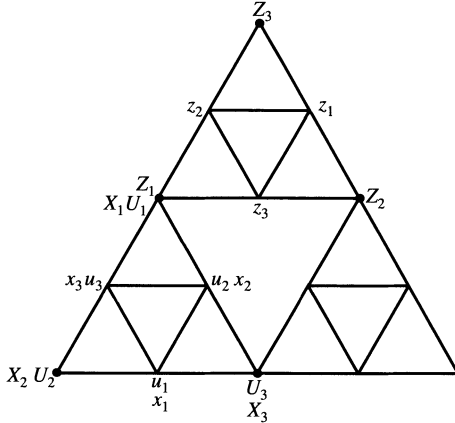


Fig. B.1. The second generation of the 2D Sierpinski gasket. Symbols u_i and U_i denote displacements of the vibrating sites they label. Symbols x_i , X_i , z_i , and Z_i represent eigenmode amplitudes belonging to the eigenfrequency ω at the sites they label

where $\lambda = \omega^2/\omega_0^2$ with $\omega_0 = \sqrt{K/m}$. Sites corresponding to x_1, \dots, X_3 are depicted in Fig. B.1. By the same procedure, we obtain similar relations for x_2 and x_3 ,

$$x_1 + (\lambda - 4)x_2 + x_3 = -X_3 - X_1 , \quad (\text{B.3})$$

and

$$x_1 + x_2 + (\lambda - 4)x_3 = -X_1 - X_2 . \quad (\text{B.4})$$

From (B.2)–(B.4), we obtain

$$x_2 + x_3 = -\frac{2(\lambda - 4)X_1 + (\lambda - 6)(X_2 + X_3)}{(\lambda - 2)(\lambda - 5)} . \quad (\text{B.5})$$

Noting that $X_1 = Z_1$, we have a similar relation to (B.5) for $z_2 + z_3$, which is written in the form

$$z_2 + z_3 = -\frac{2(\lambda - 4)Z_1 + (\lambda - 6)(Z_2 + Z_3)}{(\lambda - 2)(\lambda - 5)} . \quad (\text{B.6})$$

On the other hand, the equation for X_1 is

$$\lambda X_1 = 4X_1 - (x_2 + x_3 + z_2 + z_3) . \quad (\text{B.7})$$

Substituting (B.5) and (B.6) into (B.7) yields

$$\lambda' X_1 = 4X_1 - (X_2 + X_3 + Z_2 + Z_3) , \quad (\text{B.8})$$

where

$$\lambda' = \lambda(5 - \lambda) . \quad (\text{B.9})$$

Equation (B.8) giving a relation between capital letters can be regarded as a renormalized version of (B.7) with the renormalized frequency λ' . The relation (B.9) is valid only for the 2D Sierpinski gasket. The general form of the renormalized frequency λ' for a d -dimensional gasket is given by

$$\lambda' = \lambda(d + 3 - \lambda). \quad (\text{B.10})$$

At lower frequencies, i.e., $\lambda = \omega^2/\omega_0^2 \ll 1$, we obtain from (B.10)

$$\omega'^2 = (d + 3)\omega^2. \quad (\text{B.11})$$

If ω is the eigenfrequency of the Sierpinski gasket of size L , the renormalized frequency ω' is that of size $L/2$, namely, $\omega' = \omega(L/2)$. Thus, the relation (B.11) leads to

$$\omega(L/2) = (d + 3)^{1/2}\omega(L). \quad (\text{B.12})$$

Assuming the dispersion relation $\omega \propto L^{-a}$ [(5.41)], the eigenfrequency satisfies

$$\omega(L/b) = b^a\omega(L), \quad (\text{B.13})$$

where b is a scaling factor. Comparing (B.12) with (B.13) gives

$$a = \frac{\log(d + 3)}{2 \log 2}. \quad (\text{B.14})$$

This is the exact expression for the exponent a for the dispersion relation of the Sierpinski gasket.

Using the relation $a = D_f/\tilde{d}_s$ from (5.44), where $D_f = \log(d + 1)/\log 2$ for the Sierpinski gaskets, we obtain the spectral dimension \tilde{d}_s of the d -dimensional Sierpinski gasket as

$$\tilde{d}_s = \frac{2 \log(d + 1)}{\log(d + 3)}. \quad (\text{B.15})$$

We see from (B.15) that the upper bound of \tilde{d}_s for the Sierpinski gaskets is 2. This upper bound is a general result for fractal systems in which renormalization treatments are applicable. It should be noted that the three dimensions, d , D_f , and \tilde{d}_s , calculated for the Sierpinski gasket family are ordered according to

$$d > D_f > \tilde{d}_s. \quad (\text{B.16})$$

B.2 Mandelbrot–Given Fractal

For the Mandelbrot–Given fractal, it is difficult to apply similar arguments to evaluate the value of \tilde{d}_s . This is because sites in the Mandelbrot–Given fractal are not equivalent to each other, while all sites except for apexes of the whole triangle are

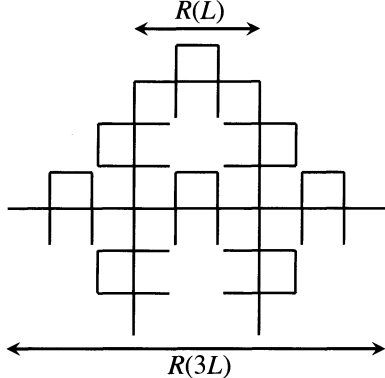


Fig. B.2. The second generation of the Mandelbrot–Given fractal. The resistance of the Mandelbrot–Given fractal of size x is $R(x)$

equivalent in the case of the Sierpinski gasket. Thus, we will have different renormalized frequencies depending on the choice of renormalized site. Using an alternative method, however, the analytical expression of \tilde{d}_s for the Mandelbrot–Given fractal is easily obtained as follows. We first calculate the resistance of the n th generation of the Mandelbrot–Given fractal (see Fig. B.2). Assuming that the resistance of the $(n-1)$ th generation of size L is $R(L)$, the resistance of the n th generation of size $3L$ is given by

$$R(3L) = \frac{11}{4} R(L) . \quad (\text{B.17})$$

If we denote $R(L) \propto L^\zeta$, we have

$$\zeta = \frac{\log 11 - \log 4}{\log 3} . \quad (\text{B.18})$$

This exponent ζ can be related to the diffusion exponent \tilde{d}_w through the Einstein relation

$$\sigma_{dc} \propto nD , \quad (\text{B.19})$$

where σ_{dc} is the dc conductivity, n the particle density, and D the diffusion coefficient. Since diffusion on fractals is anomalous, D depends on time t . From the relation $\langle r^2(t) \rangle \propto t^{2/\tilde{d}_w}$ [(5.15)], the effective diffusion coefficient D defined by $\langle r^2(t) \rangle \propto Dt$ is given by

$$D \propto t^{2/\tilde{d}_w - 1} . \quad (\text{B.20})$$

At times satisfying $\langle r^2(t) \rangle \approx L^2$, the diffusion coefficient becomes

$$D \propto L^{2-\tilde{d}_w} . \quad (\text{B.21})$$

The density n in (B.19) is proportional to the density of sites, i.e.,

$$n \propto L^{D_f - d} . \quad (\text{B.22})$$

Therefore, (B.19) becomes

$$\sigma_{dc} \propto L^{2 - \tilde{d}_w + D_f - d} . \quad (\text{B.23})$$

On the other hand, the conductivity σ_{dc} is related to the conductance G and the resistance R by

$$\sigma_{dc} = L^{2-d} G = \frac{L^{2-d}}{R} . \quad (\text{B.24})$$

The relation $R \propto L^\zeta$ gives

$$\sigma_{dc} \propto L^{2-d-\zeta} . \quad (\text{B.25})$$

Comparing (B.23) and (B.25), we obtain the scaling relation

$$\tilde{d}_w = D_f + \zeta . \quad (\text{B.26})$$

Since ζ is given by (B.18) and $D_f = \log 8 / \log 3$ for the Mandelbrot–Given fractal, the diffusion exponent \tilde{d}_w is expressed as

$$\tilde{d}_w = \frac{\log 22}{\log 3} . \quad (\text{B.27})$$

Therefore, the spectral dimension defined by (5.19) is given by

$$\tilde{d}_s = \frac{2 \log 8}{\log 22} = 1.345 \dots . \quad (\text{B.28})$$

To summarize, the spectral (or fracton) dimension can be obtained exactly for deterministic fractals. In the case of the d -dimensional Sierpinski gasket, the spectral dimension is expressed by (B.15), which is always less than 2. For the Mandelbrot–Given fractal, \tilde{d}_s is given by (B.28). It should be noted that the value of the spectral dimension \tilde{d}_s for the Mandelbrot–Given fractal is close to $\tilde{d}_s \approx 4/3$ for percolating networks, in addition to the similarity of the fractal dimension D_f . This is because the Mandelbrot–Given fractal has a nodes–links–blobs structure, as in the case of percolating networks.

C. Diffusion and Dynamics on Networks

The diffusion of a random walker on a network is described by the master equation

$$\frac{dP_i}{dt} = \sum_{j \neq i} w_{ij} (P_j - P_i) , \quad (\text{C.1})$$

where P_i is the occupation probability of the diffusing particle on site i , and w_{ij} is the probability that the diffusing particle hops from site i to j , with the relation $w_{ij} = w_{ji}$. Introducing new quantities W_{ij} defined by $W_{ij} = w_{ij}$ if $i \neq j$ and $W_{ii} = -\sum_{j \neq i} w_{ij}$, the master equation (C.1) can be written as

$$\frac{dP_i}{dt} = \sum_j W_{ij} P_j . \quad (\text{C.2})$$

From the definition of W_{ij} , we have

$$\sum_j W_{ij} = 0 , \quad (\text{C.3})$$

which guarantees the conservation of the transition probability.

If we consider a conducting network with conductance G_{ij} of the bond (ij) , we have an equation for RC circuits taking the same form as (C.1), i.e.,

$$C \frac{dV_i}{dt} = \sum_{j \neq i} G_{ij} (V_j - V_i) , \quad (\text{C.4})$$

where V_i is the voltage at site i and C the capacitance. This relation comes from the current conservation law (Kirchhoff's equation), because the current I_i coming into the site i is

$$I_i = \frac{dq_i}{dt} = C \frac{dV_i}{dt} , \quad (\text{C.5})$$

where $q_i = CV_i$ is the charge at site i . The similarity between (C.4) and (C.1) implies that the problem of the RC circuit can be reduced to the diffusion problem described by the master equation. As seen from this example, the master equation plays a key role in understanding many types of dynamics in network systems. We give below detailed relations between diffusion and atomic vibrations, spin waves, and superconducting properties.

C.1 Atomic Vibrations

The equation of motion for atomic vibrations with scalar displacements is given by

$$\ddot{u}_i = \sum_j K_{ij} u_j , \quad (\text{C.6})$$

where u_i is the displacement of the atom at site i , and K_{ij} ($i \neq j$) is given by $K_{ij} = k_{ij}/m_i$, with k_{ij} the spring constant connecting two atoms at sites i and j and m_i the mass. The diagonal element K_{ii} is obtained from the condition for the balance of forces at site i ,

$$\sum_j K_{ij} = 0 . \quad (\text{C.7})$$

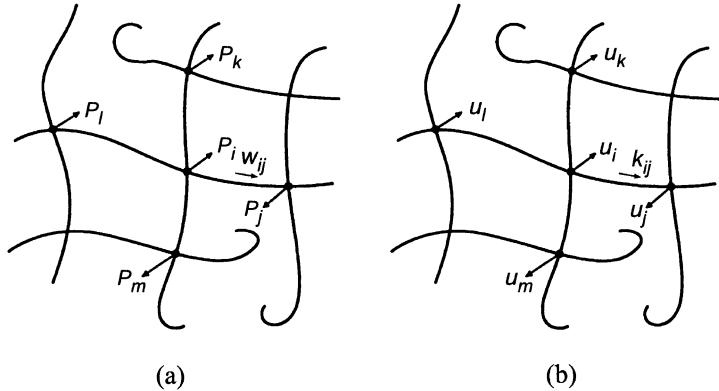


Fig. C.1. Equivalence between (a) diffusion and (b) atomic vibrations on a network. The relation satisfied by the occupation probability P_i of a diffusing particle is given by (C.2), and the relation satisfied by the displacement u_i of the atomic vibration is given by (C.6), which takes the same form as (C.2), except for the order of the time derivatives

This reflects the translational symmetry of the system, i.e., the uniform translation ($u_i \rightarrow u_i + u_0$) gives rise to no additional energy. Note that the difference between (C.2) and (C.6) is only of the order of the time derivatives. This indicates that these equations are equivalent as eigenvalue problems. This statement is expressed by the following correspondence between derivatives and eigenvalues:

$$\frac{d}{dt} \rightarrow -\omega , \quad (\text{C.8})$$

and

$$\frac{d^2}{dt^2} \rightarrow -\omega^2 . \quad (\text{C.9})$$

Figure C.1 shows the corresponding relations between diffusion and atomic vibrations on a network.

The equivalence between (C.2) and (C.6) relates the return probability of a diffusing particle to the spectral density of states of atomic vibrations. The Laplace transform of (C.2) is

$$\omega \tilde{P}_i(\omega) - \sum_j W_{ij} \tilde{P}_j(\omega) = P_i(0) , \quad (\text{C.10})$$

where $\tilde{P}_i(\omega)$ is defined by

$$\tilde{P}_i(\omega) = \int_0^\infty P_i(t) e^{-\omega t} dt . \quad (\text{C.11})$$

Taking the initial condition as

$$P_i(0) = \delta_{i0} , \quad (\text{C.12})$$

$\tilde{P}_i(\omega)$ represents the Green function of the master equation (C.2). The spectral density of states $\mathcal{D}(\omega)$ for (C.2) is given by [C.1, C.2]

$$\mathcal{D}(\omega) = -\frac{1}{\pi} \text{Im } \tilde{P}_0(-\omega + i0^+) . \quad (\text{C.13})$$

This relation can be understood by considering the partial differential equation for continuous diffusion given by

$$\frac{\partial P(x, t)}{\partial t} - \frac{\partial^2 P(x, t)}{\partial x^2} = 0 , \quad (\text{C.14})$$

where $P(x, t)$ is the probability of finding a particle at position x and time t . The diffusion constant is assumed to be unity. Under the initial condition

$$P(x, 0) = \delta(x) , \quad (\text{C.15})$$

corresponding to (C.12), the Laplace transform of (C.14) becomes

$$\omega \tilde{P}(x, \omega) - \frac{\partial^2}{\partial x^2} \tilde{P}(x, \omega) = \delta(x) . \quad (\text{C.16})$$

The function $\tilde{P}(0, \omega)$ is the Green function of the diffusion equation (C.14). The Fourier transform of (C.16) yields

$$\Pi(k, \omega) = \frac{1}{\omega + k^2} , \quad (\text{C.17})$$

where $\Pi(k, \omega)$ is the Fourier transform of $\tilde{P}(x, \omega)$ with respect to x . Using $\Pi(k, \omega)$, the Green function $\tilde{P}(0, \omega)$ can be expressed as

$$\tilde{P}(0, \omega) = \int_{-\infty}^{\infty} \Pi(k, \omega) dk . \quad (\text{C.18})$$

From (C.17), the function $\Pi(k, -\omega + i0^+)$ is written as

$$\Pi(k, -\omega + i0^+) = \frac{1}{-\omega + k^2} - i\pi\delta(\omega - k^2) , \quad (\text{C.19})$$

The relation (C.18) thus gives

$$\mathcal{D}(\omega) = -\frac{1}{\pi} \text{Im } \tilde{P}(0, -\omega + i0^+) . \quad (\text{C.20})$$

Here the definition of the spectral density of states $\mathcal{D}(\omega) = \sum_k \delta(\omega - k^2)$ has been used. We expect a similar relation to (C.20) to hold for the master equation describing diffusion on a discrete lattice. We thus have (C.13). A rigorous derivation of (C.13) is presented in [C.1]. The relationship between time derivatives and eigenvalues

[(C.8) and (C.9)] gives the spectral density of states $D(\omega^2)$ for the atomic vibration as $D(\omega^2) = \mathcal{D}(\omega)$. Hence,

$$D(\omega^2) = -\frac{1}{\pi} \text{Im } \tilde{P}_0(-\omega^2 + i0^+) , \quad (\text{C.21})$$

or, using the relation $D(\omega^2)d\omega^2 = D(\omega)d\omega$ with $d\omega^2 = 2\omega d\omega$,

$$D(\omega) = -\frac{2\omega}{\pi} \text{Im } \tilde{P}_0(-\omega^2 + i0^+) . \quad (\text{C.22})$$

The relation (C.21) [or (C.22)] shows that we can calculate the spectral density of states for the atomic vibration with scalar displacements from the Laplace transform of the return probability $P_0(t)$ of the corresponding diffusion problem.

It is also possible to relate eigenmodes of (C.6) to $P(r, t)$ in the diffusion problem. We denote the orthonormal eigenvector for the dynamical matrix $\{K_{ij}\}$ in (C.6) belonging to an eigenfrequency ω_λ by ψ_i^λ , where λ is the index of the eigenvalue. An arbitrary displacement $u_i(t)$ can be expanded as

$$u_i(t) = \sum_{\lambda} C_{\lambda} \psi_i^{\lambda} e^{-i\omega_{\lambda} t} , \quad (\text{C.23})$$

where C_{λ} is an expansion coefficient. Here we impose the initial condition

$$u_i(0) = \delta_{i0} . \quad (\text{C.24})$$

From (C.23), we have

$$u_i(0) = \sum_{\lambda} C_{\lambda} \psi_i^{\lambda} . \quad (\text{C.25})$$

Multiplying (C.25) by $\psi_i^{\lambda'}$ and carrying out the summation over i , the coefficient C_{λ} is given by

$$C_{\lambda} = \psi_0^{\lambda} . \quad (\text{C.26})$$

Here we have used the relation (C.24) and the orthonormality condition $\sum_i \psi_i^{\lambda} \psi_i^{\lambda'} = \delta_{\lambda\lambda'}$. Substituting (C.26) into (C.23) yields

$$u_i(t) = \sum_{\lambda} \psi_0^{\lambda} \psi_i^{\lambda} e^{-i\omega_{\lambda} t} . \quad (\text{C.27})$$

Similar arguments for the corresponding master equation (C.2) lead to

$$P_i(t) = \sum_{\lambda} \psi_0^{\lambda} \psi_i^{\lambda} e^{-\omega_{\lambda}^2 t} . \quad (\text{C.28})$$

If the system is isotropic, the ensemble-averaged $P_i(t)$ becomes a function of t and the radial distance r between the site i and the origin. In this case, (C.28) gives

$$P(r, t) = \sum_{\lambda} \phi_{\lambda}(r) e^{-\omega_{\lambda}^2 t}, \quad (\text{C.29})$$

where $\phi_{\lambda}(r)$ is the ensemble average of $\psi_0^{\lambda} \psi_i^{\lambda}$, i.e., $\phi_{\lambda}(r) = \langle \psi_0^{\lambda} \psi_i^{\lambda} \rangle$. The summation over λ in (C.29) can be replaced by integration with respect to ω , by introducing the spectral density of states $D(\omega)$, and we obtain

$$P(r, t) = \int_0^{\infty} D(\omega) \phi(r, \omega) e^{-\omega^2 t} d\omega. \quad (\text{C.30})$$

We should note that $D(\omega)$ is normalized to unity.

C.2 Spin Waves in Diluted Ferro- and Antiferromagnets

Spin waves in magnets provide another example of dynamics equivalent to particle diffusion. The Heisenberg Hamiltonian for a spin system is written as

$$H = \frac{1}{2} \sum_{i,j} J_{ij} \mathbf{S}_i \cdot \mathbf{S}_j, \quad (\text{C.31})$$

where \mathbf{S}_i is the spin angular momentum at site i and J_{ij} the exchange integral. This Hamiltonian describes ferromagnets when $J_{ij} < 0$ and antiferromagnets when $J_{ij} > 0$. Elementary excitations of this spin system are collective spin deviations called spin waves or magnons when quantized. The collective motions are rotations of spin directions around the directions of ordered spins. To describe this rotational spin motion, we introduce the quantities $S_i^{\pm} = S_i^x \pm iS_i^y$, whereby the Hamiltonian becomes

$$H = \frac{1}{2} \sum_{i,j} J_{ij} \left[\frac{1}{2} (S_i^+ S_j^- + S_i^- S_j^+) + S_i^z S_j^z \right]. \quad (\text{C.32})$$

This Hamiltonian leads to the Heisenberg equation

$$i\hbar \frac{\partial S_i^+}{\partial t} = \frac{1}{2} \sum_{j \neq i} J_{ij} \left\{ [S_i^+, S_i^+ S_j^- + S_i^- S_j^+] + [S_i^+, S_i^z S_j^z] \right\}. \quad (\text{C.33})$$

Using the relations $[S_i^+, S_j^-] = 2\delta_{ij} S_i^z$ and $[S_i^z, S_j^{\pm}] = \pm\delta_{ij} S_i^{\pm}$ in (C.33), we have the equation of motion for spin waves

$$i\hbar \frac{\partial S_i^+}{\partial t} = \sum_{j \neq i} J_{ij} (S_i^z S_j^+ - S_i^z S_j^+). \quad (\text{C.34})$$

If the amplitude of spin waves is small, namely, $S_i^x, S_i^y \approx S$, we can replace S_i^z by S for the ferromagnetic case. Thus, (C.33) can be approximated by a linearized equation of the form

$$i\hbar \frac{\partial S_i^+}{\partial t} = \sum_{j \neq i} j_{ij} (S_j^+ - S_i^+) , \quad (\text{C.35})$$

where $j_{ij} = SJ_{ij}$. This equation is equivalent to (C.1).

For antiferromagnets, we replace $S_i^z = S$ used in (C.35) by $S_i^z = \sigma_i S$, where $\sigma_i = -1$ for down spins and $\sigma_i = 1$ for up spins. We then have the linearized equation of motion for antiferromagnetic spin waves

$$i\hbar \frac{\partial S_i^+}{\partial t} = \sigma_i \sum_{j \neq i} j_{ij} (S_j^+ + S_i^+) . \quad (\text{C.36})$$

We should note how this differs from (C.35), i.e., there is a prefactor σ_i in (C.36) and the second term on the right-hand side has a different sign. This is crucial when characterizing the difference between spin waves in diluted ferromagnets and in antiferromagnets.

C.3 Superconducting Networks

It is now possible to fabricate superconducting networks with the advent of modern microfabrication. An example is the superconducting fractal network. The linearized equation describing superconducting states in networks is derived from the Ginzburg–Landau free energy, as shown below [C.3].

The order parameter $\Delta(\mathbf{r})$ of a superconductor is a pair potential or a local energy gap. The free-energy density can be expanded in terms of $\Delta(\mathbf{r})$ as

$$F = F_0 + a|\Delta(\mathbf{r})|^2 + \frac{b}{2}|\Delta(\mathbf{r})|^4 + c \left| \hat{\mathbf{u}} \cdot \left(-i\hbar\nabla + \frac{2e\mathbf{A}}{\hbar c} \right) \Delta(\mathbf{r}) \right|^2 , \quad (\text{C.37})$$

where \mathbf{A} is the vector potential and $\hat{\mathbf{u}}$ is a unit vector along a bond. Provided that $\Delta(\mathbf{r})$ is small at $T \rightarrow T_c$ or $H \rightarrow H_{c2}$, we can neglect the term proportional to $|\Delta(\mathbf{r})|^4$. The equilibrium equation is obtained from the condition $\delta \int F d\mathbf{r} = 0$ as

$$-\frac{\Delta(s)}{\xi_{sc}^2} + \left(i \frac{\partial}{\partial s} - \kappa \right)^2 \Delta(s) = 0 , \quad (\text{C.38})$$

where $\kappa = 2e\hat{\mathbf{u}} \cdot \mathbf{A}/(\hbar c)$, $s = \hat{\mathbf{u}} \cdot \mathbf{r}$, and $\xi_{sc}^{-2} = -a/c$. Substituting the solution $\Delta(s) = f(s)e^{-i\kappa s}$ into (C.38), we have

$$-\frac{f(s)}{\xi_{sc}^2} + \frac{\partial^2 f(s)}{\partial s^2} = 0 . \quad (\text{C.39})$$

From this equation, the solution of (C.38) becomes

$$\Delta(s) \propto e^{-i\kappa s} (\alpha e^{is/\xi_{sc}} + \beta e^{-is/\xi_{sc}}) . \quad (\text{C.40})$$

We consider the boundary conditions $\Delta_{ij}(i) = \Delta_i$ and $\Delta_{ij}(j) = \Delta_j$, where $\Delta_{ij}(i)$ is the order parameter at the terminal site i on the bond (ij) . These boundary conditions

guarantee matching $\Delta(s)$ at the nodes. Using these conditions to determine α and β in (C.40), we have

$$\Delta_{ij}(s) = \left\{ \Delta_i \frac{\sin[(l_{ij} - s)/\xi_{sc}]}{\sin \theta_{ij}} + \Delta_j e^{i\gamma_{ij}} \frac{\sin(s/\xi_{sc})}{\sin \theta_{ij}} \right\} e^{-ik_{ij}s}, \quad (\text{C.41})$$

where l_{ij} is the length of the bond (ij) , $\theta_{ij} = l_{ij}/\xi_{sc}$, and $\gamma_{ij} = \int_i^j \kappa_{ij} ds \approx \kappa_{ij} l_{ij}$.

We impose Kirchhoff's law at node i . This is given by

$$\sum_{j \neq i} \left(i \frac{\partial}{\partial s_{ij}} - \kappa_{ij} \right) \Delta_{ij}(s) \Big|_i = 0. \quad (\text{C.42})$$

Substituting (C.41) into (C.42), we have

$$-\frac{\Delta_i}{\xi_{sc}} \sum_{j \neq i} \cot \theta_{ij} + \frac{1}{\xi_{sc}} \sum_{j \neq i} \frac{\Delta_j e^{i\gamma_{ij}}}{\sin \theta_{ij}} = 0. \quad (\text{C.43})$$

Using the trigonometric relation $\tan(x/2) - (1/\sin x) = -\cot x$, we can rewrite this equation as

$$-\frac{m_i \Delta_i}{\xi_{sc}^2} = \sum_{j \neq i} d_{ij} (\eta_{ij} \Delta_j - \Delta_i), \quad (\text{C.44})$$

where

$$\eta_{ij} = e^{i\gamma_{ij}}, \quad (\text{C.45})$$

$$d_{ij} = \frac{1}{\xi_{sc} \sin \theta_{ij}}, \quad (\text{C.46})$$

and

$$m_i = \frac{1}{\xi_{sc} \sum_{j \neq i} \tan(\theta_{ij}/2)}. \quad (\text{C.47})$$

Equation (C.44) is the basic equation for superconducting networks.

If the magnetic field is absent, the quantity η_{ij} becomes unity. In this case, (C.44) takes the same structure as the eigenvalue equation for network vibrations. The corresponding relations between superconducting networks and elastic networks are summarized as

$$\Delta_i \longrightarrow u_i,$$

$$d_{ij} \longrightarrow K_{ij},$$

$$m_i \longrightarrow \text{mass},$$

and

$$1/\xi^2 \longrightarrow \text{eigenvalue}.$$

The equivalence between these problems implies that superconducting properties of networks can be understood by solving the corresponding diffusion or vibrational problems.

D. Wigner Distributions

Here we derive the Wigner distribution functions (9.32)–(9.34) for Hamiltonians belonging to the Gaussian orthogonal ensemble (GOE), the Gaussian unitary ensemble (GUE), and the Gaussian symplectic ensemble (GSE). An arbitrary Hamiltonian H belonging to the GOE, the GUE, or the GSE is mapped onto a Hamiltonian H' in the same ensemble by an orthogonal, unitary, or symplectic transformation. Hence, these ensembles are invariant under such transformations. This invariance can be written as

$$R(H')dH' = R(H)dH , \quad (\text{D.1})$$

where $R(H)dH$ is the probability that the Hamiltonian H has its matrix elements in the volume element $dH = \prod_{i < j} dH_{ij}$. Since the matrix elements of H are statistically independent, the probability density $R(H)$ can be written as

$$R(H) = \prod_{i < j} f_{ij}(H_{ij}) , \quad (\text{D.2})$$

where f_{ij} is a function of a single matrix element. A mathematical consequence drawn from (D.1) and (D.2) is that the probability density (the matrix-element distribution function) $R(H)$ should take the form [D.1]

$$R(H) = \exp(-\alpha \text{tr} H^2 + \beta \text{tr} H + \gamma) , \quad (\text{D.3})$$

where α is a real positive constant and β must be real. γ is determined by the normalization condition.

Let us find the level-spacing distribution function $P(s)$ for the extended regime. The random matrix theory gives precise forms of $P(s)$ for the GOE, the GUE, and the GSE after mathematical manipulations. Here, we calculate $P(s)$ by reducing the order of Hamiltonian matrices, which approximates $P(s)$ well without mathematical complexity. The quantities α and β in (D.3) are fixed as $\alpha = 1/2$ and $\beta = 0$, for simplicity. We start with the GOE. In this case, the general form of a random Hamiltonian matrix with the smallest order is a 2×2 real symmetric matrix

$$H = \begin{pmatrix} r_1 + r_2 & r_3 \\ r_3 & r_1 - r_2 \end{pmatrix} , \quad (\text{D.4})$$

where r_1 , r_2 , and r_3 are real constants. Using (D.3), the distribution function of the matrix elements is then given by

$$R(H) = \frac{1}{\pi^{3/2}} \exp \left[-(r_1^2 + r_2^2 + r_3^2) \right] . \quad (\text{D.5})$$

On the other hand, the difference between two eigenvalues of H , i.e., the level spacing $\Delta(H)$, is

$$\Delta(H) = 2\sqrt{r_2^2 + r_3^2} . \quad (\text{D.6})$$

Thus, the probability density $P(\Delta)$ that the level spacing $\Delta(H)$ coincides with Δ is given by

$$\begin{aligned} P(\Delta) &= \int R(H)\delta[\Delta - \Delta(H)] dH \\ &= \frac{1}{\pi^{3/2}} \int_{-\infty}^{\infty} \int_{-\infty}^{\infty} \int_{-\infty}^{\infty} \exp[-(r_1^2 + r_2^2 + r_3^2)] \\ &\quad \times \delta\left(\Delta - 2\sqrt{r_2^2 + r_3^2}\right) dr_1 dr_2 dr_3. \end{aligned} \quad (\text{D.7})$$

Using the 2D polar coordinate for integrals over r_2 and r_3 , we have

$$P(\Delta) = \frac{\Delta}{2} e^{-\Delta^2/4}. \quad (\text{D.8})$$

The mean level spacing $\bar{\Delta}$ for this distribution function is $\bar{\Delta} = \int \Delta P(\Delta) d\Delta = \sqrt{\pi}$. Therefore, the level-spacing distribution $P(s)$ is found to be

$$P(s) = \frac{\pi}{2} s e^{-\pi s^2/4}, \quad (\text{D.9})$$

as a function of the rescaled level spacing $s \equiv \Delta/\bar{\Delta}$, and this gives (9.32). This function is certainly zero at $s = 0$ due to level repulsion. For $s \ll 1$, $P(s)$ is proportional to s .

Next, we calculate $P(s)$ for the GUE. The general form of a Hamiltonian matrix with the smallest order is a 2×2 complex Hermitian matrix:

$$H = \begin{pmatrix} r_1 + r_2 & r_3 + ir_4 \\ r_3 - ir_4 & r_1 - r_2 \end{pmatrix}, \quad (\text{D.10})$$

where r_1, r_2, r_3 , and r_4 are real constants. The distribution function $R(H)$ and the level spacing $\Delta(H)$ are given by

$$R(H) = \frac{1}{\pi^2} \exp[-(r_1^2 + r_2^2 + r_3^2 + r_4^2)], \quad (\text{D.11})$$

and

$$\Delta(H) = 2\sqrt{r_2^2 + r_3^2 + r_4^2}. \quad (\text{D.12})$$

Using 3D polar coordinates for the integrals over r_2 , r_3 , and r_4 in $P(\Delta) = \int R(H)\delta[\Delta - \Delta(H)] dH$ leads to

$$P(\Delta) = \frac{\Delta^2}{2\sqrt{\pi}} e^{-\Delta^2/4}. \quad (\text{D.13})$$

Since the mean level spacing $\bar{\Delta}$ becomes $4/\sqrt{\pi}$, the distribution $P(s)$ is given by

$$P(s) = \frac{32}{\pi^2} s^2 e^{-4s^2/\pi}. \quad (\text{D.14})$$

This is the Wigner distribution function for the GUE, which is proportional to s^2 for $s \ll 1$.

Finally, we give the function $P(s)$ for the GSE. In this case, each energy level must be twofold degenerate (Kramers degeneracy). Thus, in order to examine the level spacing, at least a 4×4 Hamiltonian matrix should be considered. The general form of a 4×4 self-dual Hermitian matrix can be written in the form

$$H = \begin{pmatrix} r_1 + r_2 & 0 & r_3 + ir_4 & r_5 + ir_6 \\ 0 & r_1 + r_2 & -r_5 + ir_6 & r_3 - ir_4 \\ r_3 - ir_4 & -r_5 - ir_6 & r_1 - r_2 & 0 \\ r_5 - ir_6 & r_3 + ir_4 & 0 & r_1 - r_2 \end{pmatrix}, \quad (\text{D.15})$$

where r_1, r_2, \dots, r_6 are real constants. The distribution function is

$$R(H) = \left(\frac{2}{\pi}\right)^3 \exp\left(-2 \sum_{i=1}^6 r_i^2\right). \quad (\text{D.16})$$

Two pairs of eigenvalues among four of the Hamiltonian H are twofold degenerate. The level spacing between these two pairs is given by

$$\Delta(H) = 2 \sqrt{\sum_{i=2}^6 r_i^2}. \quad (\text{D.17})$$

The level-spacing distribution function $P(\Delta)$ can be calculated from

$$P(\Delta) = \left(\frac{2}{\pi}\right)^3 \int_{-\infty}^{\infty} \exp\left(-2 \sum_{i=1}^6 r_i^2\right) \delta\left(\Delta - 2 \sqrt{\sum_{i=2}^6 r_i^2}\right) \prod_{i=1}^6 dr_i. \quad (\text{D.18})$$

The integration with respect to r_2, r_3, \dots, r_6 can be performed by the polar coordinate transformation

$$\int \prod_{i=2}^6 dr_i = \frac{8}{3}\pi^2 \int dr r^4,$$

and we have

$$P(\Delta) = \frac{1}{3} \sqrt{\frac{2}{\pi}} \Delta^4 e^{-\Delta^2/2}. \quad (\text{D.19})$$

Since the mean level spacing of this distribution is

$$\bar{\Delta} = \frac{3}{8} \sqrt{\frac{2}{\pi}},$$

the distribution function of s is given by

$$P(s) = \left(\frac{8}{3\sqrt{\pi}}\right)^6 s^4 \exp\left(-\frac{64}{9\pi}s^2\right), \quad (\text{D.20})$$

This is the Wigner distribution function (9.34) of the GSE, which is proportional to s^4 for $s \ll 1$.

References

The references listed below for each chapter are suggestions for additional reading related to problems and questions which are incompletely covered in this book. They are not intended to provide a complete account of the various contributions to any particular field.

Chapter 1

- 1.1 J. Feder: *Fractals* (Plenum, New York 1988)
- 1.2 B.B. Mandelbrot: *Fractals: Form, Chance and Dimension* (Freeman, San Francisco 1977)
- 1.3 B.B. Mandelbrot: *The Fractal Geometry of Nature* (Freeman, San Francisco 1982)
- 1.4 L.P. Kadanoff: *Phase Transitions and Critical Phenomena* Vol. 5A, ed. by C. Domb and M.S. Green (Academic Press, New York 1976)
- 1.5 D. Avnir (Ed.): *The Fractal Approach to Heterogeneous Chemistry* (Wiley, Chichester 1989)
- 1.6 H. Takayasu: *Fractals in the Physical Sciences* (Manchester University Press, Manchester 1990)
- 1.7 A. Bunde, S. Havlin (Eds.): *Fractals and Disordered Systems* (Springer-Verlag, Berlin 1991)
- 1.8 T. Vicsek: *Fractal Growth Phenomena*, 2nd edn. (World Scientific, Singapore 1993)
- 1.9 A. Bunde, S. Havlin (Eds.): *Fractals in Science* (Springer-Verlag, Berlin 1994)
- 1.10 D. Stauffer, H.E. Stanley: *From Newton to Mandelbrot: A Primer in Theoretical Physics*, 2nd edn. (Springer-Verlag, Berlin 1995)
- 1.11 A.-L. Barabási, H.E. Stanley: *Fractal Concepts in Surface Growth* (Cambridge University Press, Cambridge 1995)
- 1.12 P.G. de Gennes: La Recherche **7**, 919 (1976)
- 1.13 Y. Gefen, A. Aharony, A. Alexander: Phys. Rev. Lett. **50**, 77 (1983)
- 1.14 S. Alexander, R. Orbach: J. Phys. (Paris) Lett. **43**, L625 (1982)

Chapter 2

- 2.1 B.B. Mandelbrot, J. Given: Phys. Rev. Lett. **52**, 1853 (1984)
- 2.2 J. Feder: *Fractals* (Plenum, New York 1988)
- 2.3 B.B. Mandelbrot: *The Fractal Geometry of Nature* (Freeman, San Francisco 1982)
- 2.4 A.-L. Barabási, H.E. Stanley: *Fractal Concepts in Surface Growth* (Cambridge University Press, Cambridge 1995)

- 2.5 H. Takayasu: *Fractals in the Physical Sciences* (Manchester University Press, Manchester 1990)
- 2.6 S.S. Kistler: J. Phys. Chem. **36**, 52 (1932)
- 2.7 R. Vacher, T. Woignier, J. Pelous, E. Courtens: Phys. Rev. B **37**, 6500 (1988)
- 2.8 A. Einstein: Ann. Phys. **17**, 549 (1905)
- 2.9 A. Einstein: Ann. Phys. **19**, 371 (1906)
- 2.10 J. Perrin: *Les atomes* (Gallimard, Paris 1913)

Chapter 3

- 3.1 S.R. Broadbent, J.M. Hammersley: Proc. Cambridge Philos. Soc. **53**, 629 (1957)
- 3.2 J.M. Hammersley: Ann. Isr. Phys. Soc. **5**, 47 (1983)
- 3.3 A.L. Efros: *Physics and Geometry of Disorder* (Mir Publishers, Moscow 1986)
- 3.4 H.E. Stanley: J. Phys. A **10**, 121 (1977)
- 3.5 D. Stauffer, A. Aharony: *Introduction to Percolation Theory*, 2nd edn. (Taylor and Francis, London/Philadelphia, 1992)
- 3.6 S.R. Broadbent: J. R. Stat. Soc. B **16**, 68 (1954)
- 3.7 M.P.M. den Nijs: J. Phys. A **12**, 1857 (1979)
- 3.8 B. Nienhuis, E.K. Riedel, M. Schick: J. Phys. A **13**, 189 (1980)
- 3.9 R.B. Pearson: Phys. Rev. B **22**, 2579 (1980)
- 3.10 B. Nienhuis: J. Phys. A **15**, 199 (1982)
- 3.11 D.S. Gaunt, M.F. Sykes: J. Phys. A **16**, 783 (1983)
- 3.12 J. Adler, A. Aharony, A.B. Harris: Phys. Rev. B **30**, 2832 (1984)
- 3.13 N. Jan, D.C. Hong, H.E. Stanley: J. Phys. A **18**, L935 (1985)
- 3.14 J. Adler, Y. Meir, A. Aharony, A.B. Harris: Phys. Rev. B **41**, 9183 (1990)
- 3.15 E. Stoll, M. Kolb, E. Courtens: Phys. Rev. Lett. **68** 2472 (1992)
- 3.16 H.E. Stanley: J. Stat. Phys. **36**, 843 (1984)
- 3.17 H.J. Herrmann, H.E. Stanley: J. Phys. A **21**, L829 (1988)
- 3.18 A.S. Skal, B.I. Shklovskii: Sov. Phys. Semicond. **8**, 1029 (1975)
- 3.19 P.G. de Gennes: J. Phys. (Paris) Lett. **37**, L1 (1976)
- 3.20 A. Coniglio: J. Phys. A **15**, 3829 (1982)
- 3.21 A. Coniglio: Phys. Rev. Lett. **46**, 250 (1982)

Chapter 4

- 4.1 C.J. Allègre, E. Lewin: Earth Planet. Sci. Lett. **132**, 1 (1995)
- 4.2 B.B. Mandelbrot: J. Fluid Mech. **62**, 231 (1974)
- 4.3 P. Meakin, H.E. Stanley, A. Coniglio, T.A. Witten: Phys. Rev. A **32**, 2364 (1985)
- 4.4 H.E. Stanley, P. Meakin: Nature **335**, 405 (1988)
- 4.5 L. de Arcangelis, S. Redner, A. Coniglio: Phys. Rev. B **31**, 4725 (1985)
- 4.6 J.G. Gao, I. Rubin: Electron. Lett. **36**, 101 (2000)
- 4.7 B.B. Mandelbrot: J. Fluid Mech. **62**, 331 (1976)
- 4.8 T.C. Halsey, M.H. Jensen, L.P. Kadanoff, I. Procaccia, B.I. Shraiman: Phys. Rev. A **33**, 1141 (1986)
- 4.9 J. Feder: *Fractals* (Plenum, New York 1988)
- 4.10 B.B. Mandelbrot: *Fractals and Multifractals: Noise, Turbulence and Galaxies* (Springer, New York 1988)
- 4.11 P. Meakin: *Fractals, Scaling and Growth Far from Equilibrium* (Cambridge University Press, Cambridge 1998)

- 4.12 D. Sornette: *Critical Phenomena in Natural Sciences: Chaos, Fractals, Selforganization and Disorder: Concepts and Tools* (Springer, Berlin 2000)
- 4.13 J.F. Gouyet: *Physics and Fractal Structures* (Springer, New York 1996)
- 4.14 U. Frisch: *Turbulence* (Cambridge University Press, Cambridge 1995)
- 4.15 C. Beck, F. Schlogl: *Thermodynamics of Chaotic Systems* (Cambridge University Press, Cambridge 1993)
- 4.16 T. Vicsek: *Fractal Growth Phenomena*, 2nd edn. (World Scientific, Singapore 1992)
- 4.17 J.P. Bouchaud, M. Potters: *Theory of Financial Risk* (Cambridge University Press, Cambridge 1999)
- 4.18 B.B. Mandelbrot: *Multifractals and 1/f Noise* (Springer, New York 1998)
- 4.19 G. Paladin, A. Vulpiani: Phys. Rep. **156**, 147 (1987)
- 4.20 L. de Arcangelis, S. Redner, A. Coniglio: Phys. Rev. B **34**, 4656 (1986)
- 4.21 A. Coniglio: Phys. Rev. Lett. **46**, 250 (1982)
- 4.22 G.A. Edgar: *Integral, Probability, and Fractal Measures* (Springer, New York 1997)
- 4.23 J.D. Farmer, E. Ott, J.A. York: Physica **7D**, 153 (1983)
- 4.24 J. Balatoni, A. Renyi: Pub. Math. Inst. Hungarian Acad. Sc. **1**, 9 (1956)
- 4.25 P. Grassberger, I. Procaccia: Phys. Rev. Lett. **50**, 346 (1983)
- 4.26 A. Chhabra, R.V. Jensen: Phys. Rev. Lett. **62**, 1327 (1989)
- 4.27 M.E. Cates, J.M. Deutsch: Phys. Rev. A **35**, 4907 (1987)
- 4.28 M.E. Cates, T.A. Witten: Phys. Rev. A **35**, 1809 (1987)
- 4.29 W. Pook, M. Janssen: Z. Phys. B **82**, 295 (1991)
- 4.30 M. Barthélémy, S.V. Buldyrev, S. Havlin, H.E. Stanley: Phys. Rev. E **61**, R3283 (2000)
- 4.31 T.A. Witten, L.M. Sander: Phys. Rev. Lett. **47**, 1400 (1981)
- 4.32 P. Meakin: Phys. Rep. **235**, 189 (1993)
- 4.33 Y. Hayakawa, S. Sato, M. Matsushita: Phys. Rev. A **36**, 1963 (1987)

Chapter 5

- 5.1 P.G. de Gennes: La Recherche **7**, 919 (1976)
- 5.2 Y. Gefen, A. Aharony, S. Alexander: Phys. Rev. Lett. **50**, 77 (1983)
- 5.3 S. Alexander, J. Bernasconi, W.R. Schneider, R. Orbach: Rev. Mod. Phys. **53**, 175 (1981)
- 5.4 T. Nakayama: Physica A **191**, 386 (1992)
- 5.5 S. Alexander, R. Orbach: J. Phys. (Paris) Lett. **43**, L625 (1982)
- 5.6 R. Rammal, G. Toulouse: J. Phys. (Paris) **44**, L13 (1983)
- 5.7 R. Rammal: J. Phys. (Paris) **45**, 191 (1984)
- 5.8 E. Abrahams, P.W. Anderson, D.C. Licciardello, T.V. Rama-Krishnan: Phys. Rev. Lett. **42**, 673 (1979)
- 5.9 S. Alexander: Phys. Rev. B **40**, 7953 (1989)

Chapter 6

- 6.1 M. Born, K. Huang: *Dynamical Theory of Crystal Lattices* (Clarendon, Oxford, 1954)
- 6.2 T. Nakayama: Physica A **191**, 386 (1992)
- 6.3 T. Nakayama, K. Yakubo: Phys. Rep. **349**, 239 (2001)
- 6.4 K. Yakubo, T. Nakayama: Phys. Rev. B **40**, 517 (1989)
- 6.5 T. Terao, T. Nakayama: Phys. Rev. B **53**, R2918 (1996)
- 6.6 S. Alexander, C. Laermans, R. Orbach, H.M. Rosenberg: Phys. Rev. B **28**, 4615 (1983)
- 6.7 A. Aharony, S. Alexander, O. Entin-Wohlman, R. Orbach: Phys. Rev. Lett. **31**, 2565 (1985)

- 6.8 K. Yakubo, E. Courtens, T. Nakayama: Phys. Rev. B **42**, 1078 (1990)
 6.9 R. Rammal: J. Phys. (Paris) **45**, 191 (1984)
 6.10 A. Bunde, H.E. Roman: Philos. Mag. B **65**, 191 (1992)
 6.11 S. Havlin, A. Bunde: Physica D **38**, 184 (1989)
 6.12 K. Yakubo, T. Nakayama: J. Phys. Soc. Jpn. **58**, 1504 (1989)
 6.13 T. Nakayama: Jpn. J. Appl. Phys. **34**, 2519 (1995)
 6.14 P.N. Keating: Phys. Rev. B **152**, 774 (1996)
 6.15 Y. Kantor, I. Webman: Phys. Rev. Lett. **52**, 1891 (1984)
 6.16 S. Feng: Phys. Rev. B **32**, 510 (1985)
 6.17 S. Feng: Phys. Rev. B **32**, 5793 (1985)
 6.18 P.G. de Gennes: J. Phys. (Paris) Lett. **37**, L1 (1976)
 6.19 K. Yakubo, K. Takasugi, T. Nakayama: J. Phys. Soc. Jpn. **59**, 1909 (1990)

Chapter 7

- 7.1 J.M. Carpenter, C.A. Pelizzari: Phys. Rev. B **12**, 2391 (1975)
 7.2 D.L. Price, J.M. Carpenter: J. Non-Cryst. Solids **92**, 153 (1987)
 7.3 S. Alexander, E. Courtens, R. Vacher: Physica A **195**, 286 (1993)
 7.4 S.W. Lovesey: *Theory of Thermal Neutron Scattering* (Clarendon Press, Oxford 1984)
 7.5 G.L. Squires: *Introduction to the Theory of Neutron Scattering* (Cambridge University Press, London 1984)
 7.6 T. Nakayama, K. Yakubo: Phys. Rep. **349**, 239 (2001)
 7.7 T. Terao, T. Nakayama: Phys. Rev. B **53**, R2918 (1996)
 7.8 T. Nakayama, K. Yakubo: J. Phys. Soc. Jpn. **61**, 2601 (1992)
 7.9 A.F. Ioffe, A.R. Regel: Prog. Semicond. **4**, 237 (1960)
 7.10 S. John, H. Sompolinsky, M. Stephen: Phys. Rev. B **27**, 5592 (1983)
 7.11 Y. Tsujimi, E. Courtens, J. Pelous, R. Vacher: Phys. Rev. Lett. **60**, 2757 (1988)
 7.12 V. Mazzacurati, M. Montagna, O. Pilla, G. Villani, G. Ruocco, G. Signorelli: Phys. Rev. B **45**, 2126 (1992)

Chapter 8

- 8.1 H. Ikeda, J.A. Fernandez-Baca, R.M. Nicklow, M. Takahashi, I. Iwasa: J. Phys.: Condens. Matter **6**, 10543 (1994)
 8.2 H. Ikeda, S. Itoh, M.A. Adams, J.A. Fernandez-Baca: J. Phys. Soc. Jpn. **67**, 3376 (1998)
 8.3 Y.J. Uemura, R.J. Birgeneau: Phys. Rev. B **36**, 7024 (1987)
 8.4 E.F. Shender: Sov. Phys. JETP **70**, 1174 (1976)
 8.5 E.F. Shender: Sov. Phys. JETP **48**, 175 (1978)
 8.6 L.E. Reichl: *A Modern Course in Statistical Physics* (University of Texas Press, Austin 1980)
 8.7 A.B. Harris, K. Kirkpatrick: Phys. Rev. B **16**, 542 (1977)
 8.8 W. Brenig, G. Döhler, P. Wölfe: Z. Phys. **246**, 1 (1971)
 8.9 S. Kirkpatrick: Rev. Mod. Phys. **45**, 574 (1973)
 8.10 K. Yakubo, T. Terao, T. Nakayama: J. Phys. Soc. Jpn. **63**, 3431 (1994)
 8.11 T. Nakayama, K. Yakubo: Phys. Rep. **349**, 239 (2001)
 8.12 A. Christou, R.B. Stinchcombe: J. Phys. C **19**, 5895 (1986)
 8.13 A. Christou, R.B. Stinchcombe: J. Phys. C **19**, 5917 (1986)
 8.14 T. Terao, K. Yakubo, T. Nakayama: Phys. Rev. B **40**, 566 (1994)
 8.15 T. Terao, T. Nakayama: Phys. Rev. B **51**, 11479 (1995)

- 8.16 T. Terao, T. Nakayama: Phys. Rev. B **66**, 132409 (2002)
 8.17 T. Terao, K. Yakubo, T. Nakayama: Phys. Rev. B **49**, 12281 (1994)

Chapter 9

- 9.1 Y. Aharonov, D. Bohm: Phys. Rev. **115**, 485 (1959)
 9.2 Y. Imry: *Introduction to Mesoscopic Physics* (Oxford University Press, New York 1997)
 9.3 P.W. Anderson: Phys. Rev. **109**, 1492 (1958)
 9.4 G. Bergmann: Phys. Rev. B **28**, 2914 (1983)
 9.5 D.E. Khmel'nitskii: Physica **126B**, 235 (1984)
 9.6 A.I. Larkin, D.E. Khmel'nitskii: Usp. Fiz. Nauk **136**, 536 (1982) [Sov. Phys. Usp. **25**, 185 (1982)]
 9.7 S. Hikami, A.I. Larkin, Y. Nagaoka: Prog. Theor. Phys. **63**, 707 (1980)
 9.8 B.L. Altshuler, D.E. Khmel'nitskii, A.I. Larkin, P.A. Lee: Phys. Rev. B **22**, 5142 (1980)
 9.9 Y. Kawaguchi, S. Kawaji: J. Phys. Soc. Jpn. **48**, 699 (1980)
 9.10 See, for example, C.W. Beenakker, H. van Houten: In *Solid State Physics 44*, ed. by H. Ehrenreich, D. Turnbull (Academic Press, New York 1991) pp. 1–228
 9.11 J.J. Sakurai: *Modern Quantum Mechanics*, 2nd edn. (Addison-Wesley, Massachusetts 1994)
 9.12 G. Bergmann: Phys. Rep. **107**, 1 (1984)
 9.13 E. Abrahams, P.W. Anderson, D.C. Licciardello, T.V. Ramakrishnan: Phys. Rev. Lett. **42**, 673 (1979)
 9.14 F. Wegner: Z. Phys. B **25**, 327 (1976)
 9.15 M. Janssen: *Fluctuations and Localization in Mesoscopic Electron Systems* (World Scientific, Singapore 2001)
 9.16 J.L. Cardy: *Scaling and Renormalization in Statistical Physics* (Cambridge University Press, Cambridge 1996)
 9.17 M.L. Mehta: *Random Matrices*, 2nd edn. (Academic Press, New York 1991)
 9.18 C.W. Beenakker: Rev. Mod. Phys. **69**, 731 (1997)
 9.19 T. Guhr, A. Müller-Groeling, H.A. Weidenmüller: Phys. Rep. **299**, 189 (1998)
 9.20 K.B. Efetov: *Supersymmetry in Disorder and Chaos* (Cambridge University Press, Cambridge 1997)
 9.21 E. Hofstetter, M. Schreiber: Phys. Rev. Lett. **73**, 3137 (1994)
 9.22 T. Ando: Phys. Rev. B **40**, 5325 (1989)
 9.23 S.N. Evangelou: Phys. Rev. Lett. **75**, 2550 (1995)
 9.24 Y. Asada, K. Slevin, T. Ohtsuki: Phys. Rev. Lett. **89**, 256601 (2002)
 9.25 A. MacKinnon, B. Kramer: Z. Phys. B **53**, 1 (1983)
 9.26 B. Kramer, A. MacKinnon: Rep. Prog. Phys. **56**, 1469 (1993)
 9.27 I. Varga, E. Hofstetter, J. Pipek: Phys. Rev. Lett. **82**, 4683 (1999)
 9.28 B. Huckestein: Rev. Mod. Phys. **67**, 357 (1995)
 9.29 See, for example, K. Slevin, T. Ohtsuki: Phys. Rev. Lett. **82**, 382 (1999)
 9.30 L.W. Engel, D. Shahar, Ç. Kurdak, D.C. Tsui: Phys. Rev. Lett. **71**, 2638 (1993)
 9.31 H. Shima, T. Nakayama: J. Phys. Soc. Jpn. **67**, 2189 (1998)
 9.32 H. Shima, T. Nakayama: Phys. Rev. B **60**, 14066 (1999)
 9.33 T. Nakayama, K. Yakubo: Phys. Rep. **349**, 239 (2001)
 9.34 B.M. Gammel, W. Brenig: Phys. Rev. B **53**, 13279 (1996)
 9.35 T. Ohtsuki, T. Kawarabayashi: J. Phys. Soc. Jpn. **66**, 314 (1997)
 9.36 J. Zhong, R.B. Diener, D.A. Steck, W.H. Oskay, M.G. Raizen, E.W. Plummer, Z. Zhong, Q. Niu: Phys. Rev. Lett. **86**, 2485 (2001)
 9.37 J.T. Chalker, G.J. Daniell: Phys. Rev. Lett. **61**, 592 (1988)
 9.38 L. Schweitzer: J. Phys. Condens. Matter **7**, L281 (1995)

- 9.39 B. Huckestein, R. Klesse: Phil. Mag. B **77**, 1181 (1998)
 9.40 J.T. Chalker, P.D. Coddington: J. Phys. C **21**, 2665 (1988)

Chapter 10

- 10.1 H. Aoki: J. Phys. C **13**, 3369 (1980)
 10.2 H. Aoki: J. Phys. C **16**, L205 (1983)
 10.3 F. Wegner: Z. Phys. B **36**, 209 (1980)
 10.4 See, for example, M. Janssen: Int. J. Mod. Phys. B **8**, 943 (1994)
 10.5 W. Pook, M. Janssen: Z. Phys. B **82**, 295 (1991)
 10.6 T. Terao, T. Nakayama, H. Aoki: Phys. Rev. B **54**, 10350 (1996)
 10.7 K. Pracz, M. Janssen, P. Freche: J. Phys. Condens. Matter **8**, 7147 (1996)
 10.8 C. Castellani, L. Peliti: J. Phys. A **19**, L429 (1986)
 10.9 V.I. Fal'ko, K.B. Efetov: Phys. Rev. B **52**, 17413 (1995)
 10.10 I.E. Smolyarenko, B.L. Altshuler: Phys. Rev. B **55**, 10451 (1997)
 10.11 A.W.W. Ludwig, M.P.A. Fisher, R. Shanker, G. Grinstein: Phys. Rev. B **50**, 7526 (1994)
 10.12 D.V. Khveshchenko, A.G. Yashenkin, I.V. Gomyi: Phys. Rev. Lett. **86**, 4668 (2001)
 10.13 T.K. Ng: Phys. Rev. Lett. **82**, 3504 (1999)
 10.14 H.E. Castillo, C. Chamon, E. Fradkin, P.M. Goldbart, C. Mudry: Phys. Rev. B **56**, 10668 (1997)
 10.15 T. Fujiwara, M. Kohmoto, T. Tokihiro: Phys. Rev. B **40**, 7413 (1989)
 10.16 D. Domínguez, C. Wiecko, J.V. José: Phys. Rev. B **45**, 13919 (1992)
 10.17 D.R. Hofstadter: Phys. Rev. B **14**, 2239 (1976)
 10.18 C. Tang, M. Kohmoto: Phys. Rev. B **34**, 2041 (1986)
 10.19 R. Ketzmerick, G. Petschel, T. Geisel: Phys. Rev. Lett. **69**, 695 (1992)
 10.20 B. Huckestein, L. Schweitzer: Phys. Rev. Lett. **72**, 713 (1994)
 10.21 B. Huckestein, R. Klesse: Phys. Rev. B **55**, R7303 (1997)
 10.22 M. Janssen: Phys. Rep. **295**, 1 (1998)
 10.23 J.T. Chalker: Physica **167A**, 253 (1990)
 10.24 T. Brandes, B. Huckestein, L. Schweitzer: Ann. Phys. (Leipzig), **5**, 633 (1996)
 10.25 J. Cardy: *Scaling and Renormalization in Statistical Physics* (Cambridge University Press, Cambridge 1996)
 10.26 J. Cardy: J. Phys. A **18**, L757 (1985)
 10.27 Y. Deng, H.W.J. Blöte: Phys. Rev. Lett. **88**, 190602 (2002)
 10.28 B. Huckestein: Rev. Mod. Phys. **67**, 357 (1995)
 10.29 D.H. Lee, Z. Wang, S. Kivelson: Phys. Rev. Lett. **70**, 4130 (1993)
 10.30 K. Yakubo: Phys. Rev. B **62**, 16756 (2000)
 10.31 B.I. Halperin, P.A. Lee, N. Read: Phys. Rev. B **47**, 7312 (1993)
 10.32 J.K. Jain: Phys. Rev. Lett. **63**, 199 (1989)
 10.33 B. Huckestein: Phys. Rev. B **53**, 3650 (1996)

Appendix

- A.1 R. Rammal, G. Toulouse: J. Phys. (Paris) **44**, L13 (1983)
 C.1 A. Alexander, J. Bernasconi, R. Orbach: J. Physique Colloq. **39**, C6-706 (1978)
 C.2 A. Alexander, J. Bernasconi, R. Schneider, R. Orbach: Rev. Mod. Phys. **53**, 175 (1981)
 C.3 J.S. Alexander: Phys. Rev. B **27**, 1541 (1983)
 D.1 M.L. Mehta: *Random Matrices*, 2nd edn. (Academic Press, New York 1991)

Subject Index

- aerogel 13, 100
Aharonov–Bohm effect 116
Alexander–Orbach conjecture 63, 107, 108
Anderson localization 115, 117
Anderson transition 1, 115, 120, 134, 149
Ando model 130
anomalous diffusion 59, 61, 65
anomalous scaling 39
ant in the labyrinth 59
antilocalization 120
asymmetric matrix 104
atomic vibration 70
average cluster size 20, 24
- β -function 67, 121–123
backbone 33
ballistic transport 116
Bethe lattice 29
biorthogonality condition 104
blob 32, 33
block-spin transformation 163
blue bond 34
box-counting method 12, 47, 49
Brownian motion 15
- capacity dimension 9, 10
Cayley tree 29
Chalker–Coddington network model 146, 158
chemical dimension 28
chemical distance 28, 93
cluster–cluster correlation 14
coherent back-scattering 117
compact fractal 63, 67
conformal invariance 3, 162, 172
conformal mapping 165
correlation dimension 9, 43, 151, 160, 171, 178
correlation function 12
– density–density ~ 14, 89
- energy ~ 143
– of box measures 48
– two-particle ~ 142, 165, 166
correlation integral 43
correlation length 14, 20, 25, 73, 112
critical concentration 20
critical conductance 123
critical disorder 133
critical wavefunction 2, 3, 115, 149, 152
curdling fractal 44
- de l’Hôpital’s theorem 43, 44, 178
dead end 33, 61, 81
Debye density of states 64
density fluctuation 90
dephasing 115
deterministic fractal 1, 5, 8, 34
diffusion function 136, 137, 143, 161
diffusion length 134, 144
diffusion-limited aggregation 35, 56
diffusion-limited cluster-aggregation 13
diffusive transport 116
diluted Heisenberg antiferromagnet 101, 113
dimensionless conductance 120
dipole-induced-dipole mechanism 98
Dirac fermion 154, 155
direct mechanism 98
dispersion relation 65, 66, 68, 83
dissipative conductivity 137
distribution
– level-spacing ~ 127, 132, 194
– log-normal ~ 40, 55, 152, 153
– of clusters of size s 20
– of energy dissipations 38
– of local densities 6, 7
– of measure 54
– of voltage drops 35, 37, 39, 177
– Poisson ~ 125, 127
– Wigner ~ 127, 194
Drude formula 115

- dynamic structure factor 89, 110, 142
- effective percolation threshold 31
- Einstein relation 60, 135, 137, 147
- electron interferometer
 - Fabry–Pérot ~ 116
 - Mach–Zender ~ 116
- exponent
 - anomalous diffusion ~ 61
 - conductivity ~ 60, 66, 84
 - correlation ~ 50–54, 154, 178
 - dynamical ~ 106, 108, 135
 - elasticity ~ 85
 - Lipschitz–Hölder ~ 45, 47, 50–54, 168, 179–182
 - localization length ~ 123, 133
 - order parameter ~ 23
 - specific heat ~ 24
 - susceptibility ~ 108
- Fibonacci chain 157
- finite-size scaling 29, 84, 131–134, 159, 172
- fixed point Hamiltonian 162
- flux quantum 116
- forced oscillator method 72, 94, 98, 107, 112, 137
- Fourier transform 12, 90, 110, 135, 138, 142–145, 189
- fractal dimension 2, 7, 10, 17, 26, 27, 35, 43, 57, 68
 - of the shortest path 29
- fracton 59, 64, 67, 71, 72, 75, 91, 100
 - antiferromagnetic spin-wave ~ 106, 109, 113
 - bending ~ 84–86
 - ferromagnetic spin-wave ~ 101
 - localization of ~ 66, 79
 - mode pattern of ~ 80
 - stretching ~ 83, 85, 87
- fracton dimension 62, 64
- Gaussian orthogonal ensemble 126, 129, 141, 143, 155, 194
- Gaussian symplectic ensemble 126, 130, 143, 155, 196
- Gaussian unitary ensemble 126, 129, 155, 195
- generalized dimension 40, 42, 50–54, 151, 178
 - for spectral measure 157
- generalized master equation 140
- generalized susceptibility 110, 111
- Ginzburg–Landau free energy 192
- global scale transformation 162, 164
- growth probability 56
- Guinier regime 14
- gyromagnetic ratio 105
- Harper model 155, 157
- Hausdorff dimension 9
- Heisenberg antiferromagnet 102
- Heisenberg equation of motion 102
- Heisenberg Hamiltonian 191
- hierarchical resistor network model 35, 41, 42, 44, 45, 54, 55, 177
- hump 74, 76
- hydrodynamic regime 105
- hyperscaling relation 27, 29
- inelastic light scattering 89, 96
- inelastic neutron scattering 89
- information dimension 9, 42, 52, 178
- interference
 - constructive ~ 118
 - destructive ~ 118
 - quantum ~ 115
- inverse participation ratio 150, 151
- Ioffe–Regel condition 95, 96
- irrelevant scaling length 169
- Kirchhoff's law 187, 193
- Kramers degeneracy 196
- Laplace transform 64, 80, 140, 141, 188–190
- left eigenvector 104, 112
- Legendre transform 46, 48, 180
- level repulsion 126
- level spacing 125
- link 32, 33
- local density of states 3, 155, 157–159
- local scale transformation 3, 163, 164
- localization length 79, 121
- magnon 112, 191
- magnon–fracton crossover 106, 112, 113
- Mandelbrot–Given fractal 5, 8, 9, 34, 63, 184
- mass exponent 40, 46, 47, 50–54, 151
 - of spectral measure 155
- master equation 71, 186
- mean level spacing 134
- mean-square displacement 16, 17, 59
- measure 10, 40
 - box ~ 41, 45, 55
 - Lebesgue ~ 40

- multifractal ~ 177
- probability ~ 173
- Riemann ~ 40
- spectral ~ 155
- memory function 140
- metal-insulator transition 115, 120, 123
- missing mode 74, 75
- molecular adsorption method 11
- multifractal 2, 35, 41, 149, 177
- multifractal spectrum 44, 47, 50–55, 57, 152, 153, 171, 178–182
- Néel temperature 102
- negative magnetoresistance 119
- node 33
- nodes-links-blobs model 32, 35, 36, 77, 82, 83, 85, 186
- non-Hermitian matrix 104
- nonlinear sigma model 154
- number of finite clusters 20, 24
- one-parameter scaling 122, 149, 157, 160, 169, 173
- order parameter 20, 23, 31, 149, 158, 159
- pair potential 192
- parabolic approximation 54, 152–154
- Peierls phase 130
- percolating network 10, 19, 36, 59, 81, 86
 - antiferromagnetic ~ 101, 102, 105–110, 112, 113
 - bond-~ 13, 20, 28, 71, 94, 98, 107, 112
 - elastic ~ 71
 - ferromagnetic ~ 101
 - site-~ 13, 20, 28, 107
- percolation threshold 20
- phase coherence length 115
- phonon 68
- phonon-fracton crossover 68, 73, 75, 91, 95, 100
- polarizability 96
- Porod regime 14
- q*-microscope 48
- q*-th moment 25, 38, 40, 41, 46, 172
- quantum fluctuation 134
- quantum Hall system 133, 143, 149, 150, 152–155, 158, 168–172, 176
- quantum percolation transition 67
- Raman coupling coefficient 97–100
- Raman scattering intensity 80, 89, 96, 98, 100
- random fractal 1, 5, 9, 15, 40
- random magnetic field 154, 176
- random matrix theory 126, 194
- random potential
 - long-range ~ 171
 - short-range ~ 171
- random walk 2, 56, 59
- RC circuit 187
- red bond 34
- renormalization group 149, 163
- renormalized frequency 184
- return probability 64, 117–120
- right eigenvector 104, 112
- rigidity threshold 82
- rotationally-invariant Hamiltonian 81
- scale transformation 5
- scaling amplitude 132, 133, 162, 167, 172
- scaling ansatz 20, 30
- scaling correction 133
- scaling function 30, 61, 121
 - two-variable ~ 135, 173
- scaling hypothesis 121, 131
- scaling relation 29
- scaling theory 20
- scattering experiment 12
- second lowest Landau level 169
- self-affine fractal 6
- self-dual Hermitian matrix 196
- self-similarity 1, 150
- Sierpinski gasket 5, 8, 63, 77, 182
- similarity dimension 8
- single-length-scale postulate 89, 91, 94, 96, 98, 101, 109, 113
- spectral density of states 64, 65, 68, 71, 155, 189
- spectral dimension 59, 62–66, 68, 71, 73
 - antiferromagnetic ~ 104, 108
 - for bending fracton 85, 86
 - for deterministic fractal 182
 - for stretching fracton 84
- spin deviation 102, 110
- spin wave 101, 191
- spin-orbit interaction 119, 124, 130, 151
- staggered magnetization 105
- staggered transverse field 110
- stationary phase approximation 141
- steepest descent method 46
- stiffness constant 105
- strain tensor 92
- structure factor 12, 28
- superconducting fractal network 192
- susceptibility 25

- symmetry
 - dilatational ~ 1, 5, 162
 - rotational ~ 162
 - spin-rotational ~ 119, 126, 130
 - time-reversal ~ 118, 126, 129
- temporal autocorrelation function 138, 143, 161
- time-reversal operator 119, 126
- translational invariance 12
- transverse susceptibility 105
- two-point susceptibility 110
- typical value
 - of μ_b 56
- of local density of states 158, 159, 167
- universality class 26, 84, 125
- upper critical dimension 29, 106, 108
- valence force field 81
- vector elasticity 81, 86
- Wannier function 125
- weak localization 120
- Wegner scaling law 124, 147
- yellow bond 34
- Young's modulus 85

Springer Series in Solid-State Sciences

Editors: M. Cardona P. Fulde K. von Klitzing H.-J. Queisser

- 1 **Principles of Magnetic Resonance**
3rd Edition By C. P. Slichter
- 2 **Introduction to Solid-State Theory**
By O. Madelung
- 3 **Dynamical Scattering of X-Rays in Crystals** By Z. G. Pinsker
- 4 **Inelastic Electron Tunneling Spectroscopy**
Editor: T. Wolfram
- 5 **Fundamentals of Crystal Growth I**
Macroscopic Equilibrium and Transport Concepts
By F. E. Rosenberger
- 6 **Magnetic Flux Structures in Superconductors**
2nd Edition By R. P. Huebener
- 7 **Green's Functions in Quantum Physics**
2nd Edition By E. N. Economou
- 8 **Solitons and Condensed Matter Physics**
Editors: A. R. Bishop and T. Schneider
- 9 **Photoferroelectrics** By V. M. Fridkin
- 10 **Phonon Dispersion Relations in Insulators** By H. Bilz and W. Kress
- 11 **Electron Transport in Compound Semiconductors** By B. R. Nag
- 12 **The Physics of Elementary Excitations**
By S. Nakajima, Y. Toyozawa, and R. Abe
- 13 **The Physics of Selenium and Tellurium**
Editors: E. Gerlach and P. Grosse
- 14 **Magnetic Bubble Technology** 2nd Edition
By A. H. Eschenfelder
- 15 **Modern Crystallography I**
Fundamentals of Crystals
Symmetry, and Methods of Structural Crystallography
2nd Edition
By B. K. Vainshtein
- 16 **Organic Molecular Crystals**
Their Electronic States By E. A. Silinsh
- 17 **The Theory of Magnetism I**
Statics and Dynamics
By D. C. Mattis
- 18 **Relaxation of Elementary Excitations**
Editors: R. Kubo and E. Hanamura
- 19 **Solitons Mathematical Methods for Physicists**
By G. Eilenberger
- 20 **Theory of Nonlinear Lattices**
2nd Edition By M. Toda
- 21 **Modern Crystallography II**
Structure of Crystals 2nd Edition
By B. K. Vainshtein, V. L. Indenbom, and V. M. Fridkin
- 22 **Point Defects in Semiconductors I**
Theoretical Aspects
By M. Lannoo and J. Bourgoin
- 23 **Physics in One Dimension**
Editors: J. Bernasconi and T. Schneider
- 24 **Physics in High Magnetic Fields**
Editors: S. Chikazumi and N. Miura
- 25 **Fundamental Physics of Amorphous Semiconductors** Editor: F. Yonezawa
- 26 **Elastic Media with Microstructure I**
One-Dimensional Models By I. A. Kunin
- 27 **Superconductivity of Transition Metals Their Alloys and Compounds**
By S. V. Vonsovsky, Yu. A. Izumov, and E. Z. Kurmaev
- 28 **The Structure and Properties of Matter**
Editor: T. Matsubara
- 29 **Electron Correlation and Magnetism in Narrow-Band Systems** Editor: T. Moriya
- 30 **Statistical Physics I** Equilibrium Statistical Mechanics 2nd Edition
By M. Toda, R. Kubo, N. Saito
- 31 **Statistical Physics II** Nonequilibrium Statistical Mechanics 2nd Edition
By R. Kubo, M. Toda, N. Hashitsume
- 32 **Quantum Theory of Magnetism**
2nd Edition By R. M. White
- 33 **Mixed Crystals** By A. I. Kitaigorodsky
- 34 **Phonons: Theory and Experiments I**
Lattice Dynamics and Models of Interatomic Forces By P. Brüesch
- 35 **Point Defects in Semiconductors II**
Experimental Aspects
By J. Bourgoin and M. Lannoo
- 36 **Modern Crystallography III**
Crystal Growth
By A. A. Chernov
- 37 **Modern Crystallography IV**
Physical Properties of Crystals
Editor: L. A. Shuvakov
- 38 **Physics of Intercalation Compounds**
Editors: L. Pietronero and E. Tosatti
- 39 **Anderson Localization**
Editors: Y. Nagaoka and H. Fukuyama
- 40 **Semiconductor Physics An Introduction**
6th Edition By K. Seeger
- 41 **The LMTO Method**
Muffin-Tin Orbitals and Electronic Structure
By H. L. Skriver
- 42 **Crystal Optics with Spatial Dispersion, and Excitons** 2nd Edition
By V. M. Agranovich and V. L. Ginzburg
- 43 **Structure Analysis of Point Defects in Solids**
An Introduction to Multiple Magnetic Resonance Spectroscopy
By J.-M. Spaeth, J. R. Niklas, and R. H. Bartram
- 44 **Elastic Media with Microstructure II**
Three-Dimensional Models By I. A. Kunin
- 45 **Electronic Properties of Doped Semiconductors**
By B. I. Shklovskii and A. L. Efros
- 46 **Topological Disorder in Condensed Matter**
Editors: F. Yonezawa and T. Ninomiya
-

Springer Series in Solid-State Sciences

Editors: M. Cardona P. Fulde K. von Klitzing H.-J. Queisser

- 47 **Statics and Dynamics of Nonlinear Systems**
Editors: G. Benedek, H. Bilz, and R. Zeyher
- 48 **Magnetic Phase Transitions**
Editors: M. Ausloos and R. J. Elliott
- 49 **Organic Molecular Aggregates**
Electronic Excitation and Interaction Processes
Editors: P. Reineker, H. Haken, and H. C. Wolf
- 50 **Multiple Diffraction of X-Rays in Crystals**
By Shih-Lin Chang
- 51 **Phonon Scattering in Condensed Matter**
Editors: W. Eisenmenger, K. Laßmann, and S. Döttinger
- 52 **Superconductivity in Magnetic and Exotic Materials**
Editors: T. Matsubara and A. Kotani
- 53 **Two-Dimensional Systems, Heterostructures, and Superlattices**
Editors: G. Bauer, F. Kuchar, and H. Heinrich
- 54 **Magnetic Excitations and Fluctuations**
Editors: S. W. Lovesey, U. Balucani, F. Borsa, and V. Tognetti
- 55 **The Theory of Magnetism II** Thermodynamics and Statistical Mechanics By D. C. Mattis
- 56 **Spin Fluctuations in Itinerant Electron Magnetism** By T. Moriya
- 57 **Polycrystalline Semiconductors**
Physical Properties and Applications
Editor: G. Harbecke
- 58 **The Recursion Method and Its Applications**
Editors: D. G. Pettifor and D. L. Weaire
- 59 **Dynamical Processes and Ordering on Solid Surfaces** Editors: A. Yoshimori and M. Tsukada
- 60 **Excitonic Processes in Solids**
By M. Ueta, H. Kanazaki, K. Kobayashi, Y. Toyozawa, and E. Hanamura
- 61 **Localization, Interaction, and Transport Phenomena** Editors: B. Kramer, G. Bergmann, and Y. Bruynseraege
- 62 **Theory of Heavy Fermions and Valence Fluctuations** Editors: T. Kasuya and T. Sasó
- 63 **Electronic Properties of Polymers and Related Compounds**
Editors: H. Kuzmany, M. Mehring, and S. Roth
- 64 **Symmetries in Physics** Group Theory Applied to Physical Problems 2nd Edition
By W. Ludwig and C. Falter
- 65 **Phonons: Theory and Experiments II**
Experiments and Interpretation of Experimental Results By P. Brüesch
- 66 **Phonons: Theory and Experiments III**
Phenomena Related to Phonons By P. Brüesch
- 67 **Two-Dimensional Systems: Physics and New Devices**
Editors: G. Bauer, F. Kuchar, and H. Heinrich
- 68 **Phonon Scattering in Condensed Matter V**
Editors: A. C. Anderson and J. P. Wolfe
- 69 **Nonlinearity in Condensed Matter**
Editors: A. R. Bishop, D. K. Campbell, P. Kumar, and S. E. Trullinger
- 70 **From Hamiltonians to Phase Diagrams**
The Electronic and Statistical-Mechanical Theory of sp-Bonded Metals and Alloys By J. Hafner
- 71 **High Magnetic Fields in Semiconductor Physics**
Editor: G. Landwehr
- 72 **One-Dimensional Conductors**
By S. Kagoshima, H. Nagasawa, and T. Sambongi
- 73 **Quantum Solid-State Physics**
Editors: S. V. Vonsovsky and M. I. Katsnelson
- 74 **Quantum Monte Carlo Methods in Equilibrium and Nonequilibrium Systems** Editor: M. Suzuki
- 75 **Electronic Structure and Optical Properties of Semiconductors** 2nd Edition
By M. L. Cohen and J. R. Chelikowsky
- 76 **Electronic Properties of Conjugated Polymers**
Editors: H. Kuzmany, M. Mehring, and S. Roth
- 77 **Fermi Surface Effects**
Editors: J. Kondo and A. Yoshimori
- 78 **Group Theory and Its Applications in Physics**
2nd Edition
By T. Inui, Y. Tanabe, and Y. Onodera
- 79 **Elementary Excitations in Quantum Fluids**
Editors: K. Ohbayashi and M. Watabe
- 80 **Monte Carlo Simulation in Statistical Physics**
An Introduction 4th Edition
By K. Binder and D. W. Heermann
- 81 **Core-Level Spectroscopy in Condensed Systems**
Editors: J. Kanamori and A. Kotani
- 82 **Photoelectron Spectroscopy**
Principle and Applications 2nd Edition
By S. Hüfner
- 83 **Physics and Technology of Submicron Structures**
Editors: H. Heinrich, G. Bauer, and F. Kuchar
- 84 **Beyond the Crystalline State** An Emerging Perspective By G. Venkataraman, D. Sahoo, and V. Balakrishnan
- 85 **The Quantum Hall Effects**
Fractional and Integral 2nd Edition
By T. Chakraborty and P. Pietiläinen
- 86 **The Quantum Statistics of Dynamic Processes**
By E. Fick and G. Sauermann
- 87 **High Magnetic Fields in Semiconductor Physics II**
Transport and Optics Editor: G. Landwehr
- 88 **Organic Superconductors** 2nd Edition
By T. Ishiguro, K. Yamaji, and G. Saito
- 89 **Strong Correlation and Superconductivity**
Editors: H. Fukuyama, S. Maekawa, and A. P. Malozemoff

Springer Series in Solid-State Sciences

Editors: M. Cardona P. Fulde K. von Klitzing H.-J. Queisser

- 90 **Earlier and Recent Aspects of Superconductivity**
Editors: J. G. Bednorz and K. A. Müller
- 91 **Electronic Properties of Conjugated Polymers III** Basic Models and Applications
Editors: H. Kuzmany, M. Mehring, and S. Roth
- 92 **Physics and Engineering Applications of Magnetism** Editors: Y. Ishikawa and N. Miura
- 93 **Quasicrystals** Editors: T. Fujiwara and T. Ogawa
- 94 **Electronic Conduction in Oxides** 2nd Edition
By N. Tsuda, K. Nasu, F. Atsushi, and K. Siratori
- 95 **Electronic Materials**
A New Era in Materials Science
Editors: J. R. Chelikowsky and A. Franciosi
- 96 **Electron Liquids** 2nd Edition By A. Isihara
- 97 **Localization and Confinement of Electrons in Semiconductors**
Editors: F. Kuchar, H. Heinrich, and G. Bauer
- 98 **Magnetism and the Electronic Structure of Crystals** By V.A. Gubanov, A.I. Liechtenstein, and A.V. Postnikov
- 99 **Electronic Properties of High-T_c Superconductors and Related Compounds**
Editors: H. Kuzmany, M. Mehring, and J. Fink
- 100 **Electron Correlations in Molecules and Solids** 3rd Edition By P. Fulde
- 101 **High Magnetic Fields in Semiconductor Physics III** Quantum Hall Effect, Transport and Optics By G. Landwehr
- 102 **Conjugated Conducting Polymers**
Editor: H. Kiess
- 103 **Molecular Dynamics Simulations**
Editor: F. Yonezawa
- 104 **Products of Random Matrices**
in Statistical Physics By A. Crisanti, G. Paladin, and A. Vulpiani
- 105 **Self-Trapped Excitons**
2nd Edition By K. S. Song and R. T. Williams
- 106 **Physics of High-Temperature Superconductors**
Editors: S. Maekawa and M. Sato
- 107 **Electronic Properties of Polymers**
Orientation and Dimensionality of Conjugated Systems Editors: H. Kuzmany, M. Mehring, and S. Roth
- 108 **Site Symmetry in Crystals**
Theory and Applications 2nd Edition
By R. A. Evarestov and V. P. Smirnov
- 109 **Transport Phenomena in Mesoscopic Systems** Editors: H. Fukuyama and T. Ando
- 110 **Superlattices and Other Heterostructures**
Symmetry and Optical Phenomena 2nd Edition
By E. L. Ivchenko and G. E. Pikus
- 111 **Low-Dimensional Electronic Systems**
New Concepts
Editors: G. Bauer, F. Kuchar, and H. Heinrich
- 112 **Phonon Scattering in Condensed Matter VII**
Editors: M. Meissner and R. O. Pohl
- 113 **Electronic Properties of High-T_c Superconductors**
Editors: H. Kuzmany, M. Mehring, and J. Fink
- 114 **Interatomic Potential and Structural Stability**
Editors: K. Terakura and H. Akai
- 115 **Ultrafast Spectroscopy of Semiconductors and Semiconductor Nanostructures**
2nd Edition By J. Shah
- 116 **Electron Spectrum of Gapless Semiconductors**
By J. M. Tsindlekovski
- 117 **Electronic Properties of Fullerenes**
Editors: H. Kuzmany, J. Fink, M. Mehring, and S. Roth
- 118 **Correlation Effects in Low-Dimensional Electron Systems**
Editors: A. Okiji and N. Kawakami
- 119 **Spectroscopy of Mott Insulators and Correlated Metals**
Editors: A. Fujimori and Y. Tokura
- 120 **Optical Properties of III–V Semiconductors**
The Influence of Multi-Valley Band Structures
By H. Kalt
- 121 **Elementary Processes in Excitations and Reactions on Solid Surfaces**
Editors: A. Okiji, H. Kasai, and K. Makoshi
- 122 **Theory of Magnetism**
By K. Yosida
- 123 **Quantum Kinetics in Transport and Optics of Semiconductors**
By H. Haug and A.-P. Jauho
- 124 **Relaxations of Excited States and Photo-Induced Structural Phase Transitions**
Editor: K. Nasu
- 125 **Physics and Chemistry of Transition-Metal Oxides**
Editors: H. Fukuyama and N. Nagaosa
-